Chiral and Helical Boundary Modes Coupled to a Superconductor

Anthony David

THÈSE

Pour obtenir le grade de

DOCTEUR DE L'UNIVERSITÉ GRENOBLE ALPES

École doctorale : PHYS - Physique
Spécialité : Physique Théorique
Unité de recherche : PHotonique, ELectronique et Ingéniérie QuantiqueS

Modes de Bord Chiraux et Hélicoïdaux Couplés à un Supraconducteur

Chiral and Helical Boundary Modes Coupled to a Superconductor

Présentée par :

Anthony DAVID

Direction de thèse :

Manuel HOUZET Directeur de recherche, CEA Centre de Grenoble	Directeur de thèse
Julia MEYER Professeur des Universités, Université Grenoble Alpes	Co-directrice de thèse

Rapporteurs :

JEROME CAYSSOL
Professeur des Universités, UNIVERSITE DE BORDEAUX
SOPHIE GUERON
Directeur de recherche, CNRS DELEGATION ILE-DE-FRANCE SUD

Thèse soutenue publiquement le **7 juillet 2023**, devant le jury composé de :

DENIS BASKO Directeur de recherche, CNRS DELEGATION ALPES	Président
JEROME CAYSSOL Professeur des Universités, UNIVERSITE DE BORDEAUX	Rapporteur
SOPHIE GUERON Directeur de recherche, CNRS DELEGATION ILE-DE-FRANCE SUD	Rapporteure
VINCENT RENARD Maître de conférences HDR, UNIVERSITE GRENOBLE ALPES	Examinateur

GRENOBLE ALPES UNIVERSITY

DOCTORAL SCHOOL OF PHYSICS

P H D T H E S I S

to obtain the title of

PhD of Science

of the Grenoble Alpes University
Specialty : Theoretical Physics

Defended by

Anthony David

Chiral and Helical Boundary Modes Coupled to a Superconductor

Thesis Advisors: Manuel Houzet and Julia Meyer

prepared at the Quantum Photonics, Electronics and Engineering Laboratory (PHELIQS)

defended on July 7, 2023

Jury :

Reviewers:	Jérôme Cayssol	-	Université de Bordeaux, LOMA
	Sophie Guéron	-	CNRS, LPS
Examinators:	Denis Basko (President)	-	CNRS, LPMMC
	Vincent Renard	-	Université Grenoble Alpes, PHELIQS

Modes de Bord Chiraux et Hélicoïdaux Couplés à un Supraconducteur

Résumé:
Depuis la découverte de l'effet Hall quantique (QH), les physiciens ont réalisé que la distinction entre un isolant et un conducteur n'est pas aussi simple que la théorie des bandes des solides le suggère. En effet, un métal normal dans le régime QH devient isolant dans son coeur et présente des états de bord conducteurs. Un tel système avec un coeur isolant et une frontière conductrice est appelé un isolant topologique, qui est à l'origine du domaine de recherche moderne des phases topologiques de la matière. Dans cette thèse, nous étudions les conséquences de l'induction de corrélations supraconductrices dans différents types de modes de bord à travers trois projets.
Nous considérons d'abord une région QH en contact avec un supraconducteur (SC), c'est-à-dire une jonction QH-SC. En raison de réflexions d'Andreev successives, l'interface QH-SC héberge des états de bord hybrides d'électrons et de trous appelés états de bord d'Andreev chiraux (CAES). Nous étudions théoriquement le spectre d'énergie et les propriétés de transport de ces CAES en utilisant des approches microscopiques, de liaisons fortes, et effective. De manière intéressante, nous trouvons que leurs propriétés de transport dépendent fortement de la géométrie du contact supraconducteur et de la valeur du facteur de remplissage.
Le second projet est une extension du premier dans lequel nous étudions le couplage entre des paires de CAES contre-propageantes dans des jonctions QH-SC-QH. La présence de la deuxième région QH permet les processus de diffusion non locaux de co-tunnellisation élastique et de réflexion d'Andreev croisée, tandis que les réflexions normales et d'Andreev sont toujours autorisées. Nous étudions le spectre d'énergie des paires de CAES contre-propageantes en utilisant un modèle microscopique bidimensionnel et nous développons un modèle effectif unidimensionnel pour étudier les propriétés de transport de la jonction.
Dans le dernier projet, nous étudions les effets des couplages Zeeman et supraconducteur sur les modes hélicoïdaux de charnière d'un isolant topologique d'ordre supérieur. Le couplage Zeeman divise spatialement la paire hélicoïdale en deux états chiraux, créant une région de Hall quantique anormale, tandis que le couplage supraconducteur divise les modes hélicoïdaux en deux modes de Majorana hélicoïdaux. La combinaison des couplages Zeeman et supraconducteur conduit à différents scénarios de séparation en fonction du rapport entre les deux couplages. Nous dérivons les fonctions d'onde correspondantes et analysons les différents scénarios de séparation en effectuant des simulations de liaisons fortes.
Mots clés: Effet Hall Quantique, Supraconductivité, Réflexion d'Andreev, Modes de Bord, Isolants Topologiques, Modes de Majorana

Chiral and Helical Boundary Modes Coupled to a Superconductor

Abstract:
Since the discovery of the quantum Hall (QH) effect, physicists have realized that the distinction between an insulator and a conductor is not as simple as the band theory of solids would suggest. Indeed, a normal metal in the QH regime becomes insulating in the bulk and exhibits conducting edge states. Such a system with an insulating bulk and a conducting boundary is called a topological insulator, which is the origin of the modern research field of the topological phases of matter. In this thesis, we study the consequences of inducing superconducting correlations in different types of boundary modes through three projects.
We first consider a QH region in contact with a superconductor (SC), i.e., a QH-SC junction. Due to successive Andreev reflections, the QH-SC interface hosts hybridized electron and hole edge states called chiral Andreev edge states (CAES). We theoretically study the energy spectrum and the transport properties of these CAES by using microscopic, tight-binding and effective approaches. Interestingly, we find that their transport properties strongly depend on the contact geometry and the value of the filling factor.
The second project is an extension of the first one in which we study the coupling between counter-propagating pairs of CAES in QH-SC-QH junctions. The presence of the second QH region allows for the non-local scattering processes of elastic co-tunneling and crossed Andreev reflection while normal and Andreev reflections are still allowed. We study the energy spectrum of the counter-propagating pairs of CAES by using a two-dimensional microscopic model and we develop a one-dimensional effective model to investigate the transport properties the junction.
In the last project, we consider the helical modes of a higher order topological insulator (HOTI). A HOTI generalizes the concept of topological insulator so that the boundary modes appear at corners or hinges. Here we investigate the effects of Zeeman and superconducting couplings on helical hinge modes. The Zeeman coupling spatially splits the helical pair into two chiral states enclosing a quantum anomalous Hall region, while the superconducting coupling divides the helical modes into two helical Majorana modes. The combination of both Zeeman and superconducting couplings leads to different splitting scenarios depending on the ratio between the two couplings. We derive the corresponding wave functions and analyze the different splitting scenarios by performing tight-binding simulations.
Keywords: Quantum Hall Effect, Superconductivity, Andreev Reflection, Boundary Modes, Topological Insulators, Majorana Modes

Acknowledgments

Writing this manuscript marks the end of my studies. Although it has not always been a smooth ride, it has been an exciting time. I would like to thank everyone who has supported me during this period.

First of all, I would like to thank my supervisors, Julia and Manuel, for giving me the opportunity to do my PhD in the field I wanted to. Among other things, you taught me to be rigorous and autonomous, and these qualities will serve me for the rest of my life. Thank you for guiding me through this thesis.

My thanks are also due to my colleagues in the office, Baptiste, Yoan and Thomas. Our exchanges on our respective projects have been fascinating and often a source of inspiration. I also enjoyed discussing everyday things with you in our free time, and it is certain that these PhD years would not have been the same without you.

I would also like to thank all the members of the theory group for being so kind to me when I first arrived and for helping me find solutions to some of the problems I encountered in my research. I would especially like to thank Christoph and Xavier for answering my many questions about using Kwant.

I'm not forgetting the people I met in the different teams in Grenoble. I think of the members of Pheliqs, the Néel Institute and the LPMMC. I have a thought for all of you.

I am also grateful to all those with whom I have had the opportunity to exchange ideas at conferences and physics schools. These meetings have been enriching and have often allowed me to see my work in a new light. Special thanks to Alexey for the enlightening discussions about chiral Andreev edge states.

I also have a thought for my undergraduate and graduate classmates. I think of those with whom I had many discussions about our lectures and who accompanied me in the development of my passion for theoretical physics. In particular, I would like to thank Léo, Liam, Alexis, Lucas, Valéry and Louis for contributing to the success of my studies.

And as they say in French, "j'ai gardé le meilleur pour la fin". It is of course my family that I am thinking of while writing this. Thank you all for always being there for me and for your unconditional support. Thank you, my grandparents, for your interest in my studies and for your moral and financial assistance. Thank you to my sister and my childhood friends for encouraging me and helping me when I needed it, especially during my many moves. Finally, thank you Mom and Dad, it is mainly because of you that I was able to do these studies and I will never find enough words to tell you how grateful I am. I love you all.

Contents

List of Acronyms

Chapter 1

Introduction

Solid-state systems are an important area of study within condensed matter physics, focusing on the properties and behavior of materials in their solid state. In this thesis, we focus on crystalline solids (as opposed to amorphous solids), in which the atoms are arranged in a highly ordered and periodic crystal lattice. A fundamental property of solids is that electrons are shared between atoms, allowing them to move around the crystal. The available states for these mobile electrons form energy bands, which can be calculated thanks to the Bloch theorem. According to the Pauli principle, at zero temperature the states are filled up to a threshold known as the Fermi level. Since driving a current requires creating excitations, there must be states near the Fermi level for the solid to be a conductor. If there are no states at the Fermi level, the solid is an insulator. Thus, in a conductor (also called a metal) the Fermi level is within a band, while in an insulator the Fermi level is between two bands, i.e. in an energy gap. In condensed matter physics, the bulk of a material refers to its interior, as opposed to the boundary, which refers to its edge or surface. In many cases, knowledge of the bulk spectrum is sufficient to characterize the transport properties of the system. However, this idea was completely overturned with the discovery of the quantum Hall effect by von Klitzing in 1980 [von Klitzing *et al.* 1980], which we are about to discuss.

Indeed, von Klitzing discovered that when a two-dimensional system of electrons is subjected to a strong perpendicular magnetic field, the transverse resistance of the material, also called the Hall resistance, becomes quantized. This experimental discovery earned von Klitzing the Nobel Prize in Physics in 1985. The Hall resistance is a measure of the transverse voltage that is produced by an applied current in a magnetic field. Consider a magnetic field $\vec{B}$ in the z-direction, an applied current I_x in the x-direction, and a transverse voltage V_y, see Fig. 1.1a. Then the classical Hall effect is due to the Lorentz force acting on the electric current I_x (which is subject to the magnetic field) leading to a non-zero transverse voltage V_y, called the Hall voltage, perpendicular to the magnetic field. The effect can be observed by measuring the Hall resistance, defined as $R_H = V_y/I_x$, and classically one observes a linear increase of R_H with the magnetic field. For the quantum Hall effect, on the other hand, the Hall resistance exhibits plateaus that take on the quantized values $R_H = (1/\nu)h/e^2$, where ν is a positive integer, e is the electron charge, h is Planck's constant, and the ratio $h/e^2 \simeq 26k\Omega$ is the quantum of resistance. A measurement of the Hall resistance against the strength of the applied magnetic field is shown in Fig. 1.1b. In this figure we observe a linear increase of the Hall resistance at low fields and we clearly see the Hall plateaus at high fields. Classically, when a two-dimensional electron system is subjected to a perpendicular magnetic field, the electrons in the bulk move in circular cyclotron orbits at the cyclotron frequency $\omega_c = eB/m$, where m is the electron mass. Along the edges of the sample, however, the cyclotron orbits cannot be executed in such a way that the trajectory bounces back, resulting in unidirectional propagation of the electrons along the edges, as shown in Fig. 1.2. These edge states are the so-called chiral edge states of the quantum Hall effect. It turns out that the integer ν, which appears in the quantum definition of the Hall resistance, is nothing else than the number of chiral edge states. Thus, we can understand the quantum Hall effect as the consequence of a quantized number of chiral edge states participating in the Hall conductance, which is the inverse of the Hall resistance. Quantum mechanically, the confinement of the electrons to the cyclotron orbits leads to the formation of Landau levels [Landau 1930], which are quantized energy levels given by $E_n = (n + 1/2)\hbar\omega_c$, where n is a positive integer (note that each Landau level is spin-degenerate). Two consecutive Landau levels are thus separated by an energy gap $\hbar\omega_c$. In general, the Fermi energy is in such an energy gap, making the bulk of the material insulating. However, the Landau levels are bent upward in energy for states localized near the edges, so that at the edges the Fermi level is no longer in an energy gap and conducting edge states appear [Halperin 1982]. From this point of view, the number of chiral edge states is given by the

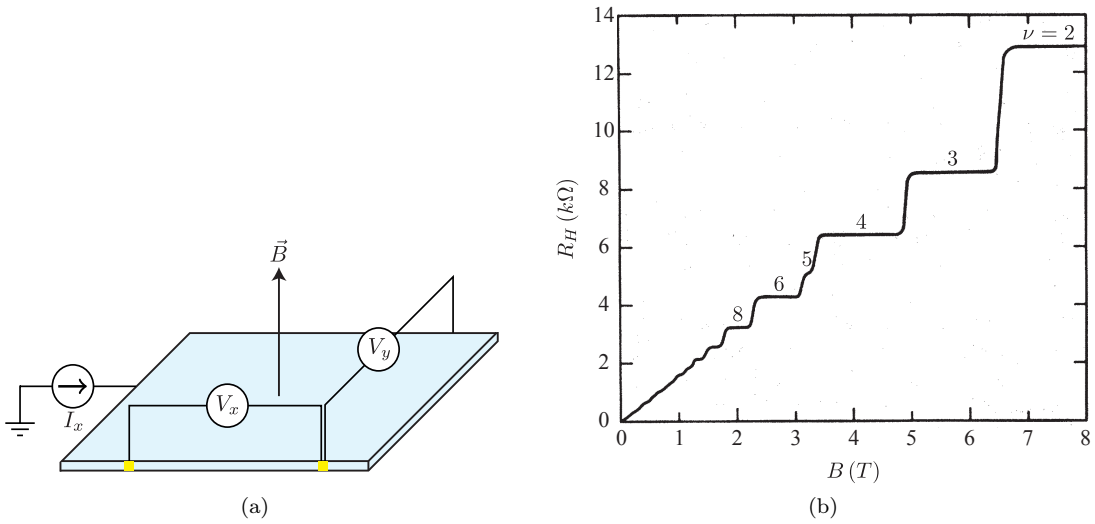

Figure 1.1: Quantum Hall effect. In (a) we show a setup that can be used to measure the Hall resistance $R_H = V_y/I_x$ and in (b) we show the measurement of R_H against the strength of the applied magnetic field B reported in Ref. [Paalanen *et al.* 1982]. As expected, in the classical regime of low B-fields, the Hall resistance increases linearly with B while it exhibits steps at large fields. The associated Hall plateaus are labelled by $\nu = 2, 3, \cdots$.

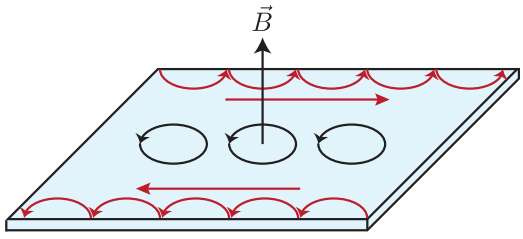

Figure 1.2: Chiral edge states of the quantum Hall effect. At the boundaries of the sample, the circular cyclotron motion cannot be performed due to collisions and so the trajectories are a sequence of skipping orbits leading to a unidirectional motion along the edges. Such a unidirectional motion is said to be chiral and, at opposite edges, the electrons move in opposite directions.

number of Landau levels below the Fermi level multiplied by two to account for spin-degeneracy. Such a material with an insulating bulk and conducting edge states is now called a topological insulator. In fact, the quantum Hall effect is the first example of such materials, and its topological origin was proposed by Thouless, Kohmoto, Nightingale, and den Nijs (TKNN) in 1982 [Thouless *et al.* 1982], who showed that the integer ν is actually a topological invariant called the Chern number (or TKNN invariant for the special case of the quantum Hall effect). For this discovery, Thouless was awarded half of the 2016 Nobel Prize in Physics, together with Haldane and Kosterlitz, "for theoretical discoveries of topological phase transitions and topological phases of matter". Hence, this discovery marked the birth of topological insulators, which are explained by a new band theory called topological band theory. Indeed, these materials have a peculiar band structure characterized by a bulk band gap insulating the material's interior and topologically protected metallic edge states allowing electron transport. The metallic edge states are protected by the topology of the electronic wave functions, which cannot be smoothly changed without closing and reopening the bulk gap. This makes the edge states of topological insulators highly resistant to the formation of defects or impurities that would otherwise disrupt the flow of electrons. Because of this robustness, the quantum Hall effect has a number of important applications in metrology and precision measurement, as the quantized Hall resistance provides a standard for electrical resistance.

So far we have only discussed the quantum Hall effect and characterized it as a topological insulator due to the presence of chiral edge states that appear when a strong magnetic field is applied. However, there are also materials that exhibit chiral edge states without an applied magnetic field. These materials have the same quantized resistance as for the quantum Hall effect and are called quantum anomalous Hall insulators, where the word anomalous comes from the fact that no external magnetic field is required. The effect was first proposed by Haldane in a tight-binding model on a honeycomb lattice with real nearest-neighbor hopping and complex next-neighbor hopping [Haldane 1988]. Haldane showed that this model allows for a non-zero Chern number even if no external magnetic field is applied. Hence, the quantum Hall and quantum anomalous Hall effects are two phases exhibiting chiral edge states, the number of which is given by the Chern number. Such topological insulators are called Chern insulators. Note that Chern insulators break time-reversal symmetry, since reversing the direction of time would cause the electrons to move in the opposite direction.

Chern insulators are only the beginning. In fact, there are many other topological phases. In two dimensions, another possible topological phase is the quantum spin Hall insulator in which time-reversal symmetry is preserved. This phase is thus referred as a time-reversal invariant topological insulator. A consequence of time-reversal invariance is that every state at a given energy has a time-reversal symmetric partner at the same energy. This is known as Kramers degeneracy. As a consequence of Kramers degeneracy, a two-dimensional time-reversal invariant topological insulator exhibits helical edge states, which are pairs of counter-propagating electronic states of opposite spins (thus we speak of spin-momentum locking) [Kane & Mele 2005]. This phase has been predicted [Bernevig *et al.* 2006] and, soon after, observed [Konig *et al.* 2007] in HgTe quantum wells via longitudinal resistance measurements. These helical edge states survive as long as time-reversal symmetry is not broken, i.e., they are protected by time-reversal symmetry. In addition, quantum spin Hall insulators are also characterized by a topological invariant $\nu_{\mathbb{Z}_2}$, called the $\mathbb{Z}_2$ invariant, which tells whether there is a helical pair of edge states ($\nu_{\mathbb{Z}_2} = 1$, topological phase) or no edge states ($\nu_{\mathbb{Z}_2} = 0$, trivial phase). Thus, there is only two possible phases for time-reversal invariant insulators while Chern insulators have an infinite number of phases (the Chern number can be any integer).

We have explained the existence of the chiral edge states of the quantum Hall effect in terms of the semi-classical skipping orbits or in terms of the bending of the Landau levels. We can give another explanation based on the low-energy description of the edge states. Indeed, since they have a linear dispersion at low energy, we can describe the edge states using Dirac-like Hamiltonians. Actually, a Dirac Hamiltonian without a mass term gives a gapless linear dispersion, while the presence of a mass term m leads to an energy gap. Describing the quantum Hall effect as a junction between a two-dimensional electron gas (2DEG) and the vacuum, where the bulk of the 2DEG as well as the vacuum are gapped, the corresponding Dirac Hamiltonian should have a mass term m that is non-zero in these regions but vanishes at the 2DEG-vacuum interface. In fact, the bending of the Landau levels indicates that such a mass term changes sign at the 2DEG-vacuum interface, where it is negative inside the 2DEG, tends to infinity in the vacuum, and passes through zero at the interface. The junction thus forms a mass domain

wall, and it can be shown that for such domain walls there is always a localized state where the mass term vanishes [Jackiw & Rebbi 1976]. It turns out that we can always understand the presence of edge states by using Dirac Hamiltonians with a mass term that changes sign at the edge [Shen *et al.* 2011]. The corresponding system always consists in a junction between two phases with different topological invariants. For the edge states of Chern insulators this corresponds to a junction between a phase with a non-zero Chern number and a phase with a Chern number equal to zero, while for the quantum spin Hall insulator the junction consists of a region with $\nu_{\mathbb{Z}_2} = 0$ and one with $\nu_{\mathbb{Z}_2} = 1$.

Until now we have only considered two-dimensional topological insulators, which host one-dimensional edge states. The concept of a topological insulator can be generalized to d dimensions as follows: a d-dimensional topological insulator hosts $(d-1)$-dimensional boundary states. Thus, a three-dimensional topological insulator has two-dimensional surface states, and a one-dimensional topological insulator has point-like modes at the ends of the one-dimensional wire. Conventional topological insulators are those in which the edge states are protected by time-reversal (quantum spin Hall insulators), particle-hole, or chiral symmetry, or those in which none of these symmetries is present (Chern insulators). Depending on the symmetries that are present or absent, different types of phases are possible. In fact, there are ten possible classes, known as the 10-fold classification of topological phases [Altland & Zirnbauer 1997]. However, new classes are possible when considering crystalline symmetries. Indeed, there are materials with topological boundary modes that are protected by a crystal symmetry such as inversion, rotation, or mirror symmetry. Topological insulators whose boundary modes are protected by a crystal symmetry are called topological crystalline insulators [Fu 2011]. It turns out that topological crystalline insulators have boundaries that do not always preserve the relevant crystalline symmetry by themselves, but preserve it at their $(d-n)$-dimensional boundaries. In this case the material is called a higher order topological insulator and exhibits $(d-n)$-dimensional boundary modes, where n is the order. In this work we are interested in a three-dimensional topological insulator of order two that preserves time-reversal symmetry. Namely, a three-dimensional material (such as a cube) with one-dimensional helical hinge modes. Here the hinges realize natural mass domain walls where the mass term on two adjacent faces has opposite signs. Such helical hinge modes protected by mirror symmetry were first predicted in strained SnTe [Schindler *et al.* 2018a]. Shortly thereafter, helical hinge modes protected by a combination of mirror and inversion symmetry have been predicted and observed in bismuth using scanning tunneling microscopy and Josephson interferometry [Schindler *et al.* 2018b].

In the preceding we have discussed one milestone of condensed matter physics which is the discovery and the theoretical understanding of the quantum Hall effect leading to the concept of topological insulators. Another cornerstone in condensed matter physics is the phenomenon of superconductivity. Superconductivity is a phenomenon in which a material (a superconductor) can conduct electricity with zero resistance, meaning that electrical current can flow through it without any loss of energy. This is in contrast to normal conductors, where there is always some resistance to the flow of electrical current, which causes energy to be lost as heat. Superconductivity was first observed in 1911 by the Dutch physicist Kamerlingh Onnes, who was investigating the properties of metals at low temperatures (for a review, see [van Delft & Kes 2010]). He found that the resistance of mercury dropped dramatically to zero as he cooled it below a critical temperature. This marked the discovery of superconductivity and led Onnes to the 1913 Nobel Prize in Physics. Since then, superconductivity has been observed in a wide variety of metals, alloys, and compounds, including elementary metals such as aluminum, lead, and tin, as well as complex compounds such as cuprates, iron pnictides, and heavy fermion compounds. In addition to being a perfect conductor of electricity, a superconductor also repels magnetic fields as long as they are not stronger than a so-called critical magnetic field. This repulsion of magnetic fields is known as the Meissner effect, named after its discoverer, Walter Meissner [Meissner & Ochsenfeld 1933]. The effect occurs because when a magnetic field is applied to a superconductor, it induces electric currents on the surface of the material which generate an opposing magnetic field that exactly cancels out the applied field. Above the critical field, the superconductor transitions to the normal state, where it behaves like a normal conductor. In general, the critical field increases with decreasing temperature.

The first microscopic theory of superconductivity was developed by Bardeen, Cooper, and Schrieffer (BCS) and proposed that superconductivity arises due to the formation of pairs of electrons known as Cooper pairs [Bardeen *et al.* 1957]. The formation of Cooper pairs is explained by an effective attractive

interaction between electrons resulting from the exchange of phonons. Phonons are quanta of lattice vibrations, and they can mediate an effective attractive interaction between electrons in a metal. To simplify the problem of describing the attractive interaction between electrons, BCS theory introduces a simplified model. In this model, the attractive interaction between electrons is assumed to be a constant value in an energy window around the Fermi level. This assumption is based on the idea that the main contribution to the effective attractive interaction comes from interactions between electrons near the Fermi level. The final step in BCS theory is to use mean-field theory to describe the attraction between the electrons. Mean-field theory is a method that allows one to approximate the interactions between particles in a system as a mean or average field. The formation of Cooper pairs leads to a gap 2Δ in the energy spectrum of the metal, where Δ is called the superconducting gap. This gap 2Δ corresponds to the energy required to break a Cooper pair and is a signature of superconductivity. Bardeen, Cooper, and Schrieffer were awarded the 1972 Nobel Prize in Physics for their theory of superconductivity. In this thesis we always consider BCS (or s-wave) superconductors in which the Cooper pairs are made of two electrons having opposite spins and momenta.

A striking effect of superconductivity occurs when a normal metal is brought into contact with a superconductor, forming a normal metal-superconductor junction. In such a junction, an incident electron from the normal metal with energy $|E| < \Delta$ cannot enter the superconductor, and so it is reflected. The striking effect then comes from the way this incident electron is reflected. Indeed, it can be reflected as an electron via a normal reflection process, but it can also be reflected as a hole via the process of Andreev reflection, while at the same time a Cooper pair is transferred into the superconductor [Andreev 1965]. Note that in this Andreev reflection process, the total charge of the outgoing particles (a Cooper pair of charge $-2e$ and a hole of charge $+e$) is equal to the charge of the incoming electron, so charge conservation is ensured.

Having discussed the edge states of topological insulators and the phenomenon of superconductivity, we now ask how the edge states are affected by superconductivity. First, consider a junction between a quantum Hall insulator and a superconductor. When propagating along the superconductor, the chiral edge states of the quantum Hall effect become hybridized electron-hole edge states, called chiral Andreev edge states. Since we study the chiral Andreev edge states extensively in this thesis, we will discuss them in more detail below. Second, inducing superconducting correlations in the helical edge states of a quantum spin Hall insulator leads to an effective p-wave pairing and opens a gap in the spectrum (p-wave pairing corresponds to Cooper pairs made of spin-polarized electrons). However, due to domain walls created by the combination of superconducting and magnetic regions, a Majorana zero mode is expected to appear at the interface between a superconductor and a ferromagnet when they are deposited on top of a quantum spin Hall insulator [Fu & Kane 2008] (the concept of a Majorana zero mode is introduced below). On the other hand, inducing superconducting correlations in the helical hinge modes of a higher-order topological insulator can have a different effect. In fact, under certain conditions, the helical pair of fermionic modes can remain gapless and be transformed into two pairs of helical Majorana modes [Queiroz & Stern 2019]. We will give more details on this at the end of this introduction, as it is the subject of the last research project of the manuscript.

Superconductivity and the quantum Hall effect were initially thought to be incompatible because the latter requires a strong magnetic field, which tends to destroy superconductivity. However, in the early 2000s, advances in materials processing and the discovery of superconductors with high critical magnetic fields, such as NbN, made it possible to design hybrid systems composed of these two phases. The conceptually simplest system involving both the quantum Hall effect and superconductivity consists of a quantum Hall-superconductor (QH-SC) junction and provides a new type of edge states, called chiral Andreev edge states (CAES), due to Andreev reflections occurring at the QH-SC interface. From a semi-classical point of view, these CAES result from alternating skipping orbits of electrons and holes due to successive Andreev reflections (see Fig. 1.3a), while from a quantum point of view, the edge states along the QH-SC interface are described as hybridized electron and hole states (see Fig. 1.3b). One of the first experiments reporting clear evidence for the influence of Andreev reflection on the transport properties of edge states is presented in Ref. [Eroms *et al.* 2005]. In this paper, the authors used an InAs-Nb hybrid structure consisting of several Nb stripes, where the Nb stripes have a critical field of up to 2.6 T, allowing to enter the Hall regime with a large number of edge states (from $\nu = 16$ to

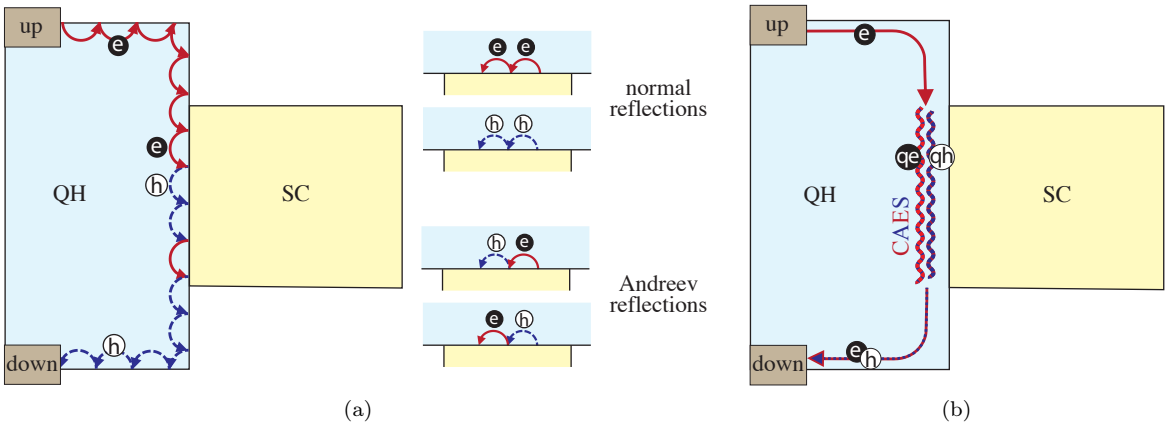

Figure 1.3: Chiral Andreev edge states at a QH-SC interface. An incoming electron (e) from the upstream (up) reservoir can be transmitted to the downstream (down) reservoir as an electron or as a hole after propagating along the QH-SC interface as a chiral Andreev edge state. (a) Semi-classical picture of electron and hole alternating in skipping orbits due to successive reflection processes. Note that the hole has the same chirality as the electron, because the signs of its charge and mass are both opposite to those of the electron so that the Lorentz force acts the same way on both particles. Here we show the situation where the incoming electron exits the superconductor as a hole. We have depicted the different reflection processes which are categorized between normal and Andreev reflections. (b) Quantum picture where the incoming electron propagates along the QH-SC interface as a superposition of quasi-electron (qe) and quasi-hole (qh) CAES and exits the superconductor in a superposition of electron and hole.

$\nu = 60$). Note that we are not in the quantum regime here, since there are no Hall plateaus at these values of ν. The experiment then consisted in measuring the longitudinal resistance of the junction as a function of the applied magnetic field, i.e. the magnetoresistance, and showed enhanced magnetoresistance oscillations in the superconducting phase, interpreted as electron-hole interference. This was a clear signature of CAES interference, but it involved a large number of edge states. This could have been the end of the story but, as often happens, a discovery has once again revolutionized this field of research. Indeed, the possibility to isolate graphene monolayers has given a second life to the study of two-dimensional systems. A graphene monolayer is a single layer of carbon atoms arranged in a two-dimensional honeycomb lattice structure and it has numerous applications in physics, electronics, materials science and engineering due to its remarkable electronic and mechanical properties. It has been properly isolated for the first time in 2004 [Novoselov *et al.* 2004] leading A. Geim and K. Novoselov to the 2010 Nobel Prize in Physics "for groundbreaking experiments regarding the two-dimensional material graphene". Owing to its unique band structure, graphene requires a relatively weak magnetic field (of the order of one Tesla) to enter the quantum Hall effect regime where a single Landau level is filled. This has allowed new experiments on CAES where there is only one or a few quantum Hall edge states [Lee *et al.* 2017, Zhao *et al.* 2020] and even in the fractional quantum Hall regime [Gül *et al.* 2022]. More recently, advances in fabrication techniques have also allowed CAES to be observed in the regime of a few quantum Hall edge states using an InAs heterostructure [Hatefipour *et al.* 2022]. In these recent experiments the superconductivity is not destroyed up to strong enough magnetic fields such that only one spin-degenerate Landau level is filled, i.e., there are two chiral edge states. Introducing particle-hole space to be able to incorporate superconductivity, we can describe one spin state as an electron state and the other spin state as a hole state. In these experiments, the authors observed evidence for CAES in the so-called downstream conductance. Namely, the downstream conductance measures the conversion of upstream electrons into downstream holes, involving the transfer of Cooper pairs into the superconductor along the interface. For one incoming electron, it is given by $G_d = G_0(1 - 2P_h)$, where $G_0 = 2e^2/h$ is the quantum of conductance (here the factor two stands for the spin-degeneracy) and P_h is the probability for the incoming electron from the upstream reservoir to be transmitted into the

downstream reservoir as a hole, see Fig. 1.3b. It follows that a negative downstream conductance is a clear signature of the conversion of the incoming electron into an outgoing hole and thus a hallmark of CAES propagation along the superconducting interface. While the experiments discussed above have indeed measured negative downstream conductances, the observed signal is much smaller than expected. Furthermore, it either shows an irregular pattern [Lee *et al.* 2017, Zhao *et al.* 2020, Gül *et al.* 2022] or remains roughly constant [Hatefipour *et al.* 2022] as the field or the position of the Fermi level is swept, while simple models predict a regular oscillation. This has stimulated further theoretical research. A suppression of the measured signal can be explained by the absorption of quasiparticles in the superconductor [Zhao *et al.* 2020, Kurilovich *et al.* 2022, Manesco *et al.* 2022, Schiller *et al.* 2022], while the oscillations can be strongly affected by disorder [Kurilovich *et al.* 2022, Manesco *et al.* 2022].

In this thesis, we explore a different aspect that has not been addressed before: the role of the geometry. Namely the downstream conductance does not probe only the properties of the QH-SC interface, but also the scattering properties at the point where this interface meets the QH-vacuum interface. We find that these scattering probabilities strongly depend on the geometry of the contact region and on the position of the Fermi level. Thus, a full two-dimensional description of the system is required, implying that the simple one-dimensional models commonly used in the literature are not sufficient. In particular, a strong dependency on the angle between the QH-vacuum interface and the QH-SC interface is observed. Interestingly, this opens up the possibility of creating asymmetric structures where these angles are different on both sides of the superconductor, which may exhibit an overall enhanced electron-hole conversion probability. This may even lead to a situation where the downstream conductance becomes negative on average. Moreover, we show that the most general effective one-dimensional model containing a complex pairing potential localized in the region where the QH-vacuum edge meets the QH-SC edge allows one to reproduce these dependencies. However, there is no way to fix the effective parameters unless performing a full two-dimensional simulation, implying that a two-dimensional description of the system is necessary. Our results are published in Ref. [David *et al.* 2023].

However, in the experiments of Refs. [Lee *et al.* 2017, Gül *et al.* 2022], the authors used a geometry with a finger-shaped superconductor as depicted in Fig. 1.4. In this figure, we represent two different regimes depending on the width of the superconducting finger W compared with the superconducting

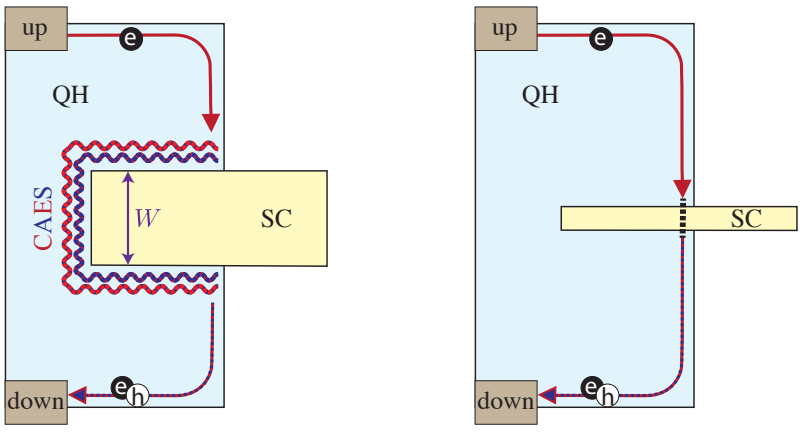

Figure 1.4: Andreev reflection of quantum Hall edge states with a superconducting finger. In (a) the width W of the finger is large compared to the superconducting coherence length. In this case, the incoming electron propagates along the superconductor as a CAES and exits as a superposition of electron and hole. In (b) we represent a narrow finger so that the incoming electron tunnels through it and is transmitted on the other side as an electron by elastic co-tunnelling or as a hole by crossed Andreev reflection.

coherence length ξ (in the BCS theory the superconducting coherence length characterizes the size of a Cooper pair and is given by $\xi = \hbar v_F/\Delta$, where v_F is the Fermi velocity). If $W \gg \xi$, the incoming electron will propagate along the edge of the superconductor as a CAES (Fig. 1.4a). This situation is similar to the one discussed above, as it involves only the propagation of CAES along the superconductor. However, when $W \ll \xi$ there are new scattering processes. Indeed, in this case the incoming electron can tunnel through the superconducting finger and continue to flow on the other side as an electron via elastic co-tunnelling or as a hole via crossed Andreev reflection (Fig. 1.4b).

In this manuscript, we study the non-local processes of crossed Andreev reflection by considering a quantum Hall-superconductor-quantum Hall (QH-SC-QH) junction with a ribbon geometry. We use a microscopic model to determine the energy spectrum of the junction. In this geometry, the edge states on either side of the superconductor are gapped due to their hybridization by elastic co-tunnelling and crossed Andreev reflections. This hybridization gap decays exponentially with the width of the superconductor on the scale of the superconducting coherence length.

As a next step, we performed a preliminary study of the transport properties using an effective one-dimensional model, which allows one to gain a qualitative understanding of the effect of these new processes. We determine the effective parameters using our microscopic results, allowing a semi-analytical study of the spectrum and transport properties of this type of junction (semi-analytical because the secular equation determining the energy spectrum is solved numerically). As expected, for $W/\xi \to \infty$ we find that the QH-SC-QH junction behaves as two independent QH-SC interfaces with no non-local processes. Interestingly, we find regimes where the crossed Andreev reflection is dominant. Note that, to obtain quantitative results, a two-dimensional model should be used to calculate them. Indeed, as we discussed for the QH-SC junction, the scattering probabilities depend strongly on the geometry of the system, which cannot be taken into account with an effective one-dimensional model. We did not use a two-dimensional model to calculate the transport properties due to time constraints, but it would be interesting to see how the effects of geometry change our results. This work is a preliminary step towards studying a system with a finger-shaped superconductor. Moreover, as we discuss below, it would be interesting in further studies to consider the case of spin-polarized electrons because of its potential for topologically protected quantum computing.

The use of a superconducting finger in the experiments [Lee *et al.* 2017, Gül *et al.* 2022] was motivated by the possibility of creating a Majorana zero mode at the end of the finger when it is spin-polarized. A Majorana zero mode is a type of quasiparticle excitation in condensed matter physics that is its own antiparticle (unlike electrons and positrons). This concept was introduced by the Italian physicist Ettore Majorana in 1937 [Majorana 1937] in the context of particle physics, and in this context we speak of Majorana fermions. Because it is its own antiparticle, a Majorana fermion is electrically neutral. This led Majorana to suggest that neutrinos might actually be Majorana fermions. However, despite intensive efforts, Majorana fermions have never been observed in particle physics experiments. On the other hand, condensed matter physicists are also searching for Majorana modes in a wide variety of solid state systems (for a review, see [Alicea 2012]). A famous proposal for such a realization is the toy model proposed by Kitaev [Kitaev 2001], known as the Kitaev chain (see Fig. 1.5). It is a chain of spinless electrons that

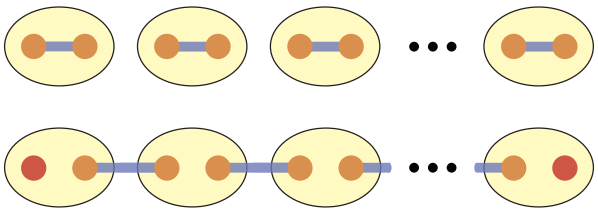

Figure 1.5: Kitaev model. One can imagine each electron located at the sites of a chain as the superposition of two half-electrons. In usual superconductors (top), the two half-electrons of the same site remain strongly bound. On the other hand, in a topological superconductor (bottom), the bonding is realized between two half-electrons of adjacent sites. This leaves two free half-electrons (red circles) at each end of the chain: the Majorana zero modes.

can move between sites in a one-dimensional lattice, in the presence of an attractive potential between

two electrons located on adjacent sites. In a generic way, each ordinary electron can be represented by a complex number, whose real and imaginary parts describe the two Majorana quasiparticles of which it is made up: two "half-electrons" (this is known as the Majorana representation of the electron). As long as these two Majorana quasiparticles are linked, such a decomposition remains formal, because it has no measurable consequence. Kitaev has shown that there is a phase of the chain, a topological phase, where two Majorana quasiparticles on neighboring sites recombine to form an ordinary fermionic state with finite energy. This leaves one Majorana zero mode without a partner at each of the sites at the two ends of the chain. The major problem of the Kitaev model is that spinless superconductors do not exist in nature since electrons have a spin. However, it is possible to make systems that behave like spinless superconductors in the laboratory. This requires applying a magnetic field to a wire with strong spin-orbit coupling in the vicinity of a BCS superconductor [Lutchyn *et al.* 2010, Oreg *et al.* 2010]. The idea is to spin-polarize the wire with the magnetic field thanks to the Zeeman effect, thus mimicking spinless electrons by freezing the spin degree of freedom. The next step is to connect the spin-polarized wire to the BCS superconductor to make it superconducting by the proximity effect. Moreover, since the wire is spin-polarized, it should have a strong spin-orbit coupling such that Cooper pairs can form. It turns out that the quantum Hall-superconductor hybrid system with a narrow superconducting finger (Fig. 1.4b) is a perfect match to engineer the Kitaev chain. Indeed, if the applied magnetic field is strong enough to fill only one spin-polarized Landau level, and if the two-dimensional electron system is made of a material with strong spin-orbit coupling, such as InAs, this platform has all the necessary ingredients to mimic a one-dimensional spinless superconductor. In this case, the quantum Hall region below the superconducting finger corresponds to the required wire, and a Majorana zero mode is expected at the end of the finger, as shown in Fig. 1.6.

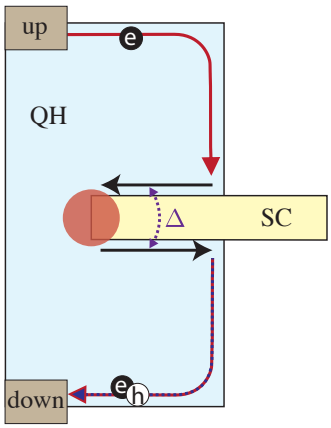

Figure 1.6: Quantum Hall-superconductor hybrid system where the superconducting electrode has a finger shape. The counter-propagating CAES (black arrows) are coupled and gapped by Δ, resulting in a Majorana zero mode at the end of the superconductor (red circle).

Majorana zero modes have attracted a lot of interest in the scientific community due to their potential applications in topological quantum computing. Unlike classical bits, quantum bits, or qubits, can exist in multiple states simultaneously, making them a powerful tool for performing certain computational tasks. However, qubits are also fragile and can be easily perturbed by their environment, leading to computational errors. Majorana zero modes, which are robust and topologically protected, are considered promising candidates for implementing qubits that are relatively immune to errors caused by external perturbations. One important property contributing to this immunity is the spatial separation between the Majorana modes (see Fig. 1.5), which makes them non-local and less sensitive to decoherence [Kitaev 2001]. Moreover, Majorana zero modes are non-Abelian anyons, meaning that when two Majorana zero modes are exchanged, the state of the system is transformed in a non-trivial way. This property makes them promising for implementing certain types of quantum gates that are more robust to errors than other types of gates [Nayak *et al.* 2008].

As discussed above, another platform where the induction of superconductivity in boundary modes leads to the formation of Majorana modes is provided by the helical hinge modes of a higher-order topological insulator. In this case, however, the Majorana modes are one-dimensional states that propagate unidirectionally, rather than zero-dimensional point-like modes as in the Kitaev chain. In this manuscript we study the effects of a Zeeman field B^z and a superconducting coupling Δ on such helical hinge modes protected by mirror symmetry (see Fig. 1.7a). As already discussed, in the absence of couplings the hinges of the higher-order topological insulator realize natural domain walls where the mass surface gap m vanishes, leading to the appearance of the hinge states. When the couplings are added, the system acquires an effective mass where different terms from the different couplings compete. Considering a single hinge at $y = 0$, this effective mass can be written as $m_{sn}(y) = m(y) + sm_Z + nm_\Delta$, where $s, n = \pm$ and $m(y)$ vanishes at $y = 0$, while m_Z and m_Δ come from the Zeeman and superconducting couplings, respectively. The competition between the different terms then causes the effective mass to vanish at different locations depending on the values of the coupling, leading to the spatial splitting of the hinge modes. This idea was first proposed by Queiroz and Stern [Queiroz & Stern 2019]. In our study, however, we derive a more general formula for the wave functions of the hinge modes and we explore splitting scenarios not considered by these authors, thus extending this proposal. The splitting scenarios proposed by these authors are the following. If only a Zeeman field is applied, the helical mode is divided into two chiral fermionic modes (see Fig. 1.7b) while if we consider only a superconducting coupling we can obtain two pairs of helical Majorana modes which surround the superconducting region (see Fig. 1.7c). Finally, the combination of Zeeman and superconducting couplings leads to the separation of the helical Majorana modes into four chiral Majorana modes (see Fig. 1.7d), where two of them gap each other when $m_Z \simeq m_\Delta$. As a new scenario, we found a parameter regimes in which the helical hinge modes are split into two pairs of chiral Majorana modes. Our work is a preliminary step for the study of interferometers and Josephson junctions obtained by combining regions with different types of splitting, for which we proposed some examples.

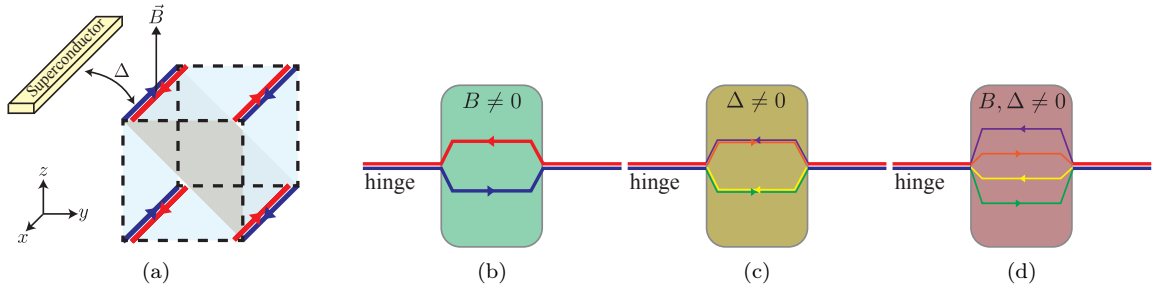

Figure 1.7: Splitting of helical hinge modes by a Zeeman field and a superconducting coupling. (a) Sketch of the helical pairs of hinge modes propagating for a higher order topological insulator having periodic boundary conditions along the x-direction. We have represented the superconducting coupling Δ as well as the Zeeman field $\vec{B}$ which are applied on a single hinge. Highlighted in gray is a plane invariant under mirror symmetry. In (b), (c), and (d) we represent the different splitting scenarios that are possible depending on the values of the Zeeman and superconducting couplings. We see that (b) in the case where there is only a Zeeman field the helical mode divides into two chiral modes while (c) in the presence of only a superconducting coupling the helical mode is splitted into two pairs of helical Majorana modes. (d) The combination of both Zeeman and superconducting couplings leads to four chiral Majorana modes.

The thesis is organized as follows.

In Chap. 2 we present the basic physical theories that are essential for understanding the work presented in this manuscript. We begin by studying the phenomena of Andreev reflection and crossed Andreev reflection that occur in normal metal-superconductor hybrid systems. We derive the corresponding scattering probabilities and consider the conductance of a normal metal-superconductor junction. We

then review the theory of the quantum Hall effect. In particular, we show how chiral edge states arise and discuss the topological origin of the quantization of the Hall resistance. Finally, we present toy models of two-dimensional topological insulators and end the chapter by discussing the concept of higher-order topological insulators.

In Chap 3 we study the downstream conductance mediated by CAES when a single, spin-degenerate, Landau level is occupied (i.e., in the regime $\nu = 2$). In particular, we discuss the geometry dependence of the downstream conductance as well as its dependence on the position of the Fermi level (which lies between the zeroth and the first Landau level). We also consider the effects of a Fermi level mismatch and the presence of a potential barrier at the QH-SC interface. We use a microscopic model of an infinitely long interface and perform tight-binding simulations to study these effects.

In Chap 4 we consider a QH-SC-QH junction with a ribbon geometry in the regime $\nu = 2$. We calculate the energy spectrum of the counter-propagating CAES by using a microscopic model and we use a one-dimensional effective model to calculate the local and non-local conductances of the junction. Interestingly, we find regimes where the non-local conductance is negative, which is a probe of the crossed Andreev reflection occurring in the system.

In Chap 5 we investigate the splitting of the helical hinge modes of higher order topological insulators when subjected to Zeeman and superconducting couplings. We derive the model Hamiltonian and solve the corresponding Schrödinger equation to obtain the energy spectrum and the wave functions of the split hinge modes. In particular, we find splitting scenarios that have not been considered in the literature.

Finally, we conclude and provide perspectives in Chap. 6.

Chapter 2

Basics: Andreev Reflection, Quantum Hall Effect and Topological Insulators

Contents

In this chapter, we detail important physical theories that are necessary for the understanding of this thesis. A large part of the manuscript is devoted to the study of chiral Andreev edge states, which are formed when edge states of the quantum Hall effect propagate along a superconducting interface by performing successive Andreev reflections. Thus, we dedicate the first two sections of this chapter to the study of Andreev reflection and the quantum Hall effect, respectively. The former allows an incoming electron from a normal metal to be reflected as a hole after hitting a superconducting interface, while the latter leads to the formation of chiral states propagating along the edges of a two-dimensional electron gas (2DEG) under a perpendicular magnetic field. In the last part of the thesis we study the effects of Zeeman and superconducting couplings on the helical boundary modes of a higher order topological insulator. A prerequisite for understanding this is therefore the concept of topological insulators, which we introduce in the last section of this chapter by focusing on two-dimensional systems. In particular, we present the phenomenon of localized states at a mass domain wall, an essential idea for understanding the last research project of the thesis (Chap. 5).

In Sec. 2.1 we introduce the Andreev reflection that occurs in normal metal-superconductor (NS) junctions. Here we first discuss the basics of superconductivity and use a Bogoliubov-de Gennes (BdG) Hamiltonian to derive the normal and Andreev reflection probabilities. Knowing these probabilities then allows us to calculate the conductance of a NS junction. Finally, we introduce the crossed Andreev reflection that occurs in normal metal-superconductor-normal metal (NSN) junctions. Understanding

this non-local process will be useful when dealing with NSN junctions where the normal metals are in the quantum Hall regime (Chap. 4 of the thesis). As we said, the quantum Hall effect is a central concept of this work, and we explain it in detail in Sec. 2.2. In particular, we will understand how chiral modes appear at the edges of a 2DEG subjected to a strong perpendicular magnetic field. On the other hand, in Sec. 2.3 we present the theory of topological insulators. Here we will see how helical states can appear at the boundaries of a two-dimensional surface, preserving time-reversal symmetry, in contrast to the chiral edge states of the quantum Hall effect (where time-reversal symmetry is broken). In the last part of this section we discuss the helical hinge modes of higher order topological insulators, as used in Chap. 5.

2.1 Andreev Reflection

The phenomenon of superconductivity has many interesting physical consequences. One of them is known as Andreev reflection (AR). In a Bardeen, Cooper, and Schrieffer (BCS) superconductor, the electrons are condensed into so-called Cooper pairs and the energy spectrum is gapped by 2Δ, where Δ is called the superconducting gap and 2Δ corresponds to the energy required to destroy a Cooper pair. Because of this gap, an electron with energy $|E| < \Delta$ cannot enter the superconductor, and so it is reflected. If it is reflected as an electron, this is called normal reflection, since it is the only possible reflection process for a non-superconducting junction. On the other hand, AR corresponds to the situation where the incident electron is reflected as a hole after hitting the superconducting interface, while a Cooper pair is formed in the superconductor. These two reflection processes are illustrated in Fig. 2.1.

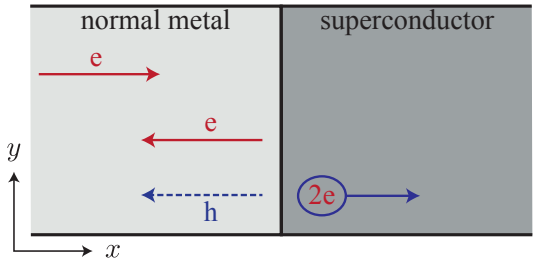

Figure 2.1: Normal and Andreev reflections in a normal metal-superconductor junction. An incoming electron from the normal metal reaches the superconductor before being reflected back. It can be reflected as an electron via normal reflection or as hole via Andreev reflection. In the last process, a Cooper pair is created in the superconductor so that the total outgoing charge is equal to the one of the incoming electron.

We begin this section with a reminder of the basics of superconductivity, where we present the gap equation, the BdG Hamiltonian, and the corresponding energy spectrum. We then give the real-space Hamiltonian of the normal metal-superconductor (NS) junction and its solutions in the normal and superconducting bulk. Next, we use the matching procedure of Ref. [Blonder *et al.* 1982] to calculate the Andreev reflection probability, which we then use to compute the conductance of the NS junction. We end the section by calculating the probability of crossed Andreev reflection (CAR) in normal metal-superconductor-normal metal (NSN) junctions, since we will study this effect in the thesis by considering normal metals in the quantum Hall regime.

2.1.1 Basics of superconductivity

In this manuscript we consider only conventional superconductors, which are well described by the BCS theory, and we always use the mean-field approximation as described in App. B. Here we recall some important results from that appendix. The BCS theory consists in adding to the Hamiltonian of a normal metal an attractive electron-electron interaction, where the two electrons have energies in an energy window near the Fermi level, and bounded by the Debye energy $\hbar\omega_D$. The resulting BCS

Hamiltonian is derived in Eq. (B.17) and is as follows

$$\mathcal{H} = \sum_{\vec{k},\alpha} \xi_{\vec{k}} c^{\dagger}_{\vec{k},\alpha} c_{\vec{k},\alpha} - \frac{g}{V_{vol}} \sum_{\vec{k}}{}' \sum_{\vec{k}'}{}' c^{\dagger}_{-\vec{k}',\downarrow} c^{\dagger}_{\vec{k}',\uparrow} c_{\vec{k},\uparrow} c_{-\vec{k},\downarrow}, \tag{2.1}$$

where g is the (positive) interaction constant, V_{vol} is the volume of the superconductor, $c_{\vec{k},\alpha}$ ($c^{\dagger}_{\vec{k},\alpha}$) annihilates (creates) an electron with momentum $\vec{k}$ and spin $\alpha =\uparrow,\downarrow$, the symbol Σ' indicates that the sum must be carried over the states in an energy window near the Fermi level and delimited by the Debye energy, and $\xi_{\vec{k}}$ is the single-particle energy in the normal state[1]. As described in App. B.3, by introducing the complex pair potential

$$\Delta e^{i\phi} \equiv \frac{g}{V_{vol}} \sum_{\vec{k}}{}' \left\langle c_{\vec{k},\uparrow} c_{-\vec{k},\downarrow} \right\rangle, \tag{2.2}$$

where ϕ is the superconducting phase and Δ is the superconducting gap, the mean-field Hamiltonian of superconductivity can be written as (B.28),

$$\mathcal{H}_{MF} = \sum_{\vec{k}} C^{\dagger}_{\vec{k}} H_{BdG}(\vec{k}) C_{\vec{k}} + \frac{V_{vol}\Delta^2}{g}, \tag{2.3}$$

where $C_{\vec{k}} = \left(c_{\vec{k},\uparrow}\, c^{\dagger}_{-\vec{k},\downarrow} \right)^T$ is a Nambu spinor in electron-hole space and H_{BdG} is the so-called BdG Hamiltonian [de Gennes 2018],

$$H_{BdG}(\vec{k}) = \begin{pmatrix} \xi_{\vec{k}} & \Delta e^{i\phi} \\ \Delta e^{-i\phi} & -\xi_{\vec{k}} \end{pmatrix}. \tag{2.4}$$

Since the second term in the mean-field Hamiltonian (2.3) is just an energy shift it is not relevant and we neglect it in the following. The energy spectrum obtained from the BdG Hamiltonian is given by,

$$E_{\pm}(\vec{k}) = \pm\sqrt{\xi^2_{\vec{k}} + \Delta^2} = \pm E_{\vec{k}}, \tag{2.5}$$

where the sign + (−) corresponds to an electron-like (hole-like) quasiparticle[2]. As mentioned above, this spectrum is gapped by 2Δ, so that an incoming particle with $|E| < \Delta$ cannot enter a superconductor. One last important thing to discuss is the value of the pair potential. As shown in Eq. (B.47), it is given by a self-consistent relation,

$$\Delta e^{i\phi} = \frac{g}{V_{vol}} \sum_{\vec{k}} \frac{\Delta e^{i\phi}}{2E_{\vec{k}}} \tanh\left(\frac{E_{\vec{k}}}{2k_B T} \right), \tag{2.6}$$

which is known as the gap equation. Here k_B is the Boltzmann constant and T is the temperature. At zero-temperature, the superconducting gap Δ_0 is given by (B.55), $\Delta_0 = 1.76 k_B T_c$, where T_c is the critical temperature of the superconductor. Let us also mention that the the typical size of the Cooper pair is given by the superconducting coherence length which, in the BCS theory, can be written as $\xi = \hbar v_F/\Delta$, with v_F the Fermi velocity.

[1] Note that we use a non-interacting model to describe the normal state. This is justified by Landau's theory of Fermi liquids, in which the low-energy excitations of the system can be treated as independent quasiparticles. This allows a normal metal (where the electron-electron interactions can be very strong) to be treated as a non-interacting system. The price for this is the introduction of renormalized properties such as an effective electron mass. More details can be found in [Girvin & Yang 2019, Sec. 15.11]. Although the excitations of a normal metal are described as quasiparticles in Fermi liquid theory, we will refer to them as electrons and holes throughout this manuscript.

[2] Here we cannot talk about pure electron and hole states because they are coupled by the pair potential, so we talk about quasiparticles. An electron-like (hole-like) quasiparticle, or quasi-electron (quasi-hole), is defined as the state that becomes a pure electron (hole) as $\Delta \to 0$.

2.1.2 Solutions of the Bogoliubov-de Gennes Hamiltonian in real space

We consider a two-dimensional NS junction as shown in Fig. 2.1. We denote the transverse coordinate by y and the longitudinal coordinate by x. The normal side of the junction is at $x < 0$ and the superconducting side is at $x > 0$, so the NS interface is at $x = 0$. In the bulk of the superconductor ($x \gg \xi$) the pair potential has amplitude Δ and phase ϕ. Because the system is made of a single superconductor, the superconducting phase can always be gauged away so that we set $\phi = 0$ for the remainder of this chapter (this will be detailed after introducing the real-space Hamiltonian of the system in Eq. (2.11)). The spatial dependence of the amplitude Δ is determined self-consistently,

$$\Delta(\vec{r}) = \frac{g(\vec{r})}{V_{vol}} \sum_{E>0} u(\vec{r}) v^*(\vec{r}) \tanh\left(\frac{E}{2k_B T}\right), \tag{2.7}$$

where u, v, and E are obtained from the BdG equations [de Gennes 2018],

$$\begin{pmatrix} -\frac{\hbar^2\nabla^2}{2m} - \mu & \Delta(\vec{r}) \\ \Delta(\vec{r}) & \frac{\hbar^2\nabla^2}{2m} + \mu \end{pmatrix} \begin{pmatrix} u(\vec{r}) \\ v(\vec{r}) \end{pmatrix} = E \begin{pmatrix} u(\vec{r}) \\ v(\vec{r}) \end{pmatrix}. \tag{2.8}$$

Note that we have used the BdG Hamiltonian (2.4) to write the above equation where we considered $\xi_{\vec{k}} = \hbar^2\vec{k}^2/(2m) - \mu$ with the substitution $\vec{k} \to -i\vec{\nabla}$. Here μ is the chemical potential and m is an effective mass.Moreover, for a homogeneous superconductor, we have $E = E_{\vec{k}}$ and the values of u and v are given by Eq. (B.35) such that Eq. (2.7) recovers the gap equation (2.6). Since the value of g drops abruptly to zero at the NS interface and is equal to zero in the normal region (where there is no pairing interaction), we can use the step-function model to describe the spatial variation of the superconducting gap [Beenakker 1994],

$$\Delta(\vec{r}) = \Delta(x) = \Delta\theta(x). \tag{2.9}$$

Assuming the separation of variables between transversal and longitudinal coordinates we can write the wave function as,

$$\Psi(\vec{r}) = \psi(x)\phi(y), \tag{2.10}$$

where $\psi(x)$ is the longitudinal wave function and $\phi(y)$ is the transverse wave function. The former will be derived in the following, while for the latter we assume an infinite transverse direction, so that we can write $\phi(y) = e^{ik_y y}/\sqrt{S}$, where S is the cross section of the junction. Moreover, the corresponding transverse energy is given by $\varepsilon_{k_y} = \hbar^2 k_y^2/(2m)$, where k_y is continuous because we consider an infinite transverse direction. To determine the longitudinal wave function, we need the Hamiltonian describing the system along the x coordinate. However, since the total energy is given by the sum of the transverse and longitudinal energies, the chemical potential for the longitudinal propagation is renormalized by the transverse subbdand so that $\mu \to \tilde{\mu} = \mu - \varepsilon_{k_y}$. We model the NS interface at $x = 0$ by a Dirac-δ potential $V_0\delta(x)$ and describe the junction by the following one-dimensional BdG Hamiltonian in real space,

$$H = \begin{pmatrix} -\frac{\hbar^2}{2m}\partial_x^2 - \tilde{\mu} + V_0\delta(x) & \Delta\theta(x) \\ \Delta\theta(x) & \frac{\hbar^2}{2m}\partial_x^2 + \tilde{\mu} - V_0\delta(x) \end{pmatrix}. \tag{2.11}$$

As mentioned above, the fact that there is a single superconductor in the system allowed us to consider a real superconducting order parameter. We can see that by performing a unitary transformation on the Hamiltonian by using the operator $U = e^{-i\frac{\phi}{2}\tau_z}$. For the NS junction we can consider a constant value of ϕ in all the system and a non-zero amplitude Δ only in the superconductor. The real-space BdG Hamiltonian can thus be written as,

$$H(x) = \begin{pmatrix} -\frac{\hbar^2}{2m}\partial_x^2 - \tilde{\mu} + V_0\delta(x) & \Theta(x)\Delta e^{i\phi} \\ \Theta(x)\Delta e^{-i\phi} & \frac{\hbar^2}{2m}\partial_x^2 + \tilde{\mu} - V_0\delta(x) \end{pmatrix}. \tag{2.12}$$

Performing the transformation we obtain,

$$\tilde{H}(x) = U^\dagger H(x) U = \begin{pmatrix} -\frac{\hbar^2}{2m}\partial_x^2 - \tilde{\mu} + V_0\delta(x) & \Theta(x)\Delta \\ \Theta(x)\Delta & \frac{\hbar^2}{2m}\partial_x^2 + \tilde{\mu} - V_0\delta(x) \end{pmatrix}, \tag{2.13}$$

which is the Hamiltonian given in Eq. (2.11). If we have N superconductors we must define a superconducting phase for each of them. In that case, the superconducting phases will appear as phase differences in the terms describing the transfer of electrons between two superconductors.

We now solve the x-dependent Schrödinger equation in each region. In the normal side ($x < 0$) we set $\Delta = 0$ and we must solve,

$$\pm\left(-\frac{\hbar^2}{2m}\partial_x^2 - \tilde{\mu}\right)\chi_\pm(x) = E\chi_\pm(x). \tag{2.14}$$

The solutions are found to be,

$$\chi_\pm(x) = a_\pm e^{ik_\pm x} + b_\pm e^{-ik_\pm x}, \tag{2.15}$$

where $a_\pm$, $b_\pm$ are constants and,

$$k_\pm = \frac{1}{\hbar}\sqrt{2m(\tilde{\mu} \pm E)} = \tilde{k}_F\sqrt{1 \pm E/\tilde{\mu}}, \tag{2.16}$$

with $\tilde{k}_F = (1/\hbar)\sqrt{2m\tilde{\mu}}$. Here the + (−) solutions describe an electron (a hole) belonging to the energy branch ξ_{k_x} ($-\xi_{k_x}$) with $\xi_{k_x} = \hbar^2 k_x^2/(2m) - \tilde{\mu}$ (this translates in the terms $\pm E$ in the above expressions). In order to have propagating waves in the normal metal, we consider $|E| < \tilde{\mu}$ such that $k_\pm$ is always real and positive. From the energy dispersions we can calculate the velocity of an electron or a hole in the x-direction as $v_\pm(k_x) = \pm(1/\hbar)\partial_{k_x}\xi_k = \pm\hbar k_x/m$ so that the group velocity of a hole, $v_-(k_x)$, is negative in the x-direction for $k_x > 0$. Hence, the terms $a_+e^{ik_+x}$ and $b_-e^{-ik_-x}$ describe right-moving particles while the terms $b_+e^{-ik_+x}$ and $a_-e^{ik_-x}$ describe left-moving particles. The full wave function in the normal region can then be written as,

$$\psi_N(x) = \begin{pmatrix} 1 \\ 0 \end{pmatrix}\chi_+(x) + \begin{pmatrix} 0 \\ 1 \end{pmatrix}\chi_-(x). \tag{2.17}$$

In the superconductor ($x > 0$) we have $\Delta > 0$ and we need to solve the BdG equation,

$$\begin{pmatrix} -\frac{\hbar^2}{2m}\partial_x^2 - \tilde{\mu} & \Delta \\ \Delta & \frac{\hbar^2}{2m}\partial_x^2 + \tilde{\mu} \end{pmatrix}\begin{pmatrix} u(x) \\ v(x) \end{pmatrix} = E\begin{pmatrix} u(x) \\ v(x) \end{pmatrix}, \tag{2.18}$$

where $u(x)$ and $v(x)$ respectively describe electron-like and hole-like quasiparticles. Since the Hamiltonian doesn't depend on the x-coordinate we can assume plane wave solutions $\sim e^{iqx}$ where the state is propagating if q is real and it is evanescent in the superconductor if q has a positive imaginary part (for e^{iqx} it is evanescent if the imaginary part is positive since $x > 0$ while the state is not normalizable is the imaginary part is negative). The possible wave vectors are then found by solving,

$$\begin{vmatrix} \frac{\hbar^2 q^2}{2m} - \tilde{\mu} - E & \Delta \\ \Delta & -\frac{\hbar^2 q^2}{2m} + \tilde{\mu} - E \end{vmatrix} = 0, \tag{2.19}$$

from which we obtain four solutions for q, namely $q = q_\pm$ and $q = -q_\pm$, with

$$q_\pm = \frac{1}{\hbar}\left[2m\left(\tilde{\mu} \pm i\sqrt{\Delta^2 - E^2}\right)\right]^{1/2} = \tilde{k}_F\sqrt{1 \pm i\frac{\sqrt{\Delta^2 - E^2}}{\tilde{\mu}}}. \tag{2.20}$$

Here the momenta with index + (−) describe a quasi-electron (quasi-hole) belonging to the energy branch E_{k_x} ($-E_{k_x}$), with $E_{k_x} = \sqrt{\xi_{k_x}^2 + \Delta^2}$. These momenta are real if $|E| > \Delta$ (supra-gap) and they have an

imaginary part for $|E| < \Delta$ (sub-gap). We focus only on the latter case in this manuscript. We can then write the solutions of the BdG equation as,

$$\begin{pmatrix} u(x) \\ v(x) \end{pmatrix} = c_1 \begin{pmatrix} u_0^+ \\ v_0^+ \end{pmatrix} e^{iq_+ x} + c_2 \begin{pmatrix} u_0^+ \\ v_0^+ \end{pmatrix} e^{-iq_+ x} + d_1 \begin{pmatrix} u_0^- \\ v_0^- \end{pmatrix} e^{iq_- x} + d_2 \begin{pmatrix} u_0^- \\ v_0^- \end{pmatrix} e^{-iq_- x}, \tag{2.21}$$

with $c_{1,2}$ and $d_{1,2}$ constants. Since we focus on $|E| < \Delta$, the momentum q_+ (q_-) has an imaginary part which is positive (negative). Thus, for the wave function to be normalizable, we have to set $c_2 = d_1 = 0$ so that we keep only the terms which are evanescent in the superconductor, i.e., those vanishing as $x \to \infty$. The eigenvectors are found by solving the following matrix equation,

$$\begin{pmatrix} \frac{\hbar^2 q_\pm^2}{2m} - \mu - E & \Delta \\ \Delta & -\frac{\hbar^2 q_\pm^2}{2m} + \mu - E \end{pmatrix} \begin{pmatrix} u_0^\pm \\ v_0^\pm \end{pmatrix} = 0, \tag{2.22}$$

which leads to,

$$\begin{pmatrix} u_0^+ \\ v_0^+ \end{pmatrix} = \begin{pmatrix} 1 \\ \frac{E - i\sqrt{\Delta^2 - E^2}}{\Delta} \end{pmatrix}, \tag{2.23}$$

$$\begin{pmatrix} u_0^- \\ v_0^- \end{pmatrix} = \begin{pmatrix} \frac{E - i\sqrt{\Delta^2 - E^2}}{\Delta} \\ 1 \end{pmatrix} = \begin{pmatrix} v_0^+ \\ u_0^+ \end{pmatrix}. \tag{2.24}$$

These two vectors are related to each other due to the particle-hole symmetry[3]. Introducing the notation,

$$\gamma = \frac{E - i\sqrt{\Delta^2 - E^2}}{\Delta}, \tag{2.25}$$

where $|\gamma| = 1$, we can write the wave function in the superconductor as,

$$\psi_S(x) = c \begin{pmatrix} 1 \\ \gamma \end{pmatrix} e^{iq_+ x} + d \begin{pmatrix} \gamma \\ 1 \end{pmatrix} e^{-iq_- x}. \tag{2.26}$$

We are now in a position to calculate the normal and Andreev reflection probabilities. This is the aim of the next section.

2.1.3 Normal and Andreev reflection probabilities

The results presented here have been first introduced by Blonder, Tinkham, and Klapwijk (BTK) and so this method is often referred as the BTK model. We consider the situation where an incoming electron from the normal metal propagates toward the NS interface. Since we focus only on sub-gap states the incident electron cannot enter in the superconductor and so it is reflected back in the normal region after hitting the superconducting interface. It can be reflected as an electron with amplitude r_N (normal reflection) or as a hole with amplitude r_A (AR). The incoming state has the form $\psi_{in}(x) = (1,\, 0)^T e^{ik_+ x}$ and the reflected waves are given by $\psi_{refl}(x) = (r_N,\, 0)^T e^{-ik_+ x} + (0,\, r_A)^T e^{ik_- x}$ so that the wave function of the junction reads,

$$\psi(x) = \begin{cases} \psi_N(x) & \text{if } x < 0 \\ \psi_S(x) & \text{if } x > 0 \end{cases}, \tag{2.27}$$

with,

$$\psi_N(x) = \begin{pmatrix} 1 \\ 0 \end{pmatrix} e^{ik_+ x} + \begin{pmatrix} r_N \\ 0 \end{pmatrix} e^{-ik_+ x} + \begin{pmatrix} 0 \\ r_A \end{pmatrix} e^{ik_- x}, \tag{2.28}$$

$$\psi_S(x) = c \begin{pmatrix} 1 \\ \gamma \end{pmatrix} e^{iq_+ x} + d \begin{pmatrix} \gamma \\ 1 \end{pmatrix} e^{-iq_- x}, \tag{2.29}$$

[3]The particle-hole symmetry of the momentum-space BdG Hamiltonian is briefly discussed in App. B.4.

where we keep only the (square integrable) evanescent waves in the superconductor. Note that the holes have a negative velocity for $k_x > 0$ from where the positive sign in the phase of the reflected hole. As it is our main interest in this thesis, and because it simplifies a lot the calculation, we consider only zero-energy states, $E = 0$, such that we can write[4],

$$k_\pm = \tilde{k}_F, \quad q_\pm = \tilde{k}_F \sqrt{1 \pm i\Delta/\tilde{\mu}}, \quad \gamma = -i. \tag{2.30}$$

As another simplification we make use of the Andreev approximation [Andreev 1965, Kulik 1969] (also known as the BCS limit), $\Delta \ll \mu$, so that we can approximate,

$$q_\pm \simeq \tilde{k}_F \left(1 \pm i\frac{\Delta}{2\tilde{\mu}}\right) = \tilde{k}_F \pm i\frac{\Delta}{\hbar\tilde{v}_F} = \tilde{k}_F \pm i/\tilde{\xi}, \tag{2.31}$$

where we have introduced the renormalized Fermi velocity $\tilde{v}_F = \hbar\tilde{k}_F/m$ and the renormalized coherence length $\tilde{\xi} = \hbar\tilde{v}_F/\Delta$. As it is not relevant to interpret the final result, we choose $k_y = 0$ such that $\tilde{\mu} = \mu$ yielding $\tilde{k}_F = k_F$ and $\tilde{\xi} = \xi$. We can then rewrite the wave functions in each region as,

$$\psi_N(x) = \begin{pmatrix} 1 \\ r_A \end{pmatrix} e^{ik_F x} + \begin{pmatrix} r_N \\ 0 \end{pmatrix} e^{-ik_F x}, \tag{2.32}$$

$$\psi_S(x) = \left[c \begin{pmatrix} 1 \\ -i \end{pmatrix} e^{ik_F x} + d \begin{pmatrix} -i \\ 1 \end{pmatrix} e^{-ik_F x} \right] e^{-x/\xi}. \tag{2.33}$$

From this expression we clearly see the exponential vanishing of $\psi_S(x)$ over the coherence length. To compute the normal and Andreev reflection amplitudes we perform the matching procedure of Ref. [Blonder *et al.* 1982],

$$\psi_N(0) = \psi_S(0) \equiv \psi(0), \tag{2.34}$$

$$\psi'_S(0) - \psi'_N(0) = 2Zk_F\psi(0), \tag{2.35}$$

where the second line is obtained by integrating the Schrödinger equation in the interval $[-\varepsilon, \varepsilon]$ with $\varepsilon \to 0$ and $Z = mV_0/(k_F\hbar^2)$ quantifies the strength of the potential barrier at the NS interface. By solving the resulting system we obtain the amplitudes,

$$r_N = -\frac{[1 + 2Zk_F\xi]\,[1 + 2k_F\xi(i + Z)]}{1 + 2k_F\xi\,[k_F\xi + 2Z(1 + Zk_F\xi)]}, \tag{2.36}$$

$$r_A = -\frac{2ik_F^2\xi^2}{1 + 2k_F\xi\,[k_F\xi + 2Z(1 + Zk_F\xi)]}, \tag{2.37}$$

leading to the following reflection probabilities,

$$R_N = |r_N|^2 = \frac{\{1 + 2Zk_F\xi\}^2\,\{1 + 4k_F\xi\,[Z + k_F\xi(1 + Z^2)]\}}{\{1 + 2k_F\xi\,[k_F\xi + 2Z(1 + Zk_F\xi)]\}^2}, \tag{2.38}$$

$$R_A = |r_A|^2 = \frac{4k_F^4\xi^4}{\{1 + 2k_F\xi\,[k_F\xi + 2Z(1 + Zk_F\xi)]\}^2}, \tag{2.39}$$

with $R_N + R_A = 1$ as required. We can simplify these results by using the Andreev approximation $\Delta \ll \mu$ such that $k_F\xi = 2\mu/\Delta \gg 1$. We thus take the limit $k_F\xi \to \infty$ and get,

$$r_N = \frac{-2Z(i + Z)}{1 + 2Z^2}, \quad r_A = \frac{-i}{1 + 2Z^2}, \tag{2.40}$$

while the corresponding probabilities are given by,

$$R_N = \frac{4Z^2(1 + Z^2)}{(1 + 2Z^2)^2}, \quad R_A = |r_A|^2 = \frac{1}{(1 + 2Z^2)^2}. \tag{2.41}$$

[4] The scattering coefficients at arbitrary energies can be found in Asano's book [Asano 2021].

Thus, in the Andreev approximation, and for an ideal interface with $Z = 0$, the incoming electron is only reflected as a hole ($R_A = 1$). On the other hand, for an infinitely strong barrier with $Z \to \infty$ (i.e., the normal metal-insulator limit), the incoming electron is reflected normally ($R_N = 1$). Moreover, we can express the Andreev-approximated coefficients in terms of those obtained for a normal metal-normal metal (NN) junction where the incoming electron can be reflected black or transmitted (as an electron only) with respective amplitudes $r = -iZ(1 + iZ)$ and $t = 1/(1 + iZ)$ (see App. A.1 for a detailed calculation of r and t),

$$r_N = \frac{2r}{2-T}, \quad r_A = \frac{-iT}{2-T}, \quad R_N = \frac{4R}{(2-T)^2}, \quad R_A = \frac{T^2}{(2-T)^2}, \tag{2.42}$$

where $R = |r|^2$ and $T = |t|^2$. We can thus compute the normal and Andreev reflection coefficients (in the Andreev approximation) by using standard techniques developed for quantum transport in the normal state [Beenakker 1994].

In the next subsection we look at the conductance of the NS junction and we will see how it is related to the one of a NN junction.

2.1.4 Conductance of the NS junction

In the preceding we considered a junction with an infinite transverse direction (i.e., a junction that is infinite along the y-axis). In this case there is an infinite number of transverse modes described by the continuous energy spectrum $\varepsilon_{k_y} = \hbar^2 k_y^2/(2m)$ with a transverse eigenfunction given by a plane wave, $\phi(y) = e^{ik_y y}/\sqrt{S}$, where S is the cross section of the junction. However, to describe the conductance of the junction, it is more convenient to consider a finite transverse dimension such that a finite number of transverse modes contribute to the conductance. Hence, we now assume a finite length L_y in the y-direction which can be taken in account by adding a transverse confining potential $V(y)$ in the Hamiltonian. In that case, the transverse energies and wave functions are solutions of the Schrödinger equation,

$$[p_y^2/(2m) + V(y)]\phi(y) = E\phi(y), \tag{2.43}$$

and depend on the form of the confining potential. The resulting spectrum will be made of transverse sub-bands labelled by n, each having a one-dimensional dispersion in the x-direction, and the corresponding wave functions will be given by a certain function $\phi_n(y)$ for the n-th transverse mode. Moreover, as the confinement becomes tighter, the spacing between the sub-bands increases. Hence, for a very narrow junction in the y-direction, we can consider that only one sub-band is occupied. This is the assumption we consider in this subsection and we consider the sub-band as spin-degenerate. Moreover, here we look at the linear response conductance G_{NS} of the NS junction at zero-temperature. By using the Landauer-Büttiker formalism of quantum transport detailed in App. A.4, and considering the single-channel case, the conductance in the normal state can be written as,

$$G_{NN} = G_0 T = G_0(1 - R), \tag{2.44}$$

where $G_0 = 2e^2/h$ is the quantum of conductance (for spin-degenerate electrons). This formula makes sense as it says that the conductance from the left to the right is proportional to the probability for the incoming electron to be transmitted. We can then easily generalize this formula to superconducting junctions by replacing R by R_N and adding a positive contribution R_A due to AR (the AR contributes positively as it reflects particles of opposite charges). This was derived more rigorously in [Blonder *et al.* 1982, Takane & Ebisawa 1992] and can be written as,

$$G_{NS} = G_0(1 - R_N + R_A) = 2G_0 R_A. \tag{2.45}$$

As we have seen in the preceding subsection, considering a perfect interface ($Z = 0$) and an incoming electron at the Fermi level ($E = 0$) we hav $R = 0$ and so[5] $G_{NS} = 2G_{NN}$ which corresponds to a

[5] This is valid only in the Andreev approximation where $\Delta \ll \mu$.

current of $2e$ flowing in the superconductor for each incoming electron due to the Cooper pair creation accompanying the AR. This is known as the conductance-doubling effect of AR and it was observed in Ref. [Kjærgaard *et al.* 2016] for example. The above conductance formulas are valid for a single channel while the multi-channel generalization is easily obtained by summing over all the conducting channels as done in App. A.4 in the normal case. A detailed derivation for the NS junction can be found in the lecture notes by Beenakker [Beenakker 1994].

To finish this part on the Andreev reflection we investigate the CAR process arising in NSN junctions. This will be useful to compare the results we will obtain later in the thesis when studying a quantum Hall-superconductor-quantum Hall junction.

2.1.5 Crossed Andreev reflection in NSN junctions

We consider a NSN junction where a grounded[6] superconductor of length L is sandwiched between two normal metals as depicted in Fig. 2.2. In the previous section we studied a single NS interface and

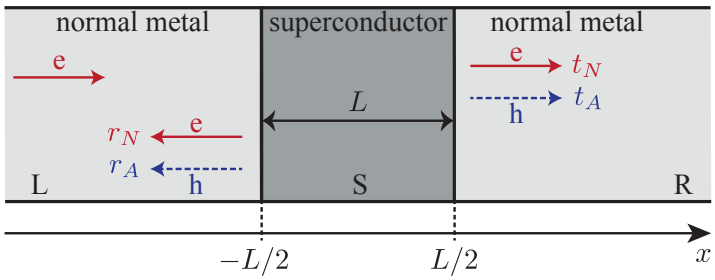

Figure 2.2: NSN junction where a superconductor of length L is sandwiched between two normal metals. An incoming electron from the left (L) reaches the superconductor (S) and can undergo different scattering processes. As previously, it can be reflected as an electron with amplitude r_N due to normal reflection or it can be reflected as a hole with amplitude r_A due to AR. Due to the presence of a second normal metal at the right (R), the incoming electron can also be transmitted to the right as an electron with amplitude t_N due to elastic co-tunneling or as a hole with amplitude t_A due to CAR.

saw that the wave function of the sub-gap states in the superconductor is evanescent and suppressed on the scale of the superconducting coherence length ξ. Thus, for the NSN junction, if the length L of the central superconductor is less than a few ξ, the evanescent wave functions of the left and right NS interfaces will overlap. This overlap allows for new scattering processes involving the two normal metals, called crossed or non-local processes. Consider an incoming electron from the left normal metal propagating toward the superconductor. As before, this incoming electron can be reflected back as an electron or as a hole with respective amplitudes r_N and r_A. On the other hand, due to the presence of the second normal metal on the right, the incoming electron can also be transmitted as an electron or as a hole with respective amplitudes t_N and t_A. This last process, which converts the incoming electron from the left into a transmitted hole at the right, is called CAR (or non-local Andreev reflection) [Deutscher & Feinberg 2000, Falci *et al.* 2001, Recher *et al.* 2001, Chtchelkatchev *et al.* 2002]. It has been observed experimentally in Ref. [Russo *et al.* 2005], for example, by measuring the voltage difference between the left and right regions. Here we use the same procedure as for the NS junction to compute the different scattering coefficients shown in Fig. 2.2. The wave function of the junction can be

[6] In the mean-field theory of superconductivity the number of particles in the ground state is not fixed so that, to fix its average, one has to introduce a superconducting chemical potential [Ketterson & Song 1999]. From that point of view, the mean field Hamiltonian describes a superconducting reservoir, i.e. the superconductor is intrinsically grounded since the number of particles is adapted to the chemical potential. To describe a floating superconductor one has to equate the current through the left and right leads such that there is a fixed number of particles travelling across it.

written as

$$\psi(x) = \begin{cases} \psi_L(x) & \text{if } x < -L/2 \\ \psi_S(x) & \text{if } -L/2 < x < L/2 \\ \psi_R(x) & \text{if } x > L/2 \end{cases}, \tag{2.46}$$

and we model the interfaces by two Dirac-δ potential barriers,

$$V(x) = V_0 \left[\delta\left(x + \frac{L}{2}\right) + \delta\left(x - \frac{L}{2}\right) \right]. \tag{2.47}$$

Starting from the general solutions (2.15) and (2.21) and using the same arguments that led us to Eqs. (2.33) and (2.32), in particular $E = 0$ and $\Delta \ll \mu$, we obtain,

$$\psi_L(x) = \begin{pmatrix} 1 \\ r_A \end{pmatrix} e^{ik_F x} + \begin{pmatrix} r_N \\ 0 \end{pmatrix} e^{-ik_F x}, \tag{2.48}$$

$$\psi_S(x) = \left[a \begin{pmatrix} 1 \\ -i \end{pmatrix} e^{-ik_F x} + b \begin{pmatrix} 1 \\ i \end{pmatrix} e^{ik_F x} \right] e^{x/\xi} + \left[c \begin{pmatrix} 1 \\ -i \end{pmatrix} e^{ik_F x} + d \begin{pmatrix} 1 \\ i \end{pmatrix} e^{-ik_F x} \right] e^{-x/\xi}, \tag{2.49}$$

$$\psi_R(x) = \begin{pmatrix} t_N \\ 0 \end{pmatrix} e^{ik_F x} + \begin{pmatrix} 0 \\ t_A \end{pmatrix} e^{-ik_F x}, \tag{2.50}$$

where we now keep two exponentially decaying terms in the superconducting wave function because of the left and right NS interfaces. To determine the scattering coefficients we perform the matching procedure at the two interfaces,

$$\psi_L(-L/2) = \psi_S(-L/2) \equiv \psi(-L/2), \tag{2.51}$$

$$\psi'_S(-L/2) - \psi'_L(-L/2) = Zk_F\psi(-L/2), \tag{2.52}$$

$$\psi_R(L/2) = \psi_S(L/2) \equiv \psi(L/2), \tag{2.53}$$

$$\psi'_R(L/2) - \psi'_S(L/2) = Zk_F\psi(L/2). \tag{2.54}$$

We then compute the scattering amplitudes by solving the above system and we define the associated transmission probabilities as,

$$T_N = |t_N|^2, \quad T_A = |t_A|^2, \tag{2.55}$$

with $R_N + R_A + T_N + T_A = 1$. Their analytical expressions are quite complicated. By taking $Z = 0$ they can be written as,

$$D = \left[4k_F^2\xi^2(1 + k_F^2\xi^2) - \cos(2k_F L) + (1 + 2k_F^2\xi^2)^2 \cosh(2L/\xi)\right]^2, \tag{2.56}$$

$$R_A = \frac{1}{D}\left\{4k_F^2\xi^2\left[\sin(2k_F L) + k_F\xi(1 + 2k_F^2\xi^2)\sinh(2L/\xi)\right]^2\right\}, \tag{2.57}$$

$$T_A = \frac{1}{D}\left\{16k_F^2\xi^2\left[k_F\xi\cos(k_F L)\sinh(L/\xi) + (1 + 2k_F^2\xi^2)\sin(k_F L)\cosh(L/\xi)\right]^2\right\}, \tag{2.58}$$

$$\begin{aligned} R_N = \frac{1}{D}\{&(1 + 2k_F^2\xi^2)[1 - 2(1 + 2k_F^2\xi^2)\cos(2k_F L)\cosh(2L/\xi) \\ &+ (1/2 + 3k_F^2\xi^2 + 4k_F^4\xi^4)\cosh(4L/\xi) - 8k_F^3\xi^3\sin(2k_F L)\sinh(2L/\xi)] \\ &+ (1 + 4k_F^2\xi^2)[(1/2)\cos(4k_F L) - 2k_F^4\xi^4]\}, \end{aligned} \tag{2.59}$$

$$T_N = 1 - (R_N + R_A + T_A). \tag{2.60}$$

Using the Andreev approximation $\Delta \ll \mu$ we have $k_F\xi = 2\mu/\Delta \gg 1$ and, in the limit $k_F\xi \to \infty$, the above scattering probabilities become,

$$R_N = T_A = 0, \quad R_A = \tanh^2(L/\xi), \quad T_N = \operatorname{sech}^2(L/\xi). \tag{2.61}$$

These scattering probabilities can be probed in experiments by measuring the local and non-local conductances respectively denoted by G_{LL} and G_{RL} and given by [Takane & Ebisawa 1992],

$$G_{LL} = G_0(1 - R_N + R_A), \tag{2.62}$$
$$G_{LR} = G_0(T_N - T_A). \tag{2.63}$$

In Fig. 2.3 we plot the probabilities as a function of L/ξ for various values of the barrier strength Z. At large lengths $L/\xi \gg 1$, the two NS interfaces are independent such that the evanescent waves at the left and right barriers do not overlap and non-local processes are not allowed ($T_N = T_A = 0$). For such lengths, we recover results similar to the ones obtained for a single NS interface. From our analytical expressions (obtained for $Z = 0$) we can write the reflection probabilities in the limit $L/\xi \to \infty$ as,

$$R_N = \frac{1 + 4k_F^2\xi^2}{\left(1 + 2k_F^2\xi^2\right)^2}, \tag{2.64}$$
$$R_A = \frac{4k_F^4\xi^4}{\left(1 + 2k_F^2\xi^2\right)^2}. \tag{2.65}$$

As we can see, these expressions recover the ones obtained for the NS junction in Eqs. (2.38) and (2.39). In the Andreev limit $k_F\xi \to \infty$, we recover the previous results of a single ideal interface, namely $R_N = 0$ and $R_A = 1$. As for the single interface, the probability of normal reflection increases with the strength of the barrier, and in the limit of a very bad interface $Z \to \infty$, only normal reflection is allowed. For small lengths, i.e. not larger than a few superconducting coherence lengths, the evanescent waves overlap and transmission via non-local processes is allowed. For $Z = 0$ the probability T_A of CAR is zero (in the Andreev limit), while the normal transmission T_N decays exponentially with L/ξ, accompanied by the increase of the AR probability R_A (see Fig. 2.3a). Moreover, as we can see in the inset of Fig. 2.3a, the probability of CAR is not exactly zero (because we did not use the Andreev approximation to plot the scattering probabilities), but rather shows small oscillations with L/ξ. These oscillations are best seen at intermediate values of Z (see Fig. 2.3b and Fig. 2.3c) and are actually Fabry-Pérot like oscillations like those discussed in App. A.3 for a junction of three normal metals separated by δ barriers (i.e., the double δ barrier problem). However, unlike the normal case, the oscillations decay exponentially with L over a distance of the order of the coherence length. In fact, in the normal case, the electrons propagate freely between the two barriers, no matter how far apart they are, while here the quasiparticles can only propagate in the superconductor over a distance of the order of the coherence length. Moreover, we observed oscillations here even when the barrier strength Z is zero, while this is not possible in the normal case. This is because in the NSN case the incoming electron can propagate as a quasi-electron or as a quasi-hole in the superconductor before being transferred to the right. On the other hand, the observed oscillations have a common origin with those observed in the normal case. Namely, they originate from the different possible trajectories to go from the left to the right side of the junction. As an illustration, some of these trajectories are shown in Fig. 2.4. Finally, for a large value of Z, we observe resonance peaks of the AR and CAR probabilities (see Fig. 2.3d where we have chosen $Z = 2$) similar to the transmission resonances of the double δ barrier discussed in App. A.3.

In this first section, we have studied Andreev reflection because it is one of the two key ingredients necessary for the formation of chiral Andreev edge states, which are extensively studied in this thesis. Chiral Andreev edge states are states that propagate unidirectionally along the interface between a normal metal in the quantum Hall regime and a superconductor by performing successive Andreev reflections. Therefore, in the next section we introduce the second key ingredient for the formation of these edge states, namely the quantum Hall effect.

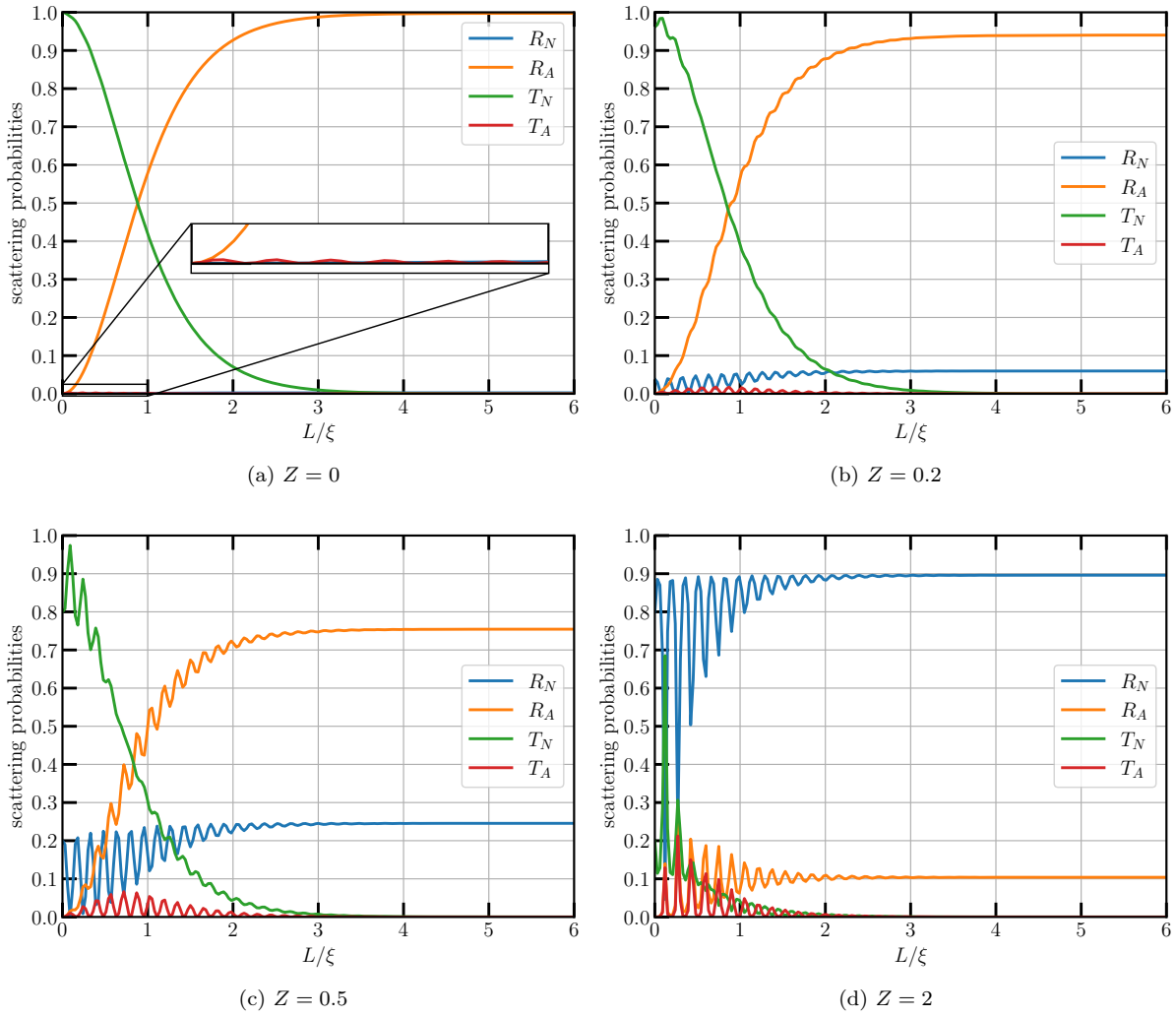

(a) $Z = 0$ (b) $Z = 0.2$

(c) $Z = 0.5$ (d) $Z = 2$

Figure 2.3: NSN scattering probabilities. We represent the normal reflection and transmission amplitudes denoted by R_N and T_N as well as the AR and the CAR respectively denoted by R_A and T_A. We consider different values of the barrier strength Z: (a) $Z = 0$, (b) $Z = 0.2$, (c) $Z = 0.5$, (d) $Z = 2$. We have set $k_F\xi = 20$.

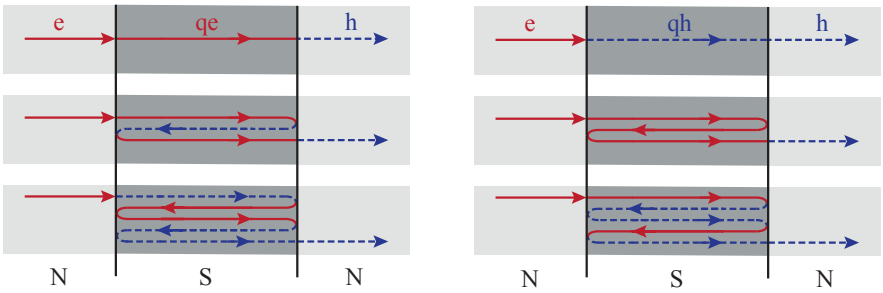

Figure 2.4: Some trajectories converting an incoming electron (e, red line) from the left to as hole at the right (h, blue dashed line). In the central superconductor, a quasi-electron (qe, red line) or a quasi-hole (qh, blue dashed line) propagates and can bounce or can be transmitted after reaching a NS interface. At each bounce, a quasi-electron (quasi-hole) can stay the same or can be converted as a quasi-hole (quasi-electron). If $Z = 0$, the interfaces are transparent and only the top trajectories are possible.

2.2 Quantum Hall Effect

The classical Hall effect, discovered by Hall in 1879 [Hall 1879], is due to the Lorentz force acting on a charged current flowing through a material subjected to a magnetic field. The Lorentz force deflects the charge carriers and produces a non-zero voltage transverse to the current and the magnetic field, called the Hall voltage. For the quantum version of the Hall effect, we consider a two-dimensional system. The quantum Hall effect (QHE) occurs when a 2DEG is subjected to a perpendicular magnetic field of a few Tesla at a temperature of a few Kelvin. It was discovered at the High Field Magnet Laboratory in Grenoble (France) by von Klitzing [von Klitzing *et al.* 1980]. Klitzing observed that the Hall resistance exhibits steps (or plateaus), and that on the plateaus it is exactly quantized in units of the resistance quantum h/e^2, regardless of the shape of the sample and the quality of the contacts, so that the QHE is now used as a universal standard for electrical resistance. In this section we will understand how this quantization occurs. As we will see, when a 2DEG is subjected to a high perpendicular magnetic field, the energy of the electrons is quantized into so-called Landau levels separated by an energy gap. We will also learn that when the chemical potential lies in such an energy gap, all the Landau levels below it are filled and contribute to the integer quantization of the Hall resistance. As we will see, the Landau levels are bent upward in energy for states localized near the edges, so that at the edges the Fermi level is no longer in an energy gap and conducting edge states appear. It turns out that each edge state contributes as e^2/h to the Hall conductance (the Hall conductance is nothing but the inverse of the Hall resistance)[7].

In the following we present the theory of the QHE. We start by deriving the energy spectrum for a homogeneous 2DEG under a perpendicular magnetic field, i.e., the Landau levels (Sec. 2.2.1). We then calculate the general wave function for a homogeneous 2DEG under a perpendicular magnetic field from which we deduce the wave functions associated to the Landau levels (Sec. 2.2.2). Afterwards, we will see that chiral edge states appear at the edges of the sample (Sec. 2.2.3) and that they give rise to a Hall conductance which is quantized in units of the conductance quantum (Sec. 2.2.4). Next we discuss about the importance of disorder in the observation of quantum Hall conductance plateaus (Sec. 2.2.5), then we present a lattice model of the system (Sec. 2.2.6), and we end this section by looking at the topological origin of the quantization of the Hall conductance (Sec. 2.2.7).

2.2.1 Landau levels in a 2DEG under a perpendicular magnetic field

Here we determine the energy levels of a homogeneous 2DEG in the $x-y$ plane submitted to a perpendicular uniform magnetic field $\vec{B} = B\hat{u}_z$ with $B > 0$. We assume spin-degenerate electrons described by the single-particle Hamiltonian,

$$H = \frac{1}{2m}(\hbar\vec{k} - e\vec{A})^2 - \mu, \tag{2.66}$$

where $\vec{A}$ is the electromagnetic vector potential, $\vec{k} = (k_x, k_y, 0)$ is the two-dimensional wave vector, μ the chemical potential, e the electron charge, and m the electron effective mass. Let's proceed by using a purely algebraic method. This method works for any gauge potential $\vec{A}$ and so we consider the form $\vec{A} = (A_x(y),\, A_y(x),\, 0)$ in the derivation. We now introduce the canonical momentum vector $\vec{\pi} = (\pi_x,\, \pi_y,\, 0)$ with components $\pi_i = \hbar k_i - eA_i$ having the following commutation relation,

$$[\pi_x,\, \pi_y] = \pi_x\pi_y - \pi_y\pi_x = ie\hbar\left(\frac{\partial A_y}{\partial x} - \frac{\partial A_x}{\partial y}\right) = ie\hbar B, \tag{2.67}$$

where we have used the relation $[k_{x,y},\, f(x,y)] = -i\partial_{x,y}f(x,y)$. We then introduce the raising and lowering operators,

$$b = \frac{1}{\sqrt{2e\hbar B}}(\pi_x + i\pi_y), \quad b^\dagger = \frac{1}{\sqrt{2e\hbar B}}(\pi_x - i\pi_y), \tag{2.68}$$

[7] We have given an oversimplified explanation here. As we will see, a full understanding of the quantization of the Hall resistance requires taking into account the disorder in the system.

which obey the same commutation relation as the ladder operators of the quantum harmonic oscillator, i.e., $[b, b^\dagger] = 1$, and we can rewrite the general Hamiltonian (2.66) in the form of a harmonic oscillator,

$$H = \frac{\pi^2}{2m} - \mu = \left(b^\dagger b + 1/2\right)\hbar\omega_c - \mu. \tag{2.69}$$

From the analogy with the harmonic oscillator we can directly write the energy spectrum as harmonic levels known as the Landau levels (LLs) [Landau 1930],

$$E_n = \left(n + \frac{1}{2}\right)\hbar\omega_c - \mu, \quad n \in \mathbb{N}, \tag{2.70}$$

where the Landau level index n is the eigenvalue of the operator $b^\dagger b$. These levels correspond to cyclotron orbits with quantized values of the cyclotron frequency $\omega_c = eB/m$. For a system with periodic boundary conditions in the y-direction (this is what we assume in the following), there exists such a Landau level for each plane wave along the transverse direction y. Note that here we consider spin-degenerate electrons such that each Landau level for a given transverse mode is made of two electrons. In Fig. 2.5 we sketch the cyclotron orbits and the LLs.

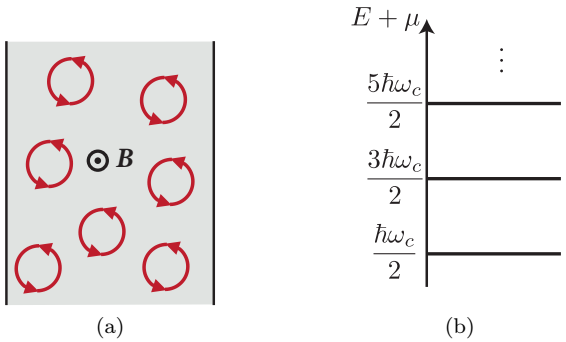

(a) (b)

Figure 2.5: Bulk of the 2DEG. In (a) we sketch the cyclotron orbits and in (b) we represent the associated LLs.

In the next subsection we determine the general wave function for a 2DEG under a perpendicular magnetic field by specifying a gauge potential $\vec{A}$ and we then discuss the degeneracy of the LLs.

2.2.2 Wave function and degeneracy of the Landau levels

Our task is to determine the general wave function $\Psi(x, y)$ solving the eigenvalue equation of the Hamiltonian (2.66). To proceed, we assume periodic boundary conditions along y such that we can make the separation ansatz,

$$\Psi(x, y) = \frac{e^{ik_y y}}{\sqrt{L_y}}\psi(x), \tag{2.71}$$

where L_y is the size of the sample in the y-direction and the periodic boundary condition implies $k_y = n2\pi/L_y$, with n an integer. (To write the above wave function we have implicitly used the substitution $\vec{k} \to -i\vec{\nabla}$.) To determine the longitudinal wave function $\psi(x)$ we must solve the x-dependent Schrödinger equation $H(x)\psi(x) = E\psi(x)$. To do so, we need to specify a gauge for the vector potential which is obtained from the relation $\vec{B} = \vec{\nabla} \times \vec{A}$. With $\vec{B} = B\hat{u}_z$, common choices (but not the only possible ones) are $\vec{A} = (-By, 0, 0)$, $\vec{A} = (0, Bx, 0)$, or $\vec{A} = (-By, Bx, 0)/2$. The two first ones are called Landau gauges and preserve the translational invariance along one direction while the third one is the symmetric gauge which preserves rotational invariance. In order to preserve the translational invariance along y we choose the y-independent Landau gauge,

$$\vec{A} = Bx\hat{u}_y, \tag{2.72}$$

and the Hamiltonian (2.66) becomes,

$$H = \frac{1}{2m}\left[(\hbar k_x)^2 + (\hbar k_y - eBx)^2\right] - \mu. \tag{2.73}$$

We then perform the substitution $k_x \to -i\partial_x$ so that the x-dependent Schrödinger equation reads,

$$\psi''(x) + \frac{2m}{\hbar^2}\left[(E+\mu) - \frac{1}{2}m\omega_c^2(x-x_0)^2\right]\psi(x) = 0. \tag{2.74}$$

One can recognize the differential equation of an harmonic oscillator oscillating at the cyclotron frequency ω_c around the guiding center coordinate $x_0 = k_y l_B^2$, with $l_B = \sqrt{\hbar/(eB)}$ the magnetic length. A physical interpretation of the magnetic length l_B is that the area $2\pi l_B^2$ includes one quantum of magnetic flux $\phi_0 = h/e$. We can anticipate that, for a homogeneous system, the solutions of Eq. (2.74) will be related to the usual Hermite polynomials of harmonic oscillators. However, let us give the general solution of Eq. (2.74) which is valid even for inhomogeneous systems in order to look later at what happens at the edges of the sample. We thus introduce the variables,

$$a = -\frac{E+\mu}{\hbar\omega_c}, \quad z = \frac{\sqrt{2}}{l_B}(x - x_0), \tag{2.75}$$

and we rewrite Eq. (2.74) as a first Weber differential equation,

$$\psi''(z) - \left(\frac{1}{4}z^2 + a\right)\psi(z) = 0. \tag{2.76}$$

The corresponding solutions vanishing as $z \to \infty$ are given by the parabolic cylinder functions[8],

$$\psi(z) = U(a, z), \tag{2.77}$$

where $U(a,z)$ is defined as [Abramowitz & Stegun 1964, Eqs. (19.2.5), (19.2.6), (19.3.1), (19.3.3), (19.3.4)],

$$U(a,z) = Y_1(a,z)\cos\left[\left(\frac{1}{4}+\frac{1}{2}a\right)\pi\right] - Y_2(a,z)\sin\left[\left(\frac{1}{4}+\frac{1}{2}a\right)\pi\right], \tag{2.78}$$

with,

$$Y_1(a,z) = \frac{1}{\sqrt{\pi}}\frac{\Gamma\left(\frac{1}{4}-\frac{1}{2}a\right)}{2^{\frac{1}{2}a+\frac{1}{2}}}y_1(a,z), \tag{2.79}$$

$$Y_2(a,z) = \frac{1}{\sqrt{\pi}}\frac{\Gamma\left(\frac{3}{4}-\frac{1}{2}a\right)}{2^{\frac{1}{2}a-\frac{1}{2}}}y_2(a,z),, \tag{2.80}$$

where Γ is the gamma function and,

$$y_1(a,z) = e^{-\frac{1}{4}z^2}M\left(\frac{1}{2}a+\frac{1}{4},\frac{1}{2},\frac{1}{2}z^2\right) \tag{2.81}$$

$$= e^{-\frac{1}{4}z^2}\left[1 + \left(a+\frac{1}{2}\right)\frac{z^2}{2!} + (a+\frac{1}{2})(a+\frac{5}{2})\frac{z^4}{4!} + \cdots\right], \tag{2.82}$$

$$y_2(a,z) = ze^{-\frac{1}{4}z^2}M\left(\frac{1}{2}a+\frac{3}{4},\frac{3}{2},\frac{1}{2}z^2\right) \tag{2.83}$$

$$= e^{-\frac{1}{4}z^2}\left[z + \left(a+\frac{3}{2}\right)\frac{z^3}{3!} + (a+\frac{3}{2})(a+\frac{7}{2})\frac{z^5}{5!} + \cdots\right], \tag{2.84}$$

[8] Here we look at the solutions vanishing as $z \to \infty$ because we will consider a semi-infinite system in the next subsection in order to see what happens at the edges of the system.

where $M(a,b,z)$ is the Kummer's function of the first kind (also known as the confluent hypergeometric function of the first kind and sometimes denoted by ${}_1F_1(a;b;z)$ or $\Phi(a;b;z)$),

$$M(a,b,z) = \sum_{n=0}^{\infty} \frac{a^{(n)} z^n}{b^{(n)} n!}, \tag{2.85}$$

with $a^{(0)} = 1$ and $a^{(n)}$ the rising factorial,

$$a^{(n)} = a(a+1)(a+2)\cdots(a+n-1). \tag{2.86}$$

We have thus found the general form of the wave function for a 2DEG under a perpendicular magnetic field with translational invariance along the y-direction. As we have seen in the previous subsection, for a homogeneous system the energy levels are given by the LLs (2.70). If we replace the energy E by the LLs in the general wave function (2.77) we get harmonic oscillator-like wave functions,

$$\psi_n(z) = U(-n-1/2, z) = 2^{-n/2} e^{-z^2/4} H_n\left(\frac{z}{\sqrt{2}}\right), \tag{2.87}$$

where n is the Landau level index and $H_n(z/\sqrt{2})$ are Hermite polynomials. Here the second equality holds because n is a positive integer [Abramowitz & Stegun 1964]. Note that in this case the wave function is normalizable in all space, i.e., it vanishes as $z \to \pm\infty$.

To conclude this subsection, let us discuss the degeneracy of the LLs. In fact, due to their non-dependence on the wavenumber k_y, the LLs are highly degenerate. To see this, consider a rectangular sample of dimensions L_x, L_y, with the left edge at $x = 0$ and the right edge at $x = L_x$. Since the wave functions are localized around the guiding center coordinate $x_0 = k_y l_B^2$, the values of k_y for which the states are inside the sample range from $k_y = 0$ to $k_y = L_x/l_B^2$. The total number of states in each Landau level is then,

$$N = \frac{L_y}{2\pi} \int_0^{L_x/l_B^2} \mathrm{d}k_y = \frac{L_x L_y}{2\pi l_B^2} = \frac{B L_x L_y}{\phi_0} \equiv N_\phi, \tag{2.88}$$

where N_ϕ is the number of flux quanta penetrating the sample. Thus, there are two states (two because of spin degeneracy) per Landau level per flux quantum.

In the next subsection we consider a 2DEG-vacuum junction in order to see that chiral edge states appear at the edges of the 2DEG.

2.2.3 Chiral edge states

We have seen that in the bulk the electrons follow cyclotron orbits with energies given by LLs. We now ask, what happens at the edges of the sample? This is easily answered semi-classically by thinking about the cyclotron motion. Indeed, near the edges, the cyclotron orbits cannot be executed in such a way that the trajectory, which is parametrized by the guiding center coordinate and the area of the orbit [Van Houten *et al.* 1989], bounces back as depicted in Fig. 2.6. This leads to the phenomenon of skipping orbits along the edges. This skipping motion forces the electrons to move unidirectionally along the two sides of the sample. Such unidirectional motion is called chiral. In addition, the electrons move in one direction at one edge and in the opposite direction at the other edge. These boundary modes are the well known chiral edge states of the QHE.

To see how the edge states appear in quantum theory, consider a junction between a semi-infinite 2DEG and the vacuum, as shown in Fig. 2.7. The 2DEG-vacuum interface is located at $x = 0$, for $x > 0$ there is the vacuum and for $x < 0$ there is the 2DEG. The wave function of the vacuum is zero and that of the 2DEG is the parabolic cylinder function $U(a, -z)$ defined in Eq. (2.78), where we recall that $a = -(E+\mu)/(\hbar\omega_c)$ and $z = \sqrt{2}(x - k_y l_B^2)/l_B$. To obtain the energy spectrum of the states living along the 2DEG-vacuum interface, we match the wave functions at $x = 0$, leading to the following equation,

$$U\left(-\frac{E+\mu}{\hbar\omega_c}, \sqrt{2} k_y l_B\right) = 0. \tag{2.89}$$

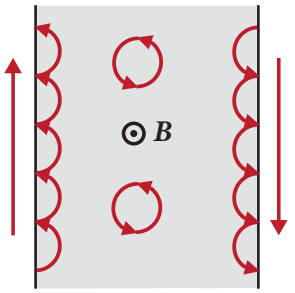

Figure 2.6: Semi-classical picture of skipping orbits. At the boundaries of the 2DEG, the circular cyclotron motion cannot be performed due to collisions and so the trajectories are a sequence of skipping orbits leading to a unidirectional motion along the edges. Such a unidirectional motion is said to be chiral and, at opposite edges, the electrons move in opposite directions (i.e., they have opposite chiralities).

By solving this equation for E we obtain the energy spectrum represented in Fig. 2.8. From this figure we see that, as the guiding center coordinate $x_0 = k_y l_B$ gets close to the 2DEG-vacuum interface, the bulk LLs are bent and become chiral edge states. This picture of bended Landau levels was first proposed by Halperin [Halperin 1982].

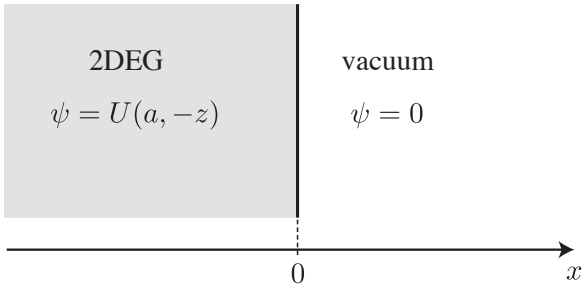

Figure 2.7: 2DEG-vacuum junction. The 2DEG is placed in the half-plan of negative-x and the positive-x half-plan is the vacuum and so the 2DEG-vacuum interface is located at $x = 0$. In the 2DEG the wave function is a parabolic cylinder function $U(a, -z)$ as introduced in Eq. (2.78) with $a = -(E + \mu)/(\hbar\omega_c)$ and $z = \sqrt{2}(x - k_y l_B^2)/l_B$, and in the vacuum the wave function is zero.

In Fig. 2.8 we can see that the number of spin-degenerate Landau levels below the Fermi level is given by the number of crossings N_c defined as

$$N_c = \text{int}(\nu/2), \tag{2.90}$$

where $\nu = N_e/N_\phi$ is the so-called filling factor of the QHE defined as the ratio between the number of electrons in the 2DEG, $N_e = n_s L_x L_y$, and the number of flux quanta penetrating the sample N_ϕ introduced in Eq. (2.88). Note that the factor $1/2$ allows not to count the spin degenerate states twice while the number of edge states is given by $2N_c$. Note that N_c is also called the number of conducting channels (where the channels are spin-degenerate here) and, as we show in the next section, it gives the number of conductance quanta on a Hall plateau (see Fig. 2.11). Writing the electron density of the 2DEG as

$$n_s = 2\,\frac{\pi k_F^2}{(2\pi)^2}, \tag{2.91}$$

where the factor of two stands for the spin-degeneracy, the filling factor can be written as,

$$\nu = \frac{n_s h}{eB} = k_F^2 l_B^2 = \frac{2\mu}{\hbar\omega_c}, \tag{2.92}$$

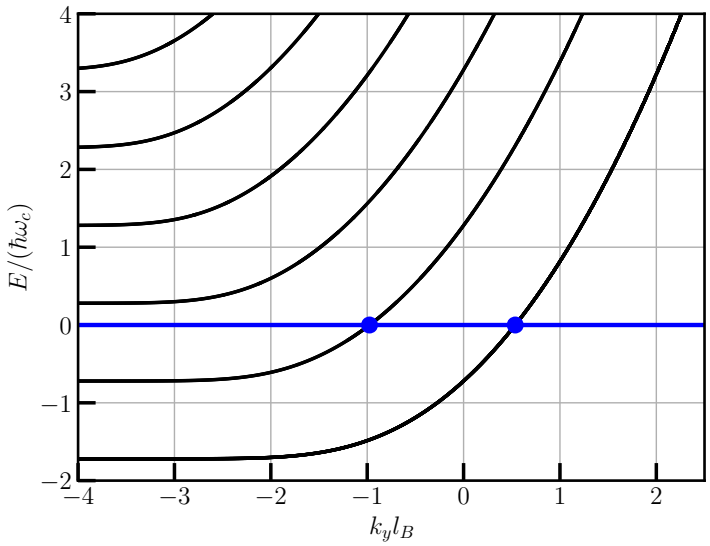

Figure 2.8: Energy spectrum of the modes living along the 2DEG-vacuum interface. The energy E (relative to the Fermi level) is plotted as a function of the momentum along the interface k_y. We observe flat LLs (for $k_y < 0$) which are bent as they get close to $k_y = 0$. Due to the linear relation between k_y and the guiding-center coordinate $x_0 = k_y l_B^2$, we interpret these bands as the Landau levels being bent as they approach the interface located at $x = 0$. We also observe two crossings at the Fermi level (Fermi level: blue line; crossings: blue dots) close to $k_y = 0$. Hence, two Landau levels are filled and participate to a non-zero current propagating along the 2DEG-vacuum interface with velocity $v_y = (1/\hbar)\partial E/\partial k_y$. These are the chiral edge states. We have set $\hbar\omega_c = 0.45\mu$.

where the last equality reflects the fact that ν is related to the number of filled LLs. In fact, the LLs are exactly filled when $\nu/2 \in \mathbb{N}$; otherwise there is a partial filling as discussed in Sec. 2.2.5. Moreover, N_c is related to a topological invariant as detailed in Sec. 2.2.7.

2.2.4 Quantized Hall conductance

The classical Hall effect can be stated as follows: due to the Lorentz force, an electric current I_x flowing through a material submitted to a magnetic field generates a voltage, called the Hall voltage V_H, perpendicular to the magnetic field. The situation is depicted in Fig. 2.9, and the Hall conductance is

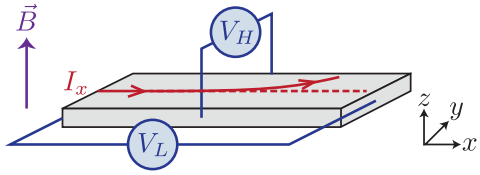

Figure 2.9: Hall setup. A current is injected along x from the left edge. Due to the Lorentz force created by the magnetic field $\vec{B}$, the electrons are deflected, which generates a transverse potential, or Hall potential, denoted V_H. The longitudinal potential is denoted V_L.

defined as,

$$G_H = \frac{I_x}{V_H}, \tag{2.93}$$

while the corresponding Hall resistance is,

$$R_H = \frac{1}{G_H} = \frac{V_H}{I_x}. \tag{2.94}$$

To derive the classical result for the Hall conductance we use the Drude model and follow [Tong 2016, Sec. 1.2.2]. For that we need to introduce temporarily two ingredients. First, we consider an electric field $\vec{E}$ which would be parallel to the direction of the current in the absence of magnetic field. Second, we add a linear friction term which describes the scattering on whatever is impeding the electron's trajectory such as impurities with a scattering time characterized by τ. With these two more ingredients the classical equation of motion reads,

$$m\frac{\mathrm{d}\vec{v}}{\mathrm{d}t} = e\left(\vec{E} + \vec{v}\times\vec{B}\right) - \frac{m\vec{v}}{\tau}, \tag{2.95}$$

where the scattering time τ can be interpreted as the average time between collisions. Looking at the equilibrium solution with $\mathrm{d}\vec{v}/\mathrm{d}t = 0$, we obtain,

$$\vec{v} - \frac{e\tau}{m}\vec{v}\times\ \vec{B} = \frac{e\tau}{m}\vec{E}. \tag{2.96}$$

The above equation is the simplest classical model of charge transport known as the Drude model. Using the classical relation between the current density $\vec{J}$ and the velocity, $\vec{J} = n_s e\vec{v}$, with n_s the density of charge carriers, we can rewrite Eq. (2.96) in a matrix form,

$$\begin{pmatrix} 1 & -\omega_c\tau \\ \omega_c\tau & 1 \end{pmatrix}\vec{J} = \frac{n_s e^2\tau}{m}\vec{E}, \tag{2.97}$$

where the current density and electric field vectors are given by,

$$\vec{J} = \begin{pmatrix} J_x \\ J_y \end{pmatrix} = \begin{pmatrix} I_x/W \\ I_y/L \end{pmatrix}, \quad \vec{E} = \begin{pmatrix} E_x \\ E_y \end{pmatrix} = \begin{pmatrix} V_L/L \\ V_H/W \end{pmatrix}, \tag{2.98}$$

while the z-components are zero. Here we have introduced the dimensions of the sample in x- and y-directions respectively given by L and W. We can then invert Eq. (2.97) to get the Ohm's law, $\vec{J} = \sigma\vec{E}$, where σ is the conductivity tensor which in the Drude model reads,

$$\sigma = \frac{\sigma_{DC}}{1+\omega_c^2\tau^2}\begin{pmatrix} 1 & \omega_c\tau \\ -\omega_c\tau & 1 \end{pmatrix}, \quad \sigma_{DC} = \frac{n_s e^2\tau}{m}, \tag{2.99}$$

with σ_{DC} the DC conductivity without magnetic field. If we now consider a clean device where there are no scattering events for the charge carriers, i.e., $\omega_c\tau \gg 1$, we obtain the following conductivity tensor,

$$\sigma = \frac{n_s e}{B}\begin{pmatrix} 0 & 1 \\ -1 & 0 \end{pmatrix}, \tag{2.100}$$

from which we obtain the classical Hall conductance[9],

$$G_H^{classical} = \frac{n_s e}{B} = \frac{\nu}{2}G_0, \tag{2.101}$$

where in the last equality we have used the filling factor ν as defined in Eq. (2.92) and the factor $1/2$ compensates for the spin-degeneracy factor 2 used in the quantum of conductance $G_0 = 2e^2/h$. Thus, classically, the Hall conductance grows linearly with n_s/B or with ν. In the quantum regime, however, the Hall conductance growths by steps. Indeed, in the regime of well separated LLs the density doesn't change in between two levels such that one has to take the integer part of $\nu/2$ in the above equation leading to $G_H^{quantum} = N_c G_0$. This is derived below by using the Landauer-Büttiker formalism (the Landauer-Büttiker formalism is detailed in App. A.4).

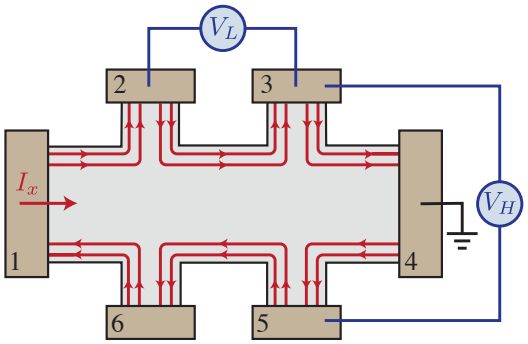

Figure 2.10: Hall bar geometry. The Hall bar is made of six contacts. The reservoir 1 is the source from where the current is injected and the reservoir 4 is the grounded drain. The longitudinal voltage is measured between reservoirs 2 and 3 and the Hall voltage is measured between reservoirs 3 and 5. Here we have sketched a situation where two edge states are propagating around the sample.

The experimental setup used to measure the QHE is the Hall bar geometry as represented in Fig. 2.10. Assuming ballistic edge states we can explain the quantization of the Hall conductance in a simple way by using the Landauer-Büttiker formalism. Indeed, this formalism provides a natural framework to deal with a multi-terminal setup such as the Hall bar geometry. As derived in App. A.4, we can write the current I_p in lead p as,

$$I_p = \int i_p(E)\mathrm{d}E, \tag{2.102}$$

$$i_p(E) = \frac{2e}{h}\sum_q \bar{T}_{pq}(E)\left[f_p(E) - f_q(E)\right], \tag{2.103}$$

where $\bar{T}_{pq}(E)$ represents the total transmission from lead q to lead p at energy E and $f_p(E) = \{1 + \exp[(E-\mu_p)/(k_BT)]\}^{-1}$ is the Fermi function in lead p. If the bias is small, $|\mu_p - \mu_q| \ll k_\mathrm{B}T$, we can linearize Eq. (2.102) to obtain,

$$I_p = \sum_q G_{pq}\left(V_p - V_q\right), \tag{2.104}$$

where we have used $\mu_p - \mu_q = e(V_p - V_q)$ and, at low temperatures $k_\mathrm{B}T \ll \hbar\omega_c$, the conductance matrix elements are given by,

$$G_{pq} = \bar{T}_{pq}G_0. \tag{2.105}$$

For the pairs (p, q) equal to (1, 6), (2, 1), (3, 2), (4, 3), (5, 4), or (6, 5), the total transmission correspond the number of channels N_c given in Eq. (2.90), $\bar{T}_{pq} = N_c$. For the other pairs (p, q) we have $\bar{T}_{pq} = 0$. Hence, it follows the conductance matrix elements,

$$\begin{array}{cccccccc} G_{pq} & q=1 & q=2 & q=3 & q=4 & q=5 & q=6 \\ p=1 & 0 & 0 & 0 & 0 & 0 & G_H \\ p=2 & G_H & 0 & 0 & 0 & 0 & 0 \\ p=3 & 0 & G_H & 0 & 0 & 0 & 0 \\ p=4 & 0 & 0 & G_H & 0 & 0 & 0 \\ p=5 & 0 & 0 & 0 & G_H & 0 & 0 \\ p=6 & 0 & 0 & 0 & 0 & G_H & 0 \end{array}, \tag{2.106}$$

[9] In general one cannot directly relate the conductivity with the conductance but these quantities are the same for a Hall measurement. In Eq. (2.116) we demonstrate the equality between the transverse resistivity and the Hall resistance.

where we have introduced,

$$G_H = N_c G_0. \tag{2.107}$$

As we show right now, G_H is the formula describing the quantization of the Hall conductance. To see that we derive the elements of the resistivity and conductivity tensors respectively denoted by ρ and σ,

$$\rho = \begin{pmatrix} \rho_{xx} & \rho_{xy} \\ \rho_{yx} & \rho_{yy} \end{pmatrix} = \begin{pmatrix} \rho_{xx} & \rho_{xy} \\ -\rho_{xy} & \rho_{xx} \end{pmatrix}, \tag{2.108}$$

$$\sigma = \begin{pmatrix} \sigma_{xx} & \sigma_{xy} \\ \sigma_{yx} & \sigma_{yy} \end{pmatrix} = \begin{pmatrix} \sigma_{xx} & \sigma_{xy} \\ -\sigma_{xy} & \sigma_{xx} \end{pmatrix}, \tag{2.109}$$

where the minus sign was obtained from the Drude model in Eq. (2.99), and we have $\sigma = \rho^{-1}$. We start by noticing that, as terminal 4 is grounded, we can set $V_4 = 0$ and rewrite Eq. (2.104) as,

$$\begin{pmatrix} I_1 \\ I_2 \\ I_3 \\ I_5 \\ I_6 \end{pmatrix} = G_H \begin{pmatrix} 1 & 0 & 0 & 0 & -1 \\ -1 & 1 & 0 & 0 & 0 \\ 0 & -1 & 1 & 0 & 0 \\ 0 & 0 & 0 & 1 & 0 \\ 0 & 0 & 0 & -1 & 1 \end{pmatrix} \begin{pmatrix} V_1 \\ V_2 \\ V_3 \\ V_5 \\ V_6 \end{pmatrix}. \tag{2.110}$$

Since the terminals 2, 3, 5, 6 are floating we can set $I_2 = I_3 = I_5 = I_6 = 0$, and we find,

$$V_1 = V_2 = V_3, \tag{2.111}$$

$$V_5 = V_6 = 0, \tag{2.112}$$

while the injected current reads,

$$I_1 = I_x = G_H V_1. \tag{2.113}$$

Afterwards we can write the longitudinal resistance as,

$$R_L = \frac{V_L}{I_x} = \frac{V_2 - V_3}{I_1} = 0, \tag{2.114}$$

and the transverse Hall resistance as,

$$R_H = \frac{V_H}{I_x} = \frac{V_3 - V_5}{I_1} = \frac{1}{G_H} = \frac{1}{N_c} R_0, \tag{2.115}$$

where $R_0 = 1/G_0$ is the (spin-degenerate) quantum of resistance. Usually, for a rectangular-shaped sample of size $L \times W$, the resistance R and the resistivity ρ are related by $R = \rho L/W$. However, in a Hall measurement, we have

$$R_H = \frac{V_H}{I_x} = \frac{E_y W}{I_x} = \frac{E_y}{I_x/W} = \frac{E_y}{J_x} = \rho_{yx}, \tag{2.116}$$

where in the last equality we have used the definition (2.121) and the classical result obtained for a clean sample, $\rho_{xx} = \rho_{yy} = 0$. Thus, the Hall resistance R_H and the transverse resistivity ρ_{yx} are found to be the same. This is crucial for the universality of the QHE. We can then write the resistivity tensor as,

$$\rho = R_H \begin{pmatrix} 0 & -1 \\ 1 & 0 \end{pmatrix}, \tag{2.117}$$

and the conductivity tensor becomes,

$$\sigma = G_H \begin{pmatrix} 0 & 1 \\ -1 & 0 \end{pmatrix}. \tag{2.118}$$

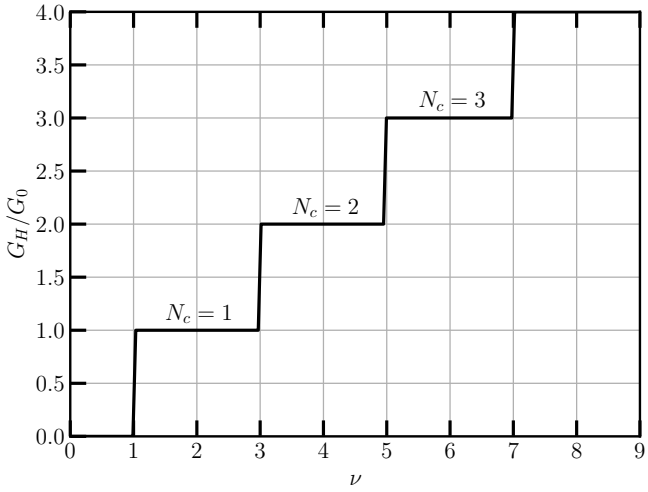

Figure 2.11: Hall conductance plateaus. The Hall conductance G_H is plotted as a function of the filling factor ν. We observe plateaus given by the number of crossings N_c defined in Eq. (2.90).

This last result is in agreement with the classical calculation (2.101) but here the pre-factor $\nu/2$ has been replaced by its integer value $N_c = \text{int}(\nu/2)$. As already discussed, this integer value is due to the fact that the density remains constant between the (clean) Landau levels. Thus, the transverse conductance is well quantized in units of the quantum of conductance as expected from the von Klitzing's experiment. We illustrate this quantization by plotting the Hall conductance plateaus in Fig. 2.11.

In all our quantum treatment of the QHE we never considered disordered samples. However, the extreme universality of the quantized Hall conductance is due to, rather than despite of, the disorder present in the system. Also, the disorder allows to have a non-zero longitudinal resistance. We thus detail the importance of disorder in the next section.

2.2.5 Importance of disorder

2.2.5.1 Hall effect without disorder revisited

Here we discuss about the importance of disorder, which is always present in real systems. However, let's first review what happens without it. In the absence of disorder the system preserves translational invariance so that we can use any inertial frame of reference. Considering only an external magnetic field such that, in the lab frame, the electromagnetic fields are,

$$\vec{E} = 0, \quad \vec{B} = B\hat{u}_z, \tag{2.119}$$

and the current density $\vec{J} = \sigma\vec{E}$ is zero. By Lorentz transforming into a frame moving at speed v in the y-direction the fields become [Jackson 1998],

$$\vec{E}' = \gamma v B\hat{u}_x \simeq vB\hat{u}_x, \quad \vec{B}' = \gamma B\hat{u}_z \simeq B\hat{u}_z, \tag{2.120}$$

where $\gamma = (1 - v^2/c^2)^{-1}$ is the Lorentz factor and $\gamma \simeq 1$ holds when v is small compared to the speed of light c. The transformed current density is $\vec{J}' = n_s e v\hat{u}_y$ and, using the following relations,

$$J'_\mu = \sigma_{\mu\nu}E'_\nu, \quad E'_\mu = \rho_{\mu\nu}J'_\nu, \tag{2.121}$$

where we consider the Einstein summation on repeated indices, one recovers the classical results

$$\rho = \frac{B}{n_s e}\begin{pmatrix} 0 & -1 \\ 1 & 0 \end{pmatrix} = \frac{2}{\nu}\begin{pmatrix} 0 & -1 \\ 1 & 0 \end{pmatrix}, \tag{2.122}$$

$$\sigma = \frac{n_s e}{B}\begin{pmatrix} 0 & 1 \\ -1 & 0 \end{pmatrix} = \frac{\nu}{2}\begin{pmatrix} 0 & 1 \\ -1 & 0 \end{pmatrix}. \tag{2.123}$$

Thus, without disorder, the Hall effect tells us nothing about the system other than its density n_s. The Hall conductivity is a linear function of the inverse magnetic field whose slope gives us the electron density. This Lorentz argument relies only on translational invariance and do not care about any mechanical process. In reality, the measured Hall conductivity is not this classical result. Hence, there must be an additional ingredient that breaks translational symmetry. It turns out that disorder do the job.

2.2.5.2 Effects of disorder: broadening of the Landau levels and non-zero longitudinal resistance

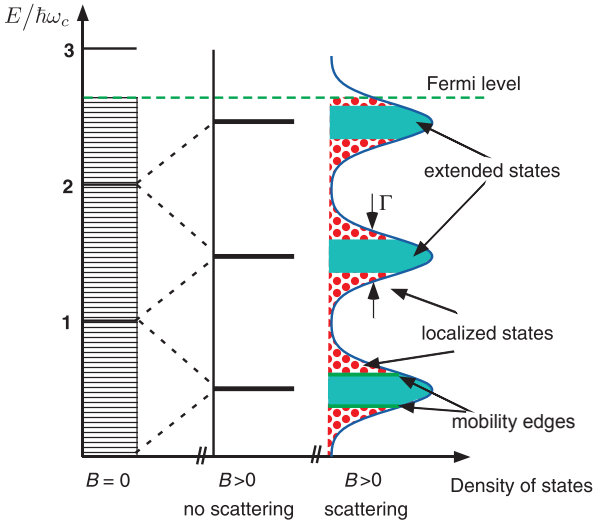

Figure 2.12: Landau levels broadening. At zero field the density of states (DOS) is continuous over the energy. At $B \neq 0$ without scattering the DOS becomes a series of Dirac δ peaks. If $B \neq 0$ with scattering the DOS acquire a Gaussian/Lorentzian profile: the states at the center of the LLs are called extended states (blue cores) while the states far away from the center are localized states (red dots). An interface between a localized and an extended region is called a mobility edge. Adapted from [Jeckelmann & Jeanneret 2007].

In the previous section on the quantization of the Hall conductance we said that, to obtain the quantum formula from the classical one, we have to replace the pre-factor $\nu/2$ by its integer value $N_c = \text{int}(\nu/2)$. We argued by considering that the DOS is made of δ peaks localized at the Landau levels but this is true only for systems without disorder, which is never the case in reality. Here we provide a more complete explanation for this quantization by taking into account impurities in the system. We will not enter into technical details but they can be found in [Prange 1981, Prange & Girvin 1990] for example. In a real system, impurities in the crystal are sources of disorder which leads to the broadening of the LLs such that a non-zero DOS is present in between them (see Fig. 2.12). The broadening is characterized by an energy width Γ, which can be expressed in terms of the scattering lifetime τ through the relation $\Gamma \sim \hbar/\tau$. This broadening allows the Fermi energy to vary continuously between the Landau levels when the magnetic field or carrier density is modified. The states far away from the unperturbed LLs are called localized states because they are localized by the impurities while the non-localized states, i.e., those at the core of the broadened LLs, are called extended states. Without giving the details, we mention that the localization of the states due to the disorder is explained by the Anderson localization [Anderson 1958]. The interested reader can have a look at Girvin's book [Girvin & Yang 2019] for more details. Moreover, a field-dependent band width $\Gamma \sim \sqrt{B}$ can be used to fit experimental results [Usher & Elliott 2009]. Thus, using this field dependence, we expect the width of the extended region to increase with the magnetic field.

When the Fermi level is located within the extended states, the material is conducting giving rise to a non-zero longitudinal conductance. On the other hand, when the Fermi level runs across the localized

states, the system behaves as an insulator and the longitudinal conductance is zero. Thus, the quantum Hall plateaus can be understood as a succession of localization-delocalization transitions as the Fermi level sweeps the DOS. This is represented in Fig. 2.13 where we have sketched the longitudinal and the transverse resistivity with the corresponding DOS as the magnetic field is increasing. Moreover, while the localized states carry no current as the Fermi level is passing through them, the remaining extended states carry an extra current which compensate exactly for that not carried by the localized states [Prange 1981]. Thus, as long as all the extended states of a given Landau level are filled, the Hall current carried by that level is exactly the same as in the absence of impurities.

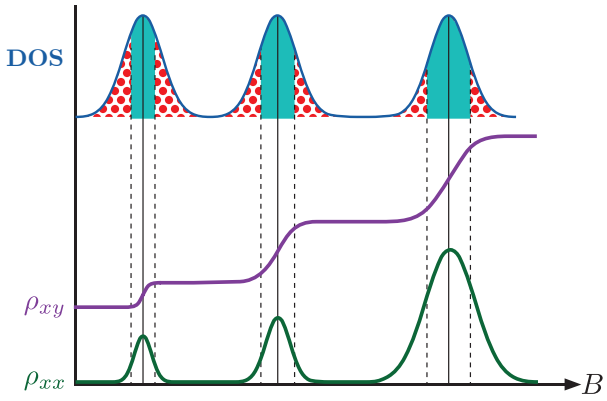

Figure 2.13: Sketch of the transverse ρ_{xy} and the longitudinal ρ_{xx} resistivity with the corresponding DOS as the magnetic field B is increasing. Across the localized states (red dots) we observe Hall plateaus while across the extended states (blue strips) we observe a non-zero longitudinal resistance. As B is running the spacing between the LLs increases leading to larger plateaus.

We have provided all the needed ingredients to explain the QHE so that we can now understand a Hall measurement as the one by Cage, Dziuba and Field [Cage *et al.* 1985] reported in Fig. 2.14. In this experiment the authors measured the Hall and longitudinal voltages as a function of the magnetic field. As the magnetic field increases, we observe the appearance of the Hall plateaus accompanied by non-zero longitudinal voltages in between them.

As we perform numerous tight-binding simulations of quantum Hall systems in Chap. 3, we present a lattice model of the QHE in the next subsection.

2.2.6 Lattice model of the quantum Hall effect

Let us first discuss the zero-field case. As shown in App. C, one can discretize a continuous Hamiltonian by using the finite difference method. For free electrons on a square lattice with no external magnetic field, the single-particle tight-binding Hamiltonian reads

$$H_{ij} = [4t - \mu]\, \delta_{\vec{r}_i,\vec{r}_j} - t \sum_{\vec{R}_a} \delta_{\vec{r}_i - \vec{r}_j, \vec{R}_a}, \tag{2.124}$$

where i, j label the lattice sites, $\vec{r}_{i,j}$ are position vectors, $\{\vec{R}_a\} = \{\hat{u}_x, -\hat{u}_x, \hat{u}_y, -\hat{u}_y\}$ is the ensemble of nearest neighbour vectors, $t = \hbar^2/(2ma^2)$ is the hopping energy with a the lattice constant and $\delta_{p,q}$ is the Kronecker-delta symbol. In the absence of an external magnetic field, the momentum vector $\vec{k}$ lies in the first Brillouin zone,

$$-\frac{\pi}{a} < k_x \leq \frac{\pi}{a}, \quad -\frac{\pi}{a} < k_y \leq \frac{\pi}{a}, \tag{2.125}$$

and, for a finite-sized sample with dimensions $L_x \times L_y$, the momenta k_i are quantized as integer multiples of $2\pi/L_i$. The total number of states in the Brillouin zone is thus given by $[(2\pi/a)/(2\pi/L_x)] \times$

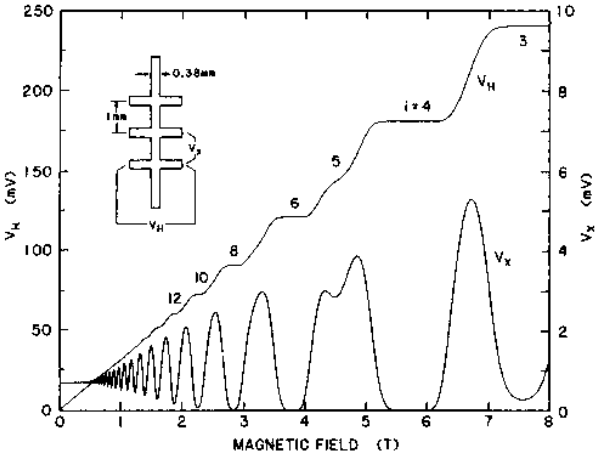

Figure 2.14: Measurements of the transverse (V_x) and Hall (V_H) voltages versus the magnetic field. The system is a GaAs-AlGaAs heterostructure cooled to 1.2K. The source-drain current is 25.5μA and the electron density is $n_s = 5.6 \times 10^{11}$electrons/cm^2. We observe Hall voltage plateaus corresponding to Hall resistances of $(h/e^2)/i$, where i is an integer, as well as non-zero longitudinal voltages in between the plateaus. At low fields where we are not in the regime of well separated LLs we recover the classical linear dependencies. Extracted from [Cage *et al.* 1985].

$[(2\pi/a)/(2\pi/L_y)] = L_xL_y/a^2$, which is nothing but the total number of lattice sites. Moreover, the tight-binding method provides a good description of the continuum model as long as $k_xa \ll 1$ and $k_ya \ll 1$ (see App. C.3).

Let's now add an external magnetic field. It can be easily incorporated into the tight-binding model by using the Peierls substitution [Peierls 1933, Hofstadter 1976]. Indeed, for a lattice with only nearest neighbor hopping, and in the presence of a magnetic field, the hopping element t between sites i and j acquires a phase factor, $t \to t_{ij} = te^{i\phi_{ij}}$, with ϕ_{ij} the Peierls phase defined as [Bernevig & Hughes 2013]

$$\phi_{ij} = \frac{e}{\hbar}\int_{\vec{r}_i}^{\vec{r}_j} \vec{A}(\vec{r}) \cdot \mathrm{d}\vec{r}, \tag{2.126}$$

where the vector potential $\vec{A}(\vec{r})$ has to be evaluated at a point halfway between sites i and j, that is, at $(\vec{r}_i + \vec{r}_j)/2$. Up to the factor $e/\hbar$, this phase is nothing but the line integral of the vector potential along the bond connecting the two sites. The tight-binding Hamiltonian describing free electrons on a square lattice in the presence of a magnetic field is thus

$$H_{ij} = [4t - \mu]\,\delta_{\vec{r}_i,\vec{r}_j} - t\sum_{\vec{R}_a} e^{i\phi_{ij}}\delta_{\vec{r}_i-\vec{r}_j,\vec{R}_a}, \tag{2.127}$$

and, in our y-independent Landau gauge $\vec{A} = Bx\hat{u}_y$ introduced in Eq. (2.72), the Peierls phase reads,

$$\phi_{ij} = \frac{\pi B}{\phi_0}(x_i + x_j)(y_j - y_i), \tag{2.128}$$

with $\phi_0 = h/e$ the quantum of magnetic flux. The tight-binding Hamiltonian (2.127) is the discretized version of the continuum Hamiltonian (2.66).

As it is important for the next subsection, we now ask if the Brillouin zone is still well defined in the presence of a magnetic field. Whereas it was easy to add the magnetic field in the tight-binding Hamiltonian, it is not obvious that the Brillouin zone survives. Indeed, the values of the lattice momenta k_i were deduced from the translational invariance of the system along the two directions of the lattice. However, our Landau gauge breaks the translational invariance along the x-axis. In fact, we can still define a periodicity in momentum space even in the presence of a magnetic field. In particular, if

the magnetic flux per plaquette $\phi = Ba^2$ is a rational multiple of ϕ_0, i.e., $\phi = (p/q)\phi_0$ with p and q integers not sharing a common divisor, the momenta k_i are periodic within the magnetic Brillouin zone [Kohmoto 1985],

$$-\frac{\pi}{qa} < k_x \leq \frac{\pi}{qa}, \quad -\frac{\pi}{a} < k_y \leq \frac{\pi}{a}. \tag{2.129}$$

In that case the number of states in a magnetic Brillouin zone is given by $L_x L_y/(qa^2)$, suggesting that the spectrum decomposes into q (degenerate) bands.

Throughout this manuscript, we perform tight-binding simulations using the Kwant software [Groth *et al.* 2014]. In Fig. 2.15, we show a Kwant system and the current density between sites computed for a mode leaving the top lead, where the current density flowing from site j to site i is given by

$$J_{ij} = \mathrm{i}\left[\psi_j^\dagger (H_{ij})^\dagger \psi_i - \psi_i^\dagger H_{ij} \psi_j\right]. \tag{2.130}$$

This allows us to illustrate a system constructed by Kwant and to visualize an edge state of the QHE.

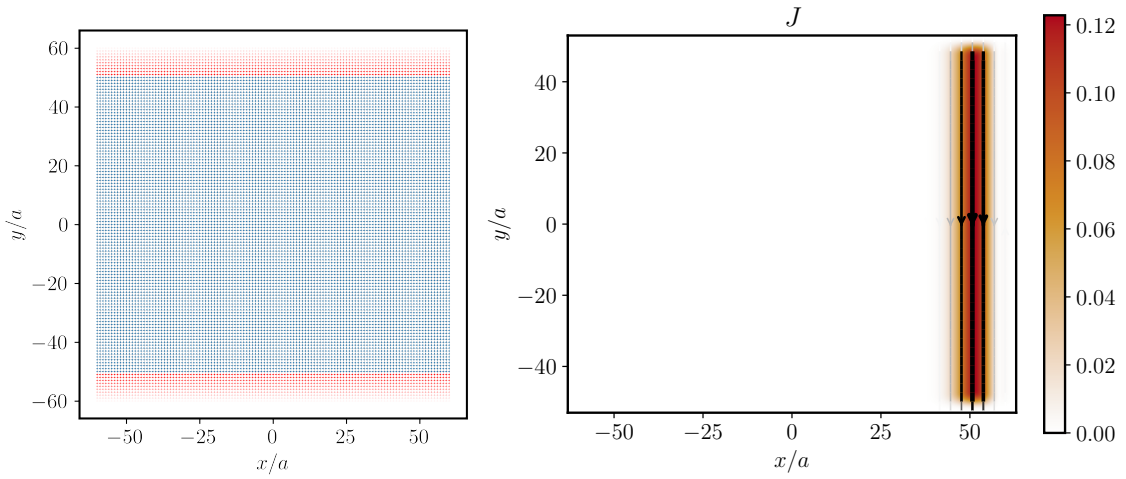

Figure 2.15: Kwant system and current. (a) Lattice used to perform the tight-binding simulations with Kwant. The scattering region is in blue and the red dots indicate the beginning of a lead. (b) Current flowing between the sites for one mode leaving the top lead. We used the Kwant routine *kwant.plotter.current* calculating the current between two sites by using Eq. (2.130). Since we are focusing on a mode that is leaving the top lead, the current is flowing from the top to the bottom, as indicated by the arrows.

2.2.7 Topological point of view of the quantum Hall effect

In this last section on the QHE we discuss about the relation between the topology of the first Brillouin zone and the quantization of the Hall conductance. Indeed, it was shown by Thouless and collaborators that the number of crossings N_c appearing in the definition of the Hall conductance (2.107) is related to a topological invariant called the first Chern number [Thouless *et al.* 1982]. For the special case of the QHE, the first Chern number is also called TKNN invariant from the names of the authors who made this discovery (Thouless, Kohomoto, Nightingale, and den Nijs). This discovery is at the origin of a new field of research in condensed matter theory, the study of topological phases of matter. For this reason, the QHE is known as the mother of topological insulators. Indeed, topological insulators correspond to materials that are insulating in the bulk and conducting at their boundaries, just as we found for the QHE. These conducting edge states are characterized by topological invariants calculated

from the bulk properties of the material. This is known as the bulk-edge correspondence. Here we follow the lecture notes of Tong [Tong 2016, Sec. 2.3.1], but there are many other references discussing this topic. The interested reader can consult the following references for more information on topological phases of matter [Hasan & Kane 2010, Bernevig & Hughes 2013, Moessner & Moore 2021]. More information on the topological point of view of the QHE is also provided in this nice *Physics Today* article [Avron *et al.* 2003].

Let's consider a particle moving on a square lattice with lattice constant a. The energy spectrum is made of q bands whose associated states are labelled by the lattice momentum which is restricted to the magnetic Brillouin zone (2.129). Because of the periodic boundary conditions of the magnetic Brillouin zone, the lattice momentum lives on a torus T^2 as depicted in Fig. 2.16. In a given band, the wave

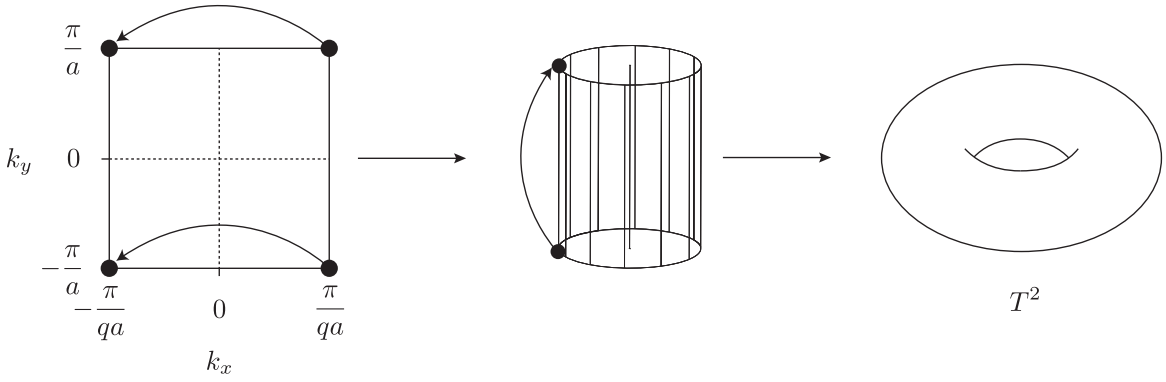

Figure 2.16: The two dimensional Brillouin zone torus T^2.

function can be written in a cell-periodic (Bloch) form,

$$\psi_{\vec{k}}(\vec{r}) = e^{i\vec{k}\cdot\vec{r}} u_{\vec{k}}(\vec{r}), \tag{2.131}$$

where $u_{\vec{k}}(\vec{r})$ is periodic within a unit cell such that $u_{\vec{k}}(\vec{r}+\hat{e}) = u_{\vec{k}}(\vec{r})$ with either $\hat{e} = (qa, 0)$ or $\hat{e} = (0, a)$. We are now in a position to describe the topology underlying the QHE. The following results apply to any system satisfying the following conditions:

- The single particle spectrum is composed of bands which are parametrized by a momentum label $\vec{k}$ living on a two-dimensional torus T^2.
- The electrons are non-interacting such that the many-particle spectrum is obtained by filling the single-particle states.
- The bands are gapped and the Fermi level lives in one of these gaps such that all the levels below the Fermi one are filled and the ones above are empty[10]. This situation corresponds to an insulating state in the band theory of solids.

Whenever these three criteria are satisfied, one can define an integer-valued topological invariant $\mathcal{C} \in \mathbb{Z}$, the first Chern number, for each band. Here the topology comes from the way the phase of the states winds as we move around the Brillouin zone torus T^2. To calculate $\mathcal{C}$, let us introduce the Berry connection,

$$\mathcal{A}_j(\vec{k}) = -i \left\langle u_{\vec{k}} \middle| \partial_{k_j} \middle| u_{\vec{k}} \right\rangle, \tag{2.132}$$

[10] In Sec. 2.2.5.2 we have seen that the gaps in between the unperturbed Landau levels are no longer empty in the presence of disorder but they are made of localized and extended states. In that case, the following result remain valid if the Fermi level lives in a region of localized states [Niu *et al.* 1985].

and the Berry curvature,

$$\mathcal{F}_{xy} = \frac{\partial \mathcal{A}_x}{\partial k_y} - \frac{\partial \mathcal{A}_y}{\partial k_x} = -i \left\langle \frac{\partial u_{\vec{k}}}{\partial k_y} \middle| \frac{\partial u_{\vec{k}}}{\partial k_x} \right\rangle + i \left\langle \frac{\partial u_{\vec{k}}}{\partial k_x} \middle| \frac{\partial u_{\vec{k}}}{\partial k_y} \right\rangle . \tag{2.133}$$

We can then compute the first Chern number by integrating the Berry curvature over the Brillouin zone torus T^2,

$$\mathcal{C} = \frac{1}{2\pi} \int_{T^2} \mathrm{d}^2 k \, \mathcal{F}_{xy}, \qquad \mathcal{C} \in \mathbb{Z}. \tag{2.134}$$

The Chern number is topological because it is invariant under smooth deformations of the Hamiltonian[11]. Indeed, small changes of the Hamiltonian result in small changes of the Berry curvature and therefore, one might think, in a small change in the Chern number. However, because the Chern number is an integer, it cannot change at all since it has to change discontinuously. Thus, we can expect a plot of the Chern number to exhibit plateaus. Assigning such a Chern number (or TKNN invariant) $\mathcal{C}_n$ to each band, the Hall conductance reads [Thouless *et al.* 1982],

$$G_H = G_0 \sum_n \mathcal{C}_n, \tag{2.135}$$

where the sum runs over all the filled bands. Here we recognize the same form as in Eq. (2.107) where the number of crossings N_c is given by the sum of the Chern numbers. Thus, the plateaus observed in the Hall conductance come from the plateau structure of the Chern number. This result shows that the quantization of the Hall conductance has a subtle origin that comes from the topology of the first Brillouin zone. For this reason, the QHE belongs to a class of systems called Chern insulators. Another phase, known as the quantum anomalous Hall (QAH) phase, is also a Chern insulator, i.e., it possesses chiral edge states whose number is determined by the Chern number (for a review, see [Liu *et al.* 2016]). While QAH insulators also break time-reversal symmetry, they don't require an external magnetic field (from where the name "anomalous"). This effect was first proposed by Haldane in a tight-binding model on a honeycomb lattice with real nearest-neighbor hopping and complex next-neighbor hopping [Haldane 1988]. This discovery led Haldane to share the 2016 Nobel Prize in Physics with Thouless and Kosterlitz. The first experimental observation of the QAH phase was done in Ref. [Chang *et al.* 2013] by using magnetically doped topological insulator thin films. The authors observed a Hall resistance plateau as a function of the gate voltage in the absence of any applied magnetic fields, indicating the achievement of the QAH state. We will present a toy model of a QAH insulator in the next section.

[11] This is the same idea that let unchanged the number of holes in a torus when one smoothly distorts it. In this process the associated topological invariant is given by the Gauss-Bonnet formula (see for example [Moessner & Moore 2021, Eq. (2.81) in Box. 2.2]).

2.3 Topological Insulators

Here we introduce the concept of topological insulators, which is essential for understanding the last part of this thesis (Chap. 5). We have seen in Sec. 2.2.7 that the QHE can be understood as a topological phase of matter. More precisely, the QHE is a special kind of topological insulator called a Chern insulator. In this section we describe Chern and time-reversal invariant (TRI) topological insulators in two dimensions. The main difference between Chern and TRI topological insulators is that the former breaks time-reversal symmetry. Indeed, a system with a non-zero Chern number breaks time-reversal symmetry [Bernevig & Hughes 2013] and, as we show in this section, exhibits chiral edge states whose chirality is related to the sign of the Chern number. Therefore, to restore time-reversal symmetry, one has to consider counter-propagating edge states so that the total Chern number is zero. This implies the presence of helical boundary modes in TRI topological insulators. Moreover, the topological invariant of Chern insulators, the Chern number, is a $\mathbb{Z}$-invariant which gives the number of chiral modes while, as we will see, TRI topological insulators are characterized by a $\mathbb{Z}_2$-invariant which says whether the number of helical pairs is even (trivial phase) or odd (topological phase).

We first present a two-dimensional lattice model of a Chern insulator, the Qi, Wu, and Zhang (QWZ) model. The lay reader is encouraged to look at App. C for a reminder on tight-binding models. We then see that chiral edge states appear at the mass domain walls of the QWZ model. Next, we show the appearance of helical edge states in TRI topological insulators by using the Bernevig, Hughes, and Zhang (BHZ) model, which corresponds to two time-reversed copies of the QWZ Hamiltonian, and then we compute the associated $\mathbb{Z}_2$ invariant. We end the section by presenting the concept of higher order topological insulators as it is essential for the understanding of the last project of this manuscript (Chap. 5). Throughout this section we set $\hbar = t = a = 1$, where t is the hopping energy and a is the lattice constant. Thus, the energies will be expressed in units of t and the momenta in units of $1/a$.

2.3.1 The QWZ model of Chern insulators

The QWZ model [Qi *et al.* 2006] is a toy model of particles with two internal degrees of freedom hopping on a two-dimensional lattice. It describes the QAH phase which is characterized by a quantized Hall conductance but doesn't require an external magnetic field. The QAH effect can be observed in materials with an intrinsic magnetization such as ferroelectrics or in magnetically doped materials. For example, it has been measured in magnetically doped topological insulator thin films by Chang and collaborators [Chang *et al.* 2013]. The QWZ model corresponds to the simplest Chern insulator having non-zero Chern numbers $\mathcal{C} = \pm 1$, i.e., one chiral edge state (as we will see, the $\pm$ sign is related to the chirality). This model will allow us to compute explicitly the Chern number and to introduce the concept of localized states at a mass domain wall. The single-particle QWZ Hamiltonian in the basis of the internal degrees of freedom is given by[12],

$$H(k_x, k_y) = \sin k_x \rho_x + \sin k_y \rho_y + (m - 2 + \cos k_x + \cos k_y)\rho_z \tag{2.136}$$

$$= \vec{d}(k_x, k_y) \cdot \vec{\rho}, \tag{2.137}$$

with $\vec{\rho}$ the vector of Pauli matrices and

$$\vec{d}(k_x, k_y) = \begin{pmatrix} d_x \\ d_y \\ d_z \end{pmatrix} = \begin{pmatrix} \sin k_x \\ \sin k_y \\ m - 2 + \cos k_x + \cos k_y \end{pmatrix}. \tag{2.138}$$

As we said, this model describes particles with two internal states hopping on a two-dimensional lattice as represented in Fig. 2.17. This is better seen by introducing the following notations,

$$U = (m-2)\rho_z, \quad T_x = \frac{\rho_z - i\rho_x}{2}, \quad T_y = \frac{\rho_z - i\rho_y}{2}, \tag{2.139}$$

[12] A derivation is provided in Asboth's book [Asbóth *et al.* 2016].

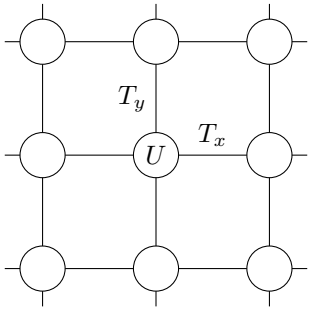

Figure 2.17: Geometry of the QWZ model. Each unit cell (circle) has two internal degrees of freedom. This can be rephrased as the particle being a spinor with the onsite potential U and the hopping amplitudes T_x and T_y being 2×2 matrices.

so that the QWZ Hamiltonian can be written as

$$H(k_x, k_y) = \frac{1}{2}U + T_x e^{ik_x} + T_y e^{ik_y} + \text{h.c.}, \tag{2.140}$$

where U is an onsite potential while T_x and T_y are hopping potentials in x and y directions, respectively. From this writing of the Hamiltonian, it is clear that the model describes a spinor particle hopping on a two-dimensional lattice. The onsite potential U corresponds to a Zeeman splitting term and the hopping potentials have a spin-z contribution as well as a spin-orbit coupling term in which the spin flips around x for the hopping in the y direction and around y for the hopping in the x direction. Note that the spinor structure can also be interpreted as a particle without internal degrees of freedom moving in a bipartite lattice. The band structure of the QWZ model is given by,

$$E(k_x, k_y) = \pm|\vec{d}(k_x, k_y)| = \pm\sqrt{\sin^2 k_x + \sin^2 k_y + (m - 2 + \cos k_x + \cos k_y)^2}, \tag{2.141}$$

and describes two energy bands separated by a gap. The band gap vanishes at four points in the two-dimensional Brillouin zone for different values of the parameter m as shown in Fig. 2.18. These four points

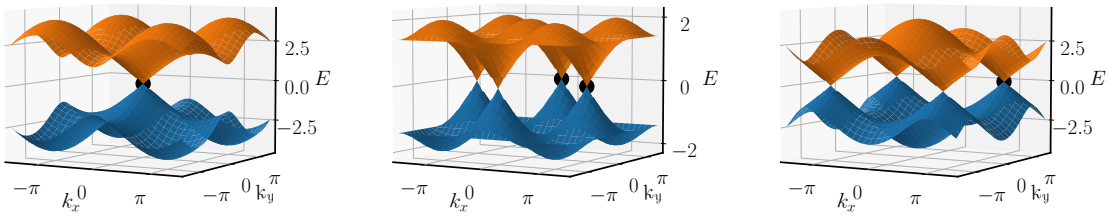

(a) (b) (c)

Figure 2.18: Dispersions and Dirac points of the QWZ model. In (a) we set $m = 0$ and we observe a Dirac point at $(0, 0)$, in (b) we set $m = 2$ and we see two inequivalent Dirac points at $(0, \pi)$ and $(\pi, 0)$, and in (c) we set $m = 4$ and find a Dirac point at (π, π). Due to the periodic boundary conditions of the first Brillouin zone the momenta $k_x = \pm\pi$ and $k_y = \pm\pi$ are equivalent.

are called Dirac points because the dispersion around them ressemble the one of massless Dirac fermions and the corresponding momenta are often referred to as time-reversal invariant momenta (TRIM) because they are unchanged under the time-reversal operation[13] $\vec{k} \to -\vec{k}$ (modulo a reciprocal lattice vector). The four TRIM and the corresponding values of m are summarized in Tab. 2.1. As it is known in the

[13] We detail time-reversal symmetry in Sec. 2.3.3.1.

(k_x, k_y)	m	name
$(0,0)$	0	Γ
$(0,\pi)$	2	X
$(\pi,0)$	2	X
(π,π)	4	M

Table 2.1: Dirac points (or TRIM) of the QWZ model. The (k_x, k_y) points in the first Brillouin zone and the associated values of m correspond to gap closing in the bulk dispersion relation of the QWZ model. The point at $(0,0)$ is the so-called Γ point that corresponds to the center of the Brillouin zone, the two inequivalent points at $(0,\pi)$ and $(\pi,0)$ are called the X points and the point at (π,π) is the M point. Note that for the M point all the possibilities for $k_x = \pm\pi$ and $k_y = \pm\pi$ are equivalent and therefore M is called the maximal symmetry point.

theory of topological insulators, gap closings are a signature of a topological phase transition. We can see that by computing the Chern number as introduced in Sec. 2.2.7. For a two-band model with $H = \vec{d}\cdot\vec{\rho}$ it is given by,

$$\mathcal{C} = \frac{1}{2\pi}\int_{\mathrm{BZ}} \mathrm{d}k_x \mathrm{d}k_y \mathcal{F}_z, \tag{2.142}$$

$$\mathcal{F}_z = \frac{1}{2}\left(\frac{\partial \hat{d}}{\partial k_x}\times\frac{\partial \hat{d}}{\partial k_x}\right)\cdot\hat{d}, \tag{2.143}$$

where we have introduced the unit vector $\hat{d} = \vec{d}/|\vec{d}|$. For the QWZ model we find,

$$\mathcal{F}_z = \frac{1}{2}\frac{\cos k_x + \cos k_y + (m-2)\cos k_x \cos k_y}{[\sin^2 k_x + \sin^2 k_y + (m-2+\cos k_x + \cos k_y)^2]^{3/2}}, \tag{2.144}$$

and, by performing a numerical integration, we get the following Chern numbers,

$$\mathcal{C} = \begin{cases} 0 & \text{for } m \in]-\infty, 0[\cap]4,\infty[\\ 1 & \text{for } m \in]0,2[\\ -1 & \text{for } m \in]2,4[\end{cases}, \tag{2.145}$$

which define the three phases of the QWZ model. For $m < 0$ and $m > 4$, the spectrum is fully gapped and the Chern number $\mathcal{C}$ is zero. This is because both $m < 0$ and $m > 4$ are adiabatically connected to the atomic limit of a trivial insulator [Bernevig & Hughes 2013]. Indeed, by adiabatic continuity, as long as the Hamiltonian is gapped and the gap does not close, it remains in the same topological phase. Thus, the regimes $m < 0$ and $m > 4$ are topologically equivalent to the vacuum for which $|m| \to \infty$, and so we have $\mathcal{C} = 0$ in these regimes. As we increase m from $m = -\infty$ and go through the gap closing at $m = 0$ and $\vec{k} = (0,0)$, the Chern number should change from zero to a non-zero value. Here it is given by $\mathcal{C} = 1$. By increasing further the mass m we reach another phase transition at $m = 2$. Here the gap closes at two points in the Brillouin zone, $(0,\pi)$ and $(\pi,0)$, giving to the Chern number two (negative) contributions yielding $\mathcal{C} = 1 - 2 = -1$. An analytical derivation of these Chern numbers can be found in [Bernevig & Hughes 2013]. We represent the evolution of the Chern number as a function of m in Fig. 2.19.

2.3.2 Chiral states at a mass domain wall

Here we show that a chiral edge state appears at the interface between two insulators with different Chern numbers. For that, we consider the QWZ model of the previous section with a position-dependent mass term,

$$m(y) = \begin{cases} -m_0 & \text{if } y < 0 \\ 0 & \text{if } y = 0 \\ m_0 & \text{if } y > 0 \end{cases}, \tag{2.146}$$

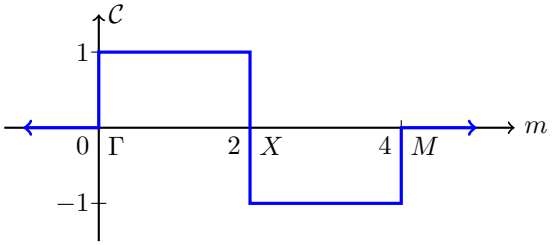

Figure 2.19: Evolution of the Chern number C of the QWZ model as a function of the onsite parameter m. The critical points at $m = \{0, 2, 4\}$ correspond to the Dirac points (Γ, X, M) of Tab. 2.1 where the Chern number is not well defined. The regions $m < 0$ and $m > 4$ are topologically equivalent to $m = \mp\infty$ respectively.

with $0 < m_0 < 2$. From the Chern numbers of the QWZ model defined in Eq. (2.145), this corresponds to a vacuum-QAH junction[14] where the vacuum has a zero Chern number and the QAH has Chern number $\mathcal{C} = 1$. Moreover, near $m = 0$, we can expand the QWZ Hamiltonian around the Dirac point at $\vec{k} = (0, 0)$ and we get the continuum Hamiltonian,

$$H(k_x, k_y) \simeq k_x \rho_x + k_y \rho_y + m(y)\rho_z, \tag{2.147}$$

which looks like a two-dimensional massive Dirac Hamiltonian where the bulk spectrum in the regions $y \neq 0$ is gapped by the mass term and reads $E = \pm\sqrt{k^2 + m_0^2}$. Since the Hamiltonian (2.147) depends only on y, we can assume plane waves in the x-direction and write the wave function in the following form,

$$\Psi(x, y) = \frac{e^{ik_x x}}{\sqrt{L_x}}\psi(y), \tag{2.148}$$

where L_x is the system's dimensions in the x-direction. To find the wave function $\psi(y)$ in the y-direction, we substitue $k_y \to -i\partial_y$ and solve the Schrödinger equation to obtain

$$\psi(y) = \begin{cases} \psi_L(y) & \text{for } y < 0 \\ \psi_R(y) & \text{for } y > 0 \end{cases}, \tag{2.149}$$

with

$$\psi_{L,R}(y) = c_{L,R} \begin{pmatrix} -\frac{\sqrt{m_0^2 - (E^2 - k_x^2)} \mp k_x}{m_0 \pm E} \\ 1 \end{pmatrix} e^{-\sqrt{m_0^2 - (E^2 - k_x^2)}|y|}, \tag{2.150}$$

where we consider $E^2 - k_x^2 < m_0^2$ so that we have kept only evanescent waves in the L and R regions. We can then obtain the state living along the vacuum-QAH interface by matching the wave functions at $y = 0$, $\psi_L(0) = \psi_R(0)$, which leads to the following system,

$$c_L = c_R = c, \tag{2.151}$$

$$\frac{\sqrt{m_0^2 - (E^2 - k_x^2)} - k_x}{m_0 + E} = \frac{\sqrt{m_0^2 - (E^2 - k_x^2)} + k_x}{m_0 - E}, \tag{2.152}$$

where the second equation is satisfied only for $E = -k_x$. We thus find a chiral edge state propagating along $-\hat{x}$ and localized where the mass term $m(y)$ changes sign with a y-dependent wave function

$$\psi(y) = \frac{1}{\sqrt{2}} \begin{pmatrix} -1 \\ 1 \end{pmatrix} e^{-m_0|y|}. \tag{2.153}$$

Hence, we have found an edge state living inside the bulk gap. In Fig. 2.20 we represent the corresponding spectrum, the squared absolute value of the wave function, as well as an illustration of the situation (i.e., a QAH insulator in the vacuum).

[14] In fact the vacuum here corresponds to $m \to -\infty$ but, as discussed above, it is adiabatically connected to $m < 0$.

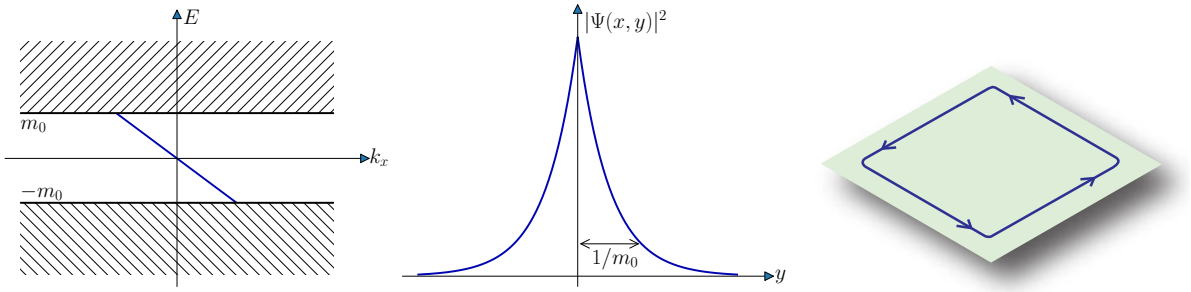

Figure 2.20: Chiral state of the QWZ model. A mass domain wall like the one of Eq. (2.146) yields a localized state at the place where the mass term changes sign. In the QHZ model we found a chiral edge state living in the bulk gap with a dispersion $E = -k_x$ as represented in (a). In (b) we plot the square modulus of the wave function of the edge state which is localized around the mass inversion point at $y = 0$ with a localization length of $1/m_0$. In (c) we show an illustration of the situation. The region with non-zero Chern number (green) is inside the vacuum with zero Chern number and a chiral state propagates along the edges of the sample. This corresponds to a QAH insulator.

More generally, for any domain wall such that the mass term has different signs as $y \to \pm\infty$, i.e.,

$$m(y) \begin{cases} < 0 & \text{if } y \to -\infty \\ > 0 & \text{if } y \to \infty \end{cases}, \tag{2.154}$$

one can show that there will always be a chiral edge state which is localized where the mass term changes sign with a wave function given by,

$$\psi(y) = \frac{1}{\sqrt{2}} \begin{pmatrix} -1 \\ 1 \end{pmatrix} e^{-\int_0^y m(y')\mathrm{d}y'}. \tag{2.155}$$

Note that the values of m at $y \to \pm\infty$ must be different from zero.

We have thus seen that, at the interface between two insulators with zero and non-zero bulk Chern numbers, a chiral edge state appear. We can thus predict what happens at the edges of the sample only by looking at its bulk properties. This is the so-called bulk-edge correspondence. Moreover, the chirality of the edge state is related to the Chern number, it is given by the sign of $-\mathcal{C}$. In the next subsection we consider a different kind of topological insulators where time-reversal symmetry is preserved.

2.3.3 Helical states of TRI topological insulators

Time-reversal symmetric (or TRI) topological insulators in two dimensions describe the so-called quantum spin Hall (QSH) effect in which pairs of helical states propagate along the edges of the sample. A helical pair of edge states corresponds to two non-interacting states of opposite spins propagating in opposite directions (spin-momentum locking). Due to time-reversal symmetry, these TRI topological insulators have a zero Chern number and so a null charge-Hall conductance but they have a non-zero spin-Hall conductance. The topological invariant describing TRI topological insulators is a $\mathbb{Z}_2$ invariant which we denote by $\nu_{\mathbb{Z}_2}$ and that can take only two values: $\nu_{\mathbb{Z}_2} = 0$ corresponding to the trivial case where there are no edge states and $\nu_{\mathbb{Z}_2} = 1$ corresponding the QSH phase with a single pair of helical edge states. Thus, TRI topological insulators have only two distinct phases, in contrast to Chern insulators where the Chern number can be any integer. Here we follow [Hasan & Kane 2010] to understand that. In Fig 2.21 we plot the energy dispersion of the edge (along x here) of a TRI two-dimensional insulator as a function of the crystal momentum k_x along that edge. We have shown only the half Brillouin zone $0 < k_x \leq \pi$ because time-reversal symmetry implies $E(\vec{k}) = E(-\vec{k})$ so that the other half is a mirror image (see Sec. 2.3.3.1). The shaded regions represent the bulk conduction and valence bands which are

separated by an energy gap. Due to time-reversal symmetry, the states at $k_x = 0$ and $k_x = \pi$ (which is the same as $k_x = -\pi$) are twofold degenerate and, in between these two points, there are two ways the states can be connected. In Fig. 2.21a they connect pairwise. Here the Fermi level E_F crosses the bands an even number of times. In such a situation, the edge modes can always be removed by pushing the states in the bulk bands so that the number of crossings will be zero (see also the explanation provided in [Girvin & Yang 2019, Fig. 14.3]). In that case the system is a trivial insulator. In contrast, in Fig. 2.21b there is an odd number of crossings with the Fermi level. In that case the edge states cannot be eliminated and the system is a topological insulator with helical boundary modes protected by time-reversal symmetry. We thus conclude that a TRI topological insulator always have an odd number of helical pairs. Although time-reversal symmetry protects one helical pair, it does not prevent two pairs from interacting. In fact, two such pairs will always interact such that only one helical pair survive when the number of pairs is odd. We thus recover the two expected values of the $\mathbb{Z}_2$ invariant. Namely, $\nu_{\mathbb{Z}_2} = 0$ when the number of helical pairs is even and no edge states are present, and $\nu_{\mathbb{Z}_2} = 1$ when the number of helical pairs is odd and one pair of helical states propagates along the boundaries of the sample. In the next section we will calculate the $\mathbb{Z}_2$ invariant for TRI topological insulators with inversion symmetry[15].

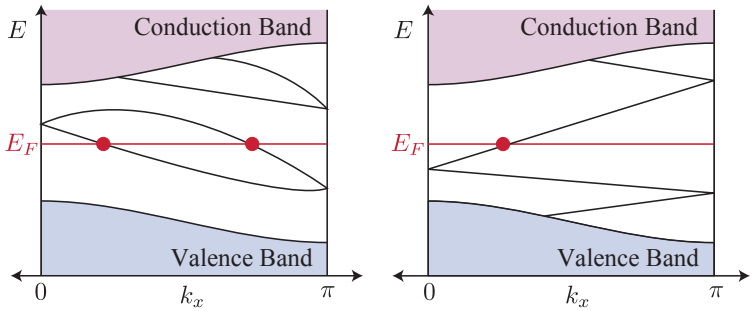

Figure 2.21: Energy dispersion between the TRIM $k_x = 0$ and $k_x = \pi$ with $k_y = 0$ or $k_y = \pi$. We show only the half Brillouin zone since time-reversal symmetry implies that the other half is a mirror image. In (a) the number of crossings with the Fermi energy E_F is even (i.e., an even number of pairs) whilst in (b) there is an odd number of crossings (i.e., an odd number of pairs). An odd number of crossings gives rise to topological boundary modes protected by time-reversal symmetry. Adapted from [Hasan & Kane 2010].

In the present section we show that the chiral edge states of Chern insulators become helical edge states when time-reversal symmetry is restored. We start by presenting the time-reversal symmetry and then we construct a simple model of a TRI topological insulator that is nothing but two time-reversed copies of the QWZ model. This model was first introduced by BHZ to describe the QSH phase in HgCdTe/HgTe/HgCdTe quantum wells [Bernevig *et al.* 2006]. This phase has been experimentally observed soon after its theoretical prediction in Ref. [Konig *et al.* 2007] via longitudinal conductance measurements, being the first big success of the theory of topological insulators (for a review, see [König *et al.* 2008]).

2.3.3.1 Time-reversal symmetry

A system is said to be time-reversal symmetric if its Hamiltonian is unchanged under time reversal $t \to -t$. Time reversal symmetry is well presented in Ref. [Bernevig & Hughes 2013, Chap. 4] and the results presented here can be found in it. Denoting the time-reversal symmetry operator by $\mathcal{T}$ we have

[15] If both time-reversal and inversion symmetry are satisfied the $\mathbb{Z}_2$ invariant is easily calculated by looking at the inversion eigenvalues of the wave function at the TRIM. In general, the computation of this invariant is much more complicated.

the following relations,

$$\mathcal{T}\hat{x}\mathcal{T}^{-1} = \hat{x}, \tag{2.156}$$

$$\mathcal{T}\hat{p}\mathcal{T}^{-1} = -\hat{p}, \tag{2.157}$$

where $\hat{x}$ and $\hat{p}$ are respectively the position and momentum operators. If we look at the action of $\mathcal{T}$ on the commutator $[\hat{x}, \hat{p}]$ we find,

$$\mathcal{T}\,[\hat{x}, \hat{p}]\,\mathcal{T}^{-1} = -i\hbar, \tag{2.158}$$

and so the following relation holds,

$$\mathcal{T}i\mathcal{T}^{-1} = -i, \tag{2.159}$$

meaning that the time-reversal operator should contain the complex conjugation. Moreover, if the system has spin $\vec{S}$, the time-reversal symmetry flips it,

$$\mathcal{T}\vec{S}\mathcal{T}^{-1} = -\vec{S}. \tag{2.160}$$

We can represent that by a rotation of π around the y axis (the y axis is chosen by convention) and, for a spin-$\frac{1}{2}$ system, we finally get,

$$\mathcal{T} = i\sigma_y\kappa, \tag{2.161}$$

where σ_y is the second Pauli matrix in spin space and κ is the complex conjugation. Note that this operator is anti-unitary with $\mathcal{T}^\dagger\mathcal{T} = 1$ and $\mathcal{T}^2 = -1$. Let us mention that for spinless particles the time-reversal symmetry operator is equal to the complex conjugation κ and squares to $+1$. A defining property of an anti-unitary operator $\mathcal{T}$ that squares to -1 is that for any pair of states $|\psi\rangle$ and $|\phi\rangle$, we have

$$\langle\mathcal{T}\phi|\mathcal{T}\psi\rangle = \langle\phi|\psi\rangle^*\,. \tag{2.162}$$

Considering this relation with $|\phi\rangle = |\mathcal{T}\psi\rangle$ we get,

$$\langle\mathcal{T}\psi|\psi\rangle^* = \left\langle\mathcal{T}^2\psi\middle|\mathcal{T}\psi\right\rangle = \langle-\psi|\mathcal{T}\psi\rangle = -\langle\mathcal{T}\psi|\psi\rangle^*\,, \tag{2.163}$$

where the minus sign comes from the anti-unitarity of $\mathcal{T}$. As a direct consequence we have $\langle\mathcal{T}\psi|\psi\rangle = 0$, which means that for every eigenstate, its time-reversed partner is orthogonal. Let us now give the action of time-reversal symmetry on the momentum-space single-particle Hamiltonian,

$$\mathcal{T}H(-\vec{k})\mathcal{T}^{-1} = H(\vec{k}) \quad \Leftrightarrow \quad U_\mathcal{T}H^*(-\vec{k})U_\mathcal{T}^\dagger = H(\vec{k}), \tag{2.164}$$

where $U_\mathcal{T} = i\sigma_y$ is the anti-unitary part of the time-reversal operator and the Hamiltonian $H^*(-\vec{k})$ is the time-reversed copy of $H(\vec{k})$. We can then use this result to find a relation between two time-reversed partners. Indeed, consider an eigenstate $|u(\vec{k})\rangle$ of the Hamiltonian,

$$H(\vec{k})|u(\vec{k})\rangle = E(\vec{k})|u(\vec{k})\rangle. \tag{2.165}$$

Using the relation (2.164) we can then write,

$$U_\mathcal{T}H^*(-\vec{k})U_\mathcal{T}^\dagger|u(\vec{k})\rangle = E(\vec{k})|u(\vec{k})\rangle. \tag{2.166}$$

Then multiplying from the left by $U_\mathcal{T}^\dagger$ and complex conjugating we obtain,

$$H^*(-\vec{k})U_\mathcal{T}^T|u(\vec{k})\rangle^* = E(-\vec{k})U_\mathcal{T}^T|u(\vec{k})\rangle^*, \tag{2.167}$$

where $E(\vec{k}) = E(-\vec{k}) = E$ for TRI systems. We have thus shown that for each eigenstate $|u(\vec{k})\rangle$ at energy E, the time-reversed partner $U_\mathcal{T}^T|u(\vec{k})\rangle^*$ is also an eigenstate at the same energy. This is known as the Kramers' degeneracy.

2.3.3.2 The BHZ model

As mentioned above, the BHZ model corresponds to two time reversed copies of the QWZ Hamiltonian (2.136) which we recall here,

$$H_{QWZ}(k_x, k_y) = \sin k_x \rho_x + \sin k_y \rho_y + (m - 2 + \cos k_x + \cos k_y)\rho_z, \tag{2.168}$$

where the Pauli matrices $\rho_{x,y,z}$ describe the internal degree of freedom of the QWZ model (orbital or valley degree of freedom for instance). The BHZ Hamiltonian is thus given by,

$$H_{BHZ}(\vec{k}) = \text{diag}\left\{H_{QWZ}(\vec{k}), H^*_{QWZ}(-\vec{k})\right\}, \tag{2.169}$$

which explicitly reads,

$$H_{BHZ}(k_x, k_y) = \sin k_x \sigma_z \rho_x + \sin k_y \sigma_0 \rho_y + (m - 2 + \cos k_x + \cos k_y)\sigma_0 \rho_z, \tag{2.170}$$

where we recall that σ matrices are Pauli matrices in spin-space while the products $\sigma_i \rho_j$ are Kronecker products. The main difference between the QWZ and BHZ Hamiltonians is the presence of σ_z in the first term of the latter. Actually, this makes a big difference. This additional term is responsible for the appearance of a helical pair of edge states as we show below. On the other hand, the QWZ and BHZ Hamiltonians have the same bulk band structure (but the bands are spin-degenerate in the BHZ model) and so they have the same Dirac points at the four TRIM of the first Brillouin zone. The energy dispersions are represented in Fig. 2.18 and the coordinates of the Dirac points with their respective values of m have been summarized in Tab. 2.1.

2.3.3.3 Helical pair of edge states in the BHZ model

In Sec. 2.3.2 we have seen that a chiral edge state with energy $E = -k_x$ appears at a mass domain wall of the QWZ model by expanding its Hamiltonian around the Dirac point at $(0, 0)$ near $m = 0$. Here we do the same with the BHZ Hamiltonian. The expansion yields,

$$H_{BHZ} = \text{diag}\{H_+, H_-\}, \tag{2.171}$$

with,

$$H_\sigma = \sigma k_x \rho_x + k_y \rho_y + m\rho_z, \tag{2.172}$$

where $\sigma = +, - = \uparrow, \downarrow$ denotes the spin. H_+ is the expanded QWZ Hamiltonian and H_- its time-reversed copy. Considering the same mass domain wall as in Sec. 2.3.2, $m(y) = m_0 \text{sgn}(y)$, we can show the presence of a helical pair of edge states where the mass term changes sign (i.e., at $y = 0$). Because H_+ and H_- are uncoupled, we can solve the Schrödinger equation separately for each of them,

$$H_\sigma \Phi_\sigma(x, y) = E_\sigma \Phi_\sigma(x, y), \tag{2.173}$$

where $\Phi_\sigma(x, y)$ is a two-component wave function describing one spin state. As H_σ depends only on y, we can again consider plane waves in the x-direction and write the wave functions as,

$$\Phi_\sigma(x, y) = \frac{e^{ik_x x}}{\sqrt{L_x}} \phi_\sigma(y), \tag{2.174}$$

with L_x the system's dimension in the x-direction. Doing the same job as in Sec. 2.3.2 to get the states living along $y = 0$ we obtain

$$\phi_\sigma(y) = c_\sigma \begin{pmatrix} -1 \\ 1 \end{pmatrix} e^{-m_0|y|}, \tag{2.175}$$

with energies,

$$E_\sigma = -\sigma k_x. \tag{2.176}$$

We thus find a helical pair (or Kramers pair) of edge states where the chiralities are determined by the value of the spin. This is the so-called spin-momentum locking. A general state can then be written as a superposition of the two helical states,

$$\Psi(x,y) = \left[c_+ \begin{pmatrix} -1 \\ 1 \\ 0 \\ 0 \end{pmatrix} e^{ik_+ x} + c_- \begin{pmatrix} 0 \\ 0 \\ -1 \\ 1 \end{pmatrix} e^{ik_- x} \right] e^{-m_0|y|}, \tag{2.177}$$

where $k_\pm = \mp E$ and the mode $+$ $(-)$ propagates in the negative (positive) x-direction. We have represented the dispersion of the helical states and an illustration of the system in Fig. 2.22.

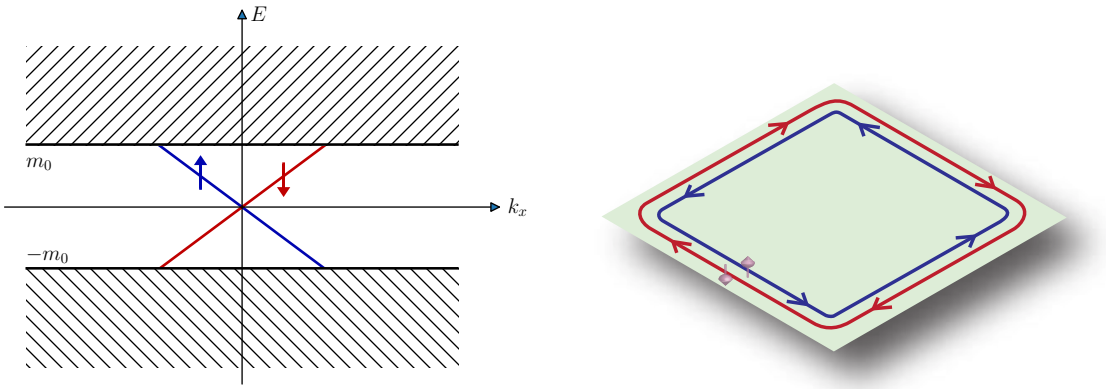

(a) (b)

Figure 2.22: Helical states of the BHZ model. In (a) we represent the dispersion of the helical pair of edge states. The opposites chiralities are associated to opposite spins indicated by arrows. In (b) we show an illustration of the situation. The region with $m > 0$ (green) is inside the vacuum with $m < 0$ and a Kramers' pair propagates along the edges of the sample. This corresponds to a QSH insulator.

In the next subsection we determine the full phase diagram of the BHZ model by computing its $\mathbb{Z}_2$ topological invariant.

2.3.4 An easy calculation of the Z_2 invariant with the BHZ model

We end this subsection by performing an easy calculation of the $\mathbb{Z}_2$ invariant of the BHZ model. This allows to determine the full phase diagram, to complete the analogy with the QWZ model, and to illustrate the concept of band inversion. In general, the calculation of the $\mathbb{Z}_2$ invariant can be cumbersome. However, it turns out to be very easy for two-dimensional TRI topological insulators with inversion symmetry. By its definition, inversion symmetry lets the system unchanged after inversion around the origin ($\vec{r} \to -\vec{r}$). The inversion symmetry operator $\mathcal{I}$ must satisfy the following relations,

$$\mathcal{I}\mathcal{I}^\dagger = \mathcal{I}^2 = 1, \tag{2.178}$$

$$\mathcal{I}H(-\vec{k})\mathcal{I}^{-1} = H(\vec{k}), \tag{2.179}$$

$$\mathcal{I}\mathcal{T} = \mathcal{T}\mathcal{I}, \tag{2.180}$$

where $\mathcal{T}$ is the time-reversal symmetry operator ($\mathcal{T} = i\sigma_y\rho_0\kappa$ for the BHZ model) and the condition $\mathcal{I}^2 = 1$ indicates that the inversion eigenvalues are ± 1. As one can check, the BHZ Hamiltonian is inversion symmetric with inversion operator,

$$\mathcal{I} = \sigma_0\rho_z. \tag{2.181}$$

To compute the $\mathbb{Z}_2$ invariant we look at the four TRIM of Tab. 2.1. We denote them by Γ_j $(j = 1, 2, 3, 4)$ with,

$$\Gamma_1 = (0,0), \quad \Gamma_2 = (0,\pi), \quad \Gamma_3 = (\pi,0), \quad \Gamma_4 = (\pi,\pi), \tag{2.182}$$

and, at these points, we have,

$$H(\Gamma_j) = H(-\Gamma_j), \tag{2.183}$$

where H can be any TRI Hamiltonian. Moreover, as already discussed, each state $|\psi\rangle$ at one of the TRIM has an orthogonal Kramers partner $\mathcal{T}|\psi\rangle$ at the same energy,

$$H(\Gamma_j)|\psi\rangle = E|\psi\rangle, \tag{2.184}$$
$$H(\Gamma_j)\mathcal{T}|\psi\rangle = E\mathcal{T}|\psi\rangle. \tag{2.185}$$

Furthermore, if H is inversion symmetric we can also choose $|\psi\rangle$ as an eigenstate of the inversion operator because of the following relation,

$$\mathcal{I}H(\Gamma_j)\mathcal{I}^{-1} = H(-\Gamma_j) = H(\Gamma_j), \tag{2.186}$$

which shows that H and $\mathcal{I}$ commute at the TRIM. Hence, the state $|\psi\rangle$ solves the inversion eigenvalue problem,

$$\mathcal{I}|\psi\rangle = \pm|\psi\rangle, \tag{2.187}$$

where the sign determines the inversion (or parity) eigenvalue, and its Kramers partner has to have the same inversion eigenvalue,

$$\mathcal{I}\mathcal{T}|\psi\rangle = \mathcal{T}\mathcal{I}|\psi\rangle = \pm\mathcal{T}|\psi\rangle. \tag{2.188}$$

We are now in a position to compute the $\mathbb{Z}_2$ invariant of the BHZ model which we denote by $\nu_{\mathbb{Z}_2}$. It is obtained by taking the product of the parity eigenvalues of the filled states at the four TRIM. Denoting these parity eigenvalues by $\xi_j = \xi(\Gamma_j)$, the $\mathbb{Z}_2$ invariant $\nu_{\mathbb{Z}_2}$ is defined as [Fu & Kane 2007]

$$\prod_j \xi_j = (-1)^{\nu_{\mathbb{Z}_2}}, \tag{2.189}$$

where we recall that $\nu_{\mathbb{Z}_2} = 0$ describes the trivial phase while $\nu_{\mathbb{Z}_2} = 1$ corresponds to the topological phase with a helical pair of edge states. To compute $\nu_{\mathbb{Z}_2}$ in the BHZ model, let us write the Hamiltonian at the TRIM,

$$H_{BHZ}(0,0) = m\sigma_0\rho_z, \tag{2.190}$$
$$H_{BHZ}(0,\pi) = H_{BHZ}(\pi,0) = (m-2)\sigma_0\rho_z, \tag{2.191}$$
$$H_{BHZ}(\pi,\pi) = (m-4)\sigma_0\rho_z. \tag{2.192}$$

We can see that the BHZ Hamiltonian at the TRIM is proportional to the inversion operator $\mathcal{I} = \sigma_0\rho_z$ and so they obviously have the same eigenstates. The filled states are the one associated to the eigenvalue -1 of ρ_z and their inversion eigenvalues are given by,

$$\xi_1 = -\mathrm{sgn}(m), \tag{2.193}$$
$$\xi_2 = \xi_3 = -\mathrm{sgn}(m-2), \tag{2.194}$$
$$\xi_4 = -\mathrm{sgn}(m-4). \tag{2.195}$$

We thus recover the topological and trivial regions of the QWZ model introduced in Eq. (2.145),

$$m<0: \begin{cases} \xi_1=+1 \\ \xi_2=\xi_3=+1 \\ \xi_4=+1 \end{cases} \Rightarrow \quad \nu_{\mathbb{Z}_2}=0 \quad \text{(trivial)}, \tag{2.196}$$

$$0<m<2: \begin{cases} \xi_1=-1 \\ \xi_2=\xi_3=+1 \\ \xi_4=+1 \end{cases} \Rightarrow \quad \nu_{\mathbb{Z}_2}=1 \quad \text{(topological)}, \tag{2.197}$$

$$2<m<4: \begin{cases} \xi_1=-1 \\ \xi_2=\xi_3=-1 \\ \xi_4=+1 \end{cases} \Rightarrow \quad \nu_{\mathbb{Z}_2}=1 \quad \text{(topological)}, \tag{2.198}$$

$$m>4: \begin{cases} \xi_1=-1 \\ \xi_2=\xi_3=-1 \\ \xi_4=-1 \end{cases} \Rightarrow \quad \nu_{\mathbb{Z}_2}=0 \quad \text{(trivial)}. \tag{2.199}$$

At the values $m=\{0,2,4\}$ we observe gap closings at different TRIM. Each time a gap closes and re-opens there is an inversion of the parity eigenvalue meaning that the valence and conduction bands have been exchanged. This is known as a band inversion. Such gap closings as a function of a parameter are signatures of topological phase transitions. In Fig. 2.23 we represent such a band inversion at the time-reversal invariant momentum $\Gamma_1=(0,0)$ which has a gap closing when $m=0$. Note that an even number of band inversions will keep the system in the same insulating phase.

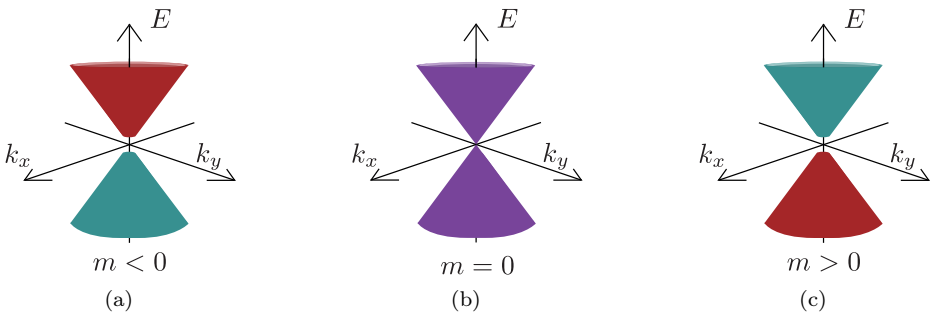

Figure 2.23: Band inversion. Evolution of the band structure around the time-reversal invariant momentum $\Gamma_1=(0,0)$ for different values of the mass term m. (a) For $m<0$ the band structure is gapped and the system is a trivial insulator. (b) At $m=0$ the gap closes and the system is metallic. (c) For $m>0$ the gap re-opens and the system becomes a topological insulator. As represented by the colors, the conduction and valence bands have been exchanged during the process of closing and re-opening of the gap. This band inversion can be tracked by comparing the inversion eigenvalue ξ_1 in Eqs. (2.196) and (2.197). Adapted from [Asbóth *et al.* 2016].

We end this chapter by discussing the concept of higher order topological insulators since we will consider one in the last part of the thesis (Chap. 5).

2.3.5 Higher order topological insulators

In all this section we focused on two-dimensional topological insulators hosting chiral or helical one-dimensional edge states. The idea of topological insulator can be generalized to d-dimensional materials as follows. A topological insulator of dimension d hosts gapless states on its $d-1$ dimensional boundaries (if $d=1$, point-like end states, if $d=2$ one-dimensional edge states, if $d=3$ two-dimensional surface states). So far we have considered two different types of boundary modes: those of Chern insulators,

which require no symmetry, and those of TRI topological insulators, which rely on the presence of time-reversal symmetry. Thus, a TRI topological insulator is protected by time-reversal symmetry, and it can be adiabatically deformed to a trivial phase after this underlying symmetry is removed. In fact, there are different topological phase classes for which the boundary modes are protected by different symmetries. For conventional topological phases, the possible symmetries are time-reversal (T), particle-hole (P), and chiral ($S = TP$). Since T and P are anti-unitary operators, they can square to ± 1, while S is unitary and always square to $+1$. We can then have many symmetry classes depending on the square value of these operators, each giving rise to a different class of topological phase. For example, the time-reversal symmetry T can square to $+1$ or -1, but it can also be absent (0), giving three possibilities. Since the same possibilities hold for the particle-hole symmetry P, the combination of the possible values for T and P gives $3 \times 3 = 9$ possible classes. Finally, a system can have neither time reversal nor particle-hole symmetry, but preserve the product of the two (chiral symmetry). This gives us ten possible classes, which are summarized in Tab. 2.2. This classification, known as the 10-fold way, was introduced by

Class name	T	P	S=TP
A	0	0	0
AI	+1	0	0
AII	-1	0	0
AIII	0	0	1
BDI	+1	+1	1
CII	-1	-1	1
D	0	+1	0
C	0	-1	0
DIII	-1	+1	1
CI	+1	-1	1

Table 2.2: The 10-fold way classification of topological phases.

Altland and Zirnbauer [Altland & Zirnbauer 1997] (for a review, see [Ludwig 2015]). Note that the QHE and QSH insulators are respectively in A and AII classes.

New classes are possible when the boundary states are protected by a crystal symmetry, such as rotation, inversion or mirror symmetries. Topological insulators in which the edge states are protected by such crystal symmetry are called topological crystalline insulators [Fu 2011] (for a pedagogical review, see [Ando & Fu 2015]). In 2012, Fu and collaborators [Hsieh *et al.* 2012] proposed the first class of topological crystalline insulator material, with SnTe as a representative. They predicted that SnTe has metallic surface states protected by mirror symmetry and characterized by an even number of Dirac cones. It is well known that the order of the conduction and valence bands in SnTe is inverted relative to PbTe [Dimmock *et al.* 1966]. Therefore, the band gap of the alloy $Pb_{1-x}Sn_xTe$ is expected to close and reopen as x goes from zero to one. Since this band inversion occurs at an even number of Dirac points, this closing and reopening of the gap cannot be associated to a topological phase transition described by a $\mathbb{Z}_2$ topological invariant with boundary modes protected by time-reversal symmetry (see Sec. 2.3.4). However, the authors of [Hsieh *et al.* 2012] showed that SnTe has topological surface states that are protected by mirror symmetry. Following this prediction, angle-resolved photoemission spectroscopy measurements have shown that SnTe is indeed a topological crystalline insulator [Tanaka *et al.* 2012]. In this experiment the authors observed Dirac-like band dispersions in SnTe at an even number of Dirac cones and showed that these Dirac cones originate from the surface states, proving that this material is a topological crystalline insulator with metallic surface modes. For completeness, they compared with the band dispersion of the material PbTe, for which they didn't observe metallic states but an energy gap, indicating a topological phase transition in $Pb_{1-x}Sn_xTe$ as x runs from zero to one.

If the protecting symmetry is not crystalline (e.g. time-reversal), all boundaries preserve it and the d-dimensional insulating bulk is surrounded by $(d-1)$-dimensional conducting states (this is the bulk-boundary correspondence of topological insulators). On the other hand, topological crystalline insulators have boundaries that do not always preserve the relevant crystalline symmetry on their own. However,

the symmetry can be preserved on $(d-n)$-dimensional boundaries, where n is referred as the order. In this case, the material exhibits $(d-n)$-dimensional boundary modes. This situation describes a so-called higher order topological insulator (HOTI). An overview of first- and higher-order topological phases is depicted in Fig. 2.24. A pedagogical introduction to HOTIs can be found in the lecture notes by Neupert and Schindler [Neupert & Schindler 2018] or in the Schindler's tutorial [Schindler 2020]. In Chap. 5 of the thesis we will focus on a three-dimensional topological insulator of order two, i.e., a three-dimensional material with gapped surfaces and conducting modes on its one-dimensional hinges (see Fig. 2.24). In short, we can understand the presence of the hinge modes by saying that the hinges of a HOTI realize natural mass domain walls [Schindler *et al.* 2018a]. At first look, these hinge modes look very similar to the edge states of a two-dimensional topological insulator. However, as mentioned above, the hinges modes are protected by a crystalline symmetry like mirror or rotation symmetry. Furthermore, we have to distinguish between two types of hinge modes: i) chiral HOTIs, where the hinge modes propagate unidirectionally and time-reversal symmetry is broken; ii) helical HOTIs, which preserve time-reversal symmetry with hinge modes consisting of counter-propagating Kramers pairs. In this thesis we are interested in the latter. Helical HOTIs were first predicted in strained SnTe, where the surface states are gapped by the strain and the hinge states are protected by mirror symmetry [Schindler *et al.* 2018a]. As another success in the field of topological phases, helical hinge modes protected by rotation and inversion symmetry have been predicted and observed in bismuth using scanning tunneling microscopy and Josephson interferometry [Schindler *et al.* 2018b]. Using scanning tunneling microscopy, the authors obtained topographic images of step edges on the (111) surface of bismuth and displayed differential conductance maps superimposed on the topographic data, revealing the presence of hinge states. Moreover, these authors investigated the transport properties of the hinge modes using a superconductor-bismuth-superconductor Josephson junction with a bismuth nanowire. At low temperature, a supercurrent flows through the nanowire. They observed three remarkable features: i) Periodic oscillations of the critical current through the nanowire caused by a magnetic field with a period corresponding to one magnetic flux quantum through the wire section perpendicular to the field. Such oscillations indicate interference between two supercurrent paths located at the nanowire edges. ii) The supercurrent persists up to very high magnetic fields, indicating that the conducting channels are extremely narrow. iii) Current-phase oscillations in an asymmetric superconducting quantum interference device with a sharp sawtooth shape. The sharp sawtooth shape indicates that the transport is ballistic, as opposed to diffusive or tunneling transport where the current-phase relationship is nearly sinusoidal. Furthermore, the position of the edge states can be deduced from these oscillations, and two paths along the two sharp edges of the (111) surface were detected. These observations clearly show that the supercurrent flows through a few narrow one-dimensional channels rather than through the surface or bulk of the nanowire. In addition, the transition metal dichalcogenides XTe_2 (X = Mo, W) were predicted to also exhibit helical hinge states protected by rotational symmetry [Wang *et al.* 2019]. This has been confirmed experimentally in WTe_2 by Josephson interferometry measurements [Choi *et al.* 2020]. Here the authors have spatially resolved the hinge states by analyzing the magnetic field interference of the supercurrent in Nb-WTe_2-Nb Josephson junctions.

In Chap. 5 we will derive the Hamiltonian describing helical hinge states protected by mirror symmetry and study the effects of Zeeman and superconducting couplings on them. Such couplings would destroy the helical edge states of a QSH insulator. Indeed, a Zeeman field breaks the time-reversal symmetry that protects the QSH phase, while coupling to an s-wave superconductor gaps the helical edge modes. In contrast, we will show that the helical hinge modes of a HOTI can survive these perturbations. Since the hinge states are protected not by time reversal but by mirror symmetry, they naturally resist a Zeeman field, while we will give a condition under which they persist even in the presence of superconducting coupling. Interestingly, we will see that when the hinge modes survive, they are spatially split by these perturbations.

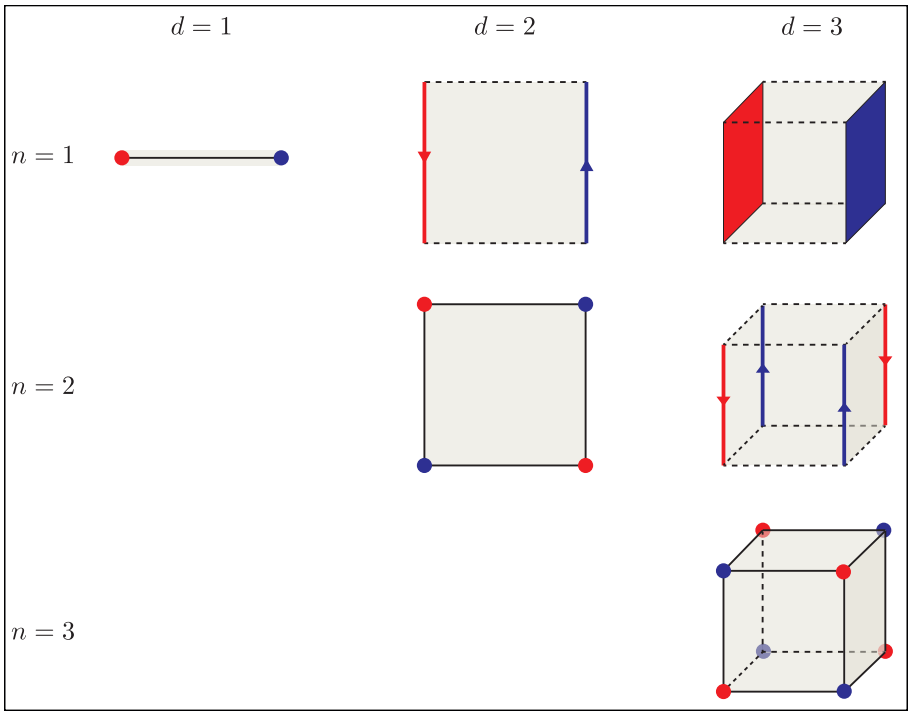

Figure 2.24: Higher-Order Topological Insulators. In the case of a unidimensional wire ($d = 1$) the only topological phase shows point-like end modes. For a two-dimensional surface ($d = 2$) we can have usual edge states ($n = 1$) or corner states ($n = 2$). Finally, in the three-dimensional case ($d = 3$), we can have surface states ($n = 1$), hinge modes ($n = 2$) or corner states ($n = 3$).

Chapter 3

Chiral Andreev edge states in quantum Hall-superconductor junctions

Contents

In this chapter we study the geometry and filling factor dependencies of the downstream conductance in quantum Hall-superconductor hybrid systems. This work is published in Ref. [David *et al.* 2023].

3.1 Introduction

Combining a system in the quantum Hall regime and a superconductor is not an easy task as the magnetic field needed to reach the quantum Hall effect tends to destroy superconductivity. However, if successful, it leads to interesting phenomena due to the superconducting correlations induced in the chiral edge states of the quantum Hall system. In particular, the formation of so-called chiral Andreev edge states (CAES) has been predicted. From a semi-classical point of view, these CAES result from skipping orbits of electrons and holes involving Andreev reflections at the quantum Hall-superconductor (QH-SC) interface [Takagaki 1998, Asano & Kato 2000, Chtchelkatchev 2001, Chtchelkatchev & Burmistrov 2007]. Quantum-mechanically, the edge states along that interface are described as hybridized electron and hole states [Hoppe *et al.* 2000, Zülicke *et al.* 2001, Giazotto *et al.* 2005, Khaymovich *et al.* 2010, van Ostaay *et al.* 2011]. The use of CAES for topologically protected quantum computing have been considered in [Nayak *et al.* 2008, Mong *et al.* 2014, Clarke *et al.* 2014].

Recently, many groups of researchers have succeeded in creating QH-SC hybrid systems, using either graphene [Lee *et al.* 2017, Zhao *et al.* 2020, Gül *et al.* 2022, Zhao *et al.* 2022] or InAS

2DEG [Hatefipour *et al.* 2022], and they demonstrated the presence CAES in the so-called downstream conductance. The latter consists in measuring the conversion of upstream electrons into downstream holes. Larger is the associated conversion probability, smaller is the downstream conductance and, in particular, it becomes negative as the conversion probability exceeds one half. Even if negative downstream conductances have been measured [Lee *et al.* 2017, Zhao *et al.* 2020, Gül *et al.* 2022, Zhao *et al.* 2022, Hatefipour *et al.* 2022], questions remain about the magnitude and parameter dependencies of the effect as they don't match simple models: the observed signal is much smaller than expected. Moreover, either irregular [Lee *et al.* 2017, Zhao *et al.* 2020, Gül *et al.* 2022] or roughly constant [Hatefipour *et al.* 2022] patterns have been observed when sweeping the field or the gate voltage, while simple models predict a regular oscillation. This stimulated further theoretical research. A suppression of the measured signal may be explained by the absorption of quasiparticles in the superconductor, for example by sub-gap states in nearby vortices [Zhao *et al.* 2020, Manesco *et al.* 2022, Kurilovich *et al.* 2022, Schiller *et al.* 2022], whereas the oscillations may be strongly affected by disorder [Manesco *et al.* 2022, Kurilovich *et al.* 2022].

Here we focus on an aspect that has not been studied before: the effects of the geometry. Indeed, the downstream conductance does not only probe the properties of the QH-SC interface, but also the scattering properties at the point where this interface meets the QH-vacuum one. We find that these scattering probabilities strongly depend on the geometry of the contact region. In particular, we observe a strong dependency in the angle between the QH-vacuum interface and the QH-SC interface. Interestingly this opens the possibility of creating asymmetric structures, where these angles are different on the two sides of the superconductor, that can display an enhanced overall electron-hole conversion probability. This may even lead to a situation where the length-averaged downstream conductance becomes negative.

Let us mention that, to study the effects of geometry, a full two-dimensional description of the system is necessary – simple one-dimensional models commonly used in the literature are not sufficient. Some aspects may be captured by using a generalized one-dimensional model, though there is no obvious way to determine the corresponding parameters.

The chapter is organized as follows. In Sec. 3.2 we present the system and we derive a formula for the downstream conductance based on edge state transport, whose parameters have to be determined. To do so, we first use a two-dimensional continuous model in Sec. 3.3 to determine the properties of the edge states at an infinitely long interface. We then use a tight-binding model in Sec. 3.4 to obtain the scattering probabilities at the points where two different interfaces, i.e., QH-vacuum and QH-SC, meet. With these two ingredients, we have all that is needed to compute the downstream conductance. In Sec. 3.5, we address the question whether the prior results may be obtained from an effective one-dimensional model. A comparison between the analytical and numerical results for the downstream conductance at zero temperature as well as the computation of the downstream conductance at non-zero temperature can be found in Sec. 3.6, before we conclude in Sec. 3.7.

3.2 System and conductance formula

We consider a QH-SC interface located at $x = 0$ with the geometry depicted in Fig. 3.1. Here an incoming electron from the upstream reservoir can, after propagating as a CAES along the superconductor, be transmitted into the downstream reservoir as an electron or as a hole with respective amplitudes p_e and p_h. We are interested in the regime where one spin-degenerate Landau level is occupied in the quantum Hall region, i.e., there are two chiral edge states. Introducing particle-hole space to be able to incorporate superconductivity, we can describe one spin state as an electron state and the other spin state as a hole state. While the chiral edge states along an edge with the vacuum are either pure electron or hole states, the CAES along an edge with a superconductor are a superposition of electron and hole components. In the following, we will call them quasi-electron when their momentum at the Fermi level is negative and quasi-hole when their momentum at the Fermi level is positive. As we will see, this choice is in agreement with the pure electron and hole states obtained when Andreev processes are suppressed. Note that electrons and holes propagate in the same direction because they have charge and mass of opposite signs, so they experience the same Lorentz force. The lengths of the QH and SC regions are respectively denoted by L_{QH} and L_{SC} and the length of the QH-SC interface is denoted by L. The width of the

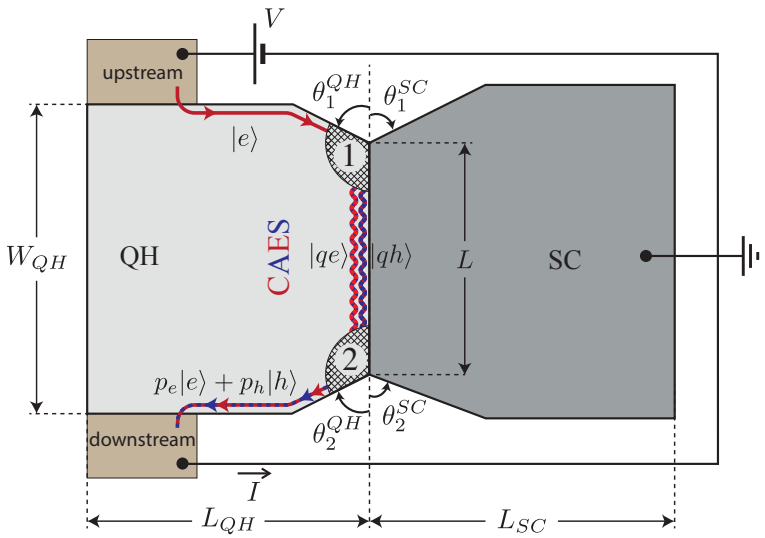

Figure 3.1: QH-SC setup: the edge of the quantum Hall region is in contact with a grounded superconductor over a finite length L. The geometry of the corners at the beginning and end of that region can be characterized by two angles each: θ_i^{QH} and θ_i^{SC}. Both the QH-vacuum and QH-SC interface host chiral edge states that can be probed by measuring the downstream conductance $G_d(E) = \partial I/\partial V|_{eV=E}$, where V is the voltage biased between the upstream reservoir and the superconductor, and I is the current entering in the downstream reservoir. While (quasi-)electron and (quasi-)hole states have opposite directions of quasi-momentum along the interface, they have the same propagation direction. A typical process contributing to G_d is shown: an incoming electron $|e\rangle$ scatters at the first corner, propagates along the QH-SC interface as a superposition of quasi-electron $|qe\rangle$ and quasi-hole $|qh\rangle$ CAES, then scatters at the second corner, and finally exits the superconductor in a superposition of electron $|e\rangle$ and hole $|h\rangle$. The hole probability $P_h = |p_h|^2$ of the outgoing state depends on the scattering processes at the corners as well as the interference of the CAES propagation along the QH-SC interface. The lengths of the QH and SC regions are respectively denoted by L_{QH} and L_{SC} and the width of the QH-vacuum interface at the left is denoted by W_{QH}.

QH region at the left hand side of the system is denoted by W_{QH}. We have respectively labelled the upstream and downstream QH-SC corners by 1 and 2 and their shapes are characterized by two angles each: θ_i^{QH} and θ_i^{SC} $(i = 1, 2)$. These are defined as the angles formed by the QH and SC regions with the continuity of the QH-SC interface (see Fig. 3.1) so that we define a negative angle when the QH (SC) region goes inside the $x > 0$ ($x < 0$) side. In all this chapter we consider sub-gap states with $|E| < \Delta$.

In this chapter we study the energy spectrum and the transport properties of the QH-SC junction by using different models. In the present section we only give the downstream conductance formula which can be derived independently from these models and is given by,

$$G_d(E) = \left.\frac{\partial I}{\partial V}\right|_{eV=E}, \tag{3.1}$$

where V is the voltage bias applied between the upstream reservoir and the superconductor while I is the current flowing in the downstream reservoir (see Fig. 3.1). We can relate the downstream conductance to the scattering probabilities $P_e = |p_e|^2$ and $P_h = |p_h|^2$ by using a generalization of the Landauer-Büttiker formalism for superconducting systems (this is similar to what we did for the Hall bar geometry in Sec. 2.2.4). Indeed, the Landauer-Büttiker formula (2.104) used in Sec. 2.2.4 doesn't take into account Andreev scattering such that we have to consider additional terms [Lambert *et al.* 1993]. Let us consider the three-terminal device depicted in Fig. 3.2. The upstream and downstream reservoirs are respectively labelled by 1 and 2 with currents and voltages denoted by $I_{1,2}$ and $V_{1,2}$, while the grounded superconductor is the third terminal with current I_3 and voltage $V_3 = 0$. For a system with only normal reservoirs, at small bias and low temperatures, the current I_p in reservoir p would be given by (2.104)[1],

$$I_p = G_0 \sum_q \bar{T}_{pq} \left(V_q - V_p\right), \tag{3.2}$$

where $\bar{T}_{pq}$ is the total transmission from reservoir q to reservoir p and $G_0 = 2e^2/h$ is the quantum of conductance. The current I_1 flowing into the upstream reservoir comes only from the downstream reservoir and takes the same form as for two adjacent reservoirs in the Hall bar geometry, i.e. $I_1 = G_0(V_2 - V_1)$. The current I_2 flowing in the downstream reservoir is made of two contributions. The first one originates from the Andreev reflection occurring at the QH-SC interface leading to the contribution $(P_e - P_h)(V_1 - V_3) = (P_e - P_h)V_1$. The second contribution comes from the usual QHE edge state along the interface with the vacuum between reservoir 3 and reservoir 2 where $\bar{T}_{23} = 1$. We thus obtain $I_2 = G_0V_1(P_e - P_h) - G_0V_2$. Finally, as the electron leaving the upstream reservoir cannot enter in the superconductor (because we consider $|E| < \Delta$), the only possible current in terminal 3 must be due the formation of a Cooper pair when the incoming electron exists the superconductor as a hole (see Sec. 2.1). This translates into $I_3 = 2G_0V_1P_h$. With these notations the downstream conductance introduced in Eq. (3.1) reads $G_d = \partial I_2/\partial V_1$, which can be written in terms of the scattering probabilities as,

$$G_d = G_0(P_e - P_h) = G_0(1 - 2P_h), \tag{3.3}$$

where we used $P_e + P_h = 1$. Note that this result is unchanged if we take $V_2 = 0$ and so we can consider a grounded downstream reservoir as in Fig. 3.1 without loss of generality.

To calculate the scattering probabilities P_e and P_h we follow the transfer matrix approach of Ref. [Khaymovich *et al.* 2010]. (The transfer matrix method and the composition law of transfer matrices is presented in App. A.) We consider a single electron-hole pair of CAES propagating along the QH-SC interface whose wave function can be written as,

$$\psi_{CAES} = \begin{pmatrix} qe \\ qh \end{pmatrix}, \tag{3.4}$$

and the states propagating along the interfaces with the vacuum at the upstream (u) and downstream (d) edges, where electrons and holes are not mixed, can be written as,

$$\psi_u = \begin{pmatrix} e_u \\ h_u \end{pmatrix}, \quad \psi_d = \begin{pmatrix} e_d \\ h_d \end{pmatrix}. \tag{3.5}$$

[1] Note that here we define the current I_p as the one entering in lead p instead of the current leaving lead p from where the voltage difference $V_q - V_p$ instead of the $V_p - V_q$ used in Eq. (2.104).

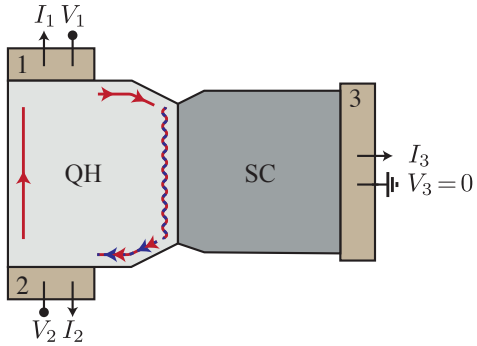

Figure 3.2: Three-terminal device. The currents flowing in between the reservoirs are represented by red and blue arrows for electron and hole respectively. The wavy line along the QH-SC interface represents the CAES.

We can then describe the scattering at the two corners by using the transfer matrices $T_{1,2}$ which couple the incident and transmitted quasiparticle waves,

$$\begin{pmatrix} qe \\ qh \end{pmatrix} = T_1 \begin{pmatrix} e_u \\ h_u \end{pmatrix}, \quad \begin{pmatrix} e_d \\ h_d \end{pmatrix} = T_2 \begin{pmatrix} qe \\ qh \end{pmatrix}. \tag{3.6}$$

The transfer matrices $T_{1,2}$ can be written explicitly as follows,

$$T_1 = \begin{pmatrix} t_{qe,e} & t_{qe,h} \\ t_{qh,e} & t_{qh,h} \end{pmatrix}, \quad T_2 = \begin{pmatrix} t_{e,qe} & t_{e,qh} \\ t_{h,qe} & t_{h,qh} \end{pmatrix}, \tag{3.7}$$

where particle-hole symmetry implies the following relations,

$$t_{qe,e} = t^*_{qh,h}, \quad t_{qh,e} = -t^*_{qe,h}, \quad t_{e,qe} = t^*_{h,qh}, \quad t_{h,qe} = -t^*_{e,qh}. \tag{3.8}$$

Moreover, for a symmetric junction where the corners have the same shapes, we have $T_1 = T_2^T$ [Khaymovich *et al.* 2010]. Introducing the transfer matrix of phase factors acquired along the QH-SC interface,

$$\Lambda_L = \begin{pmatrix} e^{ik_{qe}L} & 0 \\ 0 & e^{ik_{qh}L} \end{pmatrix}, \tag{3.9}$$

we can write the total transfer matrix S from the upstream contact to the downstream contact as

$$S = \begin{pmatrix} s_{ee} & s_{eh} \\ s_{he} & s_{hh} \end{pmatrix} = T_2 \Lambda_L T_1, \tag{3.10}$$

and the amplitudes p_e and p_h introduced above are given by

$$p_e = s_{ee}, \quad p_h = s_{he}. \tag{3.11}$$

Then, setting the following notations,

$$|t_{qe,e}|^2 = 1 - \tau_1, \quad |t_{qh,e}|^2 = \tau_1, \quad |t_{e,qe}|^2 = 1 - \tau_2, \quad |t_{e,qh}|^2 = \tau_2, \tag{3.12}$$

we can write the amplitudes P_e and P_h as

$$P_e = \tau_1\tau_2 + (1-\tau_1)(1-\tau_2) + 2\sqrt{\tau_1(1-\tau_1)\tau_2(1-\tau_2)}\cos(\delta kL + \phi_{12}), \tag{3.13}$$

$$P_h = \tau_1(1-\tau_2) + \tau_2(1-\tau_1) - 2\sqrt{\tau_1(1-\tau_1)\tau_2(1-\tau_2)}\cos(\delta kL + \phi_{12}), \tag{3.14}$$

where $\delta k = k_{qe} - k_{qh}$ and $\phi_{12} = \phi_1 + \phi_2$ with $\phi_1 = \arg(t_{qh,e}) - \arg(t_{qe,e})$ and $\phi_2 = \arg(t_{e,qe}) - \arg(t_{e,qh})$. In particular, at zero bias we have $\delta k = 2k_0$, where k_0 is the momentum value at which the spectral branch along the QH-SC interface crosses the Fermi level.

According to the zero-temperature result (3.3), $G_d = G_0(1-2P_h)$, a negative downstream conductance is a clear signature of the Andreev conversion taking place at the QH-SC interface. Furthermore, the averaged conductance is given as $\bar{G}_d = G_0 \prod_{i=1,2}(1-2\tau_i)$. For $\tau_1 = \tau_2$, it is limited to positive values, whereas $\tau_1 \neq \tau_2$ allows one to realize $\bar{G}_d < 0$. For completeness, let us mention that the maximal downstream conductance is $G_d^{\max} = G_0[1-2(\sqrt{\tau_1(1-\tau_2)} - \sqrt{\tau_2(1-\tau_1)})^2]$ while the minimal downstream conductance is $G_d^{\min} = G_0[1-2(\sqrt{\tau_1(1-\tau_2)} + \sqrt{\tau_2(1-\tau_1)})^2]$. In the symmetric case $\tau_1 = \tau_2 \equiv \tau$ this yields $G_d^{\max} = G_0$ and $G_d^{\min} = G_0[1-8\tau(1-\tau)]$. As a last piece of information, we represent in Fig. 3.3 a colormap of the averaged Andreev conversion $\bar{P}_h = \tau_1(1-\tau_2) + \tau_2(1-\tau_1)$. From this figure we see that the averaged Andreev conversion is maximal if $\tau_1 = 1$ and $\tau_2 = 0$ (or vice-versa). This could be anticipated since these values correspond to a unit probability for an incoming electron to propagate along the superconductor as a quasi-hole and then to leave it as a hole (or to propagate as a quasi-electron and exit as a hole). Thus, in order to have the higher value of $\bar{P}_h$, we need to find a regime which maximize τ_1 and minimize τ_2 (or vice-versa). As we will see, this situation is realized for highly asymmetric geometries with a filling factor close to the transition plateau.

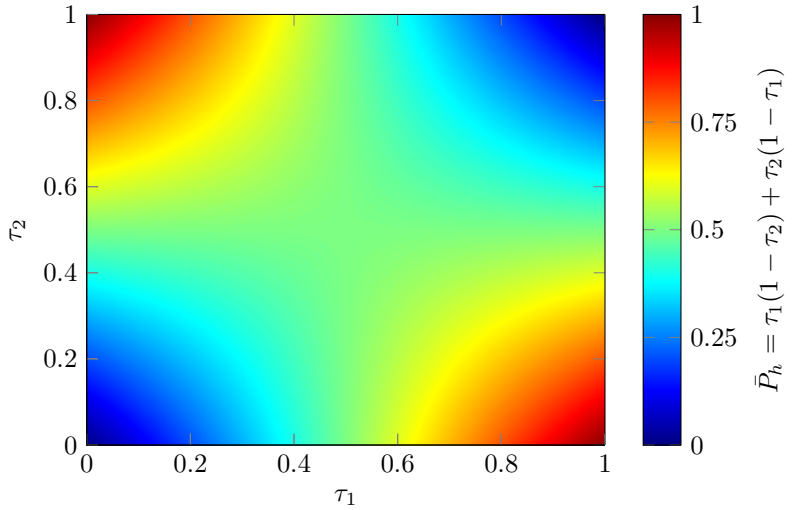

Figure 3.3: Colormap of the averaged Andreev conversion.

Thus, to model the experimentally measured downstream conductance, we need to determine k_0 as well as the probabilities τ_i associated with the contact points between the QH region, the vacuum, and the superconductor. In the following, we compute k_0 semi-analytically from a microscopic model of an infinite QH-SC interface. By contrast, there is no simple model for the probabilities τ_i. Hence, we study their dependence on system parameters and in particular the geometry of the contact points using tight-binding simulations.

3.3 Microscopic model

The main goal of this section is to determine the zero-bias momentum k_0 introduced in Sec. 3.2 to compute the downstream conductance. To do so, we first determine the wave functions in the quantum Hall and superconducting regions. We then match the wave functions and their derivatives in order to obtain a secular equation that allows to compute the energy spectrum and so the momentum value at any energy. We also derive analytical results for k_0 which are valid in the linear approximation and we end the section by calculating the electron and hole contents of the CAES wave functions.

We consider a QH-SC interface with translational invariance along the y-axis such that the region $x < 0$ is in the quantum Hall regime whereas the region $x > 0$ is a superconductor. The microscopic

Hamiltonian can be written in the form of a BdG Hamiltonian[2],

$$H(\vec{r}) = \begin{pmatrix} H_0(\vec{r}) - \mu(x) & \Delta(x) \\ \Delta^*(x) & -H_0^*(\vec{r}) + \mu(x) \end{pmatrix}, \tag{3.15}$$

with $\vec{r} = (x, y)$ and,

$$H_0(\vec{r}) = \frac{1}{2m(x)} \left(-i\hbar\vec{\nabla} - e\vec{A}(x) \right)^2 + V(x). \tag{3.16}$$

Here the x-dependent parameters are defined as,

$$m(x) = m_{QH}\Theta(-x) + m_{SC}\Theta(x), \quad \mu(x) = \mu_{QH}\Theta(-x) + \mu_{SC}\Theta(x), \tag{3.17}$$

$$\Delta(x) = \Delta\Theta(x), \quad V(x) = V_0\delta(x), \quad \vec{A}(x) = Bx\Theta(-x)\hat{u}_y, \tag{3.18}$$

where $m(x)$ is an effective mass, $\mu(x)$ is the chemical potential measured from the band bottom, $\Delta(x)$ is the superconducting order parameter (that we choose to be real in the following), $V(x)$ models an interface barrier and $\vec{A}(x)$ is the gauge potential where here we have chosen the Landau gauge that preserves translational invariance along the interface's direction. $\Theta(x)$ is the Heaviside step function and $\delta(x)$ the Dirac-delta function. Assuming periodic boundary conditions along the y-axis, the wave functions can be written as,

$$\Psi(\vec{r}) = \frac{e^{ik_y y}}{\sqrt{L_y}} \psi_{k_y}(x), \tag{3.19}$$

where L_y is the length of the system along the y-direction and ψ_{k_y} is the transverse wave function. Following the procedure of Ref. [Blonder *et al.* 1982], we can determine the spectrum of the CAES by writing the wave functions $\psi_{k_y}^{QH}(x)$ in the half-space $x < 0$ and $\psi_{k_y}^{SC}(x)$ in the half-space $x > 0$ and matching them at the interface. We give these bulk wave functions in the next subsection.

3.3.1 Bulk wave functions and characteristic scales

We have already studied independently the physics of the QH and SC regions in Chap. 2. From Sec. 2.2.2 we can write the wave function in the QH region as,

$$\psi_{k_y}^{QH}(x) = c_+^{QH} \begin{pmatrix} 1 \\ 0 \end{pmatrix} \chi_+(x) + c_-^{QH} \begin{pmatrix} 0 \\ 1 \end{pmatrix} \chi_-(x), \tag{3.20}$$

with,

$$\chi_\pm(x) = N_\pm U\left(-\frac{\mu_{QH} \pm E}{\hbar\omega_c}, -\frac{\sqrt{2}}{l_B}(x \mp k_y l_B^2) \right), \tag{3.21}$$

where $U(a, z)$ are parabolic cylinder functions vanishing as $z \to \infty$ as introduced in Eq. (2.78) and $N_\pm$ are normalization coefficients such that $\int_{-\infty}^{0} dx\ |\chi_\pm(x)|^2 = 1$. Restricting ourselves to the regime $|E| < \Delta$, we have seen from Sec. 2.1.3 that the wavefunctions in the SC region can be written as,

$$\psi_{k_y}^{SC}(x) = c_+^{SC} \begin{pmatrix} \gamma \\ 1 \end{pmatrix} \phi(x) + c_-^{SC} \begin{pmatrix} \gamma^* \\ 1 \end{pmatrix} \phi^*(x), \tag{3.22}$$

with $\phi(x) = \sqrt{2\,\mathrm{Im}\, q}\, e^{iqx}$,

$$q = \left[(k_F^{SC})^2 - k_y^2 + 2im\Delta\sqrt{1 - \varepsilon^2} \right]^{1/2}, \tag{3.23}$$

and $\gamma = \varepsilon + i\sqrt{1 - \varepsilon^2}$, where $\varepsilon = E/\Delta$.

Before going further it is instructive to compare the characteristic scales of the QH and SC regions. As discussed in the introduction of this chapter, the applied magnetic field used to reach the quantum

[2] We already used a BdG Hamiltonian to present the Andreev reflection in Chap. 2 and we derived it in App. B.3.

Hall regime must be lower than the critical field of the superconductor. We thus need a superconductor with a high critical field and so consider a type-II superconductor whose upper critical field can be written as [Girvin & Yang 2019, Eq. (19.87)],

$$H_{c_2} = \frac{\phi_0/2}{2\pi\xi^2}, \tag{3.24}$$

with $\phi_0/2$ the superconducting flux quantum (for particles with charge 2e) and ξ the superconducting coherence length. Writing the applied magnetic field as,

$$B = \frac{\phi_0}{2\pi l_B^2}, \tag{3.25}$$

and imposing $B < H_{c_2}$ we arrive at the condition $\xi < l_B$. Moreover, for a weak coupling superconductor with $\Delta \ll \hbar\omega_D \ll \mu_{SC}$, we have [Girvin & Yang 2019, Eq. (20.91)],

$$\xi \gg \frac{\hbar v_F^{SC}}{\mu_{SC}} \sim 1/k_F^{SC} \sim \lambda_F^{SC}. \tag{3.26}$$

Also, because we are interested in the regime where a single Landau level is filled, we have $\mu_{QH} \sim \hbar\omega_c$ which implies $\lambda_F^{QH} \sim l_B$. This leads to the following length and energy scales,

$$\lambda_F^{SC} \ll \xi < l_B \sim \lambda_F^{QH}, \tag{3.27}$$

$$\Delta, \frac{m_{QH}}{m_{SC}}\hbar\omega_c \sim \frac{m_{QH}}{m_{SC}}\mu_{QH} \ll \mu_{SC}. \tag{3.28}$$

In addition, considering typical values of the Fermi level in III-V semiconductors ($\sim$ 10meV) and typical values of the superconducting gap in high upper critical field superconductors ($\sim$meV) we can assume $\Delta \lesssim \mu_{QH}$. Note that these scales have been established by considering the bulk values of the QH and SC regions. However, in III-V semiconductor devices under a planar proximitization with an s-wave superconductor (for example the InAs/NbTiN structure used in Ref. [Hatefipour *et al.* 2022]), a dielectric layer is placed in between the superconductor and the 2DEG (in contrast to the case of graphene where it is edge-contacted), reducing the mismatch in between the two regions such that, close to the QH-SC interface, the superconducting mass and chemical potential are close to the ones of the QH region.

3.3.2 Energy spectrum

Since we have determined the wave functions in the different regions we can now use them to determine the energy spectrum of the states leaving along the QH-SC interface.

3.3.2.1 Secular equation

To obtain the energy spectrum of the states leaving along the QH-SC interface, namely the CAES, we use the matching procedure of Ref. [Blonder *et al.* 1982],

$$\begin{aligned} \psi_{k_y}^{QH}(0) &= \psi_{k_y}^{SC}(0) = \psi_{k_y}(0), \\ \frac{m_{QH}}{m_{SC}}\psi_{k_y}^{SC\prime}(0) - \psi_{k_y}^{QH\prime}(0) &= Z k_F^{QH}\psi_{k_y}(0), \end{aligned} \tag{3.29}$$

with $Z = 2V_0/(\hbar v_F^{QH})$ the interface's barrier strength[3]. From the resulting system we arrive at the following secular equation [Hoppe *et al.* 2000],

$$s(E,k_y) = GH\left(c^2+d^2\right) + G'H' + c\frac{E}{\sqrt{\Delta^2-E^2}}(G'H - GH') + d(G'H + GH') = 0, \tag{3.30}$$

[3]Note that this value of Z, originally introduced in [Hoppe *et al.* 2000], is twice the value used in [Blonder *et al.* 1982] to describe normal metal-superconductor junctions.

with the shorthand notations,

$$c = \frac{m_{QH}}{m_{SC}}\mathrm{Re}\{q\},\ d = \frac{m_{QH}}{m_{SC}}\mathrm{Im}\{q\} + Zk_F^{QH},$$
$$G = \chi_+(0),\ G' = \chi'_+(0),\ H = \chi_-(0),\ H' = \chi'_-(0). \tag{3.31}$$

The energy spectrum of the CAES can then be obtained by numerically solving Eq. (3.30). In Fig. 3.4 we show the resulting energy spectrum for different values of the filling factor $\nu = 2\mu_{QH}/(\hbar\omega_c)$, namely $\nu = 2$ and $\nu = 10$, and we define the number of crossings at the Fermi level as $N_c = 2\mathrm{int}(\nu/2)$. Here we have represented the case $\nu = 10$ as an illustrative example but, as already said, we are interested in the study of a single pair of CAES, i.e. $N_c = 2$, so that we restrict ourselves to the regime $\nu \in]1, 3[$ in the following. In Fig. 3.4a we have labelled the quasi-electron and quasi-hole CAES and, at low energies, they are linearly dispersing with energies $E_\pm(k_y) = \hbar v(k_y \pm k_0)$. Here v is the velocity of the CAES and k_0 is the momentum value at the Fermi-level used to compute the downstream conductance in Sec. 3.2. The value of k_0 is obtained by numerically solving the zero-energy secular equation and serves to compute the velocity,

$$k_0 = \mathrm{solve}\left[s(E = 0, k > 0) = 0,\ k\right], \tag{3.32}$$

$$v = -\frac{1}{\hbar}\left.\frac{\partial_k s(E,k)}{\partial_E s(E,k)}\right|_{\substack{E=0\\k=k_0}}. \tag{3.33}$$

We observe that, as long as $\Delta \ll \mu_{QH}, \mu_{SC}$, the momentum k_0 does not depend on Δ. In Fig. 3.5 we show the evolution of k_0 as a function of the barrier strength Z for various values of the filling factor ν. Typically, k_0 decreases with increasing ν, except for a small region of intermediate values of Z and fillings ν close to 3.

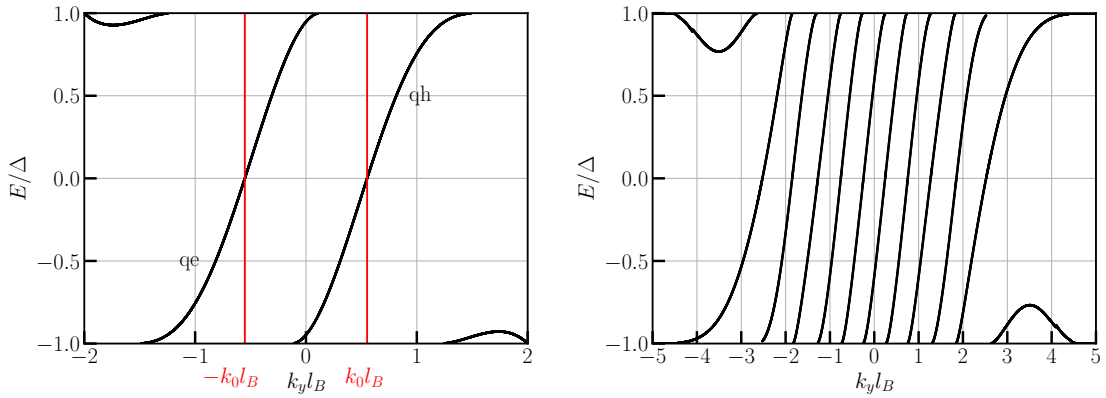

Figure 3.4: CAES energy spectrum at small and large filling. In (a) we represent a single pair of CAES with $\nu = 2$. The crossings of the CAES with the Fermi level at $k_y = \pm k_0$ are indicated by red lines, where $k_y = -k_0$ is in the quasi-electron (qe) branch and $k_y = +k_0$ in the quasi-hole (qh) branch (this choice recovers the pure electron and hole states when $V_0 \to \infty$). In (b) we show five pairs of CAES by choosing $\nu = 10$. We have set $m_{QH} = m_{SC}$, $\mu_{QH} = \mu_{SC}/2 = 10\Delta$, and $Z = 0$.

In Fig. 3.4 we observe the appearance of additional non-chiral edge states close to the gap edge. Depending on the system's parameters, these can eventually cross the Fermi level, which would modify the zero-bias conductance defined in Eq. (3.3). We study the behavior of these additional non-chiral edge states in the following.

3.3.2.2 Additional non-chiral edge states

As discussed above, additional non-chiral edge states can cross the Fermi level in certain parameter regimes. Here we show that this happens when the filling factor gets close to the transition plateau at

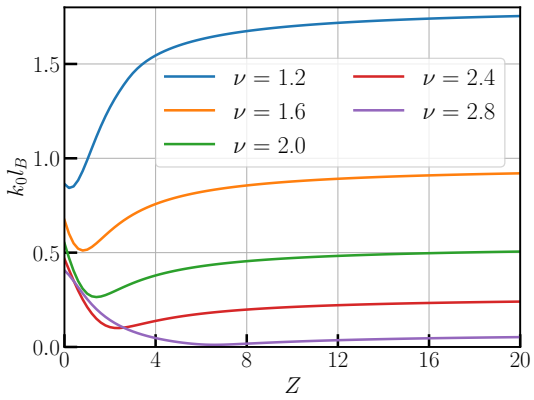

Figure 3.5: Momentum k_0 as a function of barrier strength Z for various values of the filling factor ν at $\mu_{QH} = \mu_{SC} = 10\Delta$. Except for a small region of intermediate Z and ν close to 3, the momentum k_0 decreases with increasing ν.

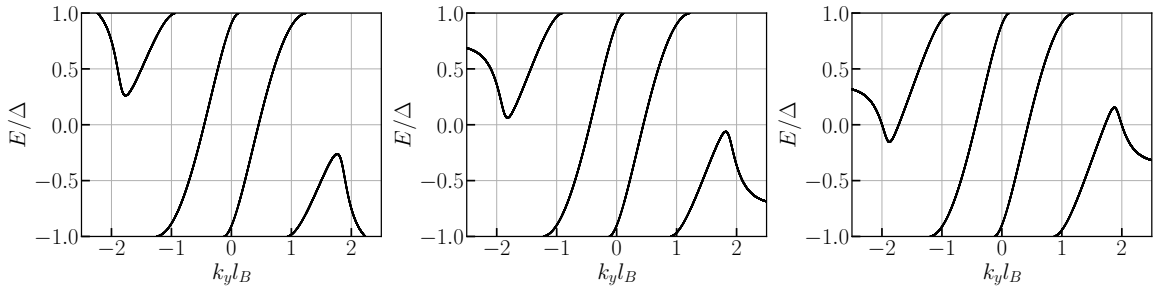

(a) $\nu = 2.7$ (b) $\nu = 2.8$ (c) $\nu = 2.9$

Figure 3.6: CAES energy spectrum for various values of the filling factor with (a) $\nu = 2.7$, (b) $\nu = 2.8$, and (c) $\nu = 2.9$. We have set $m_{QH} = m_{SC}$, $\mu_{QH} = 0.8\mu_{SC} = 10\Delta$, and $Z = 0$.

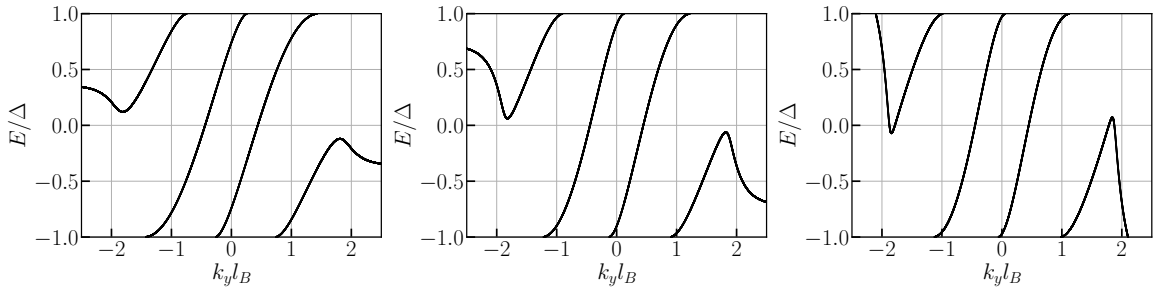

(a) $\mu_{QH}/\Delta = 5$ (b) $\mu_{QH}/\Delta = 10$ (c) $\mu_{QH}/\Delta = 20$

Figure 3.7: CAES energy spectrum for various values of the filling factor with (a) $\mu_{QH}/\Delta = 5$, (b) $\mu_{QH}/\Delta = 10$, and (c) $\mu_{QH}/\Delta = 20$. We have set $m_{QH} = m_{SC}$, $\mu_{QH} = 0.8\mu_{SC}$, $\nu = 2.8$, and $Z = 0$.

$\nu = 3$ and/or as the ratio μ_{QH}/Δ is increased (while keeping μ_{SC}/μ_{QH} constant). Moreover, we show that these additional crossings disappear as the QH-SC interface becomes non-ideal, i.e., as the barrier strength Z and/or the Fermi mismatch are increased. To see that, we first represent the energy spectrum with $m_{QH} = m_{SC}$, $Z = 0$ and $\mu_{QH} = 0.8\mu_{SC}$ in Figs. 3.6 and 3.7. In Fig. 3.6 we consider the fillings $\nu \in \{2.7, 2.8, 2.9\}$ at $\mu_{QH}/\Delta = 10$ and in Fig. 3.7 we show the ratios $\mu_{QH}/\Delta \in \{5, 10, 20\}$ at $\nu = 2.8$. In Fig. 3.6c and Fig. 3.7c we observe the appearance of additional non-chiral zero-energy edge states. As μ_{QH}/Δ increases, the critical filling ν_c above which such states are present is lowered. We can obtain it by solving the secular equation (3.30) at $E = 0$ and determining the value ν_c at which a second solution $k_y > k_0$ appears. In Fig. 3.8a we show the evolution of ν_c as a function of μ_{QH}/Δ for an ideal interface (i.e. $v_F^{QH} = v_F^{SC}$ and $Z = 0$). We observe that, at $\mu_{QH}/\Delta \gg 1$, additional zero-energy states appear for $\nu > \nu_c \simeq 2.63$ such that one never finds additional states at fillings below this value. Moreover, for non-ideal interfaces, this asymptotic value is increased. In Fig. 3.8b and Fig. 3.8c we represent the evolutions of ν_c as function of the interface barrier strength Z and mismatch μ_{SC}/μ_{QH} at $\mu_{QH}/\Delta = 10^6$. We observe that ν_c reaches 3 when $\mu_{SC}/\mu_{QH} \gtrsim 3.73$ or $Z \gtrsim 0.65$. Beyond these values, one never finds additional zero-energy states, which is likely the case in experiments.

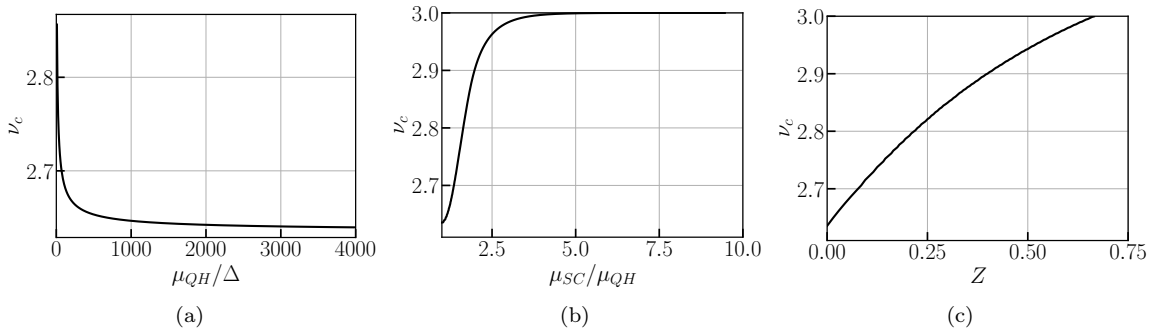

Figure 3.8: Plots of ν_c, indicating the appearance of additional non-chiral edge states at the Fermi level, as a function of different parameters. (a) Dependence of ν_c on μ_{QH}/Δ for an ideal interface, $\mu_{QH} = \mu_{SC}$ and $Z = 0$. In the limit $\mu_{QH}/\Delta \to \infty$, the critical value tends to $\nu_c \simeq 2.63$. (b) Dependence of ν_c on the mismatch μ_{SC}/μ_{QH} at $\mu_{QH}/\Delta = 10^6$ and $Z = 0$. As ν_c reaches 3, the additional non-chiral states disappear at moderate values of the mismatch. (c) Dependence of ν_c on the barrier strength.Z at $\mu_{QH}/\Delta = 10^6$ and $\mu_{QH} = \mu_{SC}$. As ν_c reaches 3, the additional non-chiral states disappear at moderate values of the barrier strength.

Finally, additional in-gap states may appear as well when the interface is smooth. In our model we considered an abrupt Fermi level mismatch, $\mu = (\mu_{SC} - \mu_{QH})\Theta(x) + \mu_{QH}$, but a more realistic profile should be smooth and a better expression would be [Manesco *et al.* 2022],

$$\mu = (\mu_{SC} - \mu_{QH}) f(x) + \mu_{QH}, \quad f(x) = \frac{1}{2}\left[1 + \tanh(x/\chi)\right], \tag{3.34}$$

where χ is the length over which the chemical potential changes its value (see Fig. 3.9). As seen from Fig. 3.9, the doping by the superconductor increases the filling factor near the QH-SC interface. This can eventually lead to additional crossings at the Fermi level. The impact of such additional edge-states on the conductance is discussed in Ref. [Manesco *et al.* 2022]. In this reference the authors claim that the additional crossings appear when $\chi \gtrsim l_B$ and $\mu_{SC} > \hbar v/l_B$, with v the velocity of the CAES.

In the next subsection we derive analytical results for the (linear) low-energy spectrum of the CAES.

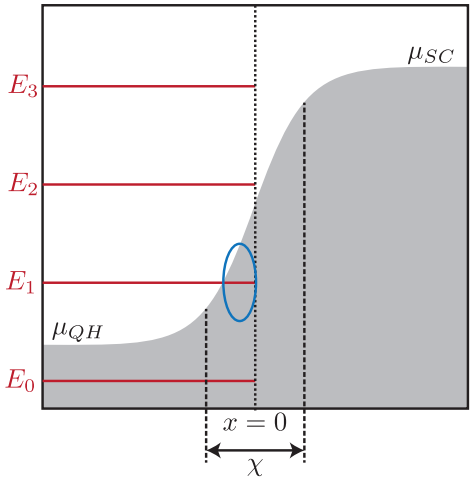

Figure 3.9: Smooth potential profile and filling factor change close to the interface. Considering a smooth Fermi level mismatch additional edge states can appear close to the interface (blue circle). The red lines represent the Landau levels.

3.3.2.3 Analytical results in the linear approximation

In order to go deeper analytically, we make the secular equation (3.30) dimensionless by multiplying it by $[m_{SC}/(m_{QH}k_F^{SC})]^2$ and obtain,

$$\tilde{s}(\varepsilon,\kappa) = A\tilde{G}\tilde{H} - B\partial_\kappa\tilde{G}\,\partial_\kappa\tilde{H} - \frac{\varepsilon}{\sqrt{\delta^2-\varepsilon^2}}C(\tilde{G}\partial_\kappa\tilde{H} + \tilde{H}\partial_\kappa\tilde{G}) + D(\tilde{G}\partial_\kappa\tilde{H} - \tilde{H}\partial_\kappa\tilde{G}) = 0, \tag{3.35}$$

where we have introduced the dimensionless quantities,

$$A = \tilde{c}^2 + \tilde{d}^2,\ B = \frac{m_{SC}\hbar\omega_c}{m_{QH}\mu_{SC}},\ C = \sqrt{B}\tilde{c},\ D = \sqrt{B}\tilde{d},\quad \tilde{c} = \frac{\mathrm{Re}\{q\}}{k_F^{SC}},\ \tilde{d} = \frac{\mathrm{Im}\{q\}}{k_F^{SC}} + Z\,\frac{v_F^{QH}}{v_F^{SC}}, \tag{3.36}$$

$$\varepsilon = \frac{E}{\hbar\omega_c},\ \kappa = \sqrt{2}l_B k_y,\ \delta = \frac{\Delta}{\hbar\omega_c},\ \tilde{G}(\varepsilon,\kappa) = U\left(-\frac{\nu}{2}-\varepsilon,\kappa\right),\ \tilde{H}(\varepsilon,\kappa) = U\left(-\frac{\nu}{2}+\varepsilon,-\kappa\right), \tag{3.37}$$

with $U(a,z)$ the parabolic cylinder function introduced in Eq. (2.78). We can then write the dimensionless linear dispersion as $\varepsilon = \tilde{v}(\kappa \pm \kappa_0)$, with the dimensionless parameters defined as,

$$\kappa_0 = \sqrt{2}l_B k_0 = \mathrm{solve}\left[\tilde{s}(\varepsilon=0,\kappa)=0,\ \kappa\right], \tag{3.38}$$

$$\tilde{v} = \frac{v}{\sqrt{2}l_B\omega_c} = -\left.\frac{\partial_\kappa\tilde{s}(\varepsilon,\kappa)}{\partial_\varepsilon\tilde{s}(\varepsilon,\kappa)}\right|_{\substack{\varepsilon=0\\ \kappa=\kappa_0}}. \tag{3.39}$$

We now derive analytical formulas for the zero-bias momentum k_0 and the velocity v and we end the subsection by giving simplified results.

Momentum k_0 Let's work with the dimensionless momentum κ_0 which is related to k_0 through the relation $k_0 = \kappa_0/(\sqrt{2}l_B)$. To compute κ_0 we need to solve the dimensionless zero-energy secular equation,

$$\tilde{s}(0,\kappa_0) = A_0\tilde{G}_0\tilde{H}_0 - B_0\partial_\kappa\tilde{G}_0\,\partial_\kappa\tilde{H}_0 + D_0(\tilde{G}_0\partial_\kappa\tilde{H}_0 - \tilde{H}_0\partial_\kappa\tilde{G}_0) = 0, \tag{3.40}$$

with,

$$A_0 = \tilde{c}_0^2 + \tilde{d}_0^2,\ B_0 = B = \frac{m_{SC}\hbar\omega_c}{m_{QH}\mu_{SC}},\ C_0 = \sqrt{B_0}\tilde{d}_0,\ D_0 = \sqrt{B_0}\tilde{d}_0, \tag{3.41}$$

$$\tilde{c}_0 = \frac{\mathrm{Re}\{q_0\}}{k_F^{SC}},\ \tilde{d}_0 = \frac{\mathrm{Im}\{q_0\}}{k_F^{SC}} + Z\,\frac{v_F^{QH}}{v_F^{SC}},\ q_0 = \sqrt{(k_F^{SC})^2 - k_0^2 + 2im_{SC}\Delta/\hbar^2}, \tag{3.42}$$

$$\tilde{G}_0 = \tilde{G}(0,\kappa_0),\ \tilde{H}_0 = \tilde{H}(0,\kappa_0),\ \partial_\kappa\tilde{G}_0 = \partial_\kappa\tilde{G}(0,\kappa)\Big|_{\kappa=\kappa_0},\ \partial_\kappa\tilde{H}_0 = \partial_\kappa\tilde{H}(0,\kappa)\Big|_{\kappa=\kappa_0}, \tag{3.43}$$

where we have introduced C_0 for later convenience. In order to go further analytically we need to simplify the parabolic cylinder functions $U(a,z)$. Using the definitions (2.78, 2.79, 2.80, 2.82, 2.84), we perform a first order expansion of $U(a,z)$ around $z=0$, and we obtain the following asymptotic form,

$$U(a,z) \simeq \frac{\Gamma\left(\frac{1}{4}-\frac{a}{2}\right)}{2^{\frac{a}{2}+\frac{1}{4}}\sqrt{\pi}}\cos\left[\left(\frac{1}{4}+\frac{a}{2}\right)\pi + \sqrt{2}\frac{\Gamma\left(\frac{3}{4}-\frac{a}{2}\right)}{\Gamma\left(\frac{1}{4}-\frac{a}{2}\right)}z\right]. \tag{3.44}$$

Because we are interested in parabolic cylinder functions of the form $U(-\nu/2,\pm\kappa_0)$, this asymptotic expansion is valid if $\kappa_0 \ll 1$. As we will see, this condition is satisfied if the filling factor is close to $\nu = 3$ and if $(m_{SC}\hbar\omega_c)/(m_{QH}\mu_{SC}) \ll 1$. By considering $\kappa_0 \ll 1$, we can simplify the momentum q_0 by,

$$q_0 \simeq \sqrt{k_{F,sc}^2 + 2im_{SC}\Delta/\hbar^2} = k_{F,sc}\sqrt{1+i\Delta/\mu_{sc}}, \tag{3.45}$$

where we have used $k_0/k_F^{SC} \ll 1$. (This is justified by using $1/k_F^{SC} = \lambda_F^{SC} \ll l_B$ from Eq. (3.27) and $k_0 \ll l_B/\sqrt{2}$ from $\kappa_0 \ll 1$.) From the asymptotic expression (3.44) we can write,

$$\tilde{G}(\varepsilon,\kappa) = U\left(-\frac{\nu}{2}-\varepsilon,\kappa\right) = F_+\cos(\alpha_+ + \beta_+), \tag{3.46}$$

$$\tilde{H}(\varepsilon,\kappa) = U\left(-\frac{\nu}{2}+\varepsilon,-\kappa\right) = F_-\cos(\alpha_- + \beta_-), \tag{3.47}$$

with,

$$F_\pm = \frac{\Gamma\left(\frac{1+\nu}{4} \pm \frac{\varepsilon}{2}\right)}{2^{\frac{1-\nu}{4}\mp\frac{\varepsilon}{2}}\sqrt{\pi}},\quad \alpha_\pm = \left(\frac{1-\nu}{4}\mp\frac{\varepsilon}{2}\right)\pi,\quad \beta_\pm = \Gamma_\pm\kappa,\quad \Gamma_\pm = \sqrt{2}\frac{\Gamma\left(\frac{3+\nu}{4} \pm \frac{\varepsilon}{2}\right)}{\Gamma\left(\frac{1+\nu}{4} \pm \frac{\varepsilon}{2}\right)}. \tag{3.48}$$

Furthermore, at $\varepsilon = 0$ and $\kappa = \kappa_0$ we have $F_+ = F_- = F_0$, $\alpha_+ = \alpha_- = \alpha_0$, and $\beta_+ = \beta_- = \beta_0$, with,

$$F_0 = \frac{\Gamma\left(\frac{1+\nu}{4}\right)}{2^{\frac{1-\nu}{4}}\sqrt{\pi}},\quad \alpha_0 = \frac{1-\nu}{4}\pi,\quad \beta_0 = \Gamma_0\kappa_0,\quad \Gamma_0 = \sqrt{2}\frac{\Gamma\left(\frac{3+\nu}{4}\right)}{\Gamma\left(\frac{1+\nu}{4}\right)}, \tag{3.49}$$

where $\Gamma_0 \in]0.8, 1.5[$ for $\nu \in]1,3[$. We can thus write the previous terms involving parabolic cylinder functions at zero bias as,

$$\tilde{G}_0 = F_0\cos(\alpha_0+\beta_0),\quad \tilde{H}_0 = F_0\cos(\alpha_0-\beta_0), \tag{3.50}$$

$$\partial_\kappa\tilde{G}_0 = -F_0\Gamma_0\sin(\alpha_0+\beta_0),\quad \partial_\kappa\tilde{H}_0 = +F_0\Gamma_0\sin(\alpha_0-\beta_0), \tag{3.51}$$

so that the dimensionless zero-energy secular equation (3.40) becomes,

$$A_0(\cos 2\alpha_0 + \cos 2\beta_0) + B_0\Gamma_0^2(\cos 2\beta_0 - \cos 2\alpha_0) + 2D_0\Gamma_0\sin 2\alpha_0 = 0. \tag{3.52}$$

Solving the above equation for β_0 and using the relation $\kappa_0 = \beta_0/\Gamma_0$, we finally obtain the following analytical result,

$$\kappa_0 = \frac{1}{2\Gamma_0}\arccos\frac{(B_0\Gamma_0^2 - A_0)\cos 2\alpha_0 - 2D_0\Gamma_0\sin 2\alpha_0}{B_0\Gamma_0^2 + A_0}. \tag{3.53}$$

As we said, the asymptotic form of the parabolic cylinder function (3.44) is valid if $\kappa_0 \ll 1$. From the above formula of κ_0, we have $\kappa_0 \ll 1$ if the argument of the arccos is close to unity, which is true if $\cos 2\alpha_0 \to -1$, $\sin 2\alpha_0 \to 0$, and $B_0 \to 0$. This is satisfied if $\nu \to 3$ and $(m_{SC}\hbar\omega_c)/(m_{QH}\mu_{SC}) \ll 1$. Note that this is the only physical case leading to $\kappa_0 \ll 1$ as the other possible limits don't respect the energy scale (3.28). Using the limits given above and the energy scale (3.28) we can simplify κ_0 as done below in Eq. (3.57).

Velocity v Let's work with the dimensionless velocity $\tilde{v}$ introduced in Eq. (3.39) which is related to v through the relation $v = \tilde{v}\sqrt{2}l_B\omega_c$. In order to simplify the ε and κ derivatives involved in the dimensionless secular equation (3.35) we neglect the energy and momentum dependencies of the momentum q, $q \simeq k_{F,sc}\sqrt{1+i\Delta/\mu_{sc}}$, such that we only need to differentiate the parabolic cylinder functions to calculate $\tilde{v}$. Moreover, we also consider $F_\pm \simeq F_0$ and $\Gamma_\pm \simeq \Gamma_0$ and we obtain

$$\tilde{v} = \frac{B_0\Gamma_0^2 + A_0}{\frac{\pi}{2\Gamma_0}(B_0\Gamma_0^2 + A_0) + \frac{1}{\delta}C_0}. \tag{3.54}$$

The calculation details are provided in App. D.1.

We have obtained analytical formulas for k_0 and v by using an asymptotic form of the parabolic cylinder functions but the results remain complicated. In the following we perform successive assumptions allowing us to write simpler results and, in particular, to recover the definition of the effective chemical potential $\mu_{eff} = -vk_0$ given in [van Ostaay *et al.* 2011, Eq. (A28)].

Simplified formulas As first simplifications we consider $Z \ll 1$ and we use the relation $\Delta \ll \mu_{SC}$ coming from our energy scale (3.28) such that $q_0 \simeq k_F^{SC}$. This leads to the simplified formulas,

$$\kappa_0 = \frac{1}{2\Gamma_0}\arccos\frac{\left(\frac{m_{SC}\hbar\omega_c}{m_{QH}\mu_{SC}}\Gamma_0^2 - 1\right)\cos 2\alpha_0 - \sqrt{\frac{m_{SC}\hbar\omega_c}{m_{SC}\mu_{SC}}}\frac{\Delta}{\mu_{SC}}\Gamma_0 \sin 2\alpha_0}{\frac{m_{SC}\hbar\omega_c}{m_{QH}\mu_{SC}}\Gamma_0^2 + 1}, \tag{3.55}$$

$$\tilde{v} = \frac{\frac{m_{SC}\hbar\omega_c}{m_{QH}\mu_{SC}}\Gamma_0^2 + 1}{\frac{\pi}{2\Gamma_0}\left(\frac{m_{SC}\hbar\omega_c}{m_{QH}\mu_{SC}}\Gamma_0^2 + 1\right) + \frac{\hbar\omega_c}{\Delta}\sqrt{\frac{m_{SC}\hbar\omega_c}{m_{QH}\mu_{SC}}}}. \tag{3.56}$$

From these relations we observe that the velocity of the CAES increases with the superconducting gap. We then use the condition $(m_{SC}\hbar\omega_c)/(m_{QH}\mu_{SC}) \ll 1$ imposed by $\kappa_0 \ll 1$ and we get,

$$\kappa_0 = \frac{\pi}{2\Gamma_0}\frac{3-\nu}{2}, \tag{3.57}$$

$$\tilde{v} = \frac{2\Gamma_0}{\pi}, \tag{3.58}$$

where we have taken, $\frac{1}{2\Gamma_0}\arccos(-\cos 2\alpha_0) = \frac{1}{2\Gamma_0}(2\alpha_0 + \pi)$, by using the relation, $\arccos[-\cos(x)] = x + \pi$, which is valid for $x \in [-\pi, 0]$. These last results can also be obtained by taking the limit $Z \to \infty$ in the general formulas (3.53, 3.54) and so they correspond to the case of a QH-vacuum interface. From these results we can write the effective chemical potential of the CAES, $\mu_{eff} = -\hbar v k_0 = -\tilde{v}\kappa_0\hbar\omega_c$, as

$$\mu_{eff} = \frac{\nu - 3}{2}\hbar\omega_c, \tag{3.59}$$

which recovers the result of Ref. [van Ostaay *et al.* 2011, Eq. (A28)].

3.3.3 Electron and hole contents at zero-bias

As they will be useful later, we now compute the electron and hole contents at the zero-bias crossings respectively defined by,

$$f_e^\pm = \int_x |u_0(x)|^2 \mathrm{d}x, \quad f_h^\pm = \int_x |v_0(x)|^2 \mathrm{d}x = 1 - f_e^\pm, \tag{3.60}$$

where the label 0 stands for $E = 0$ and the index $\pm$ denotes the quasi-electron/quasi-hole crossing where $k_y = \mp k_0$. Due to particle-hole symmetry we have $f_e^\pm = f_h^\mp$. Here $u_0(x)$ and $v_0(x)$ are respectively the electron and hole components of the zero-bias wave function,

$$\psi_0(x) = \begin{pmatrix} u_0(x) \\ v_0(x) \end{pmatrix} = \begin{cases} \psi_0^{QH}(x) = \begin{pmatrix} u_0^{QH}(x) \\ v_0^{QH}(x) \end{pmatrix} = a_0 \begin{pmatrix} 1 \\ 0 \end{pmatrix} \chi_+^0(x) + b_0 \begin{pmatrix} 0 \\ 1 \end{pmatrix} \chi_-^0(x) & \text{if } x < 0 \\ \psi_0^{SC}(x) = \begin{pmatrix} u_0^{SC}(x) \\ v_0^{SC}(x) \end{pmatrix} = d_0^+ \begin{pmatrix} i \\ 1 \end{pmatrix} \phi_0(x) + d_0^- \begin{pmatrix} -i \\ 1 \end{pmatrix} \phi_0^*(x) & \text{if } x > 0 \end{cases}, \tag{3.61}$$

with $\phi_0(x) = \sqrt{2\mathrm{Im}\{q_0\}}e^{iq_0x}$ and,

$$\chi^0_\pm(x) = N^0_\pm U^0_\pm(x), \quad U^0_\pm(x) = U\left(-\frac{\mu_{qh}}{\hbar\omega_c}, -\frac{\sqrt{2}}{l_B}(x \mp k_y l_B^2)\right), \quad N^0_\pm = \left[\int_{-\infty}^{0} |U^0_\pm(x)|^2 \mathrm{d}x\right]^{-1/2}. \tag{3.62}$$

To compute the electron and hole contents we need to determine the constants a_0, b_0 and $d_0^\pm$. For this purpose we use the matching procedure (3.29) and the normalization condition $\int_x |\psi_0(x)|^2 \mathrm{d}x = 1$. We obtain $|b_0| = \left(1 + |\alpha_0|^2 + 2|\delta_0^+|^2 + 2|\delta_0^-|^2\right)^{-1/2}$ with $\alpha_0 = a_0/b_0 = -c_0H_0/g_0$ and $\delta_0^\pm = d_0^\pm/b_0 = H_0(g_0 \pm ic_0G_0)/(2g_0\sqrt{2q_0''})$. We used the shorthand notations defined in Eq. (3.31) and we introduced $g_0 = G_0' + d_0G_0$ and $q_0'' = \mathrm{Im}\{q_0\}$. It follows $|b_0|^2 = g_0^2\left\{g_0^2 + c_0^2H_0^2\left[1 + \left(G_0^2 + g_0^2/c_0^2\right)/(2q_0)\right]\right\}^{-1}$. We then write the electron and hole densities as,

$$|u_0(x)|^2 = |u_0^{QH}(x)|^2\Theta(-x) + |u_0^{SC}(x)|^2\Theta(x), \tag{3.63}$$
$$|v_0(x)|^2 = |v_0^{QH}(x)|^2\Theta(-x) + |v_0^{SC}(x)|^2\Theta(x), \tag{3.64}$$

with,

$$|u_0^{QH}(x)|^2 = |b_0|^2|\alpha_0|^2|\chi^0_+(x)|^2, \tag{3.65}$$
$$|u_0^{SC}(x)|^2 = 2|b_0|^2|\delta_0|^2\ \left(|\phi_0(x)|^2 - 2q_0''\mathrm{Re}\{(g_0 + ic_0G_0)/(g_0 - ic_0G_0)e^{2iq_0x}\}\right), \tag{3.66}$$
$$|v_0^{QH}(x)|^2 = |b_0|^2|\chi^0_-(x)|^2, \tag{3.67}$$
$$|v_0^{SC}(x)|^2 = 2|b_0|^2\ |\delta_0|^2\left(|\phi_0(x)|^2 + 2q_0''\mathrm{Re}\{(g_0 + ic_0G_0)/(g_0 - ic_0G_0)e^{2iq_0x}\}\right), \tag{3.68}$$

where we have used $|\delta_0^+| = |\delta_0^-| = |\delta_0|$. Performing the integrals we can finally write the electron and hole contents as,

$$f_h^\pm = 1 - f_e^\pm \tag{3.69}$$
$$= 1 - c_0^2H_0^2\left\{1 + \frac{1}{4q_0''}\left[G_0^2 + \frac{1}{|q_0|^2}\left(\frac{m_{SC}}{m_{QH}}g_0 + q_0''G_0\right)^2\right]\right\}\left\{g_0^2 + c_0^2H_0^2\left[1 + \frac{1}{2q_0''}\left(G_0^2 + \frac{g_0^2}{c_0^2}\right)\right]\right\}^{-1}, \tag{3.70}$$

and we recall that the index $\pm$ stands for $k_y = \mp k_0$. In the limit $\Delta \to 0$ we have an equal repartition between electron and hole components, $f_h^+ = f_h^- = 1/2$, and in the limit $Z \to \infty$ we recover the pure electron and hole states with $f_h^+ = 0$ and $f_h^- = 1$. As illustrative examples, we plot the electron and hole densities in Fig. 3.10a and we represent the evolution of the hole content f_h^+ of the quasi-electron CAES as a function of the barrier strength Z for various values of the filling factor ν in Fig. 3.10b.

3.4 Tight-binding simulations

The main goal of this section is to compute the Andreev conversion probabilities τ_i introduced in Sec. 3.2 to compute the downstream conductance. To do so, we use a lattice model and we perform tight-binding simulations by using the Kwant software [Groth *et al.* 2014].

3.4.1 The tight-binding Hamiltonian

We obtain the tight-binding Hamiltonian by discretizing the continuous Hamiltonian (3.15) on a square lattice with lattice spacing a. (Details on the discretization procedure are provided in App. C.) Considering $m_{QH} = m_{SC} = m$ and introducing the Nambu spinor $\Psi_i = (c_i, c_i^\dagger)^T$, where $c_i^\dagger$ (c_i) is the operator that creates (annihilates) an electron at position $\vec{r}_i = (x_i, y_i)$, the second-quantized tight-binding Hamiltonian reads,

$$\mathcal{H}_{TB} = \sum_i \psi_i^\dagger\left[(4t - \mu_i + V_i)\sigma_z + \Delta_i\sigma_x\right]\psi_i + \sum_{\langle i,j\rangle}\psi_i^\dagger\left[te^{i\phi_{ij}\sigma_z}\sigma_z\right]\psi_j, \tag{3.71}$$

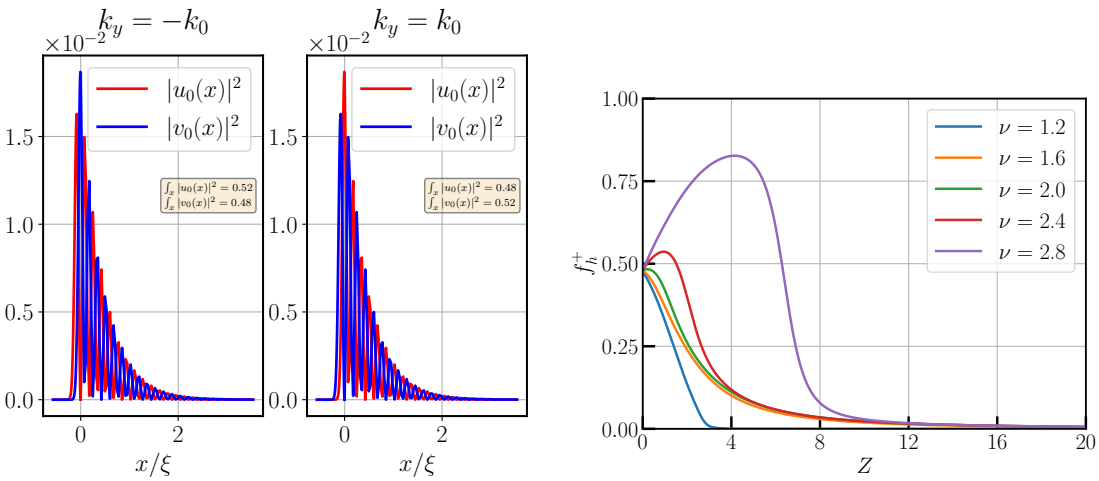

(a) (b)

Figure 3.10: (a) Transverse electron and hole densities at the quasi-electron and quasi-hole crossings as a function of x/ξ with $m_{QH} = m_{SC}$, $\mu_{QH} = \mu_{SC} = 10\Delta$, $\nu = 2$ and $Z = 0$. Due to particle hole symmetry, the values of the $|u|^2$ and $|v|^2$ are exchanged from one crossing to the other. (b) Hole content f_h^+ of the quasi-electron CAES versus the barrier's strength Z for various values of the filling factor with $m_{QH} = m_{SC}$ and $\mu_{QH} = \mu_{SC} = 10\Delta$. While at $Z = 0$ the hole content is close to $1/2$, it vanishes as $Z \gg 1$. Interestingly it is enhanced in an intermediate region for $\nu > 2$.

where $\sigma_{x/z}$ are Pauli matrices in Nambu space, and $\langle i, j \rangle$ denotes pairs of nearest neighbor sites. The barrier potential is $V_i = V_0 \delta_{x_i,0} \Theta(L/2 - |y_i|)$, where L is the length of the QH-SC interface, and $\delta_{i,j}$ is the Kronecker delta. In the QH region we set $\mu_i = \mu_{QH}$ and $\Delta_i = 0$ while in the SC region we have $\mu_i = \mu_{SC}$ and $\Delta_i = \Delta$. Using a Peierls substitution (see App. C), the hopping matrix element $t = \hbar^2/(2ma^2)$ acquires a field-dependent phase as in Eq. (2.128),

$$\phi_{ij} = -\frac{\pi B}{\phi_0}(x_i + x_j)(y_j - y_i)\Theta\left(-\frac{x_i + x_j}{2}\right). \tag{3.72}$$

As shown in App. D.2.1, this lattice model matches the continuum model well as long as the hopping energy t is the largest energy scale. In particular, we assume $\Delta \ll \mu_{QH} \leq \mu_{SC} \ll t$. When not specified, we set $t = 1$ and $\mu_{SC} = t/20$.

3.4.2 Energy spectrum and probability density

Before looking at the scattering properties of the junction, we want to check that we recover the energy spectrum obtained in the continuous model. To compute the energy spectrum with Kwant we construct an infinite QH-SC strip with $-L_{QH} \leq x \leq L_{SC}$ (see Fig. 3.11). The energy spectrum obtained from the tight-binding model provides more informations. Indeed, it allows to observe the edge states propagating along the QH-vacuum interface located at $x = -L_{QH}$ and to access out-gap energies $|E| > \Delta$. This can be seen from Fig. 3.12 where we represent the tight-binding spectrum and the comparison with the continuum model. From the tight-binding spectrum we observe three of the QH bulk Landau levels as well as the gapped bands of the SC bulk. There are four crossings at zero-energy: the two previously studied CAES close to $|k_y l_B| = 1$ and the electron and hole propagating along the QH-vacuum interface. Since the Landau levels for electrons (holes) are bent upward (downward), we can identify the Landau levels for negative (positive) momenta as being electron-like (hole-like). This coincides with our previous statement saying that the crossing at $k_y = -k_0$ $(+k_0)$ is a quasi-electron (quasi-hole). We find a good agreement between the continuum and lattice models as long as $L_{QH} \geq 4l_B$ and $L_{SC} \geq 4\xi$ (see App. D.2.1).

In order to illustrate the interference of CAES along the QH-SC interface and the Andreev conversion from the upstream to the downstream reservoir we plot the probability density $|u(\vec{r})|^2 - |v(\vec{r})|^2$ of an incoming electron in Fig. 3.13. Here we have chosen the length of the QH-SC interface such that the incoming electron mostly exits the superconductor as a hole.

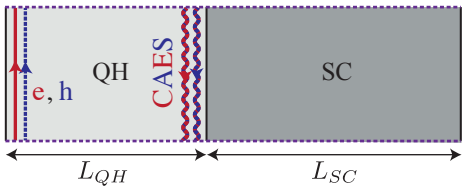

Figure 3.11: Infinite QH-SC strip used to compute the tight-binding spectrum.

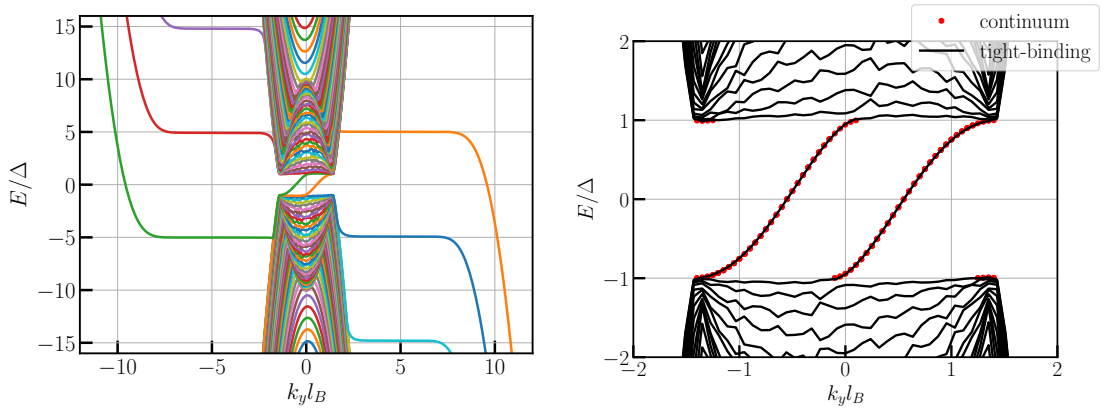

(a) (b)

Figure 3.12: (a) Tight-binding spectrum electron-like (hole-like) bulk Landau levels bending upward (downward). (b) Comparison with the continuum model. The parameters are $\mu_{QH} = \mu_{SC} = 10\Delta$, $\nu = 2$, and $Z = 0$.

3.4.3 Corner Andreev conversion τ

As the conversion probability from electron to quasi-hole at the first corner is equal to the conversion probability from quasi-electron to hole at the second corner when parameters are chosen the same [Khaymovich *et al.* 2010], $\tau_1(\theta_{QH}, \theta_{SC}) = \tau_2(\theta_{QH}, \theta_{SC}) \equiv \tau(\theta_{QH}, \theta_{SC})$, it is sufficient to simulate the first QH-SC corner. To simulate the first corner we construct a semi-infinite QH-SC interface by using a hybrid reservoir as depicted in Fig. 3.14. Before studying the behavior of τ we present how to compute all the scattering matrix elements of the single-corner system with Kwant.

3.4.3.1 Method to compute the scattering matrix elements with Kwant and choice of the dimensions

We can obtain the scattering matrix of a Kwant system at a given energy by using the routine $smatrix = kwant.smatrix(system, energy)$. Because we are interested in the zero-bias conductance we compute the scattering matrix at zero-energy. Denoting the upstream and hybrid leads represented in Fig. 3.14 by 0 and 1 respectively, we write the scattering matrix in the basis of the leads as,

$$S = \begin{pmatrix} R_0 & T_{01} \\ T_{10} & R_1 \end{pmatrix}, \tag{3.73}$$

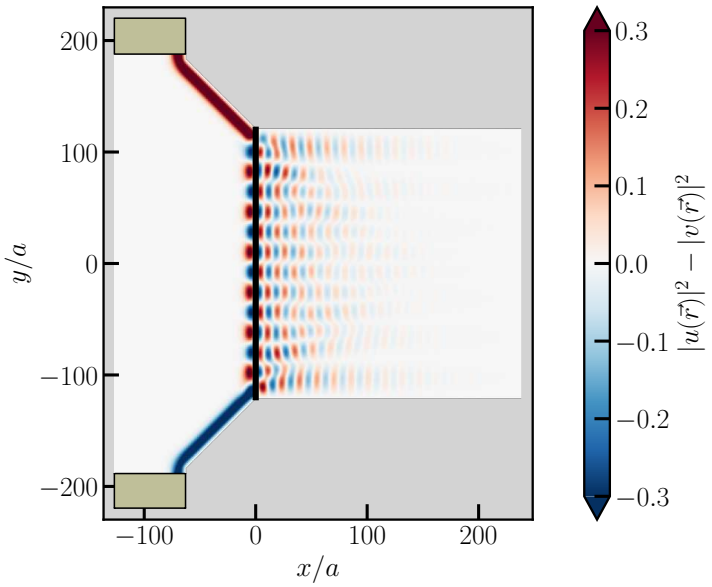

Figure 3.13: Probability density $|u(\vec{r})|^2 - |v(\vec{r})|^2$ of an incoming electron state at $E = 0$ for $\theta_{1,2}^{QH} = 45°$ and $\theta_{1,2}^{SC} = 90°$. The interference of CAES along the QH-SC interface (black line) can be clearly seen. As indicated by the blue color, the outgoing particle is mostly a hole. The parameters are $\mu_{QH} = \mu_{SC} = 10\Delta$, $\nu = 2$, and $Z = 0$.

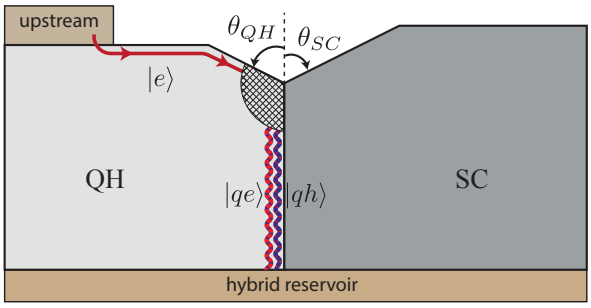

Figure 3.14: Single-corner system characterized by the angles θ_{QH} and θ_{SC}. We have represented the situation where an incoming electron propagates as a quasi-electron or as a quasi-hole along an infinite QH-SC interface after scattering at the corner. The infinite interface is materialized by the hybrid reservoir.

where T_{ji} is the transmission matrix from lead i to lead j and R_i is the reflection matrix in lead i ($R_i = T_{ii}$). To obtain the transmission matrices T_{ji} in Kwant, one has to use the routine, $T_{ji} = smatrix.submatrix(j,i)$. Moreover, these reflection and transmission matrices are related to the wave functions in the leads through the relation,

$$\psi_{in,j} = R_j \psi_{out,j} + \sum_{i \neq j} T_{ji} \psi_{out,i}, \tag{3.74}$$

where $\psi_{in,i}$ is the wave function of the modes entering in lead i and $\psi_{out,i}$ describes the modes leaving lead i. For our two-lead system we thus have,

$$\psi_{in,0} = R_0 \psi_{out,0} + T_{01} \psi_{out,1}, \tag{3.75}$$

$$\psi_{in,1} = R_1 \psi_{out,1} + T_{10} \psi_{out,0}. \tag{3.76}$$

To know the explicit form of the reflection and transmission matrices we thus have to know the form of the wave functions in the leads. In Kwant, one can use a conservation law to order the wave functions. Internally, Kwant then uses the eigenvectors of the conservation law to block diagonalize the Hamiltonian. In lead 0 (QH lead) we use the charge conservation $-\sigma_z$, such that the eigenvectors with eigenvalues -1 and 1 pick out the electron and hole blocks, respectively. This leads to wave functions of the form (e,h) in lead 0,

$$\psi_{in,0} = \begin{pmatrix} e \\ h \end{pmatrix}, \ \psi_{out,0} = \begin{pmatrix} e \\ h \end{pmatrix}. \tag{3.77}$$

In the hybrid lead we cannot use such a conservation law and the wave functions are ordered by default in the following way: first all the modes with negative velocity (i.e. those leaving the lead), then all the modes with positive velocity (i.e. those entering the lead), where the negative velocity modes are ordered by increasing momentum while the positive velocity modes are ordered by decreasing momentum.

Without additional non-chiral edge states, the wave functions in lead 1 are thus ordered as follows (see the tight-binding spectrum in Fig. 3.12a),

$$\psi_{in,1} = \begin{pmatrix} qh \\ qe \end{pmatrix}, \ \psi_{out,1} = \begin{pmatrix} e \\ h \end{pmatrix}, \tag{3.78}$$

and the reflection and transmission matrices are given by,

$$R_0 = \begin{pmatrix} r^0_{ee} & r^0_{eh} \\ r^0_{he} & r^0_{hh} \end{pmatrix}, \ T_{01} = \begin{pmatrix} t^{01}_{ee} & t^{01}_{eh} \\ t^{01}_{he} & t^{01}_{hh} \end{pmatrix}, \ T_{10} = \begin{pmatrix} t^{10}_{qh,e} & t^{10}_{qh,h} \\ t^{10}_{qe,e} & t^{10}_{qe,h} \end{pmatrix}, \ R_1 = \begin{pmatrix} r^1_{qh,e} & r^1_{qh,h} \\ r^1_{qe,e} & r^1_{qe,h} \end{pmatrix}, \tag{3.79}$$

and, if only chiral edge states are present, we must have $R_0 = R_1 = 0$. Moreover, because the states going from lead 1 to lead 0 propagate along a QH-vacuum interface, there is no Andreev reflection in this process so that $t^{01}_{eh} = t^{01}_{he} = 0$. These statements are easily checked by looking at the scattering matrix returned by Kwant.

As discussed in Sec. 3.3.2.2, additional non-chiral edge states can cross the Fermi level in the spectrum of the hybrid lead. If so, we must analyze carefully the energy spectrum in order to determine the form of the wave functions. This is done in Fig. 3.15a. Denoting the additional non-chiral edge states as $\tilde{e}$ and $\tilde{h}$, the wave functions in the hybrid reservoir read,

$$\psi_{in,1} = \begin{pmatrix} \tilde{h} \\ qh \\ qe \\ \tilde{e} \end{pmatrix}, \ \psi_{out,1} = \begin{pmatrix} e \\ \tilde{e} \\ \tilde{h} \\ h \end{pmatrix}, \tag{3.80}$$

and the reflection and transmission matrices take the following form,

$$T_{01} = \begin{pmatrix} t^{01}_{ee} & t^{01}_{e\tilde{e}} & t^{01}_{e\tilde{h}} & t^{01}_{eh} \\ t^{01}_{he} & t^{01}_{h\tilde{e}} & t^{01}_{h\tilde{h}} & t^{01}_{hh} \end{pmatrix}, \ T_{10} = \begin{pmatrix} t^{10}_{\tilde{h}e} & t^{10}_{\tilde{h}h} \\ t^{10}_{qh,e} & t^{10}_{qh,h} \\ t^{10}_{qe,e} & t^{10}_{qe,h} \\ t^{10}_{\tilde{e}e} & t^{10}_{\tilde{e}h} \end{pmatrix}, \ R_1 = \begin{pmatrix} r^1_{\tilde{h}e} & r^1_{\tilde{h}\tilde{e}} & r^1_{\tilde{h}\tilde{h}} & r^1_{\tilde{h}h} \\ r^1_{qh,e} & r^1_{qh,\tilde{e}} & r^1_{qh,\tilde{h}} & r^1_{qh,h} \\ r^1_{qe,e} & r^1_{qe,\tilde{e}} & r^1_{qe,\tilde{h}} & r^1_{qe,h} \\ r^1_{\tilde{e}e} & r^1_{\tilde{e}\tilde{e}} & r^1_{\tilde{e}\tilde{h}} & r^1_{\tilde{e}h} \end{pmatrix}, \tag{3.81}$$

while we still have $R_0 = 0$. We can then predict which matrix elements will be non-zero with the following arguments. First, since the non-chiral states exist only along the superconducting interface, and since there are no Andreev processes along the interface with the vacuum, the non-zero matrix elements of T_{01} are t^{01}_{ee} and t^{01}_{hh}. Second, all matrix elements of T_{10} can be non-zero because an incoming electron or hole can be converted into any kind of quasiparticle along the QH-SC interface. Finally, the non-zero elements of the reflection matrix R_1 are those that include the non-chiral edge states, since by definition chiral states are never reflected. The non-zero matrix elements of R_1 are thus $r_{\alpha\tilde{e}}$ and $r_{\alpha\tilde{h}}$, with $\alpha = \{\tilde{e}, \tilde{h}, qe, qh\}$. We can thus sketch the edge modes in the presence of additional non-chiral edge states as in Fig. 3.15b.

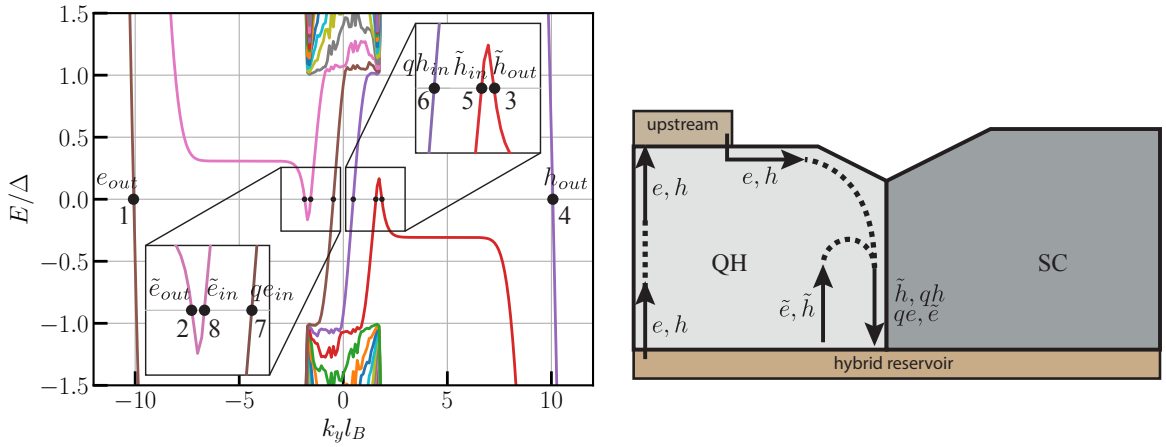

(a) (b)

Figure 3.15: (a) Energy spectrum in the hybrid lead in the presence of non-chiral zero-energy states. The modes with negative velocity are leaving the lead (*out*) while those with positive velocity are entering in the lead (*in*). We have ordered the modes (1, 2, 3, 4, 5, 6, 7, 8) as they are sorted by Kwant. (b) Sketch of the modes in the presence of non-chiral edge states. The parameters used to plot the energy spectrum are $\mu_{QH} = \mu_{SC} = \Delta/10$, $\nu = 2.9$, and $Z = 0$.

We are now able to compute the Andreev conversion at a single corner, $\tau = |t^{10}_{qh,e}|^2$, and we now give the dimensions of the system for which the value of τ has converged. In Fig. 3.16 we represent the dimensions that come into play in defining the system. We show two cases: $\theta_{QH}, \theta_{SC} < 90°$ (Fig. 3.16a) and : $\theta_{QH}, \theta_{SC} > 90°$ (Fig. 3.16b). The QH and SC regions are each separated into two parts: a part close to the QH-SC interface, characterized by the angle θ_{QH} for the QH region and by θ_{SC} for the SC region, and a rectangular part that extends the QH and SC regions to the left and right, respectively. We define the system with such rectangular regions because it is easier to implement. The parts near the QH-SC interface are delimited by L, $L^1_{QH,SC}$, $W_{QH,SC}$ and $L_{\theta_{QH},\theta_{SC}}$, while the rectangular parts are bounded by $W_{QH,SC}$ and $L^2_{QH,SC}$. Note that the lengths L_{QH} and L_{SC} represented in Fig. 3.18 are given by $L_{QH} = L^1_{QH} + L^2_{QH}$ and $L_{SC} = L^1_{SC} + L^2_{SC}$. These dimensions must be sufficiently large to obtain a value of τ that has converged.

We have shown in App. D.2.2 that the value of τ has converged if we set $L_{QH} = 40 l_B$, $L_{SC} = 6\xi$, $L_{\theta_{QH}} = 18 l_B$, $L^{\theta_{SC}\leq 90°}_{\theta_{SC}} = 2\xi$, $L^{\theta_{SC}>90°}_{\theta_{SC}} = 60 l_B$, $L^{\theta_{SC}\leq 90°} = 20 l_B$, and $L^{\theta_{SC}>90°} = 80 l_B$.

In the following we investigate the geometry and filling factor dependencies of τ.

3.4.3.2 Geometry and filling factor dependencies

Before we study the geometrical and filling factor dependencies of τ, which are the most interesting ones, let us discuss the other parameter dependencies.

We have studied in detail the dependence of τ on t/μ_{SC}, μ_{QH}/Δ, μ_{SC}/μ_{QH}, and Z in App. D.3. For ideal interfaces ($\mu_{QH} = \mu_{SC}$, $Z = 0$) with $\theta_{SC} \leq 90°$, we showed that τ becomes approximately constant

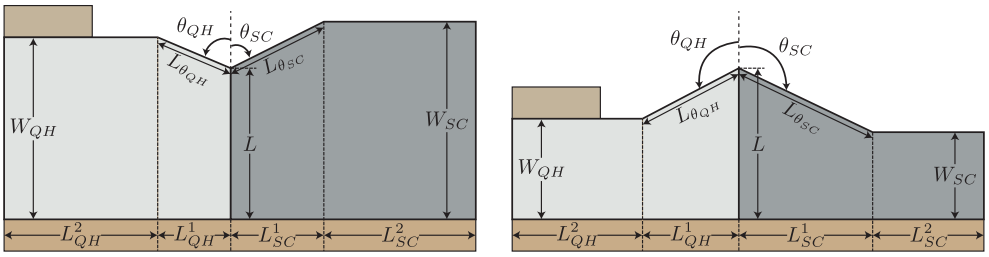

Figure 3.16: System dimensions with (a) $\theta_{QH}, \theta_{SC} < 90°$ and (b) $\theta_{QH}, \theta_{SC} > 90°$.

when $t/\mu_{SC} \gtrsim 20$ and $\mu_{QH}/\Delta \gtrsim 5$, in agreement with the analytical results of Sec. 3.3.3, which show that the properties of the edge states are almost independent of Δ in the considered parameter regime. On the other hand, when $\theta_{SC} > 90°$, the decay length of the edge state in the superconductor plays a more important role. Since the decay can reach the superconductor-vacuum interface, a stronger dependence of τ on Δ, which controls the decay length in the superconductor, is expected. This is especially true for $\theta_{SC} \gg 90°$ and ν close to 1 and 3. For non-ideal interfaces, we observed that increasing μ_{SC}/μ_{QH} decreases the value of τ and that τ vanishes as $Z \gg 1$. Interestingly, we saw that τ is enhanced at intermediate values of Z for $\nu > 2$, as we found for the hole content f_h^+ in Fig. 3.10b.

Hence, for ideal interfaces with $\theta_{SC} \leq 90°$, $t/\mu_{SC} \gtrsim 20$ and $\mu_{QH}/\Delta \gtrsim 5$, the Andreev conversion τ depends only on the corner geometry and the filling factor. In the following we choose $t/\mu_{SC} = 20$ and $\mu_{QH}/\Delta = 10$ to study these dependencies.

In Fig. 3.17 we represent the dependence of τ on θ_{QH} and θ_{SC} for various values of the filling factor with $\mu_{QH} = \mu_{SC} = 10\Delta$ and $Z = 0$. Fig. 3.17a shows the variations with θ_{SC} at $\theta_{QH} = 90°$. We see a weak dependence on θ_{SC} for angles up to 90°. This is not surprising as the propagation of the chiral edge states does not involve the SC-vacuum interface. The residual effect of θ_{SC} on the scattering probability is due to the modified decay of the edge state wave function into the bulk in the vicinity of the corner. We illustrate this in Fig. 3.18 by plotting the probability density $|u|^2 - |v|^2$ of an incoming electron state: it can be seen that it is vanishingly small at angles $< 90°$ within the SC region. By contrast, τ decreases as θ_{QH} is increased. The stronger sensitivity of τ on θ_{QH} can be understood as stemming from the fact that this angle directly determines the propagation direction of the edge state and thus the projection of the momentum of the incoming state onto the direction of the interface.

A more realistic interface is obtained when allowing for different values of μ_{QH} and μ_{SC} as well as for an interface barrier $Z \neq 0$. As an example, we show in Fig. 3.19 the evolution of τ as a function of θ_{QH} with $\mu_{SC} = 2\mu_{QH}$ and $Z = 0.7$. The behavior is qualitatively similar though the variation with angle is less pronounced. The stronger variation with ν reflects the stronger variation of f_h^+ at intermediate values of Z shown in Fig. 3.10b.

This concludes the present section on the tight-binding binding simulations. In the next section we derive an effective model of the junction allowing us to reproduce the effects presented here.

3.5 One-dimensional effective model

Effective one-dimensional models are very useful to obtain a qualitative understanding of the edge state physics. They have been extensively used in recent works [Zhao *et al.* 2020, Hatefipour *et al.* 2022, Kurilovich *et al.* 2022, Schiller *et al.* 2022, Gül *et al.* 2022, Kurilovich & Glazman 2022, Michelsen *et al.* 2023] to describe the CAES. In this section, we address the question how to incorporate the effects discussed above into such an effective model. We will start with the simplest model and show how to modify it in order to reproduce these effects.

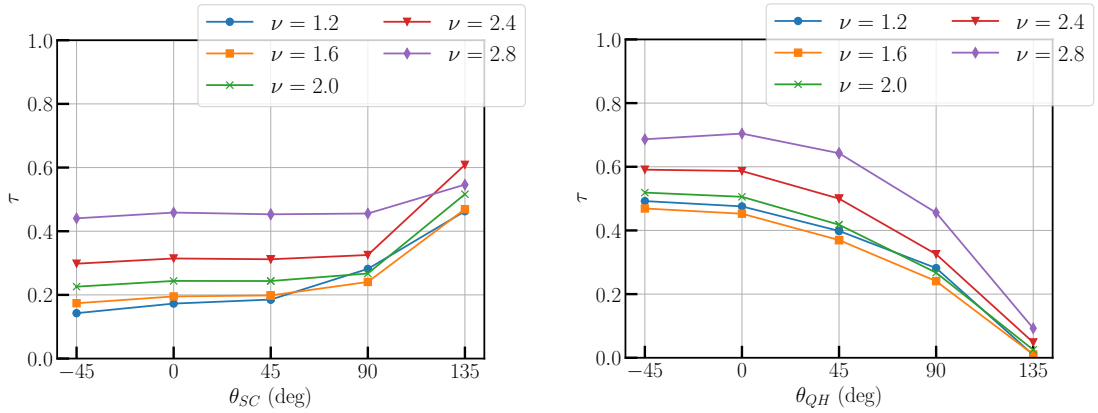

Figure 3.17: Conversion probability τ for various values of the filling factor ν as a function of (a) the SC angle θ_{SC} with $\theta_{QH} = 90°$ and (b) the QH angle θ_{QH} with $\theta_{SC} = 90°$. $\mu_{QH} = \mu_{SC} = 10\Delta$ and $Z = 0$. To minimize lattice effects, we only show commensurate angles. The solid lines are a guide to the eye.

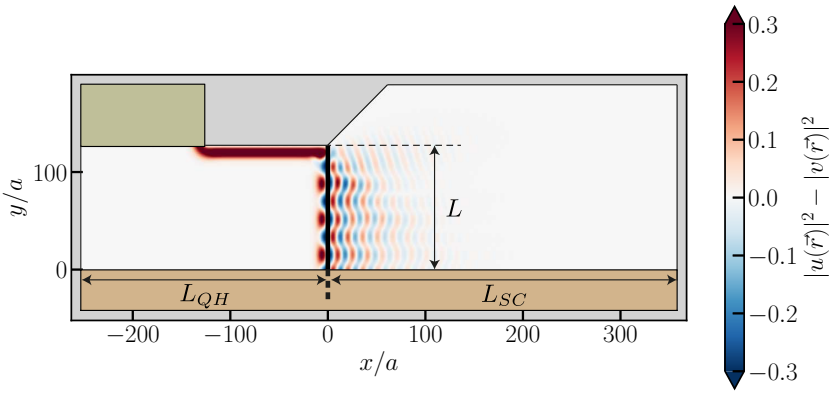

Figure 3.18: Probability density $|u(\vec{r})|^2 - |v(\vec{r})|^2$ of an incoming electron state for $\theta_{SC} = 45°$ and $\theta_{QH} = 90°$. The interference of CAES along the QH-SC interface (black line) can be clearly seen. Note that the wave function does not have any weight in the vicinity of the SC-vacuum boundary. The parameters are $\mu_{QH} = \mu_{SC} = 10\Delta$, $\nu = 2$ and $Z = 0$.

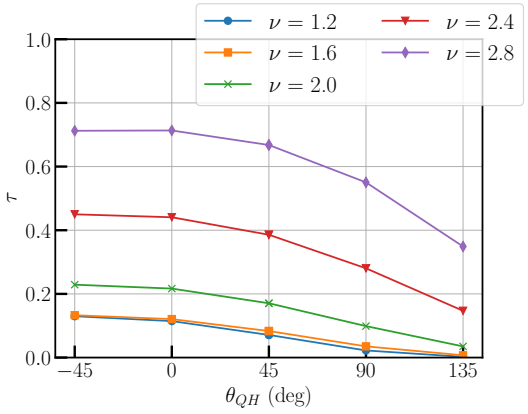

Figure 3.19: Conversion probability τ versus the angle θ_{QH} for a non-ideal interface at various values of ν. Here $\theta_{SC} = 90°$, $\mu_{SC} = 2\mu_{QH} = 20\Delta$, and $Z = 0.7$. As in Fig. 3.17, we only show commensurate angles, and the solid lines are a guide to the eye.

3.5.1 Hamiltonian and wave functions

The starting point is the one-dimensional BdG Hamiltonian,

$$\tilde{H} = \begin{pmatrix} -i\hbar\frac{1}{2}\{\tilde{v}(y), \partial_y\} - \tilde{\mu}(y) & \tilde{\Delta}(y) \\ \tilde{\Delta}^*(y) & -i\hbar\frac{1}{2}\{\tilde{v}(y), \partial_y\} + \tilde{\mu}(y) \end{pmatrix}, \tag{3.82}$$

where y denotes the coordinate along the QH edge, $\tilde{\Delta}(y)$ are the induced superconducting correlations, $\tilde{v}(y)$ is the edge state velocity, and $\tilde{\mu}(y)$ is an effective chemical potential. Furthermore, the anti-commutator $\{.,.\}$ ensures Hermiticity even if the velocity depends on the y-coordinate. We start with the simplest model of a single-corner system as the one depicted in Fig. 3.14 where the change from vacuum to superconducting edge arises at $y = 0$. We choose $\tilde{v}(y) = v_{vac}\Theta(-y) + v\Theta(y)$ and $\tilde{\mu}(y) = \mu_{vac}\Theta(-y) + \mu\Theta(y)$ where v is the CAES velocity introduced in Eq. (3.33). Moreover, the simplest model often used to describe such systems consists of choosing a step function for the induced correlations, $\tilde{\Delta}(y) = \tilde{\Delta}\Theta(y)$. Denoting an eigenvector of the BdG Hamiltonian (3.82) by $\psi(y) = (U(y), V(y))^T$, the Schrödinger equation yields the following system,

$$-i\hbar\left[\tilde{v}U' + \frac{1}{2}\tilde{v}'U\right] + \tilde{\Delta}V = (E + \tilde{\mu})U, \tag{3.83}$$

$$-i\hbar\left[\tilde{v}V' + \frac{1}{2}\tilde{v}'V\right] + \tilde{\Delta}^*U = (E - \tilde{\mu})V. \tag{3.84}$$

Since this system involves derivatives of the velocity, which is a Dirac-delta, the functions $U(y)$ and $V(y)$ are discontinuous and so we cannot use them to perform the matching procedure. To get around this problem, we set

$$U(y) = \frac{\tilde{U}(y)}{\sqrt{\tilde{v}(y)}}, \qquad V(y) = \frac{\tilde{V}(y)}{\sqrt{\tilde{v}(y)}}, \tag{3.85}$$

and the previous system becomes,

$$-i\hbar\tilde{v}\tilde{U}' + \tilde{\Delta}\tilde{V} = (E + \tilde{\mu})\tilde{U}, \tag{3.86}$$

$$-i\hbar\tilde{v}\tilde{V}' + \tilde{\Delta}^*\tilde{U} = (E - \tilde{\mu})\tilde{V}, \tag{3.87}$$

which is the same as before with $\tilde{v}'(y) = 0$ such that $\tilde{U}(y)$ and $\tilde{V}(y)$ are now continuous functions and we can use the wave function $\tilde{\psi}(y) = \left(\tilde{U}(y), \tilde{V}(y)\right)^T$ to perform the matching procedure. The most general

solutions for a superconducting edge with parameters independent of y are given by,

$$\tilde{\psi}(y) = c_1 \begin{pmatrix} u_1 \\ v_1 \end{pmatrix} e^{\lambda_1 y} + c_2 \begin{pmatrix} u_2 \\ v_2 \end{pmatrix} e^{\lambda_2 y}, \tag{3.88}$$

with $c_{1,2}$ constants and,

$$\lambda_{1,2} = \frac{i}{\hbar\tilde{v}} \left(E \pm \sqrt{\tilde{\mu}^2 + |\tilde{\Delta}|^2} \right) = ik_{1,2}, \tag{3.89}$$

$$\begin{pmatrix} u_{1,2} \\ v_{1,2} \end{pmatrix} = \begin{pmatrix} -\frac{1}{|\tilde{\Delta}|} \left(\tilde{\mu} \ \pm \sqrt{\tilde{\mu}^2 + |\tilde{\Delta}|^2} \right) e^{i\arg(\tilde{\Delta})} \\ 1 \end{pmatrix} = \begin{pmatrix} \gamma_{1,2} \\ 1 \end{pmatrix}, \tag{3.90}$$

where we have introduced the momentum of the two modes $\hbar\tilde{v}k_{1,2} = E \pm \sqrt{\tilde{\mu}^2 + |\tilde{\Delta}|^2}$. For a normal edge the solutions are given by,

$$\tilde{\psi}_{vac}(y) = c_1^{vac} \begin{pmatrix} 1 \\ 0 \end{pmatrix} e^{i\frac{E+\mu_{vac}}{\hbar v_{vac}} y} + c_2^{vac} \begin{pmatrix} 0 \\ 1 \end{pmatrix} e^{i\frac{E-\mu_{vac}}{\hbar v_{vac}} y} \ . \tag{3.91}$$

3.5.2 Hole content

Here we use the effective Hamiltonian (3.82) to compute the zero-bias hole content $f_h^{\pm}$ introduced in Sec. 3.3.3 for an infinite QH-SC interface with a real superconducting order parameter. For such an infinite interface with $E = 0$, the normalized wave functions are given by

$$\tilde{\psi}(y) = \frac{1}{\sqrt{1+\gamma_+^2}} \begin{pmatrix} \gamma_+ \\ 1 \end{pmatrix} e^{ik_0 y} + \frac{1}{\sqrt{1+\gamma_-^2}} \begin{pmatrix} \gamma_- \\ 1 \end{pmatrix} e^{-ik_0 y}, \tag{3.92}$$

where have used $\gamma_\pm = (\mu \mp \sqrt{\mu^2 + \tilde{\Delta}^2})/\tilde{\Delta}$ and we have identified the zero-bias momentum $\hbar v k_0 = -\sqrt{\mu^2 + \tilde{\Delta}^2}$. We can then write the hole content as $f_h^{\pm} = 1/(1+\gamma_\pm^2) = \left(1 \pm \mu/\sqrt{\mu^2 + \tilde{\Delta}^2}\right)/2$ and, to match the results of Sec. 3.3, we have to set $\mu = -\hbar v k_0 (1 - 2f_h^+)$ and $\tilde{\Delta} = \hbar v k_0 \sqrt{f_h^+(1-f_h^+)}$.

3.5.3 Andreev conversion τ_0 in the simplest model

In the simplest model of a single corner we consider a QH edge state propagating along an interface with the vacuum for $y < 0$ and along a superconducting interface for $y > 0$. Considering an incoming electron from the vacuum, a real parameter $\tilde{\Delta}$, and $E = 0$, the wave functions are given by,

$$\tilde{\psi}(y) = \begin{cases} \begin{pmatrix} 1 \\ 0 \end{pmatrix} e^{ik_0^{vac} y} & \text{for } y < 0 \\ \frac{t_{qe,e}}{\sqrt{1+\gamma_+^2}} \begin{pmatrix} \gamma_+ \\ 1 \end{pmatrix} e^{ik_0 y} + \frac{t_{qh,e}}{\sqrt{1+\gamma_-^2}} \begin{pmatrix} \gamma_- \\ 1 \end{pmatrix} e^{-ik_0 y} & \text{for } y > 0 \end{cases}, \tag{3.93}$$

where we have introduced $k_0^{vac} = \mu_{vac}/(\hbar v_{vac})$. The matching of the wave functions at $y = 0$ yields the conversion probability of an electron into a quasi-hole,

$$\tau_0 = f_h^+. \tag{3.94}$$

This clearly is not sufficient to correctly describe the scattering – if only because it doesn't depend on the geometry of the contact point. To obtain a conversion probability $\tau \neq \tau_0$, one needs to include a spatial variation of the induced correlations $\tilde{\Delta}(y)$ in the vicinity of $y = 0$. This is the aim of the next section.

3.5.4 Andreev conversion τ in a modified model with a barrier region

We consider a more general model with a barrier region, $-L_b/2 < y < L_b/2$, characterized by the parameters $\tilde{v}(y) = v_b$, $\tilde{\mu}(y) = \mu_b$, and $\tilde{\Delta}(y) = \Delta_b e^{i\phi_b}$. Note that the relative superconducting phase between the barrier and the bulk is allowed as time-reversal symmetry is broken by the applied field. Solving the Schrödinger equation in the three regions (QH-vacuum interface at $y < -L_b/2$, barrier, and QH-SC interface at $y > L_b/2$), matching the solutions at $y = \pm L_b/2$, and solving the resulting system, we obtain,

$$\tau = \left(\sqrt{\tau_0}\cos\beta_b + \sqrt{1-\tau_0}\sin\beta_b\right)^2 - 4\sqrt{\tau_0(1-\tau_0)}\sin\beta_b\cos\beta_b\cos^2\frac{\phi_b-\delta_b}{2}, \tag{3.95}$$

with $\alpha_b = \sqrt{\mu_b^2+\Delta_b^2}L_b/v_b$, $\sin\beta_b = \sin\alpha_b\,\Delta_b/\sqrt{\mu_b^2+\Delta_b^2}$, and $\tan\delta_b = \cot\alpha_b\sqrt{\mu_b^2+\Delta_b^2}/\mu_b$. This model has sufficient parameters to obtain an arbitrary value of τ for a given τ_0. Thus, in principal, this effective one-dimensional model can be used to describe an arbitrary geometry. However, there is no straightforward way to estimate the barrier parameters.

3.6 Downstream conductance at zero and finite temperatures

We are now in a position to compute the downstream conductance introduced in Sec. 3.2. We first give the zero temperature results and then we look at finite temperatures.

3.6.1 Zero-temperature results

We show in Fig. 3.20 the downstream conductance derived in Eq. (3.3) as a function of the length of the QH-SC interface obtained from a full tight-binding simulation of the structure shown in Fig. 3.1. Here the same parameters were used as in Fig. 3.19 with $\nu = 2.8$. It is compared with the result of the effective 1D model, where we set $L_b = \xi/10$, $v_b = v$, and $\mu_b = \mu_{SC}$. We use a numerical minimization procedure to find the values of Δ_b and ϕ_b that give the scattering probabilities τ_1 and τ_2 obtained from the tight-binding model. Fitting parameters for Fig. 3.20 are $\Delta_{b1} = 10.08\Delta$, $\phi_{b1} = 3.382$ and $\Delta_{b2} = 0.32\Delta$, $\phi_{b2} = 3.002$. (Note that this choice is not unique.) In addition, we adjust the scattering phase ϕ_{12} appearing in Eq. (3.14) so that the effective model matches the simulation at large L. A small mismatch between the values of k_0 can be attributed to lattice effects. Furthermore, deviations are visible at small lengths when the two corners cannot be treated as independent as assumed in Eq. (3.14). In particular, we need $L, W_{QH} \geq 2l_B$ for the downstream conductance to start to develop (W_{QH} being the width of the QH region introduced in Fig. 3.1).

3.6.2 Finite-temperature results

We now use Kwant to compute the finite-temperature downstream conductance [Datta 1997],

$$G_d(T) = G_0\int dE\frac{1-2P_h(E)}{4k_BT\cosh^2\left(\frac{E}{2k_BT}\right)} \approx G_0\int_{-\Delta}^{\Delta} dE\frac{1-2P_h(E)}{4k_BT\cosh^2\left(\frac{E}{2k_BT}\right)}, \tag{3.96}$$

where $P_h(E)$ is given in Eq. (3.14) and the approximation is valid as long as $k_BT \ll \Delta$ [this formula is analogous to the one introduced in the appendix on the Landauer-Büttiker formalism, see Eq. (A.72).]. As we can see, the finite-temperature conductance involves the Andreev conversions τ_i at finite-bias. Moreover, while additional non-chiral edge states are not expected to play a role at zero-bias (see Sec. 3.3.2.2), we can expect them to have an effect at finite-bias. Furthermore, at finite temperature, the linear approximation for the dispersion of the CAES may not be sufficient. Also, if δk or ϕ_{12} varies significantly with energy on the scale k_BT, the oscillations of the downstream conductance should be averaged out upon increasing temperature. However, we find numerically that these effects are small in experimentally relevant parameter regimes. To see that, we need to study the energy-dependency of the parameters determining the downstream Andreev conversion P_h. The momentum difference $\delta k(E)$ can be obtained

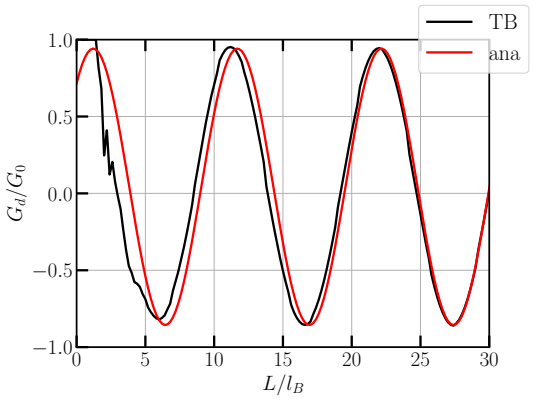

Figure 3.20: Conductance oscillations as a function of length L of an asymmetric junction, $\theta_1^{QH} = 0$ and $\theta_2^{QH} = 90°$ whereas $\theta_1^{SC} = \theta_2^{SC} = 90°$. We compare a full tight-binding simulation (TB) with the results of the effective one-dimensional model (ana). Here $\nu = 2.8$, $\mu_{SC} = 2\mu_{QH} = 20\Delta$, and $Z = 0.7$. The scattering phase ϕ_{12} in Eq. (3.14) is adjusted to match the results of the tight-binding simulation at large L.

from the microscopic model. We find that, even beyond the regime where the edge state spectrum is linear, the variation of δk remains small. We illustrate our findings in Fig. 3.21. Here the same parameters as in Fig. 3.20 were used. The spectrum is shown in Fig. 3.21a. Additional non-chiral edge states are visible at energies $|E| \gtrsim \Delta/2$. The relative deviations of $\delta k(E)$ from $\delta k(0) = 2k_0$ are shown in Fig. 3.21b. For small enough energies, the deviations are small, implying a nearly constant period of the oscillations. Figs. 3.21c and 3.21d show the energy dependence of the conversion probabilities τ_1 and τ_2. Again, the variation is weak up to the energy where additional sub-gap states appear. This is consistent with what one would obtain from our effective 1D model, where there is no energy dependence. The scattering phase (not shown) remains approximatively constant in this regime as well. These results suggest that the zero-temperature results obtained for the downstream conductance are robust as long as $k_BT \ll \Delta$. This is confirmed by a full tight-binding simulation, shown in Fig. 3.22. For $k_BT/\Delta = 0.1$, the result is almost unchanged. By contrast, at the larger temperature $k_BT/\Delta = 0.5$, a clear suppression of the amplitude of the oscillations is observed while the mean value increases as energies close to Δ start to contribute, where variations of δk become non-negligible and $\tau_i \to 0$.

3.7 Conclusion

In this chapter, we have studied the downstream conductance mediated by CAES in QH-SC junctions. In particular, we found that the geometry and the value of the filling factor play an important role. This limits the applicability of simple effective one-dimensional models that are often used to describe such systems. We showed that the most general effective one-dimensional model containing a complex pairing potential localized in the region where the QH-vacuum edge meets the QH-SC edge allows one to model an arbitrary electron-hole conversion probability even if there is no clear prescription as to how parameters have to be chosen. We note that the geometry dependence may be exploited to device asymmetric junctions, where the overall electron-hole conversion probability is enhanced and the averaged downstream conductance can become negative. This can be a way to obtain clearer signatures of the Andreev conversion at the QH-SC interface.

Our work concentrated on the clean case. It will be interesting to explore how these features are modified by disorder or in the presence of superconducting vortices. Moreover, it would be useful to study the geometry effects by considering a graphene sample as many experiments are using such devices. As another perspective, one can think about doing the same work with spin-polarized electrons. Indeed, CAES made of spin-polarized electrons are expected to be useful for topologically protected quantum computing [Nayak *et al.* 2008, Mong *et al.* 2014, Clarke *et al.* 2014]. Some works have already

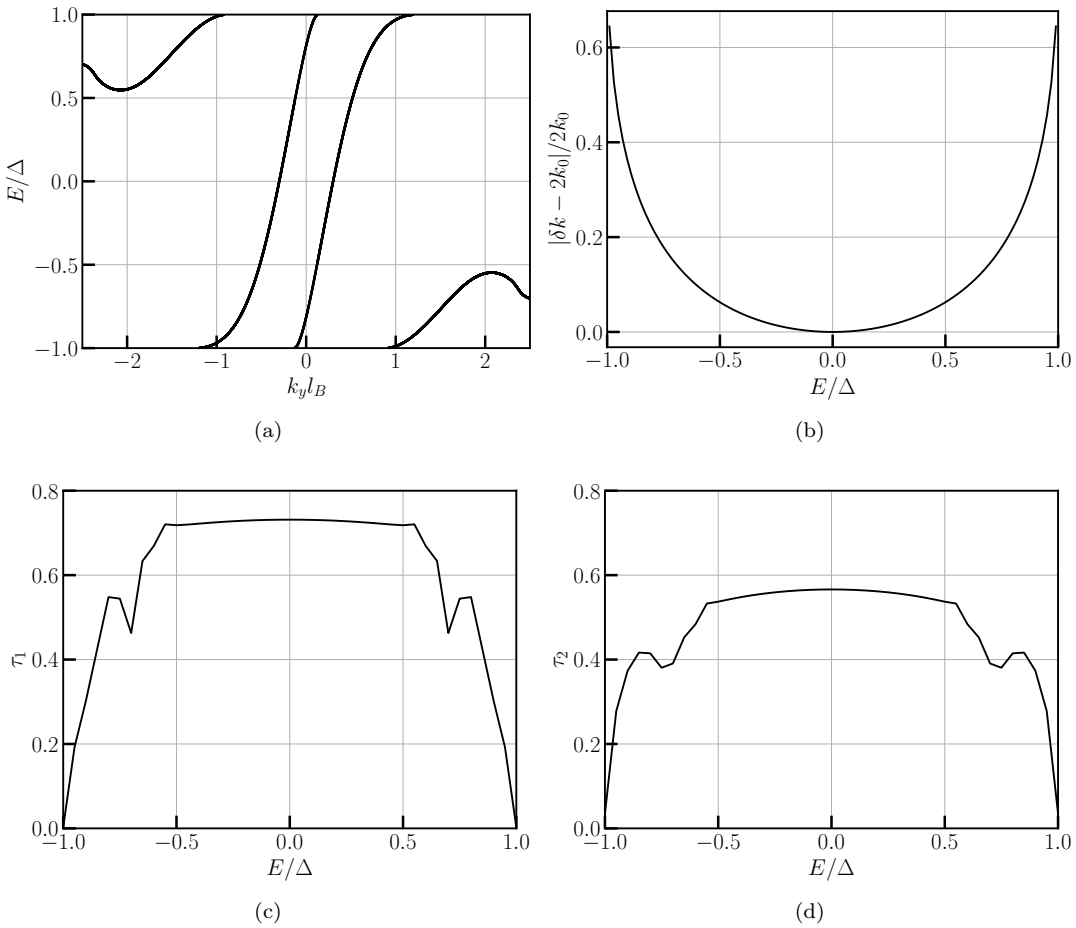

Figure 3.21: Energy dependence of various parameters necessary to determine the downstream conductance at finite temperature. Parameters are the same as in Fig. 3.96. (a) Energy spectrum. (b) Variation of the relative momentum difference $|\delta k(E) - 2k_0|/2k_0$ of the pair of CAES. (c) & (d) Conversion probability $\tau_1 = \tau(\theta_{QH} = 0, \theta_{SC} = 90°)$ and $\tau_2 = \tau(\theta_{QH} = 90°, \theta_{SC} = 90°)$ Variations in Figs. (b-d) are seen to be small as long as $|E| \ll \Delta$.

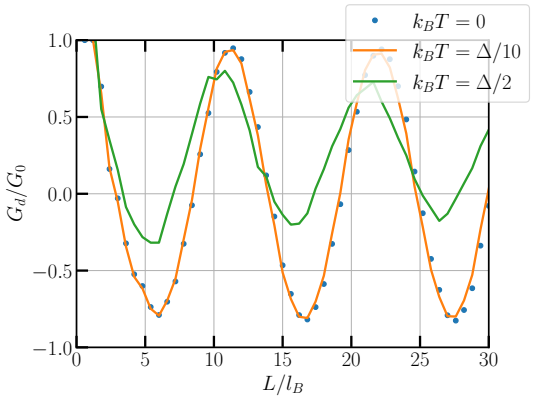

Figure 3.22: Downstream conductance at different temperatures. The zero-temperature result is shown by blue dots. At $k_BT = \Delta/10$ (orange line), there is almost no change. By contrast, a clear reduction of the amplitude of the oscillations is observed at $k_BT = \Delta/2$ (green line). Parameters are the same as in Fig. 3.20.

considered the spin-polarized case [van Ostaay *et al.* 2011, Michelsen *et al.* 2023], but a complete microscopic description is still needed. Note that spin-polarized electrons cannot form Cooper pairs when being in proximity with a s-wave superconductor such that no Andreev reflection is possible. A solution to this issue is to use a 2DEG material with a strong spin-orbit coupling (due to the Rashba effect for instance) such that Cooper pairs can be formed or to use a superconductor with a spin-triplet order parameter [Alicea 2012].

Chapter 4

Counter propagating chiral Andreev edge states in QH-SC-QH junctions

Contents

This chapter is an extension of the previous one in which we consider a second quantum Hall region at the right-hand side of the superconductor, namely we consider a quantum Hall-superconductor-quantum Hall (QH-SC-QH) junction. We study the energy spectrum and the transport properties of a QH-SC-QH junction with a ribbon geometry and made of spinful electrons, where the two QH-SC interfaces host counter-propagating pairs of CAES. The energy spectrum is determined using a microscopic model, while the transport properties are calculated using a one-dimensional effective model. This work aims at describing the crossed Andreev processes occurring in this type of junctions as observed in recent experiments [Lee *et al.* 2017, Gül *et al.* 2022], where the superconductor has a finger shape. This is a preliminary step towards the study of the spin-polarized case, which is expected to exhibit a Majorana zero mode at the end of such a superconducting finger.

4.1 Introduction

We consider a QH-SC-QH junction with a ribbon geometry as shown in Fig. 4.1. The system can be viewed as a quantum Hall sample on which a superconductor of width W is deposited, thus forming two QH-SC interfaces of length L. In continuity with the previous chapter, we focus on the situation where a single spin-degenerate Landau level is filled in the quantum Hall region so that the QH-SC interfaces host counter-propagating pairs of CAES.

When the length L of the QH-SC interfaces is infinite we can compute the energy spectrum of the counter-propagating pairs of CAES with a continuum microscopic model and, as we will see, it shows an energy gap which decreases exponentially with W/ξ, where ξ is the superconducting coherence length. Indeed, we will observe that the counter-propagating CAES are coupled because their wavefunctions extend into the region covered by the superconductor on the length scale ξ, leading to a gap in the energy spectrum.

To investigate the transport properties of the junction we must consider a finite length L of the QH-SC interfaces. As we saw in the previous chapter, the scattering probabilities depend strongly on the geometry of the system, so a full two-dimensional description is needed to calculate them. However, we have not developed such a model due to lack of time, but have used a simple one-dimensional effective model that allows us to obtain a qualitative understanding of the transport properties. When the counter-propagating CAES are well coupled, two electrons from different QH-SC interfaces can transfer into the

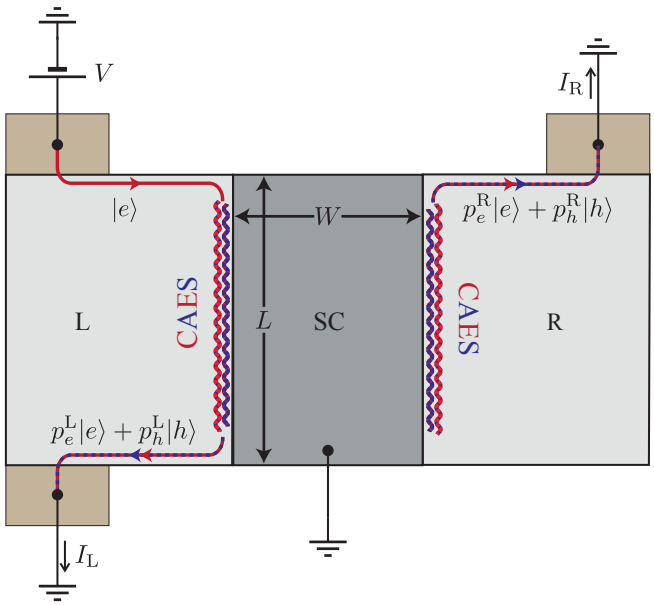

Figure 4.1: QH-SC-QH setup. An incoming electron from the top reservoir of the left (L) quantum Hall region can propagate along the left interface with the superconductor (SC) as a chiral Andreev edge state (CAES) and then be transmitted in the bottom left reservoir as an electron or as a hole with respective amplitudes p_e^{L} and p_h^{L}. Moreover, the incoming electron can tunnel through the right (R) region and propagate along the right QH-SC interface as a CAES before being transmitted in the top right reservoir as an electron or as a hole with respective amplitudes p_e^{R} and p_h^{R}. Here V is the voltage biased between the top left reservoir and the superconductor while I_{L} and I_{R} are respectively the currents flowing in the bottom left and in the top right reservoirs. The length of the QH-SC interfaces and the width of the superconductor are respectively denoted by L and W.

superconductor as a Cooper pair, annihilating an electron at one interface and leaving a hole propagating at the other interface. This process, called crossed Andreev reflection (CAR), was described in detail in Sec. 2.1.5 for a normal metal-superconductor-normal metal junction. Additionally, an electron at one side can also be transferred to the other side of the superconductor as an electron as discussed in Sec. 2.1.5. Thus, an incoming electron from the left can be transferred to the right as an electron or as a hole with respective amplitudes p_e^{R} and p_h^{R}. Since the CAES are gapped along the superconductor, these non-local processes are expected to be the only possible ones when the length L of the QH-SC interfaces tends to infinity. On the other hand, if L is comparable to $\tilde{\xi}$, where $\tilde{\xi}$ is an effective coherence length [See Eq. (4.56)], an incoming electron from the top of the left region can also be transferred to the bottom of the left region as an electron or as a hole with respective amplitudes p_e^{L} and p_h^{L}. Moreover, in the limit $W \to \infty$, an incoming electron from the upper edge of the left region will only be transferred to the lower edge of the left region, as for the single QH-SC interface studied in the previous chapter. We thus see that, in the general case, the four scattering processes characterized by $p_{e,h}^{\mathrm{L}}$ and $p_{e,h}^{\mathrm{R}}$ are in competition and depend on the system dimensions. To probe these processes in an experiment, one can measure the local and non-local conductances, denoted G_{LL} and G_{RL}, respectively. These are defined as

$$G_{\mathrm{LL}} = \frac{\partial I_{\mathrm{L}}}{\partial V} = G_0(P_e^{\mathrm{L}} - P_h^{\mathrm{L}}), \tag{4.1}$$

$$G_{\mathrm{RL}} = \frac{\partial I_{\mathrm{R}}}{\partial V} = G_0(P_e^{\mathrm{R}} - P_h^{\mathrm{R}}), \tag{4.2}$$

where V is the voltage biased between the top left reservoir and the superconductor while I_{L} and I_{R} are the currents flowing in the bottom left and top right reservoirs respectively, see Fig. 4.1. (Recall that $G_0 = 2e^2/h$ is the quantum of conductance.) Here we have introduced the scattering probabilities

$$P_e^{\mathrm{L}} = |p_e^{\mathrm{L}}|^2, \quad P_h^{\mathrm{L}} = |p_h^{\mathrm{L}}|^2, \quad P_e^{\mathrm{R}} = |p_e^{\mathrm{R}}|^2, \quad P_h^{\mathrm{R}} = |p_h^{\mathrm{R}}|^2, \tag{4.3}$$

where $P_e^{\mathrm{L}} + P_h^{\mathrm{L}} + P_e^{\mathrm{R}} + P_h^{\mathrm{R}} = 1$.

This chapter is organized as follows. In Sec. 4.2 we use a microscopic continuum model to determine the energy spectrum of the counter propagating pairs of CAES, similarly to what we did in the previous chapter. Furthermore, we use this model to study the evolution of the energy gap with the width W of the superconductor. In Sec. 4.3 we derive the one-dimensional effective Hamiltonian describing the counter-propagating CAES, and we fit the resulting effective spectrum to the microscopic spectrum to determine the effective parameters. We then use our effective model to calculate the transport properties in Sec. 4.4, and we conclude and provide perspectives in Sec. 4.5.

4.2 Energy spectrum

We consider a QH-SC-QH junction with a ribbon geometry that is invariant along the interfaces' direction y as depicted in Fig. 4.2. The junction consists in a 2DEG in the quantum Hall regime on top of which is deposited a superconductor of width W. The superconducting interfaces located at $x = \pm W/2$ exhibit each one pair of CAES with opposite chiralities. Moreover, we consider semi-infinite quantum Hall regions at the left (L) and right (R) hand sides of the superconductor.

As in Chap. 3, we describe the junction with a microscopic BdG Hamiltonian,

$$H(\vec{r}) = \begin{pmatrix} H_0(\vec{r}) - \mu(x) & \Delta(x) \\ \Delta^*(x) & -H_0^*(\vec{r}) + \mu(x) \end{pmatrix}, \tag{4.4}$$

with $\vec{r} = (x, y)$ and,

$$H_0(\vec{r}) = \frac{1}{2m(x)} \left(-i\hbar\vec{\nabla} - e\vec{A}(x) \right)^2 + V(x). \tag{4.5}$$

The spatial dependency of the parameters is given by,

$$m(x),\, \mu(x),\, \Delta(x) = \begin{cases} m_{QH},\, \mu_{QH},\, 0 & \text{for } |x| \geq W/2, \\ m_{SC},\, \mu_{SC},\, \Delta & \text{for } |x| < W/2, \end{cases} \tag{4.6}$$

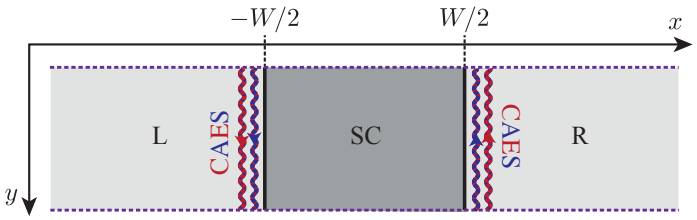

Figure 4.2: Infinite QH-SC-QH junction where a superconductor of width W is deposited on top of a 2DEG in the quantum Hall regime. We have represented the counter-propagating pairs of CAES at the superconducting interfaces located at $x = \pm W/2$.

where $m(x)$ is an effective mass, $\mu(x)$ is the chemical potential measured from the band bottom, $\Delta(x)$ is the superconducting order parameter (that we choose to be real), $\vec{A}(x) = B[(x + W/2)\Theta(-x - W/2) + (x - W/2)\Theta(x - W/2)]\hat{u}_y$ is the Landau gauge preserving translational invariance along the interfaces' direction for an external magnetic field $\vec{B} = B\hat{u}_z$, and $V(x) = V_0[\delta(x + W/2) + \delta(x - W/2)]$ models the interfaces barriers. Again, considering periodic boundary conditions along the y-axis, the wave functions can be written as,

$$\Psi(\vec{r}) = \frac{e^{ik_y y}}{\sqrt{L_y}}\psi_{k_y}(x), \tag{4.7}$$

where L_y is the length of the system along the y-direction and ψ_{k_y} is the transverse wave function. The transverse wave functions have been derived in Sec. 2.1.2 and are given by[1],

$$\psi_{k_y}(x) = \begin{cases} \psi^{\mathrm{L}}_{k_y}(x) & \text{for } x \leq -W/2 \\ \psi^{SC}_{k_y}(x) & \text{for } -L_{SC}/2 < x \leq W/2\,, \\ \psi^{\mathrm{R}}_{k_y}(x) & \text{for } x > W/2 \end{cases} \tag{4.8}$$

with,

$$\psi^{\mathrm{L/R}}_{k_y}(x) = a_{\mathrm{L/R}}\begin{pmatrix}1\\0\end{pmatrix}\chi^{\mathrm{L/R}}_{+}(x \pm W/2) + b_{\mathrm{L/R}}\begin{pmatrix}0\\1\end{pmatrix}\chi^{\mathrm{L/R}}_{-}(x \pm W/2), \tag{4.9}$$

$$\psi^{SC}_{k_y}(x) = c_1\begin{pmatrix}\gamma\\1\end{pmatrix}\phi_{+}(x) + c_2\begin{pmatrix}\gamma\\1\end{pmatrix}\phi_{-}(x) + c_3\begin{pmatrix}\gamma^*\\1\end{pmatrix}\phi^*_{+}(x) + c_4\begin{pmatrix}\gamma^*\\1\end{pmatrix}\phi^*_{-}(x), \tag{4.10}$$

where,

$$\chi^{\mathrm{L/R}}_{\pm}(s) = N^{\mathrm{L/R}}_{\pm}U^{\mathrm{L/R}}_{\pm}(s), \tag{4.11}$$

$$U^{\mathrm{L}}_{\pm}(s) = U\left[-\frac{\mu_{QH} \pm E}{\hbar\omega_c}, -\frac{\sqrt{2}}{l_B}(s \mp k_y l_B^2)\right], \quad N^{\mathrm{L}}_{\pm} = \int_{-\infty}^{-W/2} |U^{\mathrm{L}}_{\pm}(s)|^2 \mathrm{d}s, \tag{4.12}$$

$$U^{\mathrm{R}}_{\pm}(s) = U\left[-\frac{\mu_{QH} \pm E}{\hbar\omega_c}, +\frac{\sqrt{2}}{l_B}(s \mp k_y l_B^2)\right], \quad N^{\mathrm{R}}_{\pm} = \int_{W/2}^{\infty} |U^{\mathrm{R}}_{\pm}(s)|^2 \mathrm{d}s, \tag{4.13}$$

$$\phi_{\pm}(x) = \sqrt{\frac{\mathrm{Im}\{q\}}{\sinh(\mathrm{Im}\{q\}W)}}e^{\pm iqx}, \quad q = \sqrt{(k_F^{SC})^2 - k_y^2 + 2im_{SC}\sqrt{\Delta^2 - E^2}}, \quad \gamma = \frac{\Delta}{E - i\sqrt{\Delta^2 - E^2}}, \tag{4.14}$$

and $U(a, z)$ are parabolic cylinder functions as introduced in Eq. (2.78). We also used the cyclotron frequency $\omega_c = eB/m_{QH}$ and the magnetic length $l_B = \sqrt{\hbar/(eB)}$. In contrast to the previous chapter where we considered a single QH-SC interface, here we keep the four possible terms in the superconducting wave function because we have two QH-SC interfaces and so all these terms are evanescent. Note that

[1] We consider only sub-gap states with $|E| < \Delta$.

we focus here only on the case where a single electron-hole pair of CAES propagates along each QH-SC interface. For this we consider a filling factor $\nu = 2\mu_{QH}/(\hbar\omega_c)$ between 1 and 3. As in Sec. 3.3.2.1, in order to derive the secular equation which allows us to obtain the energy spectrum of the counter-propagating CAES, we have to match the wave functions and their derivatives at the two superconducting interfaces located at $x = \pm W/2$. At the left interface the matching procedure is

$$\begin{aligned} \psi_{k_y}^{QH}(-W/2) &= \psi_{k_y}^{SC}(-W/2) \equiv \psi_{k_y}(-W/2), \\ \frac{m_{QH}}{m_{SC}}\psi_{k_y}^{SC\prime}(-W/2) - \psi_{k_y}^{\mathrm{L}\,\prime}(-W/2) &= Zk_F^{QH}\psi_{k_y}(-W/2), \end{aligned} \tag{4.15}$$

and at the right interface it is

$$\begin{aligned} \psi_{k_y}^{\mathrm{R}}(W/2) &= \psi_{k_y}^{SC}(W/2) \equiv \psi_{k_y}(W/2), \\ \psi_{k_y}^{\mathrm{R}\,\prime}(W/2) - \frac{m_{QH}}{m_{SC}}\psi_{k_y}^{SC\prime}(-W/2) &= Zk_F^{QH}\psi_{k_y}(W/2), \end{aligned} \tag{4.16}$$

where $Z = 2m_{QH}V_0/(\hbar^2 k_F^{QH})$ is the barrier strength. Writing the constants $a_{\mathrm{L/R}}$ and $b_{\mathrm{L/R}}$ in terms of the constants c_i the resulting system can be written as $M \cdot C = 0$, with $C = (c_1\, c_2\, c_3\, c_4)^T$ and

$$M = \tag{4.17}$$
$$\begin{pmatrix} \gamma\left[G'_{\mathrm{L}} - G_{\mathrm{L}}\mathcal{A}_-\right]e^{-iq\frac{W}{2}} & \gamma\left[G'_{\mathrm{L}} - G_{\mathrm{L}}\mathcal{B}_-\right]e^{iq\frac{W}{2}} & \gamma^*\left[G'_{\mathrm{L}} - G_{\mathrm{L}}\mathcal{A}^*_-\right]e^{iq^*\frac{W}{2}} & \gamma^*\left[G'_{\mathrm{L}} - G_{\mathrm{L}}\mathcal{B}^*_-\right]e^{-iq^*\frac{W}{2}} \\ \left[H'_{\mathrm{L}} - H_{\mathrm{L}}\mathcal{A}_-\right]e^{-iq\frac{W}{2}} & \left[H'_{\mathrm{L}} - H_{\mathrm{L}}\mathcal{B}_-\right]e^{iq\frac{W}{2}} & \left[H'_{\mathrm{L}} - H_{\mathrm{L}}\mathcal{A}^*_-\right]e^{iq^*\frac{W}{2}} & \left[H'_{\mathrm{L}} - H_{\mathrm{L}}\mathcal{B}^*_-\right]e^{-iq^*\frac{W}{2}} \\ \gamma\left[G'_{\mathrm{R}} - G_{\mathrm{R}}\mathcal{A}_+\right]e^{iq\frac{W}{2}} & \gamma\left[G'_{\mathrm{R}} - G_{\mathrm{R}}\mathcal{B}_+\right]e^{-iq\frac{W}{2}} & \gamma^*\left[G'_{\mathrm{R}} - G_{\mathrm{R}}\mathcal{A}^*_+\right]e^{-iq^*\frac{W}{2}} & \gamma^*\left[G'_{\mathrm{R}} - G_{\mathrm{R}}\mathcal{B}^*_+\right]e^{iq^*\frac{W}{2}} \\ \left[H'_{\mathrm{R}} - H_{\mathrm{R}}\mathcal{A}_+\right]e^{iq\frac{W}{2}} & \left[H'_{\mathrm{R}} - H_{\mathrm{R}}\mathcal{B}_+\right]e^{-iq\frac{W}{2}} & \left[H'_{\mathrm{R}} - H_{\mathrm{R}}\mathcal{A}^*_+\right]e^{-iq^*\frac{W}{2}} & \left[H'_{\mathrm{R}} - H_{\mathrm{R}}\mathcal{B}^*_+\right]e^{iq^*\frac{W}{2}} \end{pmatrix},$$

where we have introduced the shorthand notations,

$$\mathcal{A}_\pm = \left(i\frac{m_{QH}}{m_{SC}}q \pm Zk_F^{QH}\right), \quad \mathcal{B}_\pm = \left(-i\frac{m_{QH}}{m_{SC}}q \pm Zk_F^{QH}\right), \tag{4.18}$$

$$G_{\mathrm{L/R}} = U_+^{\mathrm{L/R}}(0), \quad H_{\mathrm{L/R}} = U_-^{\mathrm{L/R}}(0), \tag{4.19}$$

$$G'_{\mathrm{L}} = \partial_x U_+^{\mathrm{L}}(x - W/2)\big|_{x=W/2}, \quad H'_{\mathrm{L}} = \partial_x U_-^{\mathrm{L}}(x - W/2)\big|_{x=W/2}, \tag{4.20}$$

$$G'_{\mathrm{R}} = \partial_x U_+^{\mathrm{R}}(x + W/2)\big|_{x=-W/2}, \quad H'_{\mathrm{R}} = \partial_x U_-^{\mathrm{R}}(x + W/2)\big|_{x=-W/2}, \tag{4.21}$$

with $U_\pm^{\mathrm{L}}(s)$ and $U_\pm^{\mathrm{R}}(s)$ the parabolic cylinder functions introduced in Eqs. (4.12) and (4.13). We can then write the secular equation for the QH-SC-QH junction as,

$$s(E, k_y) = \det M = 0, \tag{4.22}$$

from which we can obtain the energy spectrum. In Fig. 4.3, Fig. 4.4, and Fig. 4.5 we show the energy spectrum for various values of W at fillings $\nu = 1.2$, $\nu = 2$, and $\nu = 2.8$ respectively. For $W = 0$, we observe flat Landau levels as expected for a quantum Hall sample. When W starts to be different from zero, the Landau levels in the left and right regions become coupled by the superconductor, leading to various kind of energy branches depending on the ratio W/ξ and on the value of ν. We distinguish between two different energy gaps, which are shown in Fig. 4.4e: a gap δ_0 at $k_y = 0$ and a gap $\tilde{\delta}$ at $k = \pm\tilde{k}$. For $W/\xi \gg 1$ the counter-propagating pairs of CAES are very weakly coupled and the energy gaps become very small. We can see this in the zooms we made for the values $W/\xi = 5$ and $W/\xi = 10$. In Fig. 4.6 we plot the evolution of the gaps with the width W of the superconductor in semi-log scale. We see that they oscillate and decrease exponentially with W/ξ. From the slopes a of the lines passing through the maxima, we can determine the exponential decay rates. We see that the slope decreases with ν for the gap δ_0 (from -0.79 for $\nu = 1.2$ to -0.9 for $\nu = 2.8$), while it increases with ν for the gap $\tilde{\delta}$ (from -1.12 to -0.96). Thus, the gaps decay as $e^{-\alpha W/\xi}$ with $\alpha \approx 1$. These exponentially decreasing oscillations can be related to the oscillating exponential decay of the CAES wave functions in the superconductor, as shown in Fig. 3.10b of the previous chapter. Hence, for $W/\xi \to \infty$, the gaps tend to zero and

the system can be treated as two independent QH-SC interfaces. In that case, the momentum value $|k_y| = \tilde{k}$ at which the energy branches cross the Fermi level is the same as the momentum k_0 calculated in the previous chapter in Eq. (3.32). To better appreciate the similarity between the spectrum of the QH-SC-QH junction and the spectra of two independent QH-SC interfaces when $W/\xi \gg 1$, in Fig. 4.7 we compare the spectra obtained for $W/\xi = 10$ with those determined in the previous chapter for a QH-SC junction (see Sec. 3.3.2). In this figure we see a very nice correspondence between the energy branches of the QH-SC junction and those associated with the left QH-SC interface of the QH-SC-QH junction.

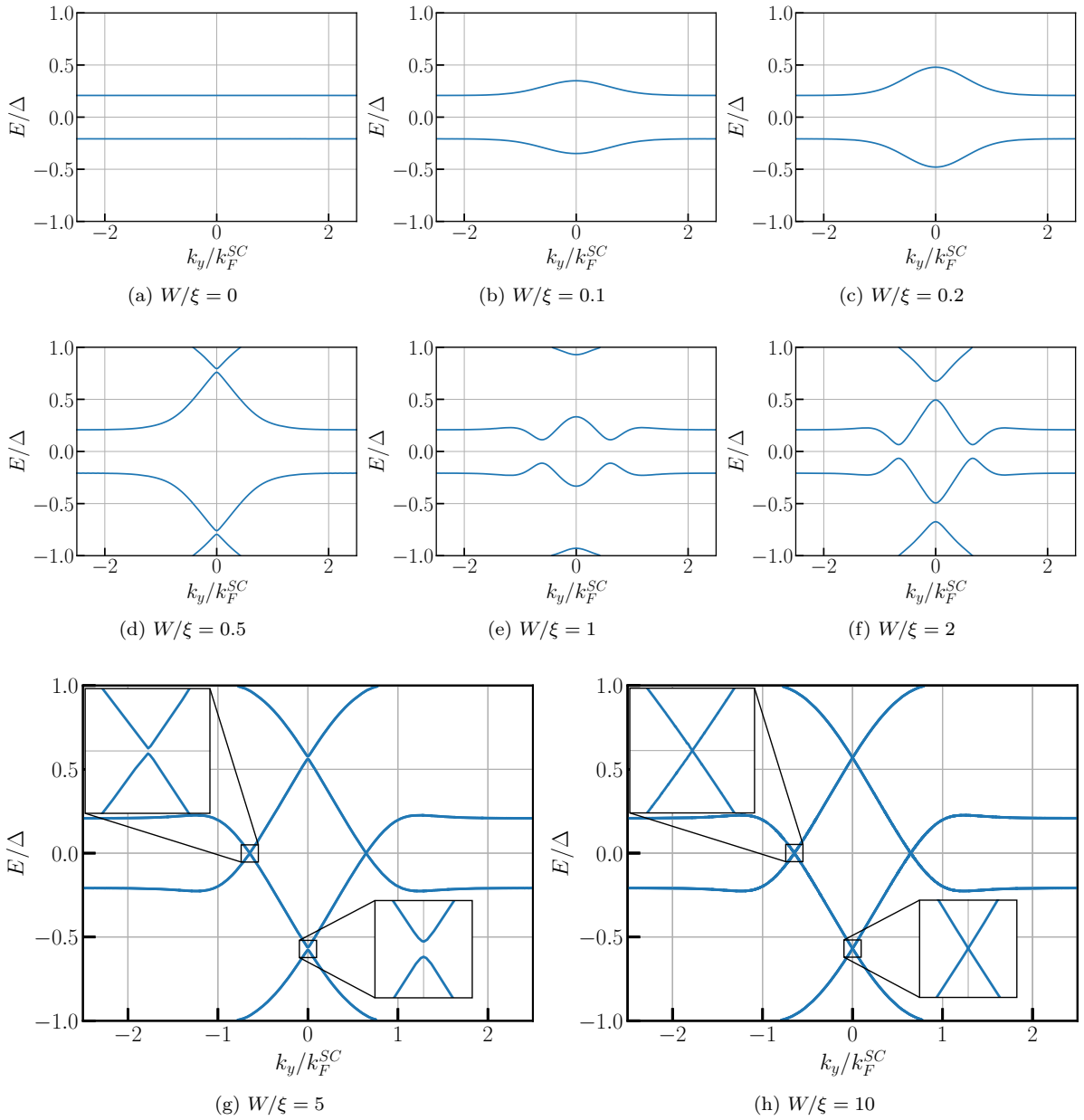

(a) $W/\xi = 0$ (b) $W/\xi = 0.1$ (c) $W/\xi = 0.2$

(d) $W/\xi = 0.5$ (e) $W/\xi = 1$ (f) $W/\xi = 2$

(g) $W/\xi = 5$ (h) $W/\xi = 10$

Figure 4.3: Energy spectrum of the QH-SC-QH junction for various values of W with $\nu = 1.2$. The parameters are $m_{QH} = m_{SC}$, $\mu_{QH} = \mu_{SC} = 1.25\Delta$, and $Z = 0$.

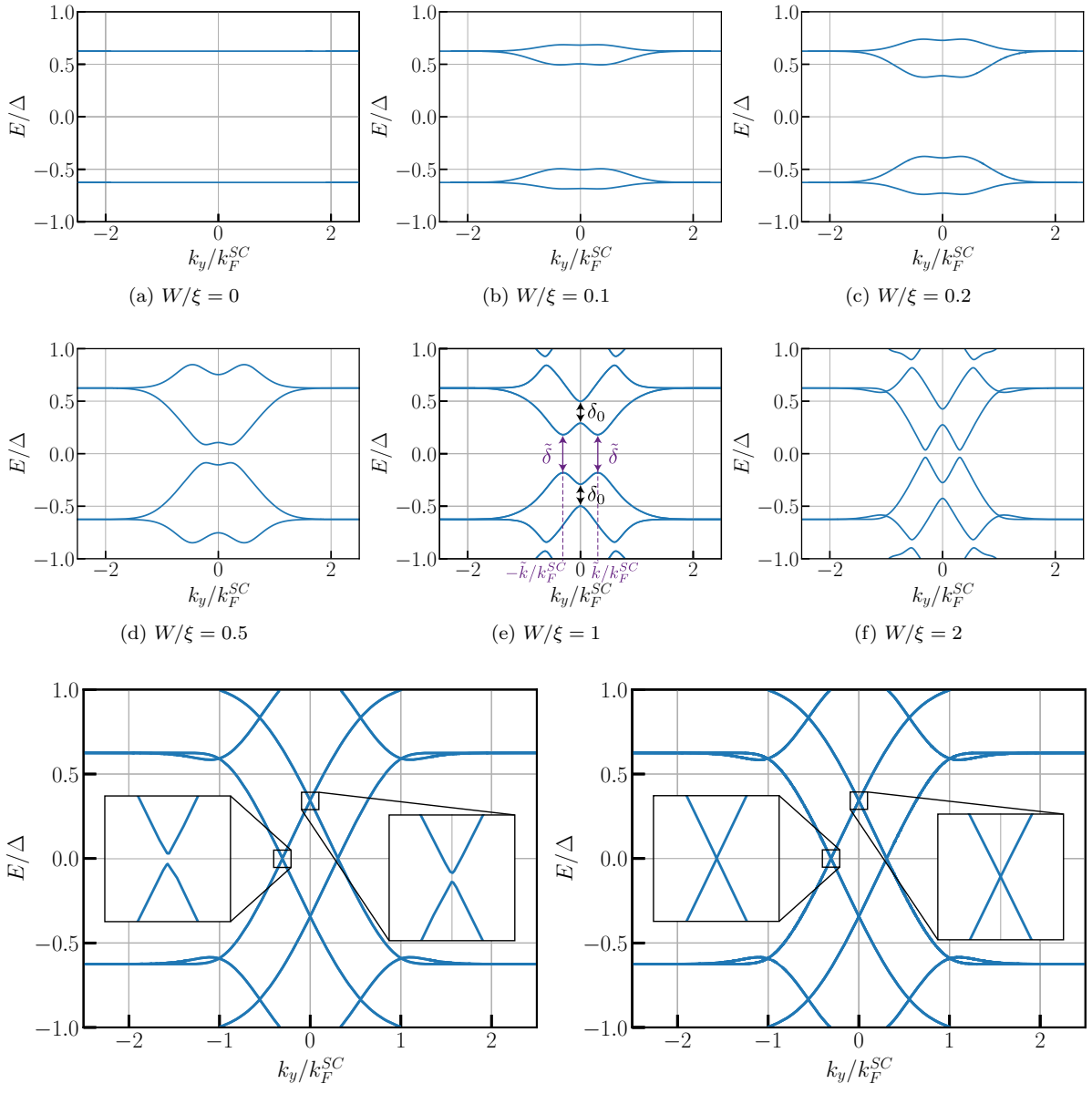

(a) $W/\xi = 0$ (b) $W/\xi = 0.1$ (c) $W/\xi = 0.2$

(d) $W/\xi = 0.5$ (e) $W/\xi = 1$ (f) $W/\xi = 2$

(g) $W/\xi = 5$ (h) $W/\xi = 10$

Figure 4.4: Energy spectrum of the QH-SC-QH junction for various values of W with $\nu = 2$. The parameters are $m_{QH} = m_{SC}$, $\mu_{QH} = \mu_{SC} = 1.25\Delta$, and $Z = 0$.

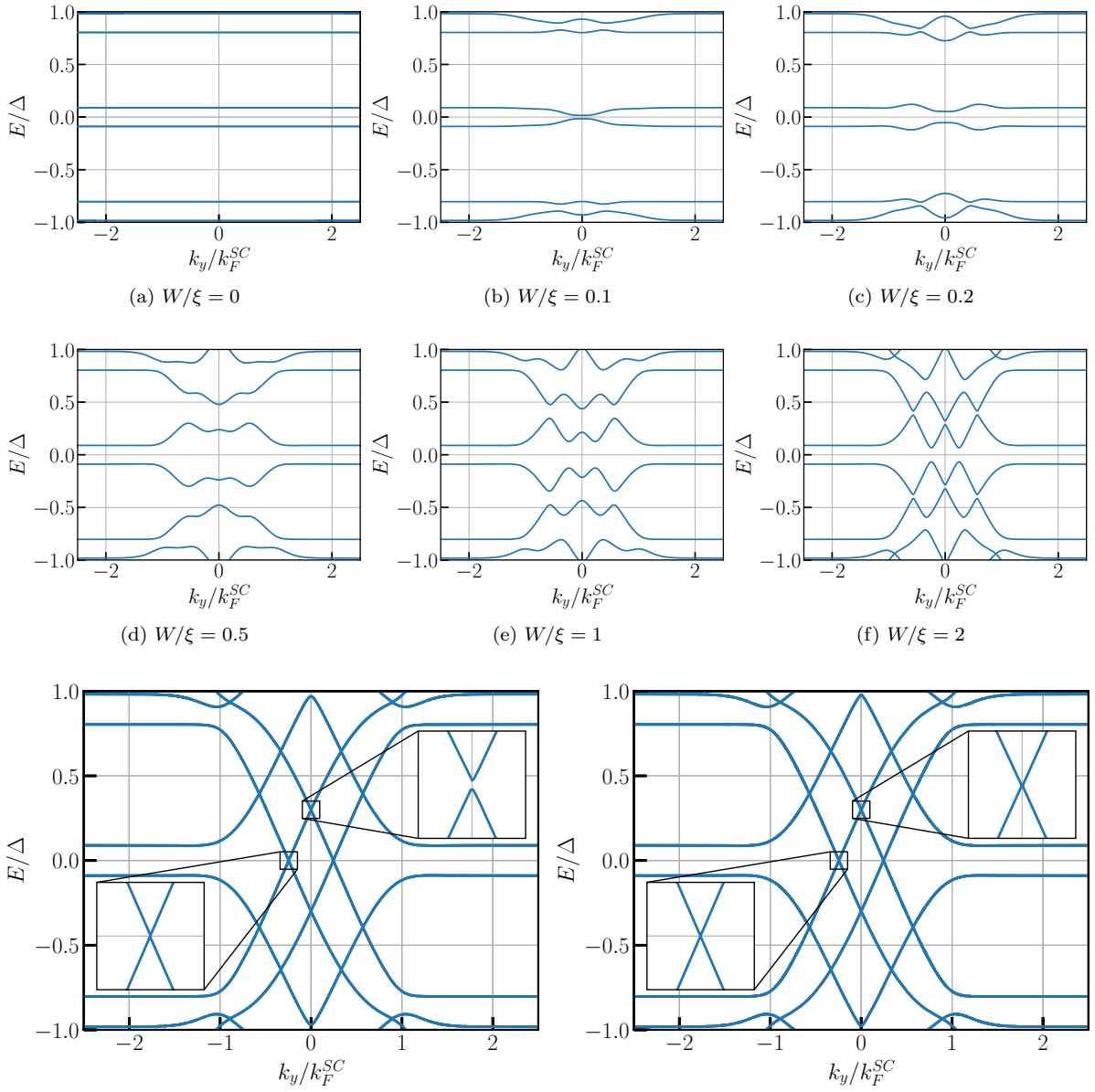

(a) $W/\xi = 0$ (b) $W/\xi = 0.1$ (c) $W/\xi = 0.2$

(d) $W/\xi = 0.5$ (e) $W/\xi = 1$ (f) $W/\xi = 2$

(g) $W/\xi = 5$ (h) $W/\xi = 10$

Figure 4.5: Energy spectrum of the QH-SC-QH junction for various values of W with $\nu = 2.8$. The parameters are $m_{QH} = m_{SC}$, $\mu_{QH} = \mu_{SC} = 1.25\Delta$, and $Z = 0$.

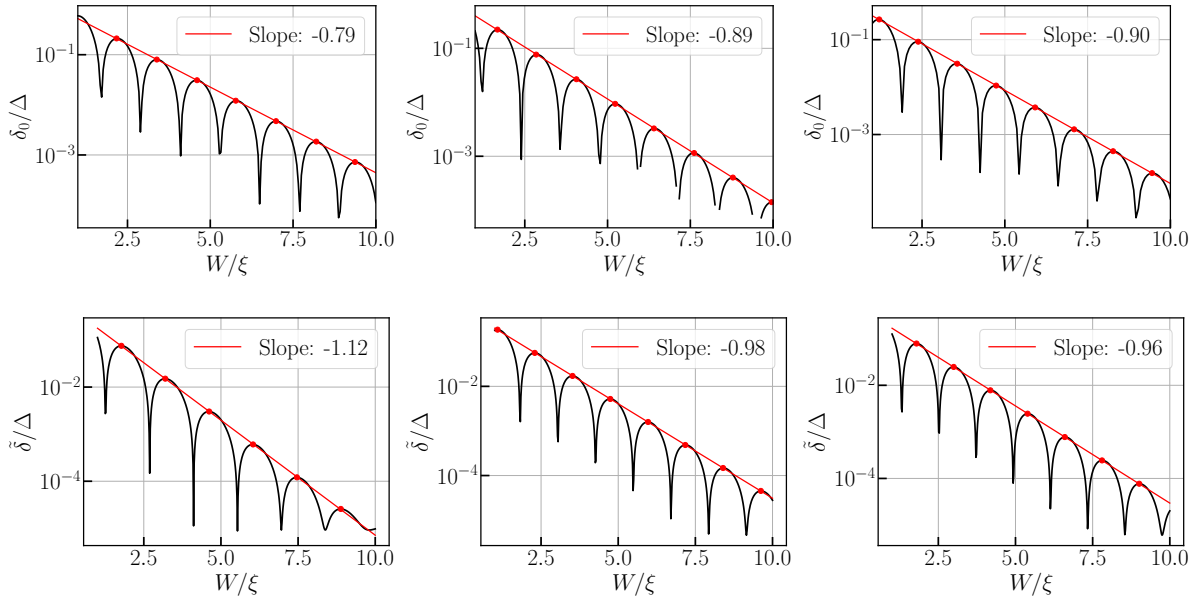

(a) $\nu = 1.2$ (b) $\nu = 2$ (c) $\nu = 2.8$

Figure 4.6: Evolution of the gaps δ_0 (top row) and $\tilde{\delta}$ (bottom row) depicted in Fig. 4.4e as a function of W/ξ for the fillings (a) $\nu = 1.2$, (b) $\nu = 2$, and (c) $\nu = 2.8$. We observe that the gaps oscillate while decreasing exponentially with W/ξ. The parameters are $m_{QH} = m_{SC}$, $\mu_{QH} = \mu_{SC} = 1.25\Delta$, and $Z = 0$.

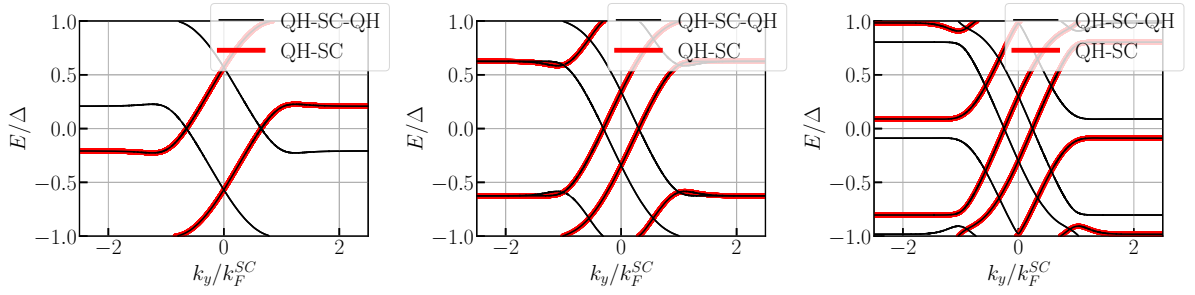

(a) $\nu = 1.2$ (b) $\nu = 2$ (c) $\nu = 2.8$

Figure 4.7: Comparison between the energy spectra obtained for a QH-SC junction and those obtained for a QH-SC-QH junction with $W/\xi = 10$. In (a) we set $\nu = 1.2$, in (b) $\nu = 2$, and in (c) $\nu = 2.8$. We see that the energy branches of the left interface of the QH-SC-QH junction perfectly match the branches of the QH-SC junction. The parameters are $m_{QH} = m_{SC}$, $\mu_{QH} = \mu_{SC} = 1.25\Delta$, and $Z = 0$.

In the next section we derive a one-dimensional effective Hamiltonian describing the counter-propagating pairs of CAES and we use it to calculate an effective energy spectrum. Then, by fitting the effective spectrum to the microscopic one, we can determine the values of the effective parameters. This allows us to study the transport properties of the junction by using our effective model in Sec. 4.4. As discussed in the previous chapter, such an effective model is not sufficient to account for the effects of geometry, but at least it allows for a qualitative understanding of the system.

4.3 Energy spectrum from a one-dimensional effective model

Here we use a one-dimensional effective model to describe the junction. We compute the energy spectrum obtained from this effective model and use it to fit the low-energy branches of the microscopic spectrum. In particular, this allows us to choose between two possible choices for the relative sign connecting the pairings at the left and right QH-SC interfaces.

In Sec. 4.3.1 we derive the effective Hamiltonian describing the counter-propagating pairs of CAES and we determine the resulting energy spectrum. In Sec. 4.3.2 we use the effective spectrum to fit the one obtained in the previous section from a microscopic model in order to determine the effective parameters.

4.3.1 Effective Hamiltonian and energy spectrum

We start by deriving the effective Hamiltonian and then we calculate the effective dispersion of the counter-propagating pairs of CAES.

4.3.1.1 Effective Hamiltonian

We consider a one-dimensional effective model as the one used in Sec. 3.5. The effective Hamiltonian for a chiral edge state with velocity v and chemical potential μ can be written as $\sum_{k,\sigma}(\hbar vk-\mu)c^\dagger_{k,\sigma}c_{k,\sigma}$, where $\sigma =\uparrow,\downarrow$ stands for the spin and k is the momentum along the edge. Since we consider counter-propagating chiral edge states, the effective Hamiltonian of the QH-SC-QH junction must contain a second copy of this Hamiltonian with $v \to -v$. Moreover, the superconducting couplings at the left and right QH-SC interfaces add a contribution to the Hamiltonian of the form $\sum_k \left[\Delta_1 c^\dagger_{k1\uparrow}c^\dagger_{-k1\downarrow} + \Delta_2 c^\dagger_{k2\uparrow}c^\dagger_{-k2\downarrow} + h.c.\right]$, where the label 1 (2) stands for the left (right) QH-SC interface. Finally, the effective Hamiltonian should contain a last contribution coming from the coupling between the CAES propagating along the left and right interfaces. This contribution takes the form $\sum_k \left[\Delta_{12} c^\dagger_{k1\uparrow}c^\dagger_{-k2\downarrow} + \Delta_{21} c^\dagger_{k2\uparrow}c^\dagger_{-k1\downarrow} + h.c.\right]$. The full effective Hamiltonian describing the QH-SC-QH junction can thus be written as,

$$\mathcal{H} = \mathcal{H}_0 + \mathcal{H}_\Delta, \tag{4.23}$$

$$\mathcal{H}_0 = \sum_k \left[(\hbar vk-\mu)c^\dagger_{k1\uparrow}c_{k1\uparrow} + (\hbar vk-\mu)c^\dagger_{k1\downarrow}c_{k1\downarrow} + (-\hbar vk-\mu)c^\dagger_{k2\uparrow}c_{k2\uparrow} + (-\hbar vk-\mu)c^\dagger_{k2\downarrow}c_{k2\downarrow}\right], \tag{4.24}$$

$$\mathcal{H}_\Delta = \sum_k \left[\Delta_1 c^\dagger_{k1\uparrow}c^\dagger_{-k1\downarrow} + \Delta_2 c^\dagger_{k2\uparrow}c^\dagger_{-k2\downarrow} + \Delta_{12} c^\dagger_{k1\uparrow}c^\dagger_{-k2\downarrow} + \Delta_{21} c^\dagger_{k2\uparrow}c^\dagger_{-k1\downarrow} + h.c.\right]. \tag{4.25}$$

Introducing the Nambu spinor $\psi_k = \left(c_{k1\uparrow},\, c_{k2\uparrow},\, c^\dagger_{-k1\downarrow},\, c^\dagger_{-k2\downarrow}\right)^T$ and the single-particle Hamiltonian

$$H(k) = \begin{pmatrix} \hbar vk-\mu & 0 & \Delta_1 & \Delta_{12} \\ 0 & -\hbar vk-\mu & \Delta_{21} & \Delta_2 \\ \Delta_1^* & \Delta_{21}^* & \hbar vk+\mu & 0 \\ \Delta_{12}^* & \Delta_2^* & 0 & -\hbar vk+\mu \end{pmatrix}, \tag{4.26}$$

we can rewrite the effective Hamiltonian (4.23) as $\mathcal{H} = \sum_k \psi_k^\dagger H(k)\psi_k$. In the following we use the single-particle Hamiltonian (4.26) to derive the energy spectrum and the wave functions of the system. To do so, we need to simplify it. First, as we have only one superconductor in the system, we can consider

the superconducting couplings as reals (see Eq. (2.13) and the related discussion). Then, from the pair potential introduced in Eq. (B.20), we can write

$$\Delta_{12} \propto \sum_k \langle c_{k1\uparrow} c_{-k2\downarrow} \rangle = -\sum_k \langle c_{-k2\downarrow} c_{k1\uparrow} \rangle = \sum_k \langle c_{k2\uparrow} c_{-k1\downarrow} \rangle \propto \Delta_{21}, \tag{4.27}$$

where in the last equality we have used [Mineev & Samokhin 1999] $\Delta_{k,\uparrow\downarrow} = -\Delta_{-k,\downarrow\uparrow}$. We thus set $\Delta_{12} = \Delta_{21}$ in the following. Moreover, the structure of the junction implies $|\Delta_1| = |\Delta_2|$ such that we have to distinguish between two possible choices: i) $\Delta_1 = \Delta_2$ and ii) $\Delta_1 = -\Delta_2$.

4.3.1.2 Energy spectrum

In the case where $\Delta_1 = \Delta_2 = \Delta_0$, the energy spectrum is given by

$$E^i_{sn}(k) = s\sqrt{\hbar^2 v^2 k^2 + \mu^2 + \Delta_0^2 + \Delta_{12}^2 + 2n\sqrt{\Delta_0^2\Delta_{12}^2 + \hbar^2 v^2 k^2(\mu^2 + \Delta_0^2)}}, \tag{4.28}$$

where $s = \pm$ stands for the chirality (+ corresponding to interface 1 and − to interface 2) and $n = \pm$ stands for the type of particle (+ for electron-like quasiparticles and − for hole-like quasiparticles). We have represented this dispersion in Fig. 4.8a in which we distinguish between two different energy gaps. At $k = 0$ there is a gap $\delta_0 = \sqrt{\mu^2 + (\Delta_0 + \Delta_{12})^2} - \sqrt{\mu^2 + (\Delta_0 - \Delta_{12})^2}$ and at $k = \pm\frac{1}{\hbar v}\sqrt{\frac{[\mu^2 + \Delta_0(\Delta_0+\Delta_{12})][\mu^2 + \Delta_0(\Delta_0-\Delta_{12})]}{\mu^2+\Delta_0^2}}$ there is a gap $\tilde{\delta} = \frac{2\mu\Delta_{12}}{\sqrt{\mu^2+\Delta_0^2}}$. On the other hand, if $\Delta_1 = -\Delta_2 = \Delta_0$, the energy spectrum reads

$$E^{ii}_{sn}(k) = s\sqrt{\hbar^2 v^2 k^2 + \mu^2 + \Delta_0^2 + \Delta_{12}^2 + 2n\hbar v|k|\sqrt{\mu^2 + \Delta_0^2}}. \tag{4.29}$$

The corresponding dispersion is shown in Fig. 4.8b. Here the states are doubly degenerate at $k = 0$ and there is a gap $\delta = 2\Delta_{12}$ at $k = \pm\frac{1}{\hbar v}\sqrt{\mu^2 + \Delta_0^2}$.

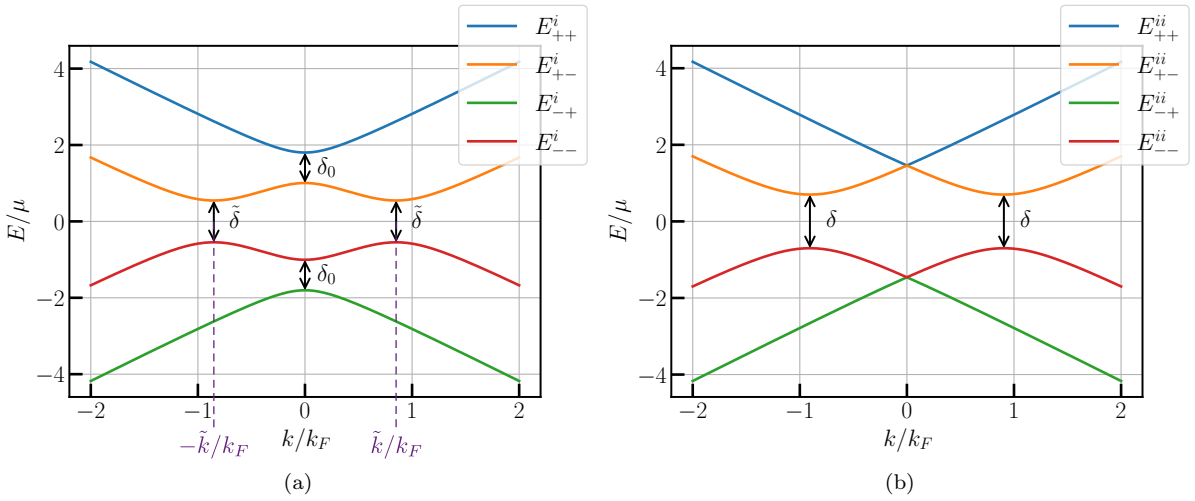

Figure 4.8: Band structures of the QH-SC-QH junction obtained from the effective Hamiltonian (4.26). In (a) the band structure has been represented in the case where $\Delta_1 = \Delta_2 = \Delta_0$. We observe two different gaps: a gap δ_0 at $k = 0$ and a gap $\tilde{\delta}$ at $k = \pm\tilde{k}$. In (b) the band structure has been represented in the case where $\Delta_1 = -\Delta_2 = \Delta_0$. Here the states are doubly degenerate at $k = 0$ and have a gap $\delta = 2\Delta_{12}$ at $k = \pm\frac{1}{\hbar v}\sqrt{\mu^2 + \Delta_0^2}$. We have chosen the parameters such that the gap δ_0 is large, namely we have set $v = 1$, $\mu = 1$, $\Delta_0 = 0.8\mu$, and $\Delta_{12} = 0.7\mu$.

In the next subsection we compare the effective spectrums with the microscopic ones in order to determine the effective parameters.

4.3.2 Comparison between the effective and microscopic spectra

Comparing these effective spectrums with those obtained from a microscopic Hamiltonian in Sec. 4.2 we can determine the relative sign between Δ_1 and Δ_2. Indeed, as discussed in Sec. 4.2, we observe an energy gap at $k = 0$ in the microscopic model. Thus, we must choose $\Delta_1 = \Delta_2 \equiv \Delta_0$ to reproduce the microscopic results. We can then estimate the effective parameters by fitting the microscopic spectrum with the effective dispersion (4.28). This is done in Figs. 4.9, 4.10, and 4.11 for $\nu = 1.2$, $\nu = 2$, and $\nu = 2.8$ respectively. Each time we consider three different values of the width W of the superconductor, namely $W/\xi = 1$, $W/\xi = 2$, and $W/\xi = 10$. The effective model provides a good fit of the low energy branches as long as $|k_y| < \tilde{k}$, where $\tilde{k} = \frac{1}{\hbar v}\sqrt{\frac{[\mu^2+\Delta_0(\Delta_0+\Delta_{12})][\mu^2+\Delta_0(\Delta_0-\Delta_{12})]}{\mu^2+\Delta_0^2}}$ is the momentum value represented in Fig. 4.8a. The velocity v is calculated from the result (3.33) obtained for the QH-SC junction and the value of Δ_{12} is chosen so that the gap $\tilde{\delta}$ matches the one calculated from the microscopic model. For $W/\xi = 10$ we use the same effective chemical potential as the one determined for the QH-SC junction in Sec. 3.5.2, namely $\mu = \hbar v k_0(1 - 2f_h^+)$, where k_0 is the positive momentum value at $E = 0$ derived in Eq. (3.32) and f_h^+ is the hole content derived in Eq. (3.70). Thus, for $W/\xi = 10$ we only have to adjust the value of Δ_0 by hand to fit the microscopic spectra, while for $W/\xi = 1$ and $W/\xi = 2$ we had to adjust μ and Δ_0 manually. The velocity v of the CAES increases with ν while the value of Δ_{12} decreases with W/ξ, as expected. On the other hand, the values of μ and Δ_0 do not show a regular evolution as a function of ν and W.

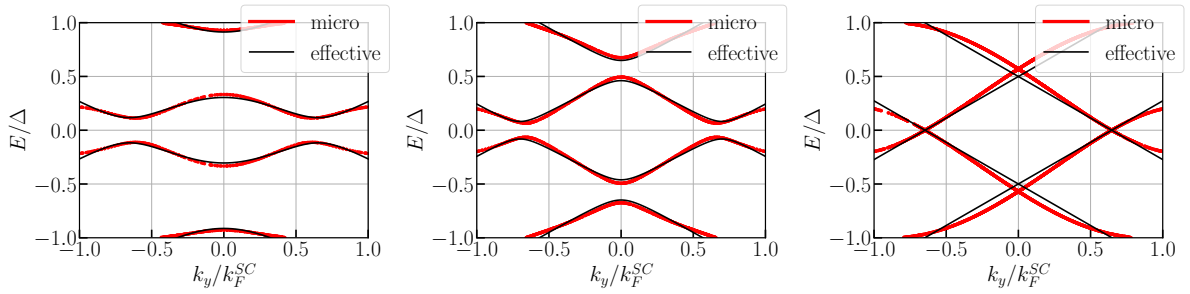

(a) $W/\xi = 1$ (b) $W/\xi = 2$ (c) $W/\xi = 10$

Figure 4.9: Comparisons between effective and microscopic (micro) spectra for $\nu = 1.2$ and various values of W/ξ. In (a) we set $W/\xi = 1$ and $\mu = \mu_{SC}/6$, $\Delta_0 = \Delta/1.8$, $\Delta_{12} = \Delta/3$. In (b) we set $W/\xi = 2$ and $\mu = \mu_{SC}/3.5$, $\Delta_0 = \Delta/2.4$, $\Delta_{12} = \Delta/8$. In (c) we set $W/\xi = 10$ and $\mu = \mu_{SC}/5.1$, $\Delta_0 = \Delta/2.3$, $\Delta_{12} = 7\Delta \times 10^{-6}$. The velocity is $v = v_F^{SC}/3.24$ and the microscopic parameters are the same as in Fig. 4.3.

In the next section we use our effective model with $\Delta_1 = \Delta_2 \equiv \Delta_0$ in order to determine the transport properties of the junction.

4.4 Transport properties

In the previous section we derived the effective Hamiltonian describing the counter-propagating pairs of CAES and we used our microscopic results to determine the effective parameters. We now compute the transport properties of the junction, namely the different scattering probabilities (Sec. 4.4.1) and the local and non-local conductances (Sec. 4.4.2).

4.4.1 Scattering probabilities

Here we consider a QH-SC-QH junction where an incoming electron from the upper edge of the left region can be transmitted to the lower edge of the left region as an electron or as a hole by normal or Andreev reflection with the respective amplitudes p_e^{L} and p_h^{L}. While these scattering processes were

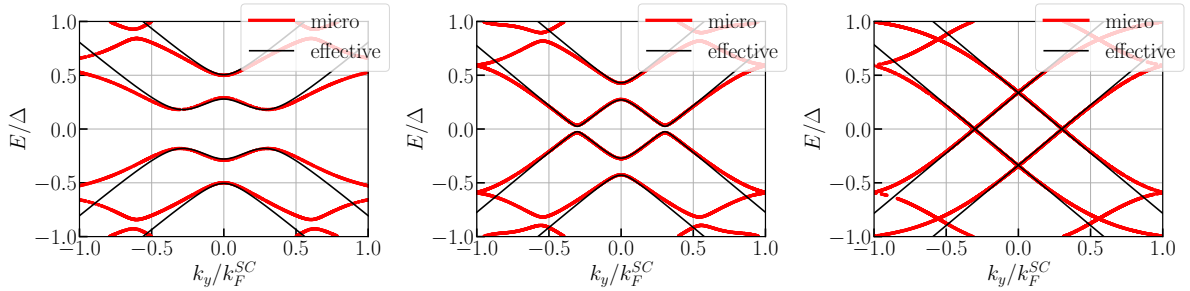

(a) $W/\xi = 1$ (b) $W/\xi = 2$ (c) $W/\xi = 10$

Figure 4.10: Comparisons between effective and microscopic (micro) spectra for $\nu = 2$ and various values of W/ξ. In (a) we set $W/\xi = 1$ and $\mu = \mu_{SC}/4.5$, $\Delta_0 = \Delta/5$, $\Delta_{12} = \Delta/4.5$. In (b) we set $W/\xi = 2$ and $\mu = \mu_{SC}/12$, $\Delta_0 = \Delta/3$, $\Delta_{12} = \Delta/12$. In (c) we set $W/\xi = 10$ and $\mu = \mu_{SC}/26.25$, $\Delta_0 = \Delta/2.95$, $\Delta_{12} = 2\Delta \times 10^{-4}$. The velocity is $v = v_F^{SC}/2.23$ and the microscopic parameters are the same as in Fig. 4.4.

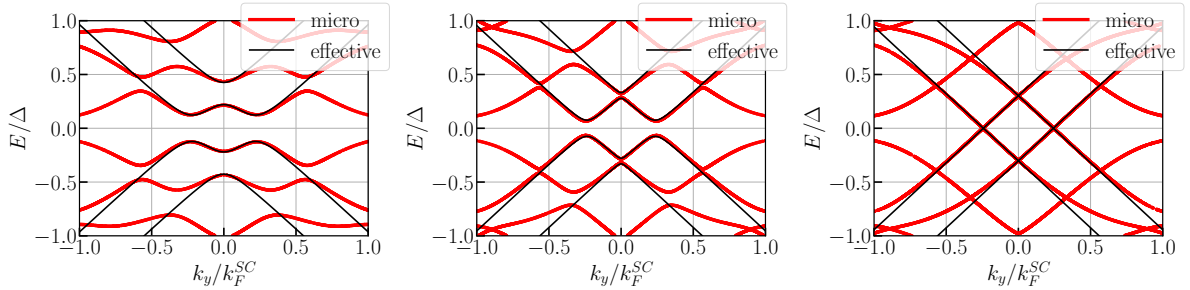

(a) $W/\xi = 1$ (b) $W/\xi = 2$ (c) $W/\xi = 10$

Figure 4.11: Comparisons between effective and microscopic (micro) spectra for $\nu = 2.8$ and various values of W/ξ. In (a) we set $W/\xi = 1$ and $\mu = \mu_{SC}/5.75$, $\Delta_0 = \Delta/5$, $\Delta_{12} = \Delta/6$. In (b) we set $W/\xi = 2$ and $\mu = \mu_{SC}/4.5$, $\Delta_0 = \Delta/10$, $\Delta_{12} = \Delta/12.5$. In (c) we set $W/\xi = 10$ and $\mu = \mu_{SC}/25.94$, $\Delta_0 = \Delta/3.35$, $\Delta_{12} = \Delta \times 10^{-4}$. The velocity is $v = v_F^{SC}/2$ and the microscopic parameters are the same as in Fig. 4.5.

the only possible ones for the QH-SC junction studied in the previous chapter, the right quantum Hall region allows the incoming electron to be transmitted to the upper right edge as an electron or as a hole via crossed Andreev reflection with respective amplitudes p_e^{R} and p_h^{R}. The situation is illustrated in Fig. 4.12, where we divide the junction into three parts: the upper part where $y \leq L/2$, the middle region containing the QH-SC interfaces where $-L/2 < y \leq L/2$, and the lower part where $y > L/2$.

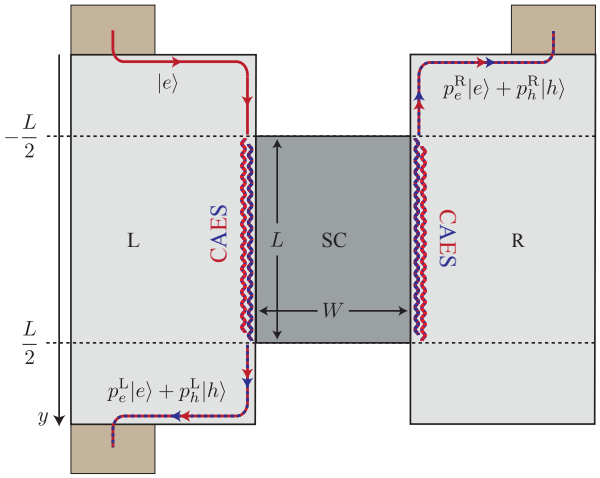

Figure 4.12: Finite QH-SC-QH junction where an incoming electron from the upper left reservoir can be transmitted to the lower left reservoir as an electron or as a hole with respective amplitudes p_e^{L} and p_h^{L}. The incoming electron can also be transferred to the upper right reservoir via non-local processes as an electron or as a hole with respective amplitudes p_e^{R} and p_h^{R}. The junction is divided into three parts: the upper part where $y \leq L/2$, the middle region including the QH-SC interfaces where $-L/2 < y \leq L/2$, and the lower part where $y > L/2$.

We now calculate the scattering amplitudes depicted in Fig. 4.12. To do so, we first need to determine the wave functions in each region of the junction. In the upper and lower regions they are respectively given by,

$$\psi_{\mathrm{up}}(y) = \begin{pmatrix} 1 \\ 0 \\ 0 \\ 0 \end{pmatrix} e^{ik_+ y} + p_e^{\mathrm{R}} \begin{pmatrix} 0 \\ 1 \\ 0 \\ 0 \end{pmatrix} e^{-ik_+ y} + p_h^{\mathrm{R}} \begin{pmatrix} 0 \\ 0 \\ 0 \\ 1 \end{pmatrix} e^{-ik_- y}, \tag{4.30}$$

$$\psi_{\mathrm{low}}(y) = p_e^{\mathrm{L}} \begin{pmatrix} 1 \\ 0 \\ 0 \\ 0 \end{pmatrix} e^{ik_+ y} + p_h^{\mathrm{L}} \begin{pmatrix} 0 \\ 0 \\ 1 \\ 0 \end{pmatrix} e^{ik_- y}, \tag{4.31}$$

where $k_\pm = (E \pm \mu)/(\hbar v)$. Since the calculation for the superconducting wave function is more complicated, we will explain it in detail. We consider the Hamiltonian (4.26) with $\Delta_{12} = \Delta_{21}$ and $\Delta_1 = \Delta_2 = \Delta_0$, and we perform the substitution $k \to -i\partial_y$ which leads to the real-space Hamiltonian,

$$H(y) = \begin{pmatrix} -i\hbar v\partial_y - \mu & 0 & \Delta_0 & \Delta_{12} \\ 0 & i\hbar v\partial_y - \mu & \Delta_{12} & \Delta_0 \\ \Delta_0 & \Delta_{12} & -i\hbar v\partial_y + \mu & 0 \\ \Delta_{12} & \Delta_0 & 0 & i\hbar v\partial_y + \mu \end{pmatrix}. \tag{4.32}$$

Writing the wave function in the middle region as $\psi_{SC}(y) = (u_1(y),\, u_2(y),\, u_3(y),\, u_4(y))^T$, the associated Schrödinger equation, $H(y)\psi_{SC}(y) = E\psi_{SC}(y)$, leads to $\psi'_{SC}(y) = A\psi_{SC}(y)$, with

$$A = \frac{i}{\hbar v} \begin{pmatrix} E+\mu & 0 & -\Delta_0 & -\Delta_{12} \\ 0 & -(E+\mu) & \Delta_{12} & \Delta_0 \\ -\Delta_0 & -\Delta_{12} & E-\mu & 0 \\ \Delta_{12} & \Delta_0 & 0 & -(E-\mu) \end{pmatrix}. \tag{4.33}$$

We can then write the wave function of the counter-propagating pairs of CAES as,

$$\psi_{SC}(y) = \sum_{\substack{s=\pm \\ n=\pm}} c_{sn}\phi_{sn}e^{\lambda_{sn}y}, \tag{4.34}$$

where c_{sn} are constants, λ_{sn} are the eigenvalues of A and ϕ_{sn} the associated eigenvectors. The eigenvalues can be written as $\lambda_{sn} = iq_{sn}$, with

$$q_{sn} = s\frac{1}{\hbar v}\sqrt{\mu^2 + \Delta_0^2 + E^2 - \Delta_{12}^2 + 2n\sqrt{\Delta_0^2E^2 + \mu^2(E^2 - \Delta_{12}^2)}}, \tag{4.35}$$

and the associated eigenvectors are given by

$$\phi_{sn} = \begin{pmatrix} E^2 + \hbar vEq_{sn} + n\sqrt{\Delta_0^2E^2 + \mu^2(E^2 - \Delta_{12}^2)} \\ \frac{\Delta_0\Delta_{12}(\mu^2 - E^2)}{\mu^2 + \hbar v\mu q_{sn} + n\sqrt{\Delta_0^2E^2 + \mu^2(E^2 - \Delta_{12}^2)}} \\ -\Delta_0(E+\mu)\frac{E^2 + \hbar vEq_{sn} + n\sqrt{\Delta_0^2E^2 + \mu^2(E^2 - \Delta_{12}^2)}}{\mu^2 + \hbar v\mu q_{sn} + n\sqrt{\Delta_0^2E^2 + \mu^2(E^2 - \Delta_{12}^2)}} \\ \Delta_{12}(E+\mu) \end{pmatrix}. \tag{4.36}$$

If we consider $\mu^2 + \Delta_0^2 + E^2 > \Delta_{12}^2$ (this is always true for the effective parameters determined above), the momentum q_{sn} is real as long as $|E| > \tilde{\delta}/2 = \mu\Delta_{12}/\sqrt{\mu^2 + \Delta_0^2}$, i.e, as long as the energy is not in the energy gap $\tilde{\delta}$ shown in Fig. 4.8a. However, since we are interested in low-energy physics, we typically consider $|E| < \tilde{\delta}/2$ such that the wave functions are evanescent along the superconducting interface. More precisely, in the following we will focus on the case $E = 0$. Note that here we have four terms in $\psi_{SC}(y)$ describing quasi-electrons and quasi-holes propagating in the positive and negative y-directions. This is in contrast to the QH-SC junction studied in the previous chapter, where we had only CAES propagating along the positive y-direction. To obtain the scattering coefficients we then need to match the wave functions as follows,

$$\psi_{\text{up}}(-L/2) = \psi_{SC}(-L/2), \tag{4.37}$$

$$\psi_{\text{low}}(L/2) = \psi_{SC}(L/2). \tag{4.38}$$

We now focus on the case $E = 0$, that greatly simplifies the analytical calculations, while the general case $E \neq 0$ can be done numerically. Knowing the scattering probabilities at zero energy is sufficient to calculate the conductance at zero temperature, whereas the calculation of the conductance at finite temperatures involves the integral of the scattering probabilities over energy, as discussed in Sec. 3.6.2 of the previous chapter. Moreover, at $E = 0$ the Fermi level is always in an energy gap, which is not the case at $E \neq 0$. When the Fermi level is not in an energy gap, the CAES can propagate along the superconductor, leading to an increase in the probabilities P_e^{L} and P_h^{L}. Furthermore, we saw numerically that in the limit $\Delta_0, \Delta_{12} \ll |E|$ the probabilities P_e^{R} and P_h^{R} tend to zero. At $E = 0$ we can rewrite the wave functions as

$$\psi_{\text{up}}(y) = \begin{pmatrix} 1 \\ 0 \\ 0 \\ 0 \end{pmatrix} e^{i\mu/(\hbar v)y} + p_e^{\text{R}}\begin{pmatrix} 0 \\ 1 \\ 0 \\ 0 \end{pmatrix} e^{-i\mu/(\hbar v)y} + p_h^{\text{R}}\begin{pmatrix} 0 \\ 0 \\ 0 \\ 1 \end{pmatrix} e^{i\mu/(\hbar v)y}, \tag{4.39}$$

$$\psi_{\text{low}}(y) = p_e^{\text{L}}\begin{pmatrix} 1 \\ 0 \\ 0 \\ 0 \end{pmatrix} e^{i\mu/(\hbar v)y} + p_h^{\text{L}}\begin{pmatrix} 0 \\ 0 \\ 1 \\ 0 \end{pmatrix} e^{-i\mu/(\hbar v)y}, \tag{4.40}$$

$$\begin{aligned} \psi_{SC}(y) = {} & c_1\begin{pmatrix} -i\left[\mu - i\Delta_{12} - \eta\right] \\ \Delta_0 \\ i\Delta_0 \\ \mu - i\Delta_{12} - \eta \end{pmatrix} e^{-i\eta/(\hbar v)y} + c_2\begin{pmatrix} -i\left[\mu - i\Delta_{12} + \eta\right] \\ \Delta_0 \\ i\Delta_0 \\ \mu - i\Delta_{12} + \eta \end{pmatrix} e^{i\eta/(\hbar v)y} + \\ & + c_3\begin{pmatrix} i\left[\mu + i\Delta_{12} - \eta^*\right] \\ \Delta_0 \\ -i\Delta_0 \\ \mu + i\Delta_{12} - \eta^* \end{pmatrix} e^{-i\eta^*/(\hbar v)y} + c_4\begin{pmatrix} i\left[\mu + i\Delta_{12} + \eta^*\right] \\ \Delta_0 \\ -i\Delta_0 \\ \mu + i\Delta_{12} + \eta^* \end{pmatrix} e^{i\eta^*/(\hbar v)y}, \end{aligned} \tag{4.41}$$

where we have introduced $\eta = \sqrt{\Delta_0^2 + (\mu - i\Delta_{12})^2}$ and the constants c_i $(i = 1, 2, 3, 4)$. Then, from the matching procedure, we obtain the following amplitudes,

$$p_e^{\mathrm{R}} = \Delta_0 \frac{\eta^* \sin[\eta L/(\hbar v)] \cos[\eta^* L/(\hbar v)] - \{\eta \cos[\eta L/(\hbar v)] + 2\Delta_{12} \sin[\eta L/(\hbar v)]\} \sin[\eta^* L/(\hbar v)]}{|\eta|^2 \{1 + \cos[\eta L/(\hbar v)] \cos[\eta^* L/(\hbar v)]\} + (\mu^2 + \Delta_0^2 + \Delta_{12}^2) \sin[\eta L/(\hbar v)] \sin[\eta^* L/(\hbar v)]} e^{-i\mu L/(\hbar v)}, \tag{4.42}$$

$$p_h^{\mathrm{R}} = \frac{\eta^*(\mu - i\Delta_{12}) \sin[\eta L/(\hbar v)] \cos[\eta^* L/(\hbar v)] - \eta(\mu + i\Delta_{12}) \sin[\eta^* L/(\hbar v)] \cos[\eta L/(\hbar v)]}{|\eta|^2 \{1 + \cos[\eta L/(\hbar v)] \cos[\eta^* L/(\hbar v)]\} + (\mu^2 + \Delta_0^2 + \Delta_{12}^2) \sin[\eta L/(\hbar v)] \sin[\eta^* L/(\hbar v)]}, \tag{4.43}$$

$$p_e^{\mathrm{L}} = \frac{|\eta|^2 \{\cos[\eta L/(\hbar v)] + \cos[\eta^* L/(\hbar v)]\} + \eta^*(i\mu + \Delta_{12}) \sin[\eta L/(\hbar v)] + \eta(i\mu - \Delta_{12}) \sin[\eta^* L/(\hbar v)]}{|\eta|^2 \{1 + \cos[\eta L/(\hbar v)] \cos[\eta^* L/(\hbar v)]\} + (\mu^2 + \Delta_0^2 + \Delta_{12}^2) \sin[\eta L/(\hbar v)] \sin[\eta^* L/(\hbar v)]} e^{-i\mu L/(\hbar v)}, \tag{4.44}$$

$$p_h^{\mathrm{L}} = -i\Delta_0 \frac{\eta \sin[\eta^* L/(\hbar v)] + \eta^* \sin[\eta L/(\hbar v)]}{|\eta|^2 \{1 + \cos[\eta L/(\hbar v)] \cos[\eta^* L/(\hbar v)]\} + (\mu^2 + \Delta_0^2 + \Delta_{12}^2) \sin[\eta L/(\hbar v)] \sin[\eta^* L/(\hbar v)]} e^{-i\mu L/(\hbar v)}. \tag{4.45}$$

As we need to take the squared absolute values of the above amplitudes to get the scattering probabilities, let us express them as sums of real and imaginary parts. To do so we write η as $\eta = a + ib$ with

$$a = \frac{1}{\sqrt{2}} \sqrt{\sqrt{(\mu^2 + \Delta_0^2 - \Delta_{12}^2)^2 + 4\mu^2 \Delta_{12}^2} + (\mu^2 + \Delta_0^2 - \Delta_{12}^2)}, \tag{4.46}$$

$$b = \frac{-1}{\sqrt{2}} \sqrt{\sqrt{(\mu^2 + \Delta_0^2 - \Delta_{12}^2)^2 + 4\mu^2 \Delta_{12}^2} - (\mu^2 + \Delta_0^2 - \Delta_{12}^2)}, \tag{4.47}$$

and we finally get the scattering probabilities,

$$P_e^{\mathrm{R}} = \Delta_0^2 \frac{\Delta_{12}^2 \left[\cos(\frac{2aL}{\hbar v}) - \cosh(\frac{2bL}{\hbar v})\right]^2 + \left[a \sinh(\frac{2bL}{\hbar v}) - b \sin(\frac{2aL}{\hbar v})\right]^2}{\left\{(a^2 + b^2)\left[1 + \left(\cos(\frac{2aL}{\hbar v}) + \cosh(\frac{2bL}{\hbar v})\right)/2\right] - (\mu^2 + \Delta_0^2 + \Delta_{12}^2)\left[\cos(\frac{2aL}{\hbar v}) - \cosh(\frac{2bL}{\hbar v})\right]/2\right\}^2}, \tag{4.48}$$

$$P_h^{\mathrm{R}} = \frac{\left[(b\Delta_{12} - a\mu) \sinh(\frac{2bL}{\hbar v}) + (a\Delta_{12} + b\mu) \sin(\frac{2aL}{\hbar v})\right]^2}{\left\{(a^2 + b^2)\left[1 + \left(\cos(\frac{2aL}{\hbar v}) + \cosh(\frac{2bL}{\hbar v})\right)/2\right] - (\mu^2 + \Delta_0^2 + \Delta_{12}^2)\left[\cos(\frac{2aL}{\hbar v}) - \cosh(\frac{2bL}{\hbar v})\right]/2\right\}^2}, \tag{4.49}$$

$$P_e^{\mathrm{L}} = 4 \frac{(a^2 + b^2)^2 \cos^2(\frac{aL}{\hbar v}) \cosh^2(\frac{bL}{\hbar v}) + \left[(a\mu - b\Delta_{12}) \sin(\frac{aL}{\hbar v}) \cosh(\frac{bL}{\hbar v}) + (b\mu + a\Delta_{12}) \cos(\frac{aL}{\hbar v}) \sinh(\frac{bL}{\hbar v})\right]^2}{\left\{(a^2 + b^2)\left[1 + \left(\cos(\frac{2aL}{\hbar v}) + \cosh(\frac{2bL}{\hbar v})\right)/2\right] - (\mu^2 + \Delta_0^2 + \Delta_{12}^2)\left[\cos(\frac{2aL}{\hbar v}) - \cosh(\frac{2bL}{\hbar v})\right]/2\right\}^2}, \tag{4.50}$$

$$P_h^{\mathrm{L}} = \frac{4\Delta_0^2 \left[a \sin(\frac{aL}{\hbar v}) \cosh(\frac{bL}{\hbar v}) + b \cos(\frac{aL}{\hbar v}) \sinh(\frac{bL}{\hbar v})\right]^2}{\left\{(a^2 + b^2)\left[1 + \left(\cos(\frac{2aL}{\hbar v}) + \cosh(\frac{2bL}{\hbar v})\right)/2\right] - (\mu^2 + \Delta_0^2 + \Delta_{12}^2)\left[\cos(\frac{2aL}{\hbar v}) - \cosh(\frac{2bL}{\hbar v})\right]/2\right\}^2}, \tag{4.51}$$

which sum to one as required.

As already discussed, in the limit $\Delta_{12} \to 0$ the system behaves as two independent QH-SC interfaces. In this limit we thus expect to find the scattering probabilities of a QH-SC junction. Taking $\Delta_{12} \to 0$ in the above formulas, we find $P_e^{\mathrm{R}} = P_h^{\mathrm{R}} = 0$ and

$$P_e^{\mathrm{L}}(\Delta_{12} \to 0) = \cos^2\left(\frac{\sqrt{\mu^2 + \Delta_0^2}}{\hbar v} L\right) + \frac{\mu^2}{\mu^2 + \Delta_0^2} \sin^2\left(\frac{\sqrt{\mu^2 + \Delta_0^2}}{\hbar v} L\right), \tag{4.52}$$

$$P_h^{\mathrm{L}}(\Delta_{12} \to 0) = \frac{\Delta_0^2}{\mu^2 + \Delta_0^2} \sin^2\left(\frac{\sqrt{\mu^2 + \Delta_0^2}}{\hbar v} L\right), \tag{4.53}$$

which are the same probabilities as those that would be obtained by using a simple one-dimensional effective model of a single QH-SC interface, i.e., by using the simple effective model considered in Sec. 3.5.3 of the previous chapter.

On the other hand, taking the limit $L \to \infty$ we have $P_e^{\mathrm{L}} = P_h^{\mathrm{L}} = 0$ and

$$P_e^{\mathrm{R}}(L \to \infty) = \frac{2\Delta_0^2}{\mu^2 + \Delta_0^2 + \Delta_{12}^2 + \sqrt{(2\mu\Delta_{12})^2 + (\mu^2 + \Delta_0^2 - \Delta_{12}^2)^2}}, \tag{4.54}$$

$$P_h^{\mathrm{R}}(L \to \infty) = 1 - P_e^{\mathrm{R}}(L \to \infty). \tag{4.55}$$

As expected, since the CAES are gapped along the superconductor, we find that the incoming electron is always transferred on the other side of the superconductor when $L \to \infty$. Moreover, when the condition $\Delta_{12}^2 > 2(\Delta_0^2 - \mu^2)$ holds, we have $P_h^{\mathrm{R}}(L \to \infty) > P_e^{\mathrm{R}}(L \to \infty)$. Namely, in that case the crossed Andreev transmission is dominant and the non-local conductance is negative.

We plot the scattering probabilities as a function of $L/\tilde{\xi}$ in Figs. 4.13, 4.14 and 4.15 for the same effective parameters in Figs. 4.9, 4.10 and 4.11, respectively. Here we have introduced the effective coherence length

$$\tilde{\xi} = \hbar v/|b|, \tag{4.56}$$

where v is the CAES velocity while b is defined in Eq. (4.47). As a reminder, the effective parameters were obtained by fitting the effective spectrum to the microscopic spectrum for different values of the filling factor ($\nu = 1.2, 2, 2.8$) and different widths of the superconductor ($W/\xi = 1, 2, 10$). In the figures below we indicate the value of the corresponding filling factor as well as the values of Δ_{12}/Δ (recall that Δ_{12} decreases with W/ξ and that Δ is the superconducting gap of the microscopic model).
For moderate values of Δ_{12}/Δ (see panels (a)-(b) of the figures below) and intermediate values of $L/\tilde{\xi}$ we observe Fabry-Pérot like oscillations, as discussed when studying a normal metal-superconductor-normal metal junction in Chap. 2 (see Sec. 2.1.5). These oscillations result from the different possible paths to be transmitted to the left or to the right, and they fade away as $L/\tilde{\xi}$ increases, giving rise to $P_e^{\mathrm{L}} \simeq P_h^{\mathrm{L}} \simeq 0$ and constant values of P_e^{L} and P_h^{R} when $L/\tilde{\xi} \gg 1$. The fact that P_e^{L} and P_h^{L} are close to zero when $L/\tilde{\xi} \gg 1$ is expected because the CAES are gapped along the superconductor. The constant values of P_e^{R} and P_h^{R} observed for $L/\tilde{\xi} \gg 1$ depend on the value of the parameters, see Eqs. (4.54) and (4.55).
For $\Delta_{12}/\Delta \lll 1$ [see panels (c)-(d)] we plot the scattering probabilities on two different scales. In panels (c) we consider the same values of $L/\tilde{\xi}$ than previously while in panels (d) we show the results on a smaller scale with a maximal value of $L/\tilde{\xi}$ of the order of 10^3-10^4. On the scale of panels (c) the probabilities P_e^{L} and P_h^{L} decrease with an exponential envelope accompanied by the increasing of P_e^{R} and P_h^{R}. Again, for $L/\tilde{\xi} \to \infty$ the probabilities P_e^{R} and P_h^{R} become constant and we have $P_e^{\mathrm{L}} = P_h^{\mathrm{L}} = 0$, as expected from the analytics. On the smaller scales of panels (d) we observe that the probabilities P_e^{R} and P_h^{R} are zero while the probabilities P_e^{L} and P_h^{L} show regular oscillations, similar to those of the single QH-SC interface studied in Chap. 3.

In the next subsection we plot the local and non-local conductances for the same parameter regimes as those considered here.

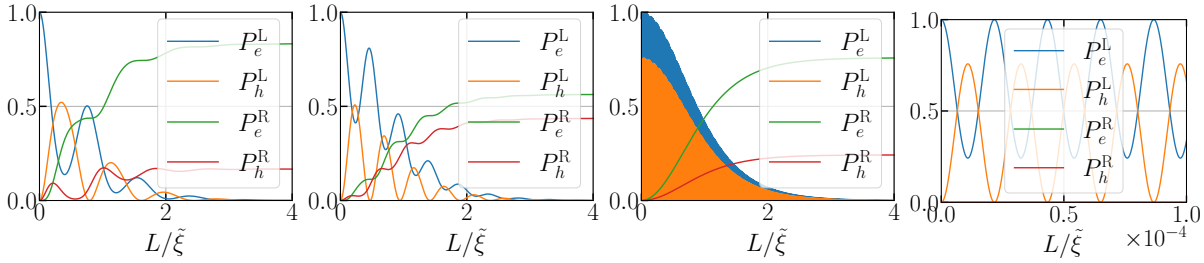

(a) $\Delta_{12} = \Delta/3$ (b) $\Delta_{12} = \Delta/8$ (c) $\Delta_{12} = 7\Delta \times 10^{-6}$ (d) $\Delta_{12} = 7\Delta \times 10^{-6}$

Figure 4.13: Scattering probabilities of the QH-SC-QH junction for $\nu = 1.2$ with the same parameters as in Fig. 4.9. We have indicated the values of Δ_{12} obtained by fitting the microscopic spectrum for (a) $W/\xi = 1$, (b) $W/\xi = 2$, and (c)-(d) $W/\xi = 10$.

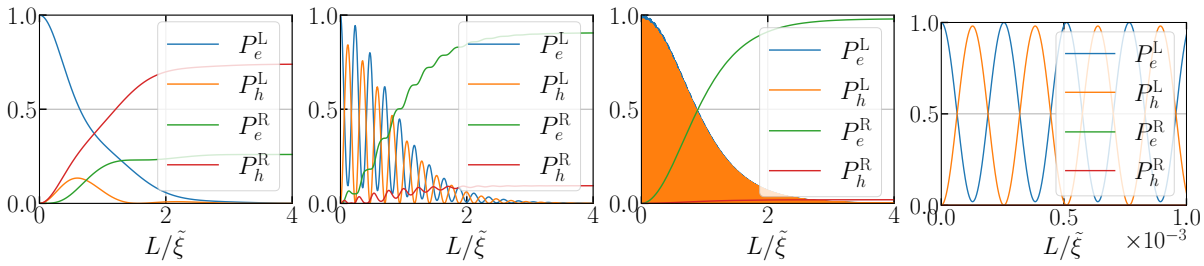

(a) $\Delta_{12} = \Delta/4.5$ (b) $\Delta_{12} = \Delta/12$ (c) $\Delta_{12} = 2\Delta \times 10^{-4}$ (d) $\Delta_{12} = 2\Delta \times 10^{-4}$

Figure 4.14: Scattering probabilities of the QH-SC-QH junction for $\nu = 2$ with the same parameters as in Fig. 4.10. We have indicated the values of Δ_{12} obtained by fitting the microscopic spectrum for (a) $W/\xi = 1$, (b) $W/\xi = 2$, and (c)-(d) $W/\xi = 10$.

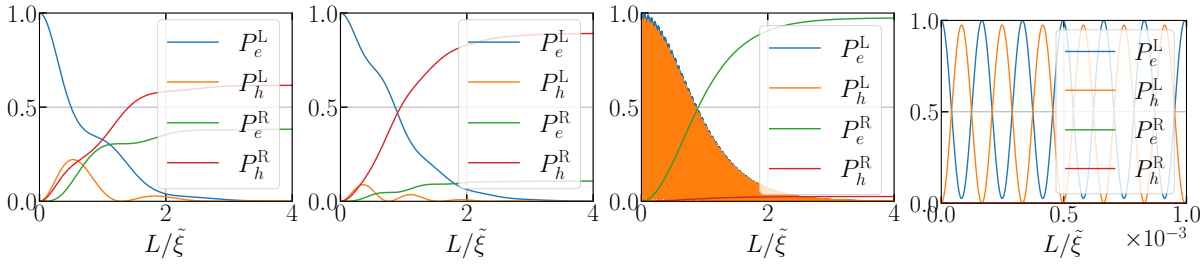

(a) $\Delta_{12} = \Delta/6$ (b) $\Delta_{12} = \Delta/12.5$ (c) $\Delta_{12} = \Delta \times 10^{-4}$ (d) $\Delta_{12} = \Delta \times 10^{-4}$

Figure 4.15: Scattering probabilities of the QH-SC-QH junction for $\nu = 2.8$ with the same parameters as in Fig. 4.11. We have indicated the values of Δ_{12} obtained by fitting the microscopic spectrum for (a) $W/\xi = 1$, (b) $W/\xi = 2$, and (c)-(d) $W/\xi = 10$.

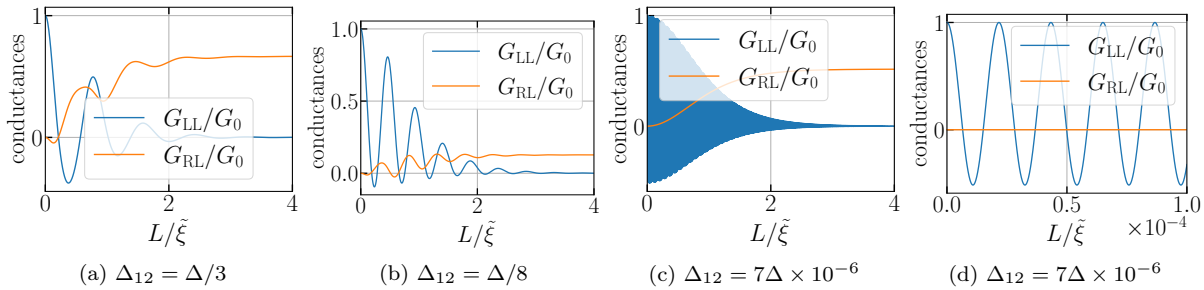

(a) $\Delta_{12} = \Delta/3$ (b) $\Delta_{12} = \Delta/8$ (c) $\Delta_{12} = 7\Delta \times 10^{-6}$ (d) $\Delta_{12} = 7\Delta \times 10^{-6}$

Figure 4.16: Local and non-local conductances of the QH-SC-QH junction for $\nu = 1.2$ with the same parameters as in Fig. 4.9. We have indicated the values of Δ_{12} obtained by fitting the microscopic spectrum for (a) $W/\xi = 1$, (b) $W/\xi = 2$, and (c)-(d) $W/\xi = 10$.

4.4.2 Local and non-local conductances

Experimentally, one can probe the different transmission processes by measuring the local and non-local conductances as introduced in Eqs. (4.1) and (4.2),

$$G_{\mathrm{LL}} = G_0(P_e^{\mathrm{L}} - P_h^{\mathrm{L}}), \tag{4.57}$$

$$G_{\mathrm{RL}} = G_0(P_e^{\mathrm{R}} - P_h^{\mathrm{R}}). \tag{4.58}$$

As illustrative examples, we plot the local and non-local conductances as a function of $L/\tilde{\xi}$ in Figs. 4.16, 4.17 and 4.18 for the same parameters as used to plot the scattering probabilities in Figs. 4.13, 4.14 and 4.15. Again, we indicate the values of Δ_{12}/Δ.
For moderate values of Δ_{12} [panels (a)-(b)] we observe that the local conductance G_{LL} goes to zero as $L/\tilde{\xi} \gg 1$, consistent with the scattering probabilities observed in Sec. 4.4.1. At the same time, the non-local conductance G_{RL} takes on a constant value when $L/\tilde{\xi} \gg 1$, depending on the values of P_e^{R} and P_h^{R}. If $P_e^{\mathrm{R}} > P_h^{\mathrm{R}}$, the non-local conductance is positive, while if $P_e^{\mathrm{R}} < P_h^{\mathrm{R}}$ it is negative. Thus, a negative non-local conductance is a clear signature of the crossed Andreev reflection occurring in the system. As discussed above [see the discussion below Eq. (4.55)], for $L/\tilde{\xi} \to \infty$ we have $P_e^{\mathrm{R}} < P_h^{\mathrm{R}}$ when $\Delta_{12}^2 > 2(\Delta_0^2 - \mu^2)$. Finally, at intermediate values of $L/\tilde{\xi}$ we observe oscillations in the local and non-local conductances due to the Fabry-Pérot type oscillations observed in the scattering probabilities. For $\Delta_{12}/\Delta \lll 1$ [panels (c)-(d)], we again show two different scales. On the scale of panels (c) the local conductance tends to zero when $L/\tilde{\xi} \gg$ while the non-local conductance takes on a constant value. On the smaller scale of panels (d) the non-local conductance is zero and the local conductance oscillates as a function of $L/\tilde{\xi}$. These local conductance oscillations are similar to the downstream conductance oscillations studied in Chap. 3 for a single QH-SC interface.

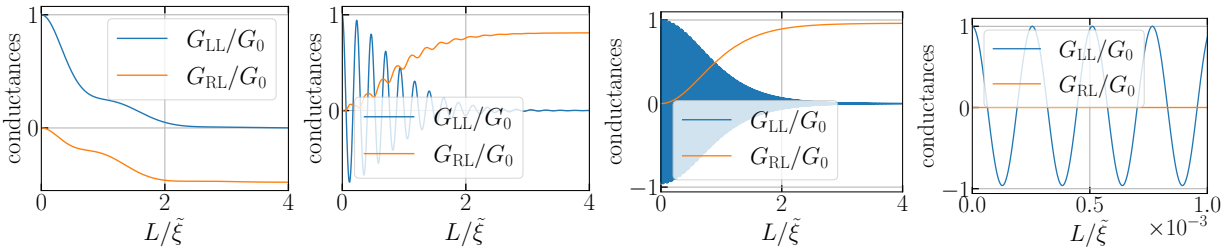

(a) $\Delta_{12} = \Delta/4.5$ (b) $\Delta_{12} = \Delta/12$ (c) $\Delta_{12} = 2\Delta \times 10^{-4}$ (d) $\Delta_{12} = 2\Delta \times 10^{-4}$

Figure 4.17: Local and non-local conductances of the QH-SC-QH junction for $\nu = 2$ with the same parameters as in Fig. 4.10. We have indicated the values of Δ_{12} obtained by fitting the microscopic spectrum for (a) $W/\xi = 1$, (b) $W/\xi = 2$, and (c)-(d) $W/\xi = 10$.

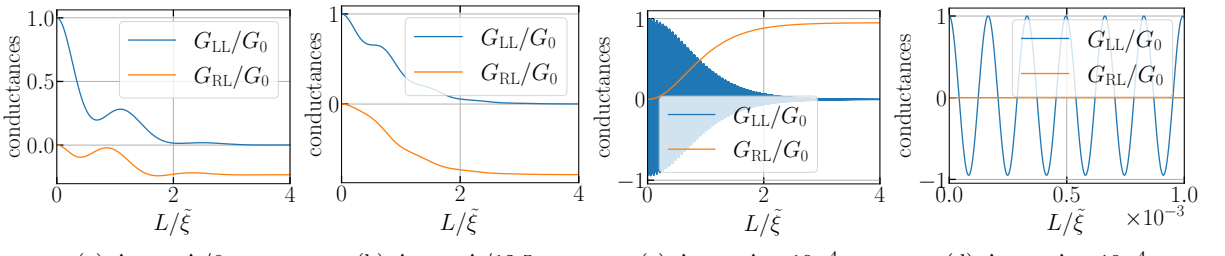

(a) $\Delta_{12} = \Delta/6$ (b) $\Delta_{12} = \Delta/12.5$ (c) $\Delta_{12} = \Delta \times 10^{-4}$ (d) $\Delta_{12} = \Delta \times 10^{-4}$

Figure 4.18: Local and non-local conductances of the QH-SC-QH junction for $\nu = 2.8$ with the same parameters as in Fig. 4.11. We have indicated the values of Δ_{12} obtained by fitting the microscopic spectrum for (a) $W/\xi = 1$, (b) $W/\xi = 2$, and (c)-(d) $W/\xi = 10$.

4.5 Conclusion

In this chapter we have studied a QH-SC-QH junction where a single spin-degenerate Landau level is filled in the quantum Hall region. We determined the spectrum of the junction by using a microscopic model and saw that the counter-propagating CAES on either side of the superconductor are gapped. As expected, we found that this energy gap decreases exponentially with W/ξ, where W is the width of the superconductor and ξ the superconducting coherence length.

We investigated the transport properties of the junction within a one-dimensional effective model, which allows a qualitative understanding. To determine the values of the effective parameters we fitted the effective energy spectrum to the microscopic spectrum. As mentioned in the introduction of this chapter, the scattering probabilities for an incoming electron are in competition and depend on the values of the length L of the QH-SC interfaces as well as on the width W of the superconductor. In agreement with intuition, we have seen that the effective superconducting coupling Δ_{12} between the two QH-SC interfaces decreases as the width W of the superconductor increases. It follows that the scattering probabilities calculated with our effective model become the same as those obtained for a QH-SC junction in the limit $\Delta_{12} \to 0$ (which corresponds to $W \to \infty$). On the other hand, as the length L of the QH-SC interfaces tends to infinity, we have seen that an incident state from one side of the superconductor is always transferred to the other side. This allows us to predict that in a quantum Hall-superconductor hybrid system where the superconductor has a finger shape of length L, such as in [Lee *et al.* 2017, Gül *et al.* 2022], an electron incident on the superconducting finger will be transferred to the other side of the finger only by non-local processes when $L/\tilde{\xi} \gg 1$ (here $\tilde{\xi}$ is an effective coherence length). We also looked at the local and non-local conductances of the junction, which are the quantities measured in the experiments. We observed oscillations in these quantities as a function of L and saw that the local conductance approaches zero and the non-local conductance becomes constant as $L/\tilde{\xi} \gg 1$, as expected from the scattering probabilities. In the limit $L \to \infty$ we gave a condition such that the non-local conductance is negative, which is a signature of the crossed Andreev reflection present in the system.

In order to get quantitative results, a two-dimensional model should be used to calculate the transport properties. Indeed, as we have seen in the previous chapter, the scattering probabilities depend strongly on the geometry of the system, which cannot be taken into account with a simple one-dimensional effective model.

For further studies, the case of spin-polarized electrons would be interesting to study because of its potential for topologically protected quantum computing. Indeed, a QH-SC-QH junction with a finger-shaped superconductor and spin-polarized electrons is a promising route to build a one-dimensional topological superconductor [Lindner *et al.* 2012, Clarke *et al.* 2013, Clarke *et al.* 2014, Mong *et al.* 2014, Prada *et al.* 2020]. Experiments with such platforms have already been performed [Lee *et al.* 2017, Gül *et al.* 2022], while tight-binding simulations [Beconcini *et al.* 2018, Galambos *et al.* 2022] and a one-dimensional model based on Green's functions [Kurilovich & Glazman 2022] have been studied. In our model, this would require adding a Zeeman splitting to lift the spin-degeneracy and a spin-orbit coupling term to allow the formation of Cooper pairs.

Chapter 5

Helical hinge modes coupled to a Zeeman field and a superconductor

Contents

In this last research project, we look at another platform where boundary modes are coupled to a superconductor. Namely, we study the effects of Zeeman and superconducting couplings on the helical hinge modes of a higher order topological insulator (HOTI) (the concept of HOTI was introduced in Sec. 2.3.5). While such couplings would gap the helical edge states of a first-order two-dimensional topological insulator, we will see in this chapter that under certain conditions they do not gap the helical hinge modes, but rather spatially split them by inducing shifts in the mass surface gap. This spatial splitting can then be used to engineer different types of topological phases and, in particular, one-dimensional Majorana modes.

5.1 Introduction

We have introduced the concept of two-dimensional topological insulators in Sec. 2.3, where we showed that these materials have a surface that is gapped by a mass term and possess chiral edge states when time-reversal symmetry is broken, while they possess helical edge states when time-reversal symmetry is preserved. We have also shown that the edges of topological insulators realize mass domain walls

where the mass term changes sign at the edges, leading to topological metallic boundary modes. In addition, in Sec. 2.3.5 we have introduced the concept of HOTIs possessing boundary modes of dimension $d-n$, where d is the material dimension while n is the order. Here the boundary modes are protected by a crystalline symmetry (e.g. inversion, rotation or mirror symmetry) which is preserved by the $(d-n)$-dimensional boundaries. Such topological insulators protected by a crystalline symmetry with $n=1$ are called topological crystalline insulators [Fu 2011]. As discussed in Sec. 2.3.5, the hinges of a three-dimensional second-order topological insulator realize natural mass domain walls leading to the appearance of one-dimensional boundary modes [Schindler *et al.* 2018a]. Hence, time-reversal invariant three-dimensional topological insulators of order two exhibit one-dimensional helical hinge modes. Such helical hinge modes have been predicted to appear in strained SnTe [Schindler *et al.* 2018a], and they have been observed for the first time in bismuth using scanning-tunnelling microscopy and Josephson interferometry [Schindler *et al.* 2018b] (this experiment is detailed in Sec. 2.3.5). In the SnTe material, the hinge modes are protected by mirror symmetry, while in bismuth they are protected by the combination of inversion and rotation symmetries. Moreover, helical hinge modes protected by rotation symmetry were also predicted in transition metal dichalcogenides XTe_2 (X = Mo, W) [Wang *et al.* 2019] and observed in WTe_2 via Josephson interferometry measurements [Choi *et al.* 2020] (here the authors have spatially resolved the hinge states by analyzing the magnetic field interference of the supercurrent in Nb-WTe_2-Nb Josephson junctions).

In this chapter we consider helical hinge states protected by mirror symmetry. We start from the surface of a topological crystalline insulator in the (xy) plane and a mirror plane in the (xz) plane. Tilting this surface creates to new surfaces where mirror symmetry is broken while the junction between these two surfaces, i.e. the hinge, is still mirror symmetric and hosts helical modes. Here we consider a hinge located at $y=0$ and study the effects of Zeeman and superconducting couplings on the helical hinge states. The HOTI surface we consider has two mirror-symmetry protected Dirac cones which are separated in momentum space by $2k_0$ and gapped by the mass surface gap m. At first glance, the surface of a HOTI hosting helical hinge modes seems very similar to the surface of a quantum spin Hall (QSH) insulator. However, the edge states of the QSH phase are protected only by time-reversal while the helical hinge modes require time-reversal and mirror symmetries. Therefore, a Zeeman field destroys the QSH phase by breaking the time-reversal symmetry. Furthermore, the helical edge states of a QSH insulator are gapped when coupled to an s-wave superconductor. In contrast, the helical hinge modes of a HOTI survive to a Zeeman field as long as the Zeeman gap is smaller than vk_0, where v is the velocity of the hinge modes. Moreover, under certain conditions which we will give in this chapter, the helical hinge modes can also survive to a superconducting coupling. When they survive to the Zeeman and/or superconducting couplings (depending whether both or only one are applied), we find that the helical modes are spatially split instead of being gapped. The spatial splitting occurs because the couplings induce shifts in the mass function such that the resulting effective mass vanishes at different spatial locations, depending on the values of the couplings. As we will see, when only a Zeeman coupling is turned on, the helical fermionic hinge mode is split into two chiral fermionic modes surrounding a quantum anomalous Hall (QAH) region with the spin of the two chiral modes of opposite polarization. On the other hand, the helical fermionic mode is split into two helical Majorana modes surrounding a surface-based helical topological superconductor when only a superconducting coupling is considered. When both Zeeman and superconducting couplings are present, different scenarios are possible depending on the ratio between the two couplings. In fact, this spatial splitting was originally proposed by Queiroz and Stern [Queiroz & Stern 2019]. However, here we derive a more general formula for the hinge mode wave functions and we study splitting scenarios not considered by these authors.

In Sec. 5.2 we derive the low-energy Hamiltonian describing the helical hinge modes and then we add the Zeeman and superconducting couplings to it. In Sec. 5.4 we determine the energy spectrum of the hinge modes whilst in Sec. 5.5 we derive their wave functions and present the different splitting scenarios. In Sec. 5.6 we analyse numerically the new scenarios and, finally, we conclude and provide perspectives in Sec. 5.7.

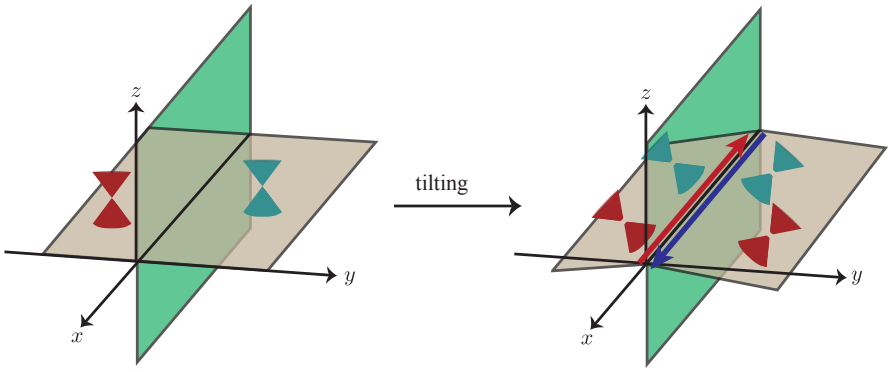

Figure 5.1: Mirror-symmetry protected surface and hinge modes preserving time-reversal invariance. We start from the surface of a topological crystalline insulator in the (xy) plane with two mirror-symmetry protected Dirac cones, where the mirror plane is in the (xz) plane and is represented in green. Tilting the surface in a mirror symmetry–preserving way gaps the Dirac cones and forms a Kramers pair of hinge states between two surfaces with opposite tilts. Note that the y-coordinate should follow the edges of the tilted surfaces.

5.2 The model Hamiltonian

The model originates from the surface in the (xy) plane of a three-dimensional topological crystalline insulator preserving time-reversal and mirror symmetries with two Dirac cones and a mirror plane in the (xz) plane, see Fig. 5.1. By tilting this surface out of its mirror symmetry plane, we obtain two surfaces connected by a hinge, each with two gapped Dirac cones. As shown in [Schindler *et al.* 2018a], if the tilt is such that the two resulting surfaces are mirror images of each other, the Dirac Hamiltonian describing them has a mass term of opposite sign on the two surfaces, and a Kramers pair of domain wall states forms at the hinge, see Fig. 5.1. These domain wall states are the helical hinge states we are interested in. In the next subsection we derive the Hamiltonian describing one of these two tilted surfaces and we then add the Zeeman and superconducting couplings to this Hamiltonian.

5.2.1 Hamiltonian of the HOTI surface

To derive the Hamiltonian of the HOTI surface we use symmetry arguments. Since the surface preserves time-reversal symmetry and has a mirror symmetry plane, it has two Dirac cones (valleys) that lie in momentum space at $\vec{k} = \pm\vec{k}_0 = \pm(k_x^0, k_y^0)$ [Schindler *et al.* 2018a]. Hence, as we consider spinful electrons, the Hamiltonian must be written in a 4×4 basis composed of spin and valley subspaces. The most general form of the Hamiltonian thus reads

$$H(\vec{k}) = \sum_{ij} h_{ij}(\vec{k})\sigma_i\rho_j, \qquad \{i,j\} = 0,x,y,z, \tag{5.1}$$

where σ_i and ρ_j represent respectively the Pauli matrices associated to the spin and valley subspaces and $\vec{k} = (k_x, k_y)$ is the surface momentum vector. To determine the value of the different terms we impose symmetries and we give the low energy contributions. Because other surface and bulk states are at higher energies, the low energy limit describes well the hinge modes. As we will see, the symmetries we consider allow us to recover the Hamiltonian given in [Schindler *et al.* 2018a] after a basis change. Moreover, the symmetries are chosen in order to reproduce the Hamiltonian of [Queiroz & Stern 2019, Supplementary Materials]. First, we impose an effective valley symmetry $V = \sigma_z\rho_x$ so that $VH(\vec{k})V^{-1} = H(\vec{k})$. This symmetry says that the system is invariant when interchanging the valleys and reversing the spins. Then we impose the time-reversal symmetry $T = i\sigma_y\kappa$, where κ is the complex conjugation (the time-reversal symmetry operator was derived in Sec. 2.3.3.1). To preserve time-reversal invariance, the Hamiltonian must satisfy $TH(\vec{k})T^{-1} = H(-\vec{k})$. In addition, since we are going to consider pairings between states

with opposite momenta, the two Dirac cones must be centered close to $\vec{k} = 0$ for an intra-cone pairing to be possible at low-energy. This implies that the momentum separation $2|\vec{k}_0|$ between the two cones must be small. As we will see, considering a small value of $\vec{k}_0$ corresponds to weakly break the inversion symmetry $I = \rho_x$ which interchanges the two valleys. Note that $I = \rho_x$ is a special type of inversion symmetry since it is restricted to the surface. As already discussed in Sec. 2.3.4, the Hamiltonian is inversion symmetric if $IH(\vec{k})I^{-1} = H(-\vec{k})$. Finally, the mirror symmetry that protects the hinge modes is given by $M = i\sigma_y\rho_z$ and the Hamiltonian must satisfy $MH(k_x, k_y)M^{-1} = H(-k_x, k_y)$ for the surface to be gapless. This relation indicates that the mirror plane described by M is in the (xz) plane, as depicted in Fig. 5.1. Moreover, the presence of ρ_z indicates that the valleys have opposite mirror eigenvalues. These symmetries are summarized in Tab. 5.1. Applying them to the general Hamiltonian (5.1) we can determine which terms preserve them. The results are summarized in Tab. 5.2. We can

Symmetry	Operator	Condition on H
Valley	$V = \sigma_z\rho_x$	$VH(\vec{k})V^{-1} = H(\vec{k})$
Time-reversal	$T = i\sigma_y\kappa$	$TH(\vec{k})T^{-1} = H(-\vec{k})$
Inversion	$I = \rho_x$	$IH(\vec{k})I^{-1} = H(-\vec{k})$
Mirror	$M = i\sigma_y\rho_z$	$MH(k_x, k_y)M^{-1} = H(-k_x, k_y)$

Table 5.1: Summary of the symmetry operators and the corresponding conditions on the Hamiltonian.

V	T	I	M
$h_{00}(\vec{k})\sigma_0\rho_0$	even	✓	✓
$h_{0x}(\vec{k})\sigma_0\rho_x$	even	✓	✗
$h_{xy}(\vec{k})\sigma_x\rho_y$	even	✗	✓
$h_{xz}(\vec{k})\sigma_x\rho_z$	odd	✓	✓
$h_{yy}(\vec{k})\sigma_y\rho_y$	even	✗	✗
$h_{yz}(\vec{k})\sigma_y\rho_z$	odd	✓	✓
$h_{z0}(\vec{k})\sigma_z\rho_0$	odd	✗	✓
$h_{zx}(\vec{k})\sigma_z\rho_x$	odd	✗	✓

Table 5.2: Symmetries of the different terms of the general Hamiltonian (5.1). The valley symmetry (V) is respected by the corresponding terms in the table. Time-reversal symmetry (T) gives the parity of the terms (odd or even) and we indicate if inversion (I) and mirror (M) symmetries are preserved (✓) or broken (✗).

express each term of Tab. 5.2 in the low energy limit in units of $\hbar = 1$ as follows:

- $h_{00}(\vec{k})\sigma_0\rho_0 = \varepsilon_0(\vec{k})\sigma_0\rho_0 = constant$ is a constant that can be set to zero.
- $h_{xz}(\vec{k})\sigma_x\rho_z$ and $h_{yz}(\vec{k})\sigma_y\rho_z$ correspond to the usual term $v\vec{k}\cdot\vec{\sigma}\rho_z$ describing the helical surface states with velocity v and same helicity in each Dirac cone.
- $h_{0x}(\vec{k})\sigma_0\rho_x$ breaks mirror symmetry and corresponds to a mass surface gap $m\rho_x$ which gap the two Dirac cones on the surface.
- $h_{xy}(\vec{k})\sigma_x\rho_y$ and $h_{yy}(\vec{k})\sigma_y\rho_y$ break inversion symmetry and correspond to a Rashba like coupling that reads $v(\vec{k}_0\times\vec{\sigma})\cdot\hat{z}\rho_y$ where we recall that $\vec{k}_0$ is the momentum separation between the two valleys and $\hat{z}$ is the unit vector normal to the surface (this is the inversion symmetry breaking term that is zero when $\vec{k}_0 = 0$). Note that the term $k_x^0\sigma_y\rho_y$ also breaks the mirror symmetry but, as we will see in the next section, it does not gap the Dirac cones.
- $h_{z0}(\vec{k})\sigma_z\rho_0$ and $h_{zx}(\vec{k})\sigma_z\rho_x$ break inversion symmetry and are odd. Such terms can be neglected at low-energy.

Hence, the low energy Hamiltonian can be written as,

$$H = v\vec{k} \cdot \vec{\sigma}\rho_z + v(\vec{k}_0 \times \vec{\sigma}) \cdot \hat{z}\rho_y + m\rho_x. \tag{5.2}$$

This Hamiltonian is the same as the one given in the supplementary material of [Queiroz & Stern 2019]. Moreover, performing the substitution $H \to UHU^{-1}$ where $U = e^{i(\pi/4)\sigma_y\rho_z}e^{i(\pi/4)\rho_x}e^{i(\pi/4)\sigma_z\rho_y}$, we recover the Hamiltonian given in Ref. [Schindler *et al.* 2018a] describing a helical HOTI with hinge modes protected by mirror symmetry $M = i\sigma_x$. In this basis, the other symmetry operators read $V = \rho_z$, $T = \sigma_y\rho_y\kappa$, and $I = \sigma_y\rho_z$. If the mass term m and k_0 are zero, the Hamiltonian (5.2) describes the surface of a three-dimensional topological crystalline insulator with mirror-protected surface states, which is exactly what we wanted. For example, the material SnTe in its rock-salt form is a topological crystalline insulator where the surfaces are not gapped and the surface states are protected by mirror symmetry [Hsieh *et al.* 2012]. However, mirror symmetry can be broken by tilting the surface (as in Fig. 5.1), leading to a non-zero mass surface gap m, and hinge modes can appear at a hinge where mirror symmetry is preserved, so strained SnTe is expected to be a HOTI [Schindler *et al.* 2018a]. As we have already said, and detailed in Chap. 2, the boundary modes of a topological insulator are located where the mass term of the Dirac Hamiltonian changes sign. Thus, in order to obtain hinge modes from this Hamiltonian, we must consider a spatially varying mass surface gap which changes sign at the hinge [Schindler *et al.* 2018a, Schindler *et al.* 2018b]. In this manuscript we will focus on a single hinge located at $y = 0$ and consider a mass profile such that $m(y \to \pm\infty) = \pm m_0$, with $m_0 > 0$ and $m(y = 0) = 0$. For example we can take,

$$m(y) = m_0 \tanh(y/y_0), \tag{5.3}$$

where y_0 is the sharpness of the mass domain wall.

Next, we add a the Zeeman and a superconducting coupling terms to the Hamiltonian. Since we are focusing on a single hinge located at $y = 0$, we can consider these couplings as applied near this hinge, as shown in Fig. 5.2.

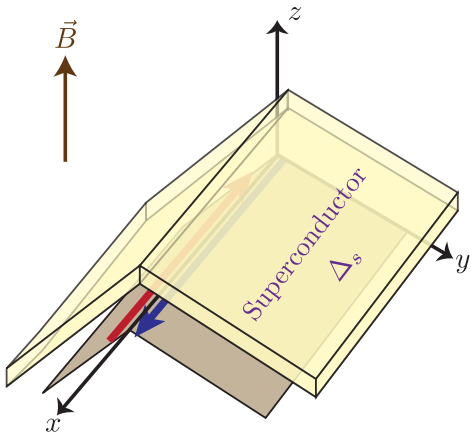

Figure 5.2: Helical hinge modes coupled to a Zeeman field $\vec{B} = B^z\hat{u}_z$ and to an s-wave superconductor with order parameter Δ_s. Since we focus on a single hinge located at $y = 0$, we present the couplings as they apply to the vicinity of a single hinge.

5.2.2 Adding the Zeeman field

We now consider applying an external Zeeman field in the z direction, either by a magnetic field or by proximity to a ferromagnet. Since the surface Dirac cones of the HOTI are separated by a distance $2k_0$, with $k_0 = |\vec{k}_0|$, a slowly varying Zeeman field $\vec{B}$ will act diagonally in the valley subspace. Hence, we can add the Zeeman field into our Hamiltonian by performing the substitution $H \to H + \vec{B} \cdot \vec{\sigma}$, with $\vec{B} = B^z\ \hat{u}_z$. Note that this additional term breaks time-reversal symmetry. For simplicity we will consider a constant value of B^z in this manuscript.

5.2.3 Adding the superconducting coupling

We now consider an additional coupling of the region around the hinge to a superconductor, so that it induces pairing at the surface by proximity effect (see Fig. 5.2). We add the superconductivity at the mean-field level by introducing a particle-hole subspace τ_z and we consider two types of singlet pairings acting differently in the valley subspace and characterized by Δ and Δ_0. Before presenting the coupling terms associated with Δ and Δ_0, it is useful to change the basis so that the results are more intuitive. Indeed, we can choose a basis where the mass term that gaps the valleys can be interpreted as an applied effective magnetic field of opposite sign at each valley [Khalaf 2018]. For our model, the change of basis can be done by performing the following unitary transformation [Queiroz & Stern 2019],

$$\tilde{H}(\vec{k}) = U^\dagger H(\vec{k}) U, \tag{5.4}$$

$$U = \frac{1}{2}\exp\{i\pi\sigma_z\rho_y/4\}(\rho_+ + \sigma_z\rho_-), \tag{5.5}$$

where $\rho_\pm = \rho_x \pm i\rho_y$ and the *tilde* notation indicates that we are in the new basis. In this new basis the modified valley degree of freedom $\rho_\pm$ can be interpreted as an orbital degree of freedom such as $|\pm\rangle = |p_\pm\rangle = |p_x \pm ip_y\rangle$. Under the above transformation the Hamiltonian becomes,

$$\tilde{H}(\vec{k}) = v\vec{k}\cdot\vec{\sigma} + \vec{B}_v\cdot\vec{\sigma}\rho_z + B^z\sigma_z, \tag{5.6}$$

where $\vec{B}_v = (vk_x^0, vk_y^0, m)$ is an effective magnetic field with opposite sign in each valley. In the new basis the symmetry operators become

$$\tilde{V} = \rho_z, \quad \tilde{T} = i\sigma_y\rho_x\kappa, \quad \tilde{I} = \sigma_z\rho_z, \quad \tilde{M} = i\sigma_y, \tag{5.7}$$

where the Pauli matrices ρ_i are now written in the new valley subspace describing orbitals $|p_x \pm ip_y\rangle$ for instance.

We now include superconductivity at the mean field level by adding a particle-hole subspace such that the (single-particle) Hamiltonian (5.6) takes the form of a BdG Hamiltonian[1],

$$\tilde{H}_{BdG}(\vec{k}) = \begin{pmatrix} \tilde{H}(\vec{k}) & \tilde{H}_\Delta \\ \tilde{H}_\Delta^\dagger & -\tilde{T}\tilde{H}(-\vec{k})\tilde{T}^{-1} \end{pmatrix}, \tag{5.8}$$

where $\tilde{H}(\vec{k})$ and $-\tilde{T}\tilde{H}(-\vec{k})\tilde{T}^{-1}$ describe the electron and hole subspaces respectively, while $\tilde{H}_\Delta$ describes the superconducting coupling. To determine $\tilde{H}_\Delta$ we need to describe the electron pairing, so we enter the second quantization formalism by introducing the creation operators $c^\dagger_{s\rho}(\vec{k})$, which creates an electron of spin $s = \uparrow, \downarrow$ in the valley $\rho = \pm$ with momentum $\vec{k}$. Introducing the spinor of fermionic operators

$$\tilde{\Psi}_{\vec{k}} = \begin{pmatrix} c_{\uparrow+}(\vec{k}) & c_{\uparrow-}(\vec{k}) & c_{\downarrow+}(\vec{k}) & c_{\downarrow-}(\vec{k}) \end{pmatrix}^T, \tag{5.9}$$

we can write the second-quantized Hamiltonian as follows,

$$\tilde{\mathcal{H}} = \tilde{\mathcal{H}}_0 + \tilde{\mathcal{H}}_\Delta, \tag{5.10}$$

$$\tilde{\mathcal{H}}_0 = \sum_{\vec{k}} \tilde{\Psi}^\dagger_{\vec{k}} \tilde{H}(\vec{k}) \tilde{\Psi}_{\vec{k}}, \tag{5.11}$$

$$\tilde{\mathcal{H}}_\Delta = \sum_{\vec{k}} \left[\Delta_0 \left(c_{\uparrow+}(\vec{k})c_{\downarrow-}(-\vec{k}) + c_{\uparrow-}(\vec{k})c_{\downarrow+}(-\vec{k}) \right) + \Delta \left(c_{\uparrow+}(\vec{k})c_{\downarrow+}(-\vec{k}) + c_{\uparrow-}(\vec{k})c_{\downarrow-}(-\vec{k}) \right) + h.c. \right], \tag{5.12}$$

where Δ_0 couples fermions of opposite orbitals (inter-orbital pairing) and Δ couples fermions of the same orbital (intra-orbital pairing). For simplicity, we assume that the inter- and intra-orbital couplings are

[1] We derived the BdG Hamiltonian describing a BCS superconductor in Eq. (B.30).

real[2] and constant. Then, introducing the following Nambu basis,

$$\tilde{\Phi}_{\vec{k}} = \Big(c_{\uparrow+}(\vec{k}) \quad c_{\uparrow-}(\vec{k}) \quad c_{\downarrow+}(\vec{k}) \quad c_{\downarrow-}(\vec{k}) \quad -c^{\dagger}_{\downarrow-}(-\vec{k}) \quad -c^{\dagger}_{\downarrow+}(-\vec{k}) \quad c^{\dagger}_{\uparrow-}(-\vec{k}) \quad c^{\dagger}_{\uparrow+}(-\vec{k})\Big)^{T}, \tag{5.13}$$

we can re-write the second-quantized Hamiltonian (5.10) in a BdG-like form,

$$\tilde{\mathcal{H}}(\vec{k}) = \frac{1}{2}\sum_{k} \tilde{\Phi}^{\dagger}_{\vec{k}} \tilde{H}_{BdG}(\vec{k}) \tilde{\Phi}_{\vec{k}}, \tag{5.14}$$

where $\tilde{H}_{BdG}$ recovers the Hamiltonian (5.8) if we take $\tilde{H}_{\Delta} = \Delta_0 + \Delta\rho_x$. Introducing the Pauli matrices τ_i in particle-hole subspace, we can finally write the single-particle BdG Hamiltonian as follows,

$$\tilde{H}_{BdG} = v\vec{k}\cdot\vec{\sigma}\tau_z + \vec{B}_v\cdot\vec{\sigma}\rho_z\tau_z + B^z\sigma_z + (\Delta_0 + \Delta\rho_x)\tau_x. \tag{5.15}$$

As any BdG-like Hamiltonian, the second-quantized and single-particle Hamiltonians (5.14) and (5.15) preserve particle-hole symmetry (particle-hole symmetry is presented in App. B.4). In particular, the second-quantized Hamiltonian must respect $\tilde{\mathcal{H}} = \tilde{P}\tilde{\mathcal{H}}\tilde{P}^{-1}$ while the single-particle Hamiltonian should preserve $\tilde{P}\tilde{H}_{BdG}(\vec{k})\tilde{P}^{-1} = -\tilde{H}_{BdG}(-\vec{k})$, with $\tilde{P}$ the particle-hole symmetry operator. This is satisfied for $\tilde{P} = i\tau_y U_{\tilde{T}}\kappa$, where $U_{\tilde{T}} = i\sigma_y\rho_x$ is the unitary part of the time-reversal symmetry operator written in the new basis.

Before we focus on the hinge states, let's plot the spectrum of the HOTI surface for different parameter regimes.

5.3 Energy spectrum of the HOTI surface

Here we look at the energy spectrum of the HOTI surface for different values of the couplings. We first consider the case where there is no Zeeman or superconducting coupling. We then consider the effect of these couplings independently, and finally discuss the case where both are present. We always give an analytical formula for the spectrum, which is obtained by diagonalizing the BdG Hamiltonian (5.15) with the help of the *Mathematica* software. In the plots presented in this subsection, the parameters are given in arbitrary units and we set $v = 1$. When considering non-zero superconducting couplings Δ and Δ_0, we give a condition on the Δ pairing that is necessary for the existence of zero-energy states. This condition will be useful when discussing the splitting of the hinge modes. Here we will observe gap closings as a function of parameters corresponding to topological phase transitions, as discussed in Sec. 2.3.4.

5.3.1 No Zeeman, no pairing

When no couplings are present, the spectrum of the surface is given by

$$E_{\sigma\rho\tau}(\vec{k}) = \sigma\tau\sqrt{v^2\left[\left(k_x + \rho k_x^0\right)^2 + \left(k_y + \rho k_y^0\right)^2\right] + m^2}, \tag{5.16}$$

where $\sigma = \pm$ describes the spin degree of freedom, $\rho = \pm$ stands for the orbital degree of freedom and $\tau = \pm$ corresponds to electron/hole particle type. This spectrum exhibits two Dirac cones located at $\vec{k} = \pm\vec{k}_0$ and gapped by $2|m|$. We represent the gapped ($m \neq 0$) and non-gapped ($m = 0$) situations in Fig. 5.3. Let us mention that the condition $m = 0$ is satisfied at the hinge of the HOTI surface, from where we expect conducting states located at the hinge.

[2] Indeed, time-reversal symmetry imposes that both gaps have the same phase such that we are left with a global phase that can be gauged out (see Eq. (2.13) and the related discussion).

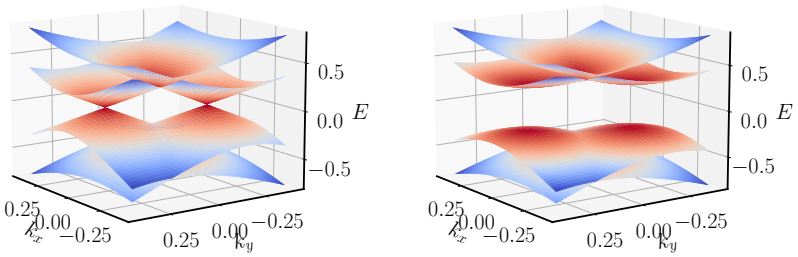

(a) (b)

Figure 5.3: Spectrum of the HOTI surface with no couplings. In (a) we set $m = 0$ and we see the two surface Dirac cones while in (b) we set $m = 0.25$. The other parameters are $k_x^0 = 0.1$, $k_y^0 = 0.2$, and $B^z = \Delta = \Delta_0 = 0$.

5.3.2 Zeeman field

When only a Zeeman field $\vec{B} = B^z \hat{u}_z$ is present, the energy spectrum of the surface is given by,

$$E_{\sigma\rho\tau}(\vec{k}) = \sigma\tau\sqrt{v^2\left[\left(k_x + \rho k_x^0\right)^2 + \left(k_y + \rho k_y^0\right)^2\right] + \left(m + \rho\tau B^z\right)^2}. \tag{5.17}$$

The two Dirac cones of this spectrum are not gapped when $m = \pm B^z$. More precisely, a Dirac cone located at $\vec{k} = -\rho\vec{k}_0$ is gapped by $2|m + \rho\tau B^z|$ and so the gap closes when $m = -\rho\tau B^z$. If the mass varies in space from $-m_0$ to $+m_0$ with $m_0 > B^z$, this yields two values $y_\pm$ where we have $m = \pm B^z$ and at each location the gap in one of the cones closes. As we will see in the next section, the two hinge modes forming the helical pair are each located in a different cone, so that the Zeeman field spatially split the helical pair into two chiral states located at $y = \pm y_Z$. Note that here the two Dirac cones are not gapped when $m = B^z$ (or $m = -B^z$) because of the electron-hole subspace. For example, if we consider only the electron subspace ($\tau = +$) with $m = B^z$, then only the Dirac cone associated to $\rho = -1$ is gapless when $m = B^z$ (considering the hole subspace it is the other Dirac cone that is not gapped). As illustrations, we plot this energy spectrum with $m = B^z$ and $m \neq B^z$ in Fig. 5.4.

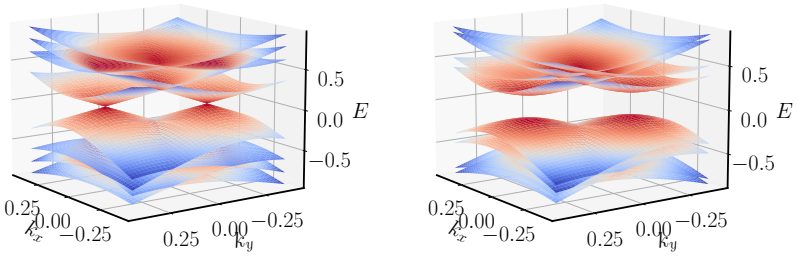

(a) (b)

Figure 5.4: Spectrum of the HOTI surface with only a Zeeman couplings. In (a) we set $m = B^Z$ and we see the two Dirac cones while in (b) we set $B^z = 0.1 \neq m$ and the spectrum is gapped. The other parameters are $m = 0.25, k_x^0 = 0.1$, $k_y^0 = 0.2$, and $\Delta = \Delta_0 = 0$.

5.3.3 Superconducting coupling

When considering only the superconducting couplings Δ and Δ_0 the energy spectrum is given by

$$E_{\sigma\rho\tau}(\vec{k}) = \sigma\tau\sqrt{v^2\left(k^2+k_0^2\right)+m^2+\Delta_0^2+\Delta^2+2\rho\sqrt{v^4\left(\vec{k}\cdot\vec{k}_0\right)^2+\Delta^2\left(v^2k_0^2+m^2+\Delta_0^2\right)}}. \tag{5.18}$$

Searching the values of $\vec{k}$ for which E^2 is minimal we find two possibilities: i) the Dirac cones are degenerate and located at $\vec{k}=0$ if $\Delta^2 > v^4k_0^4/(v^2k_0^2+m^2+\Delta_0^2)$ or ii) the Dirac cones are located at $\vec{k}=\pm\alpha\vec{k}_0$ with

$$\alpha = \frac{\sqrt{v^4k_0^4-\Delta^2(v^2k_0^2+m^2+\Delta_0^2)}}{v^2k_0^2}. \tag{5.19}$$

if $\Delta^2 < v^4k_0^4/(v^2k_0^2+m^2+\Delta_0^2)$, which corresponds to a real value of α. Let's now see if we can find conditions for which the Dirac cones are not gapped in these two cases. Replacing $\vec{k}=0$ in the spectrum formula, we have $E=\sigma\tau|\sqrt{v^2k_0^2+m^2+\Delta_0^2}+\rho\Delta|$. Thus, the cone $\rho=-1$ located at $\vec{k}=0$ becomes gapless if $m^2=\Delta^2-v^2k_0^2-\Delta_0^2$. This implies the following condition on Δ,

$$\Delta^2 > v^2k_0^2+\Delta_0^2, \tag{5.20}$$

which is in agreement with the criterion given above for the Dirac cones to be located at $\vec{k}=0$ (i.e., the criterion for which α is imaginary). When the above condition holds, the helical pair of hinge modes becomes spatially split into two helical pair of Majorana modes: one located at $y=y_\Delta$ where $m=\sqrt{\Delta^2-v^2k_0^2-\Delta_0^2}$ and the other at $y=-y_\Delta$ where $m=-\sqrt{\Delta^2-v^2k_0^2-\Delta_0^2}$. On the other hand, if we replace $\vec{k}=\alpha\vec{k}_0$ in Eq. (5.18) we obtain $E^2=[(v^2k_0^2-\Delta^2)(m^2+\Delta_0^2)+2(1+\rho)v^4k_0^4]/(v^2k_0^2)$. Here we have to distinguish between $\rho=1$ and $\rho=-1$. When $\rho=1$ we have $E^2=0$ if $m^2=[\Delta_0^2(\Delta^2-v^2k_0^2)-4v^4k_0^4]/(v^2k_0^2-\Delta^2)$ whereas when $\rho=-1$ we have $E^2=0$ if $\Delta^2=v^2k_0^2$. As the condition to have gapless states for both $\rho=1$ and $\rho=-1$ does not satisfy the criterion for which α is real, the Dirac cones at $\vec{k}=\pm\alpha\vec{k}_0$ are always gapped. As illustrations, in Fig. 5.5 we represent the energy spectrum (5.18) where condition (5.20) is respected for $m=\sqrt{\Delta^2-\Delta_0^2-v^2k_0^2}$ and for $m\neq\sqrt{\Delta^2-\Delta_0^2-v^2k_0^2}$. In the former case we observe a doubly-degenerate Dirac cone located at $\vec{k}=0$ while in the latter the spectrum is gapped.

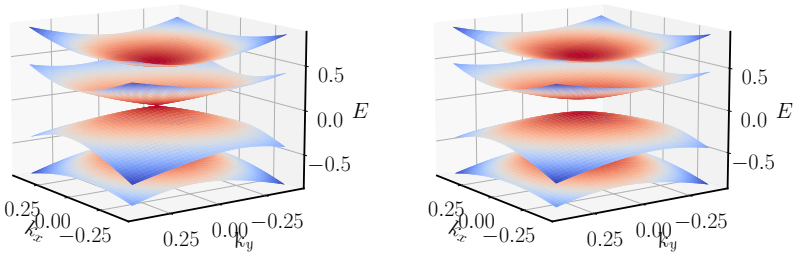

(a) (b)

Figure 5.5: Spectrum of the HOTI surface with only superconducting couplings Δ and Δ_0. In (a) we set $m=\sqrt{\Delta^2-\Delta_0^2-v^2k_0^2}$ and we see a doubly-degenerate Dirac cone located at $\vec{k}=0$ while in (b) we set $m=0.25\neq\sqrt{\Delta^2-\Delta_0^2-v^2k_0^2}$ and the spectrum is gapped. The other parameters are $k_x^0=0.1$, $k_y^0=0.2$, $B^z=0$, $\Delta=0.25$, and $\Delta_0=0.05$.

5.3.4 Zeeman and superconducting couplings

When all couplings are non-zero the surface spectrum can be written as

$$E_{\sigma\rho\tau}(\vec{k}) = \sigma\tau\left\{v^2\left(k^2+k_0^2\right)+\left(\sqrt{m^2+\Delta_0^2}+\rho\tau B^z\right)^2+\Delta^2 \right. \\ \left. +2\rho\sqrt{v^4\left(\vec{k}\cdot\vec{k}_0\right)^2+\Delta^2\left[v^2k_0^2+\left(\sqrt{m^2+\Delta_0^2}+\rho\tau B^z\right)^2\right]}\right\}^{1/2}. \tag{5.21}$$

Again, searching the values of $\vec{k}$ for which E^2 is minimal we find two possibilities: i) the Dirac cones are degenerate and located at $\vec{k}=0$ or ii) the Dirac cones are located at $\vec{k}=\pm\beta\vec{k}_0$ with

$$\beta = \frac{\sqrt{v^4k_0^4-\Delta^2\left[v^2k_0^2+\left(\sqrt{m^2+\Delta_0^2}+\rho\tau B^z\right)^2\right]}}{v^2k_0^2}. \tag{5.22}$$

Note that here we have different values for different cones because of the factor $\rho\tau$. This means that an electron, i.e. $\tau=+$, in the cone $\rho=1$ ($\rho=-1$) have the same value of β than a hole, $\tau=-$, in the cone $\rho=-1$ ($\rho=1$). Here β is imaginary when

$$\Delta^2 > \frac{v^4k_0^4}{v^2k_0^2+\left(\sqrt{m^2+\Delta_0^2}+\rho\tau B^z\right)^2}. \tag{5.23}$$

In that case the Dirac cones are located at $\vec{k}=0$, otherwise they are located at $\vec{k}=\pm\beta\vec{k}_0$. Replacing $\vec{k}=\pm\beta\vec{k}_0$ in the energy spectrum we have

$$E^2(\vec{k}=\pm\beta\vec{k}_0) = \frac{1}{v^2k_0^2}\left[\left(v^2k_0^2-\Delta^2\right)\left(\sqrt{m^2+\Delta_0^2}+\rho\tau B^z\right)^2+2v^4k_0^4(1+\rho)\right], \tag{5.24}$$

for which we have to distinguish between $\rho=1$ and $\rho=-1$. As before, for $\rho=1$ the Dirac cones are always gapped. However, for $\rho=-1$ we can have zero-energy states if $\sqrt{m^2+\Delta_0^2}-\tau B^z=0$, which corresponds to a mass gap equal to $m=\pm\sqrt{(B^z)^2-\Delta_0^2}$, implying $B^z>\Delta_0$. In that case, if the mass varies in space, the helical hinge modes are split into two pairs of chiral Majorana modes located at $y=\pm\tilde{y}$ corresponding to the positions where $m=\pm\sqrt{(B^z)^2-\Delta_0^2}$, respectively. An example of such gapless Dirac cones is shown in Fig. 5.6a where we set $m=\sqrt{(B^z)^2-\Delta_0^2}$. On the other hand, replacing $\vec{k}=0$ in the energy spectrum we get

$$E^2(\vec{k}=0) = \left(\Delta+\rho\sqrt{v^2k_0^2+\left(\sqrt{m^2+\Delta_0^2}+\rho\tau B^z\right)^2}\right)^2. \tag{5.25}$$

Here zero-energy solutions are possible when $m^2=\left(\sqrt{\Delta^2-v^2k_0^2}\ \pm B^z\right)^2-\Delta_0^2$, implying the following condition on Δ,

$$\Delta^2 > v^2k_0^2+\left(\Delta_0\pm B^z\right)^2. \tag{5.26}$$

We thus have four possible values of m for which the Dirac cones are gapless. For the mass domain wall realized by the hinge these values of m are reached at four locations $y_{sn}=sy_Z+ny_\Delta$, where $s,n=\pm$, leading to the spatial splitting of the helical hinge modes into four chiral Majorana modes. Note that if $y_Z=y_\Delta$, two of the chiral Majorana modes gap each other and the two others survive. As illustration we plot the energy spectrum where condition (5.26) holds with $m=\sqrt{\left(\sqrt{\Delta^2-v^2k_0^2}\ +B^z\right)^2-\Delta_0^2}$ in Fig. 5.6b. Here we observe the doubly degenerate gapless Dirac cones located at $\vec{k}=0$.

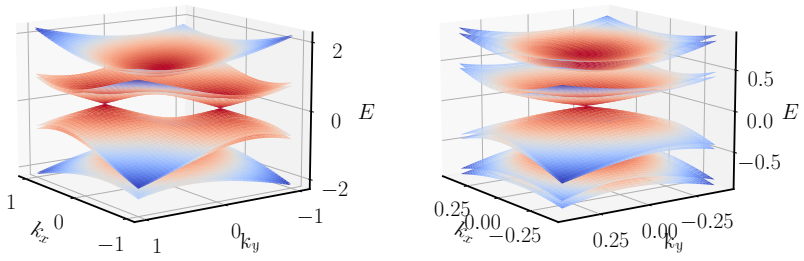

(a) (b)

Figure 5.6: Spectrum of the HOTI surface with both Zeeman and superconducting couplings. In (a) we set $k_x^0 = 0.5$, $k_y^0 = 0.5$, $B^z = 0.2$, $\Delta = 0.3$, $\Delta_0 = 0.1$ and $m = \sqrt{(B^z)^2 - \Delta_0^2}$ and we observe two gapless Dirac cones located at $\vec{k} = \pm\beta\vec{k}_0$. In (b) we set $k_x^0 = 0.1$, $k_y^0 = 0.2$, $B^z = 0.1$, $\Delta = 0.25$, $\Delta_0 = 0.15$ and $m = \sqrt{\left(\sqrt{\Delta^2 - v^2k_0^2} + B^z\right)^2 - \Delta_0^2}$ and we see a doubly-degenerate gapless Dirac cone located at $\vec{k} = 0$.

5.3.5 Summary

We can summarize our results by plotting the lines of zero energy as a function of B^z and m by using the spectrum formula (5.21). Here we can assume that m varies such that one can talk about one-dimensional modes. The corresponding diagrams are shown in Fig. 5.7 for (a) $\Delta > \sqrt{(vk_0)^2 + \Delta_0^2}$ (Fig. 5.7a), (b) $vk_0 < \Delta < \sqrt{(vk_0)^2 + \Delta_0^2}$ (Fig. 5.7b), and (c) $\Delta < vk_0$ (Fig. 5.7c). For (a) and (b) the lines of zero energy are obtained by setting $\vec{k} = 0$ while in (c) we set $\vec{k} = \beta\vec{k}_0$.

In Fig. 5.7a we observe four regimes:

1. When $B^z = 0$ there are two pairs of helical Majorana modes located where $m = \pm\sqrt{\Delta^2 - (vk_0)^2 - \Delta_0^2}$.
2. When $0 < B^z < -\Delta_0 + \sqrt{\Delta^2 - (vk_0)^2}$ we observe four chiral Majorana modes with alternating chiralities.
3. When $-\Delta_0 + \sqrt{\Delta^2 - (vk_0)^2} \leq B^z \leq \Delta_0 + \sqrt{\Delta^2 - (vk_0)^2}$ we observe two chiral Majorana modes with a right-moving (left-moving) mode in the region $m > 0$ ($m < 0$).
4. When $B^z > \Delta_0 + \sqrt{\Delta^2 - (vk_0)^2}$ we observe four chiral Majorana modes with two right-moving (left-moving) modes in the region $m > 0$ ($m < 0$).

In Fig. 5.7b we observe three regimes:

1. When $B^z < \Delta_0 - \sqrt{\Delta^2 - (vk_0)^2}$ there are no boundary modes.
2. When $\Delta_0 - \sqrt{\Delta^2 - (vk_0)^2} \leq B^z \leq \Delta_0 + \sqrt{\Delta^2 - (vk_0)^2}$ we observe two chiral Majorana modes with a right-moving (left-moving) mode in the region $m > 0$ ($m < 0$).
3. When $B^z > \Delta_0 + \sqrt{\Delta^2 - (vk_0)^2}$ we observe four chiral Majorana modes with two right-moving (left-moving) modes in the region $m > 0$ ($m < 0$).

In Fig. 5.7c we observe three regimes:

1. When $B^z < \Delta_0$ there are no boundary modes.
2. When $B^z = \Delta_0$ there are two pairs of helical Majorana modes located at $m = 0$ or, equivalently, a single pair of helical fermionic hinge modes.

3. When $B^z > \Delta_0$ there are two pairs of chiral Majorana modes or, equivalently, two single chiral fermionic modes with right-moving (left-moving) states in the region $m > 0$ ($m < 0$).

If $\Delta = \Delta_0 = 0$, we recover the result of Queiroz and Stern for which a Zeeman field spatially splits the helical fermionic hinge modes into two chiral fermionic modes.

In their paper [Queiroz & Stern 2019], Queiroz and Stern discuss only the regimes of Fig. 5.7a with $B^z \leq \Delta_0 + \sqrt{\Delta^2 - (vk_0)^2}$ as well as the cases where there is only one coupling (Zeeman or superconductivity).

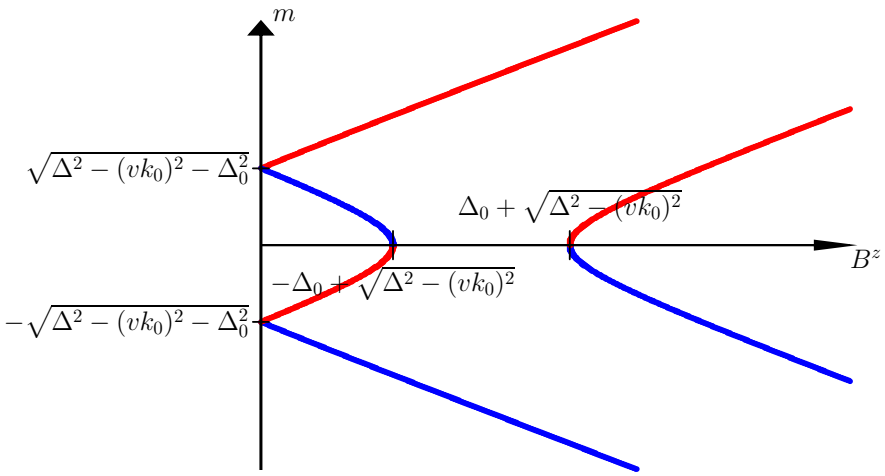

(a) $\Delta > \sqrt{(vk_0)^2 + \Delta_0^2}$

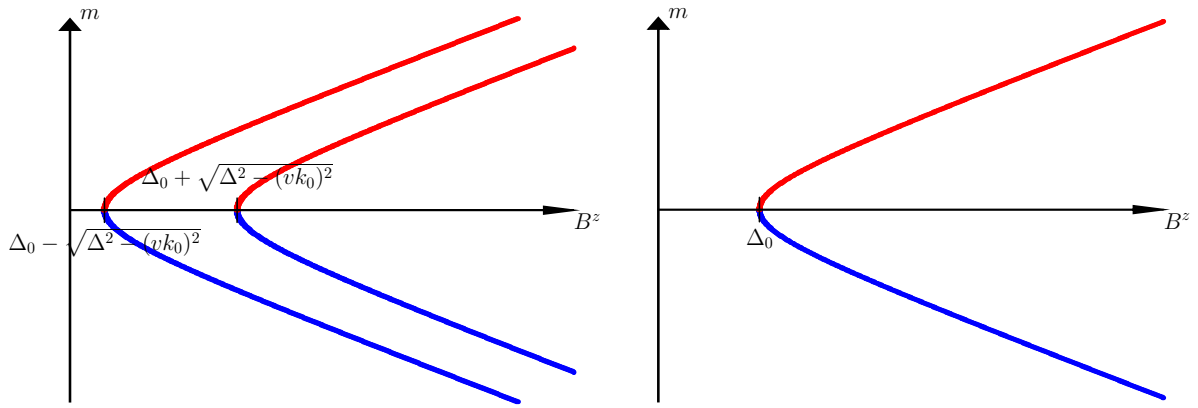

(b) $vk_0 < \Delta < \sqrt{(vk_0)^2 + \Delta_0^2}$ (c) $\Delta < vk_0$

Figure 5.7: Lines of zero energy as a function of B^z and m for (a) $\Delta > \sqrt{(vk_0)^2 + \Delta_0^2}$, (b) $vk_0 < \Delta < \sqrt{(vk_0)^2 + \Delta_0^2}$, and (c) $\Delta < vk_0$. The red and blue lines indicate respectively right-moving and left-moving Majorana modes. Note that in (c) the lines are doubly-degenerate. In (a) and (b) the lines are given by $m^2 = \left(B^z \pm \sqrt{\Delta^2 - v^2k_0^2}\right)^2 - \Delta_0^2$ and in (c) they are given by $m^2 = (B^z)^2 - \Delta_0^2$.

In the following we use the BdG Hamiltonian (5.15) to determine the energy spectrum and the wave functions of the hinge modes by focusing on a single hinge located at $y = 0$ which is at the left edge of a surface located in the (xy) plane. We will require exponentially decaying solutions in the transverse direction y while in the longitudinal direction x along the hinge the wave functions are plane waves.

5.4 Energy dispersion of the hinge modes

In the previous section we considered the two-dimensional homogeneous situation where m is constant. We now focus on a single hinge realizing a domain wall in the Dirac mass m. We consider a hinge located at $y = 0$ and a mass function of the form $m(y \to \pm\infty) = \pm m_0$, with $m(y = 0) = 0$ and m_0 a positive constant which is the largest energy scale.

To obtain the energy dispersion of the hinge modes, we start with the eigenvalue equation $\tilde{H}_{BdG}\phi = E\phi$, where $\tilde{H}_{BdG}$ is given in (5.15) and we take $\phi = (u_1, u_2, u_3, u_4, u_5, u_6, u_7, u_8)^T$. According to the Nambu basis (5.13) in which $\tilde{H}_{BdG}$ is written, the components $u_{1,3,6,8}$ are associated to the valley $+$ while $u_{2,4,5,7}$ are associated to the valley $-$. Due to the y dependence of m we have to substitute $k_y \to -i\partial_y$ in $\tilde{H}_{BdG}$ and then solve the system obtained from the eigenvalue equation to get the energies and wave functions of the hinge modes. As Δ_0 couples the two valleys, we set it to zero in order to have two valley-decoupled systems to solve, simplifying a lot the calculation. In Sec. 5.5.2 we will look at the matrix elements induced by Δ_0 and see that that, under certain conditions, the results are not affected when considering non-zero values of Δ_0. This leads to two valley-decoupled systems,

$$\text{valley } + \begin{cases} \partial_y u_3 &= -ik_y^0 u_3 + \frac{1}{v}(m + B^z)u_1 + \frac{\Delta}{v}u_6 + (k_x + k_x^0)u_3 - \frac{E}{v}u_1 \\ \partial_y u_1 &= -ik_y^0 u_1 + \frac{1}{v}(m + B^z)u_3 - \frac{\Delta}{v}u_8 - (k_x + k_x^0)u_1 + \frac{E}{v}u_3 \\ \partial_y u_8 &= +ik_y^0 u_8 - \frac{1}{v}(m + B^z)u_6 - \frac{\Delta}{v}u_1 + (k_x - k_x^0)u_8 + \frac{E}{v}u_6 \\ \partial_y u_6 &= +ik_y^0 u_6 - \frac{1}{v}(m + B^z)u_8 + \frac{\Delta}{v}u_3 - (k_x - k_x^0)u_6 - \frac{E}{v}u_8 \end{cases}, \tag{5.27}$$

$$\text{valley } - \begin{cases} \partial_y u_4 &= +ik_y^0 u_4 - \frac{1}{v}(m - B^z)u_2 + \frac{\Delta}{v}u_5 + (k_x - k_x^0)u_4 - \frac{E}{v}u_2 \\ \partial_y u_2 &= +ik_y^0 u_2 - \frac{1}{v}(m - B^z)u_4 - \frac{\Delta}{v}u_7 - (k_x - k_x^0)u_2 + \frac{E}{v}u_4 \\ \partial_y u_7 &= -ik_y^0 u_7 + \frac{1}{v}(m - B^z)u_5 - \frac{\Delta}{v}u_2 - (k_x + k_x^0)u_7 + \frac{E}{v}u_5 \\ \partial_y u_5 &= -ik_y^0 u_5 + \frac{1}{v}(m - B^z)u_7 + \frac{\Delta}{v}u_4 + (k_x + k_x^0)u_5 - \frac{E}{v}u_7 \end{cases}, \tag{5.28}$$

which we can solve independently.

5.4.1 Solving the valley-decoupled systems

Here we detail the calculation of the energy dispersion in the valley $+$ by solving the system (5.27) and then we will give the solution in the valley $-$ which can be obtained by using the same method.

Let us treat the system (5.27). Since we expect that the energy of the system is related to the surface momentum k_x it should be more comfortable to collect E and k_x together. This can be done with the following change of variables,

$$v_\pm = u_1 \pm u_3, \quad w_\pm = u_6 \pm u_8, \tag{5.29}$$

leading to,

$$\begin{aligned} \partial_y v_+ &= -ik_y^0 v_+ + \frac{1}{v}(m + B^z)v_+ + \frac{\Delta}{v}w_- - (k_x + k_x^0 + E/v)v_- \\ \partial_y v_- &= -ik_y^0 v_- - \frac{1}{v}(m + B^z)v_- - \frac{\Delta}{v}w_+ - (k_x + k_x^0 - E/v)v_+ \\ \partial_y w_+ &= +ik_y^0 w_+ - \frac{1}{v}(m + B^z)w_+ - \frac{\Delta}{v}v_- - (k_x - k_x^0 - E/v)w_- \\ \partial_y w_- &= +ik_y^0 w_- + \frac{1}{v}(m + B^z)w_- + \frac{\Delta}{v}v_+ - (k_x - k_x^0 + E/v)w_+ \end{aligned}. \tag{5.30}$$

As we consider m to be the largest energy scale away from the hinge, we need to cancel the terms that come with a factor $+m$ in order to have only exponentially decaying solutions when $y \to \infty$ (i.e. only physical states). This leads to the following relations,

$$v_+ = 0 \Leftrightarrow u_1 = -u_3 \Leftrightarrow v_- = 2u_1 = -2u_3, \tag{5.31}$$

$$w_- = 0 \Leftrightarrow u_6 = u_8 \Leftrightarrow w_+ = 2u_6 = 2u_8. \tag{5.32}$$

Replacing $v_+ = w_- = 0$ in the system (5.30) we finally get the energy dispersion along the hinge associated to the valley +,

$$E_+ = -vk_x \pm vk_x^0, \tag{5.33}$$

and so the valley + has a chirality $s = -$. Using the relations (5.31) and (5.32) we now have a system of two equations given by

$$\begin{aligned} \partial_y u_1 &= -ik_y^0 u_1 - \frac{1}{v}(m + B^z)u_1 - \frac{\Delta}{v}u_6, \\ \partial_y u_6 &= +ik_y^0 u_6 - \frac{1}{v}(m + B^z)u_6 - \frac{\Delta}{v}u_1. \end{aligned} \tag{5.34}$$

We can rewrite this system in the form of a mass inversion problem with the new variables,

$$u_{-+} = u_1 - u_6, \quad u_{--} = u_1 + u_6, \tag{5.35}$$

where the first subscript stands for the chirality $s = -$ while the second corresponds to a new quantum number $l = \pm$. This leads to the following,

$$\begin{aligned} \partial_y u_{-+} &= \frac{1}{v}[-m - B^z + \Delta]u_{-+} - ik_y^0 u_{--}, \\ \partial_y u_{--} &= \frac{1}{v}[-m - B^z - \Delta]u_{--} - ik_y^0 u_{-+}. \end{aligned} \tag{5.36}$$

The physical interpretation of this system will be discussed in Sec. 5.4.2.

We can then treat the system (5.28) of the other valley by using analogous considerations. This leads to the energy dispersion associated to the valley −,

$$E_- = +vk_x \pm vk_x^0, \tag{5.37}$$

and so the valley − has a chirality $s = +$. Again we obtain a system of two equations which reads

$$\begin{aligned} \partial_y u_{++} &= \frac{1}{v}[-m + B^z + \Delta]u_{++} + ik_y^0 u_{+-}, \\ \partial_y u_{+-} &= \frac{1}{v}[-m + B^z - \Delta]u_{+-} + ik_y^0 u_{++}, \end{aligned} \tag{5.38}$$

where the first subscript stands for the chirality $s = +$ while the second corresponds to the quantum number $l = \pm$. Here we have used the following conditions to deal with physical states,

$$v_- = 0 \Leftrightarrow u_2 = u_4 \Leftrightarrow v_+ = 2u_2 = 2u_4, \tag{5.39}$$

$$w_+ = 0 \Leftrightarrow u_5 = -u_7 \Leftrightarrow w_- = 2u_5 = -2u_7, \tag{5.40}$$

and we used the following definitions,

$$u_{++} = u_2 + u_5, \quad u_{+-} = u_2 - u_5. \tag{5.41}$$

In the following we summarize the preceding results and discuss their physical interpretation in the simple case $k_y^0 = 0$.

5.4.2 Summary and discussion about the splitting of the hinge modes

We can collect the systems (5.36) and (5.38) together into a matrix differential equation,

$$\partial_y \begin{pmatrix} u_{++} \\ u_{+-} \\ u_{-+} \\ u_{--} \end{pmatrix} = \begin{pmatrix} [-m + B^z + \Delta]/v & ik_y^0 & 0 & 0 \\ ik_y^0 & [-m + B^z - \Delta]/v & 0 & 0 \\ 0 & 0 & [-m - B^z + \Delta]/v & -ik_y^0 \\ 0 & 0 & -ik_y^0 & [-m - B^z - \Delta]/v \end{pmatrix} \begin{pmatrix} u_{++} \\ u_{+-} \\ u_{-+} \\ u_{--} \end{pmatrix}, \tag{5.42}$$

or into the following single equation,

$$\partial_y u_{sl} = \frac{1}{v}[-m + sB^z + l\Delta]u_{sl} + sik_y^0 u_{s,-l}, \tag{5.43}$$

with associated energies,

$$E_{sl} = svk_x + lvk_x^0, \tag{5.44}$$

where $s = \pm$ is the chirality of the hinge mode (valley $+/-$ having chirality $s = -/+$) and $l = \pm$ distinguishes between two Majorana modes.

Looking at the differential equation (5.43) we see that for $k_y^0 = 0$ we have four independent differential equations $\partial_y u_{sl} = (1/v)[-m + sB^z + l\Delta]u_{sl}$ which can be written as $\partial_y u_{sl} = -m_{sl}(y)u_{sl}$. Here we recognize a trivial mass inversion problem with an effective mass $m_{sl}(y) = m(y) - sB^z - l\Delta$. Since the hinge modes are located where the effective mass gap vanishes (see Sec. 2.3), we thus have four positions denoted by $y_{sl} = sy_Z + ly_\Delta$ corresponding to four spatially separated Majorana modes.

In the next section we derive analytical solutions of the system (5.42) and we will see that the discussion about the splitting of the hinge modes is still relevant when $k_y^0 \neq 0$.

5.5 Wave functions of the hinge modes

5.5.1 Derivation of the wave functions

To determine the wave functions we need to solve the differential equation (5.43). Introducing $w_{sl}^{\pm} = u_{sl} \mp iu_{s,-l}$, we can write the following system,

$$\partial_y \begin{pmatrix} w_{sl}^+ \\ w_{sl}^- \end{pmatrix} = \begin{pmatrix} \frac{1}{v}[-m + sB^z] & l[\Delta/v + sk_y^0] \\ l[\Delta/v - sk_y^0] & \frac{1}{v}[-m + sB^z] \end{pmatrix} \begin{pmatrix} w_{sl}^+ \\ w_{sl}^- \end{pmatrix}, \tag{5.45}$$

which we can diagonalize with a last change of variables,

$$\Omega_{sn} = w_{sl}^+ + nl\sqrt{\frac{\Delta + svk_y^0}{\Delta - svk_y^0}}w_{sl}^-, \tag{5.46}$$

where we have introduced a new quantum number $n = \pm$. This leads to the l-independent diagonal system,

$$\partial_y \begin{pmatrix} \Omega_{s+} \\ \Omega_{s-} \end{pmatrix} = \begin{pmatrix} \frac{1}{v}\left[-m(y) + sB^z + \sqrt{\Delta^2 - (vk_y^0)^2}\right] & 0 \\ 0 & \frac{1}{v}\left[-m(y) + sB^z - \sqrt{\Delta^2 - (vk_y^0)^2}\right] \end{pmatrix} \begin{pmatrix} \Omega_{s+} \\ \Omega_{s-} \end{pmatrix}, \tag{5.47}$$

which we can rewrite into the following differential equation,

$$\partial_y \Omega_{sn} = \frac{1}{v}\left[-m(y) + sB^z + n\sqrt{\Delta^2 - (vk_y^0)^2}\right]\Omega_{sn}, \tag{5.48}$$

and the corresponding solutions are given by,

$$\Omega_{sn}(y) = C_{sn}\exp\left\{\frac{1}{v}\left[sB^z + n\sqrt{\Delta^2 - (vk_y^0)^2}\,\right]y\right\}\exp\left\{-\frac{1}{v}\int_0^y m(r)\mathrm{d}r\right\}, \tag{5.49}$$

$$= C_{sn}f_{sn}(y), \tag{5.50}$$

where C_{sn} are normalization constants and we have introduced the function

$$f_{sn}(y) = \exp\left\{\frac{1}{v}\left[sB^z + n\sqrt{\Delta^2 - (vk_y^0)^2}\,\right]y\right\}\exp\left\{-\frac{1}{v}\int_0^y m(r)\mathrm{d}r\right\}. \tag{5.51}$$

Note that the square root appearing in the above solution is real as long as the condition (5.20) is respected. Moreover, the normalization constants are given by

$$C_{sn} = \frac{1}{|\chi_{sn}|}\left\{\int_{-\infty}^{+\infty} |f_{sn}(y)\,|^2\,\mathrm{d}y\right\}^{-1/2}, \tag{5.52}$$

and they are explicitly calculated in App. E.2 for the mass profile introduced in Eq. (5.3), i.e., $m(y) = m_0\tanh(y/y_0)$. Furthermore, to calculate the eigenvectors associated to the solutions Ω_{sn} it is useful to rewrite the previous notations by using the quantum number n,

$$\Omega_{sn} = \omega_{s+} + n\sqrt{\frac{\Delta + svk_y^0}{\Delta - svk_y^0}}\omega_{s-}, \quad \omega_{sn} = u_{s+} + nv_{s-}, \quad v_{sn} = -iu_{sn}. \tag{5.53}$$

We denote the eigenvectors associated to the solutions Ω_{sn} by χ_{sn} and we find them to be given by (we detail the calculation in App. E.1),

$$\chi_{sn} = (\chi_s, g_{sn}\chi_{-s})\,, \tag{5.54}$$

with $\chi_+ = (0,1,0,1)^T$, $\chi_- = (-1,0,1,0)^T$ and

$$g_{sn} = -\frac{sn\sqrt{\Delta^2 - (vk_y^0)^2} - ivk_y^0}{\Delta}. \tag{5.55}$$

We can finally write the transversal wave functions of the hinge states as

$$\phi_{sn}(y) = \Omega_{sn}(y)\chi_{sn}, \tag{5.56}$$

where $\Omega_{sn}(y)$ is the orbital part while χ_{sn} is the spinorial part of the wave functions. In App. E.2 we check if the states ϕ_{sn} form an orthogonal basis. Actually, we find that there is an overlap δ between the states of same s and opposite n which can hybridize and gap them. However, we find that the overlap may be negligible under certain conditions such that the states are approximatively orthogonal[3]. The result (5.56) for the hinge mode wave functions recovers the one of Ref. [Queiroz & Stern 2019] if we set $k_y^0 = 0$. In that case, the wave functions are less rich, since the term $\sqrt{\Delta^2 - (vk_y^0)^2} = \Delta$ is always real. As we will discuss in Sec. 5.5.3, the helical hinge modes can be split into helical Majorana modes when $B^z = 0$ or into single chiral Majorana modes when both Zeeman and superconducting couplings are present. This is what Queiroz and Stern have discussed in their paper. When $k_y^0 \neq 0$ we agree with Queiroz and Stern only in the regime $\Delta > vk_y^0$, which is equivalent to their result with a renormalized coupling $\Delta \to \tilde{\Delta} = \sqrt{\Delta^2 - (vk_y^0)^2}$. On the other hand, Queiroz and Stern have not discussed the regime $\Delta < vk_y^0$. In that case there is an important difference because the effective mass no longer depends on the superconducting coupling, leading to a new splitting scenario not envisaged in [Queiroz & Stern 2019] (see Sec. 5.5.3).

As we have set $\Delta_0 = 0$ to derive the wave functions, in the following we look at the matrix elements induced by this term.

5.5.2 Matrix elements induced by Δ_0

Following [Queiroz & Stern 2019], we look at the matrix elements induced by the coupling Δ_0 appearing in the Hamiltonian (5.15) as $\Delta_0\tau_x$. Indeed, we have set $\Delta_0 = 0$ in order to determine the dispersions and wave functions and now we want to see if the matrix elements induced by this parameters gap the hinge modes. These matrix elements are given by $\langle\chi_{sn}|\tau_x|\chi_{s'n'}\rangle \propto \delta_{s,-s'}$. Hence, Δ_0 couples states of opposite chiralities leading to a gap in the energy spectrum. However, as long as the hinge modes are spatially separated, the coupling induced by Δ_0 is weak and the gap may be neglected. Hence, when they are well separated, our results about the splitting of the hinge modes are valid even for non-zero values of Δ_0. We will illustrate this when performing numerical simulations in Sec. 5.6.

We discuss the physical interpretation of the hinge mode wave functions and present the different splitting scenarios in the next subsection.

[3]Indeed, considering a mass profile $m(y) = m_0\tanh(y/y_0)$, we observe that the overlap δ is exponential suppressed with y_0m_0/v.

5.5.3 Summary and discussion about the splitting of the hinge modes

Starting from the BdG Hamiltonian (5.15) and considering an infinite strip along y while setting $k_x^0 = \Delta_0 = 0$ we were able to obtain the solvable system (5.43) by using the Schrödinger equation. Solving this system we have obtained four wave functions given by $\phi_{sn}(y) = \Omega_{sn}(y)\chi_{sn}$, where $\Omega_{sn}(y)$ is the orbital part defined in Eq. (5.49) while χ_{sn} is the spinor part defined in Eq. (5.54). Moreover we recall that the quantum number $s = \pm$ is related to the chirality while the quantum number $n = \pm$ distinguishes the Majorana modes. Furthermore, the associated dispersions are given by $E_{sn} = svk_x + nvk_x^0$. If we do not specify a mass profile $m(y)$, the orbital part can be written as

$$\Omega_{sn}(y) = C_{sn} \exp\left\{-\frac{1}{v}\int_0^y m_{sn}(r)\mathrm{d}r\right\}, \tag{5.57}$$

where C_{sn} are normalization constants and we have introduced the effective mass $m_{sn}(y)$ given by,

$$m_{sn}(y) = m(y) - sB^z - n\sqrt{\Delta^2 - (vk_y^0)^2}. \tag{5.58}$$

As already discussed in Sec. 5.4.2, this corresponds to a mass inversion problem where the hinge modes are located at the zeros of the effective mass. We now distinguish between different scenarios and, in the remainder of this section, we will consider a mass profile given by $m(y) = m_0 \tanh(y/y_0)$.

In the normal case where both Zeeman and superconducting couplings are set to zero we have a helical pair of hinge modes (i.e., located at $y = 0$), as represented in Fig. 5.8. In this figure we have flattened the two surfaces forming the hinge for clarity and we have shown the mass profile $m(y)$. In all of the following figures we use the same mass profile and always show the two surfaces as flattened.

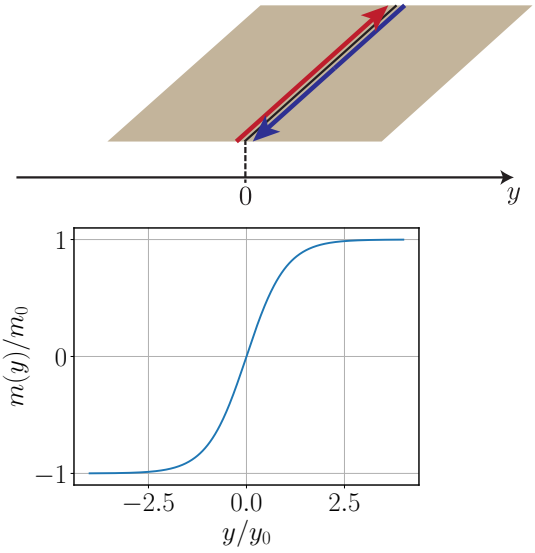

Figure 5.8: Normal case. Helical states are present at the left and right hinges of the surface.

When only a Zeeman field is present ($B^z \neq 0$ and $\Delta = 0$), the effective mass reads $m_s(y) = m(y) - sB^z$ and have two zeros that are reached at the following positions,

$$y_s = y_0 \tanh^{-1}(sB^z/m_0). \tag{5.59}$$

In that case, the helical hinge modes are split into two chiral modes as depicted in Fig. 5.9.

Considering only a superconducting coupling, namely $B^z = 0$ and $\Delta \neq 0$, the effective mass becomes $m_n(y) = m(y) - n\sqrt{\Delta^2 - (vk_y^0)^2}$. In that case the hinge modes are spatially split into two pairs of helical Majorana modes protected by time-reversal symmetry whose positions are given by

$$y_n = y_0 \tanh^{-1} \frac{n\sqrt{\Delta^2 - (vk_y^0)^2}}{m_0}. \tag{5.60}$$

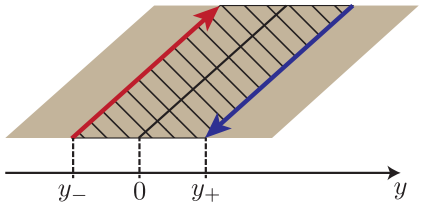

Figure 5.9: Zeeman field. The helical pair is separated into two chiral modes enclosing a quantum anomalous Hall region.

As discussed in Sec. 5.3.4, these modes are gapped when $\Delta^2 < (vk_y^0)^2$. The situation is depicted in Fig. 5.10 in which we observe the two helical pairs of Majorana modes that are separated from each other, surrounding a surface-based helical topological superconductor.

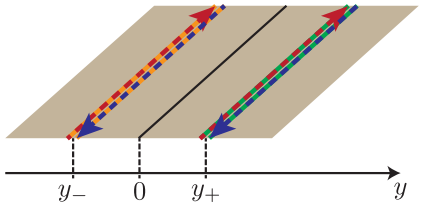

Figure 5.10: Superconductivity. The superconducting coupling alone leads to two helical Majorana modes surrounding a surface-based helical topological superconductor. The blue and red arrows indicate the direction of propagation while the green and yellow colors distinguish between the two types of Majorana modes.

When both Zeeman and superconducting couplings are present we have to treat differently the cases $\Delta^2 > (vk_y^0)^2$ and $\Delta^2 < (vk_y^0)^2$.
When $\Delta^2 > (vk_y^0)^2$ the effective mass is given by Eq. (5.58) and has four zeros located at the following positions,

$$y_{sn} = y_0 \tanh^{-1} \frac{sB^z + n\sqrt{\Delta^2 - (vk_y^0)^2}}{m_0}. \tag{5.61}$$

Here there are three possible scenarios that we list below and draw in Fig. 5.11 where, to simplify the notations, we introduced the reduced superconducting coupling $\tilde{\Delta} = \sqrt{\Delta^2 - (vk_y^0)^2}$.

1. $\tilde{\Delta} > B^z$: The Zeeman coupling is lower than the pairing $\tilde{\Delta}$ forming a QAH-$(p+ip)$-QAH junction where the two QAH regions have opposites n (see Fig. 5.11a).

2. $\tilde{\Delta} = B^z$: The Zeeman and modified superconducting coupling are equal so that $y_{-+} = y_{+-}$ and so the modes of opposite s and n are gapped by Δ_0 and two spatially separated chiral Majorana modes are left (see Fig. 5.11b). As it require a fine-tuning, this phase is not topological.

3. $\tilde{\Delta} < B^z$: The Zeeman coupling is stronger than the reduced superconducting coupling leading to four spatially separated chiral Majorana modes with two overlapping quantum anomalous Hall (QAH) regions (see Fig. 5.11c).

On the other hand, if $\Delta^2 < (vk_y^0)^2$ we can rewrite the orbital part of the wave functions as

$$\Omega_{sn}(y) = C_{sn} \exp\left\{-\frac{1}{v}\int_0^y m_s(r)\mathrm{d}r\right\} e^{-in(y/v)\sqrt{(vk_y^0)^2-\Delta^2}}, \tag{5.62}$$

with an effective mass $m_s = m(y) - sB^z$. In that case the effective mass has only two zeros that are located at the positions y_s defined in Eq. (5.59). This corresponds to two pairs of chiral Majorana modes

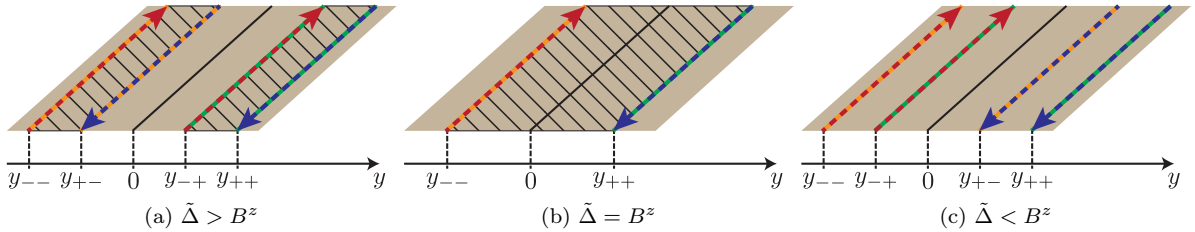

(a) $\tilde{\Delta} > B^z$ (b) $\tilde{\Delta} = B^z$ (c) $\tilde{\Delta} < B^z$

Figure 5.11: Splitting of the modes with both Zeeman and superconducting couplings when $\Delta^2 > (vk_y^0)^2$. The blue and red arrows indicate the direction of propagation while the green and yellow colors distinguish between the two types of Majorana modes.

as depicted in Fig. 5.12. Despite the fact that a pair of chiral Majorana modes is equivalent to a single chiral fermionic mode, here we can differentiate the two situations because the wave functions have a different phase factor.

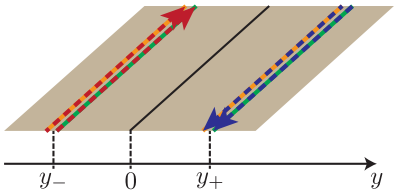

Figure 5.12: Splitting of the modes with both Zeeman and superconducting couplings when $\Delta^2 < (vk_y^0)^2$. The blue and red arrows indicate the direction of propagation while the green and yellow colors distinguish between the two types of Majorana modes. Here the hinge modes are split into two pairs of chiral Majorana modes.

As we can see, we recover the splitting scenarios already discussed in Sec. 5.3.5. The scenarios depicted in Figs. 5.9, 5.10, 5.11a, 5.11b are those discussed in [Queiroz & Stern 2019] while the scenarios presented in Fig. 5.11c and Fig. 5.12 provide new results. In the next section we perform a numerical analysis of the system with non-zero values of Δ_0 by using a lattice model. This allows us to visualize the spatial splitting by plotting the y- and k_x-resolved spectral density at the zeros of the effective mass.

5.6 Numerical results

In the preceding section we have proposed different splitting scenarios depending on the values of the Zeeman field B^z and the reduced superconducting coupling $\tilde{\Delta} = \sqrt{\Delta^2 - (vk_y^0)^2}$. Here we look at the scenarios not considered by Queiroz and Stern by computing the spectral density with the help of a tight-binding model. In particular, we focus on the case $\tilde{\Delta} < B^z$ where we have to distinguish between $\Delta > vk_y^0$ (four chiral Majorana modes) and $\Delta < vk_y^0$ (two pairs of chiral Majorana modes).

5.6.1 Lattice model

Following Queiroz and Stern, we now construct a lattice model of the surface Hamiltonian on a square lattice with lattice constant $a = 1$ (in the next the lengths are given in units of a and the momenta in units of $1/a$). To do so, we discretize the continuous Dirac Hamiltonian using the finite difference method as presented in App. C. We start with a simplified Hamiltonian without couplings,

$$H(\vec{k}) = v(\vec{k} + \vec{k}_0\rho_z) \cdot \vec{\sigma} + m\sigma_z\rho_z, \tag{5.63}$$

whilst the couplings will be easily included later as they will enter in the onsite potential. In order to describe a topological insulator we need to introduce a quadratic correction in $\vec{k}$ to the mass term

[Shen *et al.* 2011] and we thus consider,

$$H(\vec{k}) = v(\vec{k} + \vec{k}_0\rho_z)\cdot\vec{\sigma} + (m - B\vec{k}^2)\sigma_z\rho_z. \tag{5.64}$$

For our lattice model we take $B = t/2$, with t the hopping energy. To simplify the derivation we first forget about the spin and valley degrees of freedom and re-introduce them after. We thus want to discretize the following toy Hamiltonian,

$$H = v(k_x + k_y) + \frac{t}{2}(k_x^2 + k_y^2) + v(k_x^0 + k_y^0) + m. \tag{5.65}$$

Substituting $k_\alpha \to -i\partial_\alpha$, using the finite difference method, introducing the operator $c_j^\dagger$ which creates a fermion at site j whose position is given by $\vec{R}_j$, and setting $v/a = \varepsilon$ where ε has unit of energy, we obtain the following lattice Hamiltonian,

$$\mathcal{H} = \sum_j \left[v(k_x^0 + k_y^0) + m + 2t\right] c_j^\dagger c_j + \frac{1}{2}\sum_{ij}\sum_{\vec{R}_a}\left[t + i\varepsilon\left(\vec{R}_i - \vec{R}_j\right)\cdot\hat{R}\right] c_i^\dagger c_j \delta_{\vec{R}_i - \vec{R}_j, \vec{R}_a} \tag{5.66}$$

with lattice sites i, j, $\hat{R} = \hat{x} + \hat{y}$ the unitary position vector, and $\vec{R}_a$ the nearest neighbour vectors given by $\vec{R}_1 = \hat{x}$, $\vec{R}_2 = -\hat{x}$, $\vec{R}_3 = \hat{y}$, and $\vec{R}_4 = -\hat{y}$. Taking in account the spin and valley degrees of freedom the tight-binding Hamiltonian without coupling reads,

$$\mathcal{H} = \sum_{ij} \Psi_i^\dagger H_{ij} \Psi_j, \qquad \Psi_j = \left(c_{j\uparrow+}\, c_{j\uparrow-}\, c_{j\downarrow+}\, c_{j\downarrow-}\right)^T, \tag{5.67}$$

$$H_{ij} = \left[v(k_x^0\sigma_x + k_y^0\sigma_y)\rho_z + m\sigma_z\rho_z + 2t\sigma_z\rho_z\right]\delta_{\vec{R}_i,\vec{R}_j} + \frac{1}{2}\sum_{\vec{R}_a}\left[t\sigma_z\rho_z + i\varepsilon\left(\vec{R}_i - \vec{R}_j\right)\cdot\vec{\sigma}\right]\delta_{\vec{R}_i - \vec{R}_j, \vec{R}_a}. \tag{5.68}$$

It is then straightforward to include the Zeeman and superconducting couplings since they simply enter in the onsite potential. While we considered only a Zeeman field acting diagonally in the valley subspace in the analytical calculations, here we add a valley-coupling Zeeman term $B_0^z\sigma_z\rho_x$ in order to be more general. Note that this term may gap the helical hinge modes at energies close to vk_0. The real-space tight-binding Hamiltonian with Zeeman and superconducting couplings can then be written as

$$\mathcal{H} = \sum_{ij} \Phi_i^\dagger H_{ij} \Phi_j, \qquad \Phi_j = \left(c_{j\uparrow+}\, c_{j\uparrow-}\, c_{j\downarrow+}\, c_{j\downarrow-}\; -c_{j\downarrow-}^\dagger\; -c_{j\downarrow+}^\dagger\, c_{j\uparrow-}^\dagger\, c_{j\uparrow-}^\dagger\right)^T, \tag{5.69}$$

$$\begin{aligned} H_{ij} = {} & [(m - 2t)\sigma_z\rho_z\tau_z) + v(k_x^0\sigma_x + k_y^0\sigma_y)\rho_z\tau_z + B^z\sigma_z + B_0^z\sigma_z\rho_x + \Delta\rho_x\tau_x + \Delta_0\tau_x]\delta_{\vec{R}_i,\vec{R}_j} \\ & + \frac{1}{2}\sum_{\vec{R}_a}[t\sigma_z\rho_z\tau_z + i\varepsilon(\vec{R}_i - \vec{R}_j)\cdot\vec{\sigma}\tau_z]\delta_{\vec{R}_i - \vec{R}_j, \vec{R}_a}. \end{aligned} \tag{5.70}$$

Note that this tight-binding Hamiltonians recovers the one of Ref. [Queiroz & Stern 2019, Supplementary Material]. In all numerical calculations we set $\varepsilon = t = 1$ such that all energies are expressed in units of t and we use the Kwant software [Groth *et al.* 2014] to perform the tight-binding simulations.

5.6.2 Spectral density

We now visualize the splitting scenarios not discussed by Queiroz and Stern (i.e., those depicted in Fig. 5.11c and Fig. 5.12) by plotting the y- and k_x-resolved spectral density [Queiroz & Stern 2019],

$$A(y, \varepsilon, k_x) = -\frac{1}{\pi}\mathrm{Im}\sum_m \frac{|\psi_m(k_x, y)|^2}{\varepsilon - \varepsilon_m + i\eta}, \tag{5.71}$$

where $\psi_m(k_x, y)$ is the m-th eigenstate of the lattice Hamiltonian with energy ε_m, and $\eta = 0.01$ a broadening parameter determining the resolution of the plots. The spectral density allows to probe the band structure at the zeros of the effective masses. To compute it we use the Kwant software with a ribbon geometry of 121 sites along the y-direction. As the lattice sites are labelled from 0 to 120 it is convenient to shift the mass profile so that the modes are located in the region $y \geq 0$. We thus consider the following mass profile,

$$m(y) = m_0 \tanh[(y - y_{max} + 20)/y_0], \tag{5.72}$$

where y_{max} is the largest positive location of the splitted modes.

For $\Delta > vk_y^0$ we have $y_{max} = y_{s=+,n=+}$ where y_{sn} are the positions of the four chiral Majorana modes defined in Eq. (5.61). As an illustrative example we plot the effective masses $m_{sn}(y)$ with this shifted mass profile in Fig. 5.13 (recall that $m_{sn}(y) = m(y) - sB^z - n\sqrt{\Delta^2 - (vk_y^0)^2}$). In this figure we also indicate the zeros of the shifted effective masses which are denoted by $\tilde{y}_{sn}$ and are given by

$$\tilde{y}_{sn} = y_{sn} + y_{s=+,n=+} + 20, \tag{5.73}$$

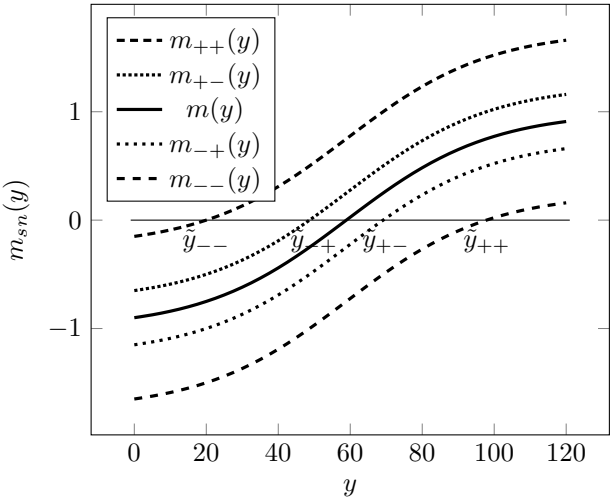

Figure 5.13: Effective masses $\tilde{m}_{sn}(y)$ and locations $\tilde{y}_{sn}$ where they vanish corresponding to the positions of the hinge modes. The parameters are $y_0 = 40$, $m_0 = 1$, $B^z = 0.5$, and $\tilde{\Delta} = 0.25$.

With $\Delta < vk_y^0$ we have $y_{max} = y_{s=+}$ where y_s are the positions of the two pairs of chiral Majorana modes defined in Eq. (5.59). These positions are modified by the shifted mass profile and become

$$\tilde{y}_s = y_s + y_{s=+} + 20. \tag{5.74}$$

Note that with our shifted mass profile the smaller location of the split modes is always given by $y = 20$. This value has been chose arbitrarily so that all the modes are away from the left and right edges respectively located at $y = 0$ and $y = 120$. In Tab. 5.3 we give explicit values of the positions of the hinge modes for the scenarios we want to illustrate.

Scenarios	vk_y^0	$\tilde{y}_{--}$	$\tilde{y}_{-+}$	$\tilde{y}_{+-}$	$\tilde{y}_{++}$	$\tilde{y}_{-}$	$\tilde{y}_{+}$
$\Delta > vk_y^0$	0.075	20	47	69	96		
$\Delta < vk_y^0$	0.5					20	64

Table 5.3: Positions of the hinge modes for the scenario not considered by Queiroz and Stern. The parameters are $B^z = 0.5$, $\Delta = 0.25$, $m_0 = 1$, and $y_0 = 40$.

In the following we plot the spectral density at the positions given in Tab. 5.3 as well as at the left ($y = 0$) and right ($y = 120$) edges where the spectrum is gapped.
In Fig. 5.14 we consider $\Delta > vk_y^0$ with $\tilde{\Delta} < B^z$ and we observe that the pair of helical fermionic hinge modes is split into four single chiral Majorana modes, as expected.
In Fig. 5.15 we consider $\Delta < vk_y^0$ and we observe that the pair of helical fermionic hinge modes is split into two pairs of chiral Majorana modes, as expected.

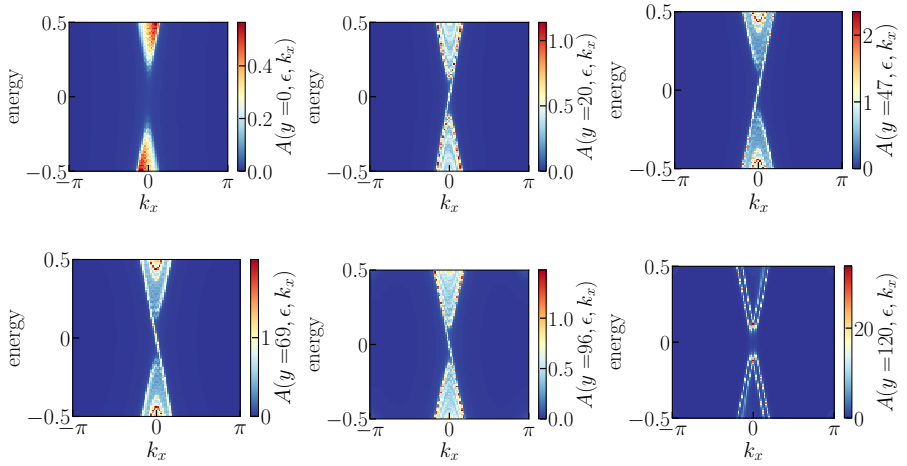

Figure 5.14: Spectral density at the positions given in Tab. 5.3 and at the left and right edges for $\Delta > vk_y^0$. As expected, the helical fermionic hinge modes are split into four chiral Majorana modes and at the edges the modes are gapped. The parameters are $B^z = 0.5$, $\Delta = 0.25$, $vk_y^0 = 0.075$, $vk_x^0 = 0.1$, $B_0^z = 0.1$, $\Delta_0 = 0.2$, $m_0 = 1$, and $y_0 = 40$.

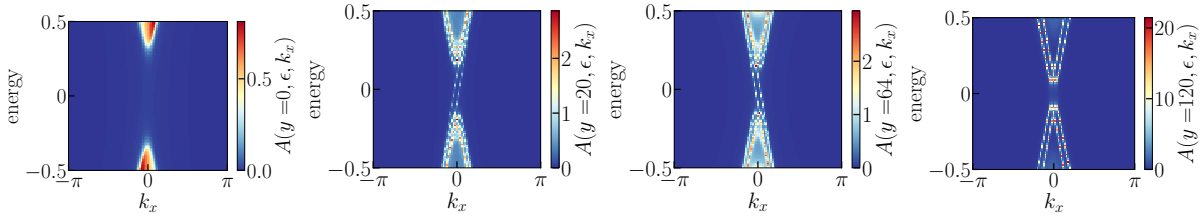

Figure 5.15: Spectral density at the positions given in Tab. 5.3 and at the left and right edges for $\Delta < vk_y^0$. As expected, the helical fermionic hinge modes are split into two pairs of chiral Majorana modes and at the edges the modes are gapped. The parameters are $B^z = 0.5$, $\Delta = 0.25$, $vk_y^0 = 0.5$, $vk_x^0 = 0.1$, $B_0^z = 0.1$, $\Delta_0 = 0.2$, $m_0 = 1$, and $y_0 = 40$.

5.7 Conclusion

In this chapter we have studied the surface of a helical HOTI having two mirror-symmetry protected Dirac cones which are gapped by a mass surface gap m and separated in momentum space by $2k_0$. Since the hinges of the surface realize natural mass domain walls, where the mass changes sign, they host helical hinge modes. Extending the work of Queiroz and Stern [Queiroz & Stern 2019], we then investigated the fate of these hinge modes when subjected to Zeeman and superconducting couplings. As discussed in [Queiroz & Stern 2019], under certain conditions these couplings can lead to the spatial splitting of the hinge modes instead of gapping them. Here we study different splitting scenarios, which depend on

the values of the couplings as well as on the value of the momentum separation between the two Dirac cones.

Our findings are supported by analytical calculations of the HOTI surface spectrum as well as by analytical calculations of the energy and wave functions of the hinge states. In particular, our result for the hinge mode wave functions is more general than the one given in [Queiroz & Stern 2019], leading to a new splitting scenario with pairs of chiral Majorana modes. In addition, we performed tight-binding simulations, which allowed us to confirm our analytical predictions.

The new findings of our study are as follows. When both Zeeman and superconducting couplings are present with $\Delta > vk_0$ and $B^z > \sqrt{\Delta^2 - (vk_y^0)^2}$, the helical pair of fermionic hinge modes is spatially separated into four chiral Majorana modes with two modes of same chirality followed by two modes of the other chirality. On the other hand, when $\Delta < vk_0$ and $B^z > \Delta_0$, the helical pair of fermionic modes is split into two pairs of chiral Majorana modes.

For further studies it would be interesting to use the spatial splitting of the hinge modes to build interferometers or to study the Josephson effect. Queiroz and Stern have already suggested a generalization of the chiral Majorana fermion interferometer proposed by Fu and Kane [Fu & Kane 2009], and by Akhmerov, Nilsson, and Beenakker [Akhmerov *et al.* 2009] where the surface of a time-reversal invariant topological insulator is gapped by ferromagnets of opposite magnetization, separated by a superconducting island. The proposal of Queiroz and Stern corresponds to two copies of that interferometer with two different chiralities. In addition to the proposal of Queiroz and Stern, the new splitting scenarios allow one to envision new types of interferometers such as the one shown in Fig. 5.16. In this figure we show a system consisting of several successive regions. If we denote a region with no couplings by N, a region with only Zeeman coupling by F (for ferromagnet), and a region with Zeeman and superconducting couplings by FS, then the system we propose consists of an N/F/FS/F/N junction (here the FS region is in the $\tilde{\Delta} < B^z$ regime). As shown in Fig. 5.16, the central region of this junction is made of two chiral Majorana interferometers with opposite chiralities. As another perspective, we also propose two types of FS/N/FS Josephson junctions as shown in Fig. 5.17. In Fig. 5.17a the FS regions are in the $\tilde{\Delta} < B^z$ regime and the supercurrent is mediated by helical Majorana modes, while in Fig. 5.17b the FS regions are in the $\tilde{\Delta} > B^z$ regime and the supercurrent is mediated by chiral Majorana modes. As a final suggestion, it would also be interesting to study a Josephson junction consisting of two FS regions, one in the $\tilde{\Delta} < B^z$ regime and the other in the $\tilde{\Delta} > B^z$ regime.

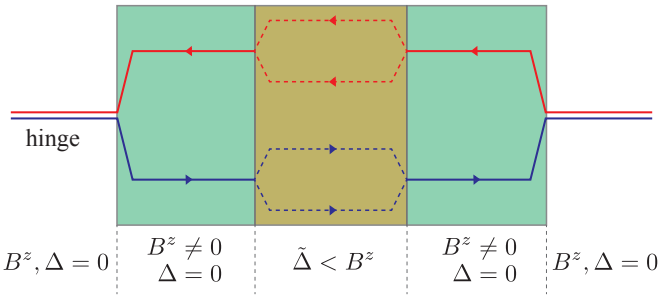

Figure 5.16: Majorana interferometers. From left to right, the helical hinge mode is first splitted by a non-zero Zeeman field into two chiral fermionic modes (left green region) and then each chiral fermionic mode is splitted into two chiral Majorana modes by the addition of a superconducting coupling (yellow region). The Majorana modes then recombine into fermionic modes in a region where there is no longer a superconducting coupling (right green region) and finally the helical hinge mode is recovered in a region where all the couplings are zero (right white region). This system can be engineered by placing a ferromagnet going from the left to the right green regions and by placing a superconductor along the yellow part. The central region where both Zeeman and superconducting couplings are present shows two Majorana interferometers of opposite chiralities.

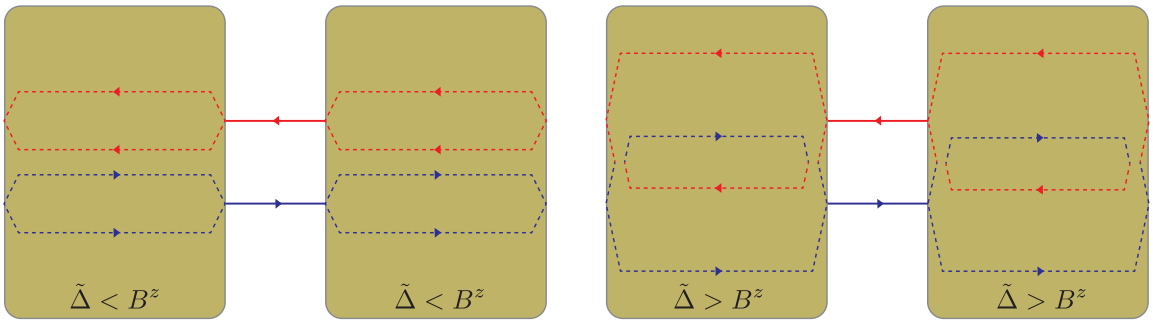

Figure 5.17: Josephson junctions. In (a) we sketch a Josephson junction where the supercurrent is mediated by helical Majorana modes by choosing $\tilde{\Delta} < B^z$ while in (b) we represent a Josephson junction where the supercurrent is mediated by chiral Majorana modes by setting $\tilde{\Delta} > B^z$.

Chapter 6

Conclusion and perspectives

The aim of this thesis was to study the coupling between a superconductor and topological boundary modes. First we considered the chiral edge states of the quantum Hall effect (Chap. 3 and Chap. 4) and then we considered the helical hinge modes of a higher-order topological insulator (Chap. 5).

The interplay between Andreev reflection and the chiral edge states of the quantum Hall effect have been examined in Chap. 3 and Chap. 4 by studying quantum Hall-superconductor hybrid systems in the regime where a single, spin-degenerate, quantum Hall edge state is present.
In Chap. 3 we considered a QH-SC junction with an arbitrary geometry and we investigated the geometrical and filling factor dependencies of the downstream conductance mediated by CAES. We found that these dependencies are quite important as they lead to strong variations of the downstream conductance. In particular, by engineering an asymmetric geometry and tuning the Fermi level close to the next Landau level, the overall electron-hole conversion probability is enhanced and the averaged downstream conductance can become negative. This provides a way to obtain clearer signatures of the Andreev conversion at the QH-SC interface. Moreover, we developed a one-dimensional effective model containing a complex pairing potential localized in the region where the QH-vacuum edge meets the QH-SC edge which allows to reproduce these dependencies, in contrast to the simple one-dimensional models commonly used in the literature. However, there is no way to compute the effective parameters unless performing a full two-dimensional simulation, implying that a two-dimensional description of the system is necessary.
In Chap. 4 we have studied a QH-SC-QH junction with a ribbon geometry where CAES propagate on both sides of the superconductor in opposite directions. While the QH-SC junction only allows an incident electron from one end of the superconductor to be converted into an electron or a hole at the other end via the normal and Andreev reflection processes, the QH-SC-QH junction allows two new so-called non-local processes. Indeed, the presence of the second QH region allows the incident electron to be transmitted to the other side of the superconductor as an electron or as a hole via the elastic co-tunneling and crossed Andreev reflection processes. We used a microscopic model to derive a secular equation allowing one to plot the energy spectrum of the counter-propagating CAES and we developed a simple one-dimensional effective model to investigate the local and non-local conductances of the junction. As we found in Chap. 3, such an effective model is not sufficient to account for the effects of geometry, but at least it allows for a qualitative understanding. To get a quantitative understanding, a full two-dimensional calculation is necessary, which we have not done due to time constraints. In the study of the energy spectrum we observed that the counter-propagating CAES are gapped and that this gap decays exponentially with the width of the superconductor. Denoting respectively by L and W the lengths of the QH-SC interfaces and the width of the superconductor, we found that only non-local processes occur when $L \to \infty$ while the system behaves as to independent QH-SC junctions when $W \to \infty$. This allows to predict that in a system where the superconductor as a finger shape, as done in some experiments, the incoming electron will be transmitted on the other side of the superconductor only via non local processes for a very long finger. Interestingly, we found regimes where the non-local conductance is negative, which is a hallmark of the crossed Andreev reflection occurring in the system. This can help experimentalists to better probe this non-local Andreev process.
For further studies, the case of spin-polarized electrons would be interesting to investigate because of its potential for topologically protected quantum computing. Indeed, a QH-SC-QH junction with a finger-shaped superconductor and spin-polarized electrons is a promising way to build a one-dimensional topological superconductor. This would require modifying our model by adding a Zeeman splitting to lift the spin-degeneracy and a spin-orbit coupling term to allow the formation of Cooper pairs.

In Chap. 5 we studied the spatial splitting of the helical hinge modes of higher-order topological insulators arising in the presence of Zeeman and superconducting couplings. This study extends the work of Queiroz and Stern who first proposed that such a spatial splitting yields one-dimensional chiral or helical Majorana modes depending on the values of the couplings [Queiroz & Stern 2019]. Indeed, we obtained a more general expression for the wave functions of the hinge modes and we explored regimes not considered by these authors leading to a new splitting scenario where two pairs of chiral Majorana modes are located at different positions. This work is a preliminary step towards transport experiments based on the split modes. We ended the chapter by suggesting some possible setups. We proposed a Majorana interferometer obtained by engineering a N/F/FS/F/N junction, where N denotes a region with no couplings, F a region with only Zeeman coupling, and FS a region with both Zeeman and superconducting couplings. Moreover, we proposed FS/N/FS Josephson junctions in different regimes such that the supercurrent is mediated by chiral or helical Majorana modes.

As the reader will have seen from this manuscript, chiral and helical boundary modes coupled to a superconductor provide rich platforms for physical phenomena. This field of research being in constant progress both theoretically and experimentally, there is no doubt that new advances will be made in the coming years. This thesis work has been an exciting adventure, and I hope you have enjoyed reading it.

Appendices

Appendix A

Scattering theory and Landauer-Büttiker formalism

Contents

In this thesis we study the transport properties of different systems experiencing only elastic scattering. A good way to describe such problems is provided by the scattering matrix formalism which involves the electron wave functions far from the structure. As an illustrative example we will first look at the Dirac-δ potential problem which is frequently used to model the interface between two materials. In this example we introduce the reflection and the transmission of an incoming particle and we then generalize these concepts with the scattering matrix formalism. We end the appendix by presenting the Landauer-Büttiker formalism which relates the to the transmission eigenvalues of the scattering matrix.

A.1 An example: the delta potential

In this thesis we widely use the delta potential barrier to model interfaces between two materials. Here we treat the 1D delta potential barrier described by $V(x) = V_0\delta(x)$ and the corresponding Schrödinger equation is given by,

$$-\frac{\hbar^2}{2m}\psi''(x) + V(x)\psi(x) = E\psi(x), \tag{A.1}$$

where we considered stationary states $\psi(x)$. In the region $x \neq 0$ the Schrödinger equation becomes, $\psi''(x) = -(2mE/\hbar^2)\psi(x)$, and the wave functions are plane waves,

$$\psi(x) = \begin{cases} \psi_+(x) = A_+e^{ikx} + B_+e^{-ikx} & \text{for } x > 0 \\ \psi_-(x) = A_-e^{ikx} + B_-e^{-ikx} & \text{for } x < 0 \end{cases}, \tag{A.2}$$

$$k = \frac{1}{\hbar}\sqrt{2mE}. \tag{A.3}$$

At $x = 0$ the wave functions $\psi_+(x)$ and $\psi_-(x)$ must be equal,

$$\psi_+(0) = \psi_-(0), \tag{A.4}$$

leading to,

$$A_+ + B_+ = A_- + B_-. \tag{A.5}$$

Because of the delta function, the derivatives are not continuous at $x = 0$. However, integrating Eq. (A.1) in the interval $[-\varepsilon, \varepsilon]$ and taking $\varepsilon \to 0$, one obtains the following condition,

$$-\frac{\hbar^2}{2m}\left[\psi'_+(0) - \psi'_-(0)\right] - V_0\psi(0) = 0, \tag{A.6}$$

leading to,

$$A_+ - B_+ - A_- + B_- = -2i\beta\,(A_+ + B_+)\,, \tag{A.7}$$

where we have introduced a dimensionless quantity β characterizing the strength of the potential barrier,

$$\beta = \frac{mV_0}{\hbar^2 k}. \tag{A.8}$$

For positive energies, the particle is free to move and it may be scattered at the delta function potential (see Fig. A.1). We consider the situation where a particle is incident on the barrier from the left

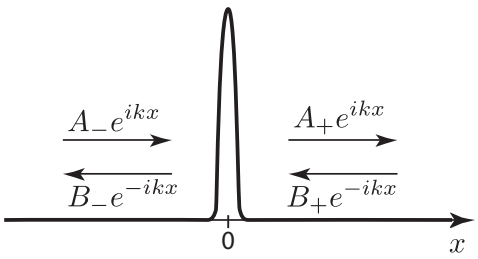

Figure A.1: Scattering from a delta potential barrier.

side (A_-). It may be reflected (B_-) or transmitted (A_+). To find the amplitudes for reflection and transmission for incidence from the left, we put in the above equations $A_- = 1$ (incoming particle), $B_- = r$ (reflection), $B_+ = 0$ (no incoming particle from the right) and $A_+ = t$ (transmission). Thus, we can write the wave function (A.2) as,

$$\psi(x) = \begin{cases} te^{ikx} & \text{for } x > 0 \\ e^{ikx} + re^{-ikx} & \text{for } x < 0 \end{cases}. \tag{A.9}$$

From the conditions (A.5) and (A.7) we have,

$$1 + r = t, \tag{A.10}$$

$$t - 1 + r = -2i\beta t, \tag{A.11}$$

and solving for r and t we obtain,

$$r = \frac{-i\beta}{1 + i\beta}, \tag{A.12}$$

$$t = \frac{1}{1 + i\beta}. \tag{A.13}$$

One can easily check the unitarity condition $R + T = 1$, where $R = |r|^2$ and $T = |t|^2$ are respectively the probabilities for the incoming electron to be reflected or transmitted. We can discuss two limits of these amplitudes. First, if $\beta = 0$ we have $t = 1$, i.e., without a barrier the incoming electron moves freely from left to right. On the other hand, if $\beta \to \infty$ we have $r = 1$, i.e., a unit probability for the incoming electron to be reflected. These two limits thus recover what the common sense would expect. In fact, the amplitudes r and t are called scattering amplitudes and they enter into a more general theory that is the scattering matrix formalism.

A.2 The scattering and transfer matrices

Here we consider one-dimensional systems. More details can be found in [Markoš & Soukoulis 2008, Chap. 1]. In a system with a localized potential, that is, a potential that is non-zero only for some finite range, such as a delta potential or a square potential, we can always analyze the scattering problem, in

which particles come in from either right or left (or both) and get transmitted or reflected. We thus consider a situation where $V = 0$ at the left and right sectors and $V \neq 0$ in the middle. In general, the wave functions in the left (L) and right (R) regions where $V = 0$ are,

$$\psi_L(x) = Ae^{ikx} + Be^{-ikx}, \tag{A.14}$$

$$\psi_R(x) = Fe^{ikx} + Ge^{-ikx}. \tag{A.15}$$

In the middle, where $V(x) \neq 0$, we can't say what the wave function will be until $V(x)$ is specified. In the example of the previous section we considered only the case of an incoming particle from the left by taking $G = 0$. However, it's not too difficult to generalize the results we've obtained to the case where we have incident particles from both sides. Since a particle coming in from the left will be either transmitted (continue to the right past the potential region) or reflected (travel back to the left), particles incident from the left cannot affect the particle stream travelling to the left on the right side of the potential region. By symmetry, particles incident from the right cannot affect the particle stream travelling to the right on the left side of the potential. That is, we can always specify A and G in the wave functions above, and express B and F in terms of them. We can write this dependence as a matrix equation,

$$\begin{bmatrix} B \\ F \end{bmatrix} = \begin{bmatrix} S_{11} & S_{12} \\ S_{21} & S_{22} \end{bmatrix} \begin{bmatrix} A \\ G \end{bmatrix}, \tag{A.16}$$

where the matrix S is called the *scattering matrix*. In fact, the scattering matrix relates the the amplitudes associated to outgoing waves to the amplitudes associated to the incoming ones such that we can write,

$$\psi_{out} = S\psi_{in}. \tag{A.17}$$

For the delta potential $V(x) = V_0\delta(x)$ we've seen that in the case where $G = 0$ we have,

$$B = \frac{-i\beta}{1+i\beta}A, \quad F = \frac{1}{1+i\beta}A, \quad \beta \equiv \frac{mV_0}{\hbar^2 k}. \tag{A.18}$$

By symmetry, if $A = 0$ so that particles come in only from the right, we have,

$$F = \frac{-i\beta}{1+i\beta}G, \quad B = \frac{1}{1+i\beta}G. \tag{A.19}$$

If both $A \neq 0$ and $G \neq 0$, we can just add up the contributions from the two cases since they don't interfere with each other, and we get,

$$\begin{bmatrix} B \\ F \end{bmatrix} = \frac{1}{1+i\beta} \begin{bmatrix} -i\beta & 1 \\ 1 & -i\beta \end{bmatrix} \begin{bmatrix} A \\ G \end{bmatrix}. \tag{A.20}$$

We've seen that in the general scattering problem, we can write the particle stream magnitudes on each side of the potential by using a scattering matrix. The scattering matrix in Eq. (A.16) expresses the outgoing particle streams on each side in terms of the incoming streams. We can also express the streams on the right in terms of the streams on the left by using a *transfer matrix*. That is, we can write,

$$\begin{bmatrix} F \\ G \end{bmatrix} = \begin{bmatrix} M_{11} & M_{12} \\ M_{21} & M_{22} \end{bmatrix} \begin{bmatrix} A \\ B \end{bmatrix}, \tag{A.21}$$

or,

$$\psi_R = M\psi_L. \tag{A.22}$$

By solving the scattering matrix equation for F and G in terms of A and B we can express the transfer matrix in terms of the scattering matrix,

$$M = -\frac{1}{S_{12}} \begin{bmatrix} S_{11}S_{22} - S_{12}S_{21} & -S_{22} \\ S_{11} & -1 \end{bmatrix}. \tag{A.23}$$

The element M_{11} is just the determinant of S so we have,

$$M = -\frac{1}{S_{12}} \begin{bmatrix} \det S & -S_{22} \\ S_{11} & -1 \end{bmatrix}. \tag{A.24}$$

Conversely, we can express the scattering matrix in terms of the transfer matrix,

$$S = -\frac{1}{M_{22}} \begin{bmatrix} -M_{21} & 1 \\ \det M & M_{12} \end{bmatrix}. \tag{A.25}$$

In the special case where the only incoming particles are from the left, $G = 0$, and from the scattering matrix, we have,

$$R_L = \frac{|B^2|}{|A|^2} = |S_{11}|^2 = \frac{|M_{21}|^2}{|M_{22}|^2}, \tag{A.26}$$

$$T_L = \frac{|F^2|}{|A|^2} = |S_{21}|^2 = \frac{|\det M|^2}{|M_{22}|^2}. \tag{A.27}$$

If the incoming particles are from the right only, $A = 0$, we get,

$$R_R = \frac{|F^2|}{|G|^2} = |S_{22}|^2 = \frac{|M_{12}|^2}{|M_{22}|^2}, \tag{A.28}$$

$$T_R = \frac{|B^2|}{|G|^2} = |S_{12}|^2 = \frac{1}{|M_{22}|^2}. \tag{A.29}$$

Because the time evolution of a Hermitian Hamiltonian H is described by a unitary operator $U = \exp\{-(i/\hbar)Ht\}$, the scattering matrix has to be unitary,

$$SS^\dagger = \mathbb{1}, \tag{A.30}$$

from which it follows the conservation of the scattering probabilities, $R_L + T_L = R_R + T_R = 1$. A usual way to write the scattering matrix is given by,

$$S = \begin{pmatrix} r & t \\ t' & r' \end{pmatrix}, \tag{A.31}$$

where the different entries correspond to,

- t: transmission of waves propagating from left to right,
- r: reflection of waves coming from the left,
- t': transmission of waves propagating from right to left,
- r': reflection of waves coming from the right.

With these notations the unitarity of the scattering matrix translates into the following equation,

$$SS^\dagger = \begin{pmatrix} |r|^2 + |t|^2 & rt'^* + tr'^* \\ t'r^* + r't^* & |r'|^2 + |t'|^2 \end{pmatrix} = \begin{pmatrix} 1 & 0 \\ 0 & 1 \end{pmatrix}, \tag{A.32}$$

and the transfer matrix can be expressed as,

$$M = \begin{pmatrix} t - r't'^{-1}r & r't'^{-1} \\ -t'^{-1}r & t'^{-1} \end{pmatrix}. \tag{A.33}$$

A useful property of the transfer matrix is that, for a system of N barriers, it can be obtained by multiplying the transfer matrices associated to each barrier. As an example let us consider a system

with two Dirac-δ barriers located at x_1 and x_2. We have thus three different regions (left, center, right) such that the wave function can be written as,

$$\psi(x) = \begin{cases} \psi_L(x) & \text{if } x < x_1 \\ \psi_C(x) & \text{if } x_1 < x < x_2 \\ \psi_R(x) & \text{if } x > x_2 \end{cases}. \tag{A.34}$$

We can then write the wave function at the right in term of the one at the left by using Eq. (A.22),

$$\psi_R = M\psi_L, \tag{A.35}$$

where M is the global transfer matrix of the system. We can also use the transfer matrices M_1 and M_2 associated to the barriers located at x_1 and x_2,

$$\psi_C = M_1\psi_L, \tag{A.36}$$

$$\psi_R = M_2\psi_C = \underbrace{M_2M_1}_{=M}\psi_L, \tag{A.37}$$

and we find the composition law $M = M_2M_1$ (as we use it in the thesis to model three terminal junctions, the double delta potential barrier is detailed in the next section). For a system of N barriers the transfer matrix is thus given by,

$$M = M_N M_{N-1} \cdots M_2 M_1. \tag{A.38}$$

Until now we considered scattering problems with a single propagating channel. All the above results can be generalized to the multi-channel case as follows. Let's consider N_L and N_R propagating channels in the left and right regions. We denote by b_L and b_R the coefficients associated to the left and right outgoing modes and by a_L and a_R the coefficients associated to the left and right incoming modes. In that case we have,

$$\begin{pmatrix} b_L(E_1) \\ b_L(E_2) \\ \vdots \\ b_L(E_{N_L}) \\ b_R(E_1) \\ b_R(E_2) \\ \vdots \\ b_R(E_{N_R}) \end{pmatrix} = \underbrace{\begin{pmatrix} r(E) & t'(E) \\ t(E) & r'(E) \end{pmatrix}}_{S(E)} \begin{pmatrix} a_L(E_1) \\ a_L(E_2) \\ \vdots \\ a_L(E_{N_L}) \\ a_R(E_1) \\ a_R(E_2) \\ \vdots \\ a_R(E_{N_R}) \end{pmatrix}, \tag{A.39}$$

where we write explicitly the energy-dependency for clarity. The scattering matrix $S(E)$ has dimension $(N_L + N_R) \times (N_L + N_R)$ and,

$$\begin{aligned} r(E) &\text{ has dimensions } N_L \times N_L, \\ r'(E) &\text{ has dimensions } N_R \times N_R, \\ t(E) &\text{ has dimensions } N_R \times N_L, \\ t'(E) &\text{ has dimensions } N_L \times N_R. \end{aligned}$$

We can then generalize the scattering matrix to a system with many leads as the one depicted in Fig. A.4. For a system with N leads we can write the scattering matrix as,

$$S = \begin{pmatrix} S_{11} & S_{12} & \cdots & S_{1N} \\ S_{21} & \ddots & \ddots & \vdots \\ \vdots & \ddots & \ddots & S_{N-1\,N} \\ S_{N1} & \cdots & S_{N\,N-1} & S_{NN} \end{pmatrix}, \tag{A.40}$$

where the diagonal elements are reflection matrices and the non-diagonal elements are transmission matrices,

$$S_{pq} = \begin{cases} r_p & \text{if } p = q \\ t_{pq} & \text{if } p \neq q \end{cases}, \tag{A.41}$$

with r_p the reflection in lead p and t_{pq} the transmission from lead q to lead p. The scattering matrix elements S_{pq} have dimension $N_p \times N_q$ with N_p and N_q the number of propagating modes in lead p and q.

In this thesis we often us a double delta barrier to model junctions where a central region is sandwiched between two leads. We thus detail this problem in the next section by using the transfer matrix method.

A.3 Another example: the double delta potential

Let us consider a L-C-R junction along the x-axis where the left (L), central (C), and right (R) regions are normal metals. We assume the system to be quasi one-dimensional and we denote by L the length of the central region. Assuming the same potential height V_0 for the left and right interfaces, the potential barriers are modeled by,

$$V(x) = V_0 \left[\delta(x - L/2) + \delta(x + L/2)\right]. \tag{A.42}$$

Here we are interested in the situation depicted in Fig. A.2 where an incoming electron from the left can be reflected back with amplitude r or transmitted to the right region with amplitude t (see Fig. A.2a). In the central region the electron can perform many round trips before being reflected back in the left reservoir or transmitted to the right reservoir. Hence, the central regions acts as a Fabry-Pérot cavity. Three possible contributions for the transmission to the right are sketched in Fig. A.2b.

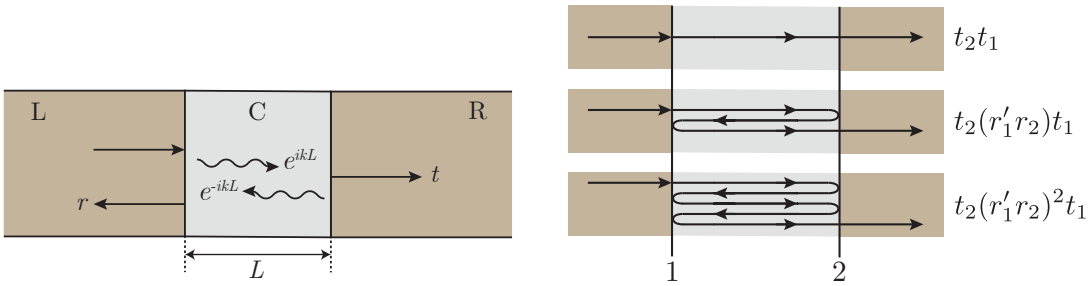

Figure A.2: Three terminal junction. In (a) we show the situation where en incoming electron from the left (L) can be reflected back to the left or transmitted to the right (R) with respective amplitudes r and t. The central region of length L forms a Fabry-Pérot cavity in which the incoming electron can perform many round trips before exiting the cavity. In (b) we show three possible processes contributing to the transmission t.

To compute the scattering amplitudes r and t we use the transfer matrix approach presented in the previous section. In particular we use the composition law $M = M_2 M_1$ derived in Eq. (A.37) and the relation (A.33) to write,

$$M = \begin{pmatrix} t - r' t'^{-1} r & r' t'^{-1} \\ -t'^{-1} r & t'^{-1} \end{pmatrix} \tag{A.43}$$

$$= \begin{pmatrix} t_1 - r_1' t_1'^{-1} r_1 & r_1' t_1'^{-1} \\ -t_1'^{-1} r_1 & t_1'^{-1} \end{pmatrix} \begin{pmatrix} t_2 - r_2' t_2'^{-1} r_2 & r_2' t_2'^{-1} \\ -t_2'^{-1} r_2 & t_2'^{-1} \end{pmatrix}. \tag{A.44}$$

From the last equality we can write the transmission amplitude t as,

$$t = t_2 \left[1 - r_1' r_2\right]^{-1} t_1. \tag{A.45}$$

The physical meaning of this result is better seen by expanding the term in square brackets in powers of $(r_1' r_2)$,

$$t = t_2 \left[1 + (r_1' r_2) + (r_1' r_2)^2 + \cdots\right] t_1. \tag{A.46}$$

The right-hand side of the above equation must be read from right to left. The first term, $t_2 t_1$, corresponds to the case where the incoming is transmitted consecutively across the two barriers. The second term, $t_2(r_1' r_2)t_1$ represents the situation where the incoming electron passes through the first barrier, reflects back at the second barrier, then reflects again on the first barrier, and finally is transmitted to the right by crossing the second barrier. So the powers $(r_1' r_2)^n$ correspond to trajectories in which the incoming particle performs n round trips. In Fig. A.2b we show three such paths. In order to derive analytical expressions we rewrite the transfer matrix as follows,

$$M = M_R \begin{pmatrix} e^{ikL} & 0 \\ 0 & e^{-ikL} \end{pmatrix} M_L, \tag{A.47}$$

where M_L and M_R are the transfer matrices of the left and right delta barriers and the diagonal matrix describes the free propagation in between the two barriers. Because we consider the same height V_0 for the left and right barriers we have $M_L = M_R = M_0$, where M_0 can be obtained from the preceding sections. By using Eq. (A.24) we can write,

$$M_0 = -\frac{1}{S_0^{12}} \begin{pmatrix} \det S_0 & -S_0^{22} \\ S_0^{11} & -1 \end{pmatrix}, \tag{A.48}$$

where S_0 is the scattering matrix of a single delta potential introduced in Eq. (A.20),

$$S_0 = \frac{1}{1 + i\beta} \begin{pmatrix} -i\beta & 1 \\ 1 & -i\beta \end{pmatrix}, \tag{A.49}$$

where we recall $\beta = mV_0/(\hbar^2 k)$. We can thus write M_0 as,

$$M_0 = \begin{pmatrix} 1 - i\beta & -i\beta \\ i\beta & 1 + i\beta \end{pmatrix}, \tag{A.50}$$

and, using $M = M_0 \,\mathrm{Diag}\{e^{ikL}, e^{-ikL}\} M_0$ and the relations (A.25) and (A.31),

$$S = \begin{pmatrix} r & t \\ t' & r' \end{pmatrix} = -\frac{1}{M_{22}} \begin{pmatrix} -M_{21} & 1 \\ \det M & M_{12} \end{pmatrix}, \tag{A.51}$$

we finally obtain,

$$T = |t|^2 = \frac{1}{1 + 4\beta^2 \left[\cos(kL) + \beta \sin(kL)\right]^2}, \tag{A.52}$$

$$R = |r|^2 = 1 - T. \tag{A.53}$$

In Fig. A.3 we plot the transmission T as a function of kL for various values of the barrier strength β. There are particular values of kL for which we observe a unit probability of transmission. These are called transmission resonances or Fabry-Pérot resonances. The resonance is reached if $\cos(kL) + \beta \sin(kL) = 0$ which is satisfied for $kL = n\pi - \arctan(1/\beta)$, with n an integer. As β increases the peaks get narrower. For $\beta \to \infty$ we recover the resonant condition of an infinite square well, $kL = n\pi$. Note that, using the wave length $\lambda = 2\pi/k$, we can rewrite the dimensionless parameter kL as $kL = 2\pi L/\lambda$. Thus, the condition $kL = n\pi$ corresponds to the situation where the distance L between the two barriers is an integer multiple of one-half of the wave length of the incoming electron.

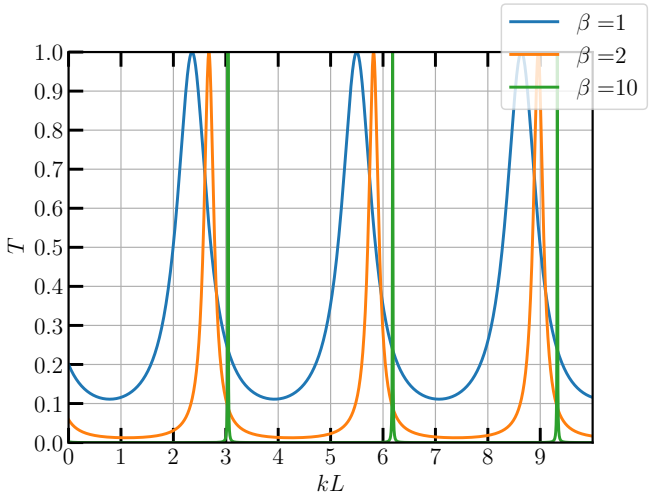

Figure A.3: Transmission T across a double delta potential as function of kL for various strengths β. Here we observe transmission resonances with peaks located at $kL = n\pi - \arctan(1/\beta)$.

A.4 The Landauer-Büttiker formalism

Here we give the main results of the Landauer-Büttiker formalism of mesoscopic transport. More details can be found in [Datta 1997, Chap. 2]. In this approach of transport originally proposed by Landauer, the conductance through a conductor is related to the probability that an electron can transmit through it [Landauer 1957, Landauer 1992]. Landauer considered the case where a conductor is connected to two reservoirs while Bütikker generalized the result to multiple probes [Büttiker 1986, Büttiker 1988]. Thus, this formalism applies to systems made of a central conductor, called the scattering region, which is connected to some leads as depicted in Fig. A.4. The results presented here are valid for ballistic conductors or, at least, as long as the transport across the conductor is coherent. The current I_p in a given lead p is defined positively if it is leaving the lead and, due to Kirchoff's rule, we must have $\sum_p I_p = 0$.

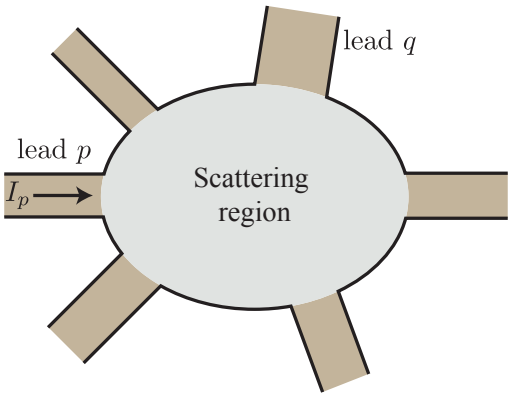

Figure A.4: Multi-terminal system. A central conductor, called the scattering region, is connected to many leads. Here we have labelled one lead by p and another one by q. The current in a given lead is positively defined if it is entering the scattering region.

Here we follow [Martin 2005] to derive the averaged current in a given lead p. We start from the

general definition of the current operator [Landau & Lifshitz 2013],

$$J_p(x) = 2 \times \frac{e\hbar}{2mi}\left[\psi_p^\dagger(x)\frac{\partial\psi_p}{\partial x} - \frac{\partial\psi_p^\dagger}{\partial x}\psi_p(x)\right], \tag{A.54}$$

where the factor of two accounts for the spin degeneracy and the fermionic field operators $\psi_p^\dagger(x)$ and $\psi_p(x)$ are defined by,

$$\psi_p^\dagger(x) = \sum_q \int \frac{\mathrm{d}k}{\sqrt{2\pi}}\left(\delta_{pq}e^{-ikx} + S_{pq}^* e^{ikx}\right)c_q^\dagger(k), \tag{A.55}$$

$$\psi_p(x) = \sum_{q'} \int \frac{\mathrm{d}k'}{\sqrt{2\pi}}\left(\delta_{pq'}e^{ik'x} + S_{pq'} e^{-ik'x}\right)c_{q'}(k'), \tag{A.56}$$

where S_{pq} is the scattering matrix element introduced in Eq. (A.41) while $c^\dagger$ and c are respectively creation and annihilation operators. After a little bit of algebra we can write the current operator as,

$$J_p(x) = \frac{\hbar e}{2m\pi}\sum_{q,q'}\int \mathrm{d}k\,\mathrm{d}k'\left[(k'+k)\left(\delta_{pq}\delta_{pq'}e^{-i(k-k')x} - S_{pq'}S_{pq}^* e^{i(k-k')x}\right)\right. \tag{A.57}$$

$$\left. + (k'-k)\left(\delta_{pq'}S_{pq}^* e^{i(k+k')x} - \delta_{pq}S_{pq'}e^{-i(k+k')x}\right)\right]c_q^\dagger(k)c_{q'}(k'), \tag{A.58}$$

and using $E = \hbar^2k^2/(2m)$ to substitue $\mathrm{d}k \to \frac{m}{\hbar^2 k}\mathrm{d}E$ we finally get,

$$J_p(x) = \sum_{q,q'}\int \mathrm{d}E\,\mathrm{d}E'\,M_p(E,E',q,q')c_q^\dagger(k)c_{q'}(k'), \tag{A.59}$$

with $M_p(E,E',q,q') = M_p^{\Sigma k} + M_p^{\Delta k}$, where,

$$M_p^{\Sigma k} = \frac{em}{2\pi\hbar^3}\left(\frac{1}{k(E)} + \frac{1}{k'(E')}\right)\left(\delta_{pq}\delta_{pq'}e^{-i(k(E)-k'(E'))x} - S_{pq'}(E')S_{pq}^*(E)e^{i(k(E)-k'(E'))x}\right), \tag{A.60}$$

$$M_m^{\Delta k} = \frac{em}{2\pi\hbar^3}\left(\frac{1}{k(E)} - \frac{1}{k'(E')}\right)\left(\delta_{pq'}S_{pq}^*(E)e^{i(k(E)+k'(E'))x} - \delta_{pq}S_{pq'}(E')e^{-i(k(E)+k'(E'))x}\right). \tag{A.61}$$

The averaged current is then given by,

$$\langle J_p(x)\rangle = \sum_{q,q'}\int \mathrm{d}E\,\mathrm{d}E'\,M_p(E,E',q,q')\left\langle c_q^\dagger(k)c_{q'}(k')\right\rangle, \tag{A.62}$$

where we can write the average of operators as,

$$\left\langle c_q^\dagger(k)c_{q'}(k')\right\rangle = f_q(E)\delta_{q,q'}\delta(k-k') = \frac{\hbar^2 k(E)}{m}f_q(E)\delta_{q,q'}\delta(E-E'), \tag{A.63}$$

where $f_q(E)$ is the Fermi function for terminal q,

$$f_q(E) = \left[1 + \exp\left(\frac{E-\mu_q}{k_\mathrm{B}T}\right)\right]^{-1}, \tag{A.64}$$

with μ_q the chemical potential in this terminal. The Dirac-δ function imposes $k = k'$ such that $M_p^{\Delta k} = 0$ and the averaged current thus takes the form,

$$\langle J_p(x)\rangle = \frac{2e}{h}\int \mathrm{d}E\left(f_p(E) - \sum_q S_{pq}^* S_{pq} f_q(E)\right), \tag{A.65}$$

which does not depends on the position. Using the unitarity of the scattering matrix we finally get the well known result,

$$\langle J_p(x)\rangle = \frac{2e}{h}\sum_q \int \mathrm{d}E\, |S_{pq}|^2 [f_p(E) - f_q(E)], \tag{A.66}$$

where $|S_{pq}|^2$ is the transmission probability from the reservoir q to the reservoir p (note that $I_p = 0$ when $p = q$). This result is the Landauer formula generalized to many channels and many leads in Refs. [Büttiker 1986, Büttiker 1988]. In the next we denote $I_p = \langle J_p(x)\rangle$ such that we can write the (averaged) current I_p in lead p as,

$$I_p = \int i_p(E)\mathrm{d}E, \tag{A.67}$$

$$i_p(E) = \frac{2e}{h}\sum_q \bar{T}_{pq}(E)\left[f_p(E) - f_q(E)\right], \tag{A.68}$$

where $\bar{T}_{pq}(E)$ represents the total transmission form lead q to lead p at energy E and can be related to the scattering matrix through the relation,

$$\bar{T}_{pq} = \mathrm{Tr}\left\{t_{pq}t_{pq}^\dagger\right\}, \tag{A.69}$$

where t_{pq} is a non-diagonal element of the scattering matrix in the basis of the leads as introduced in Eq. (A.41) and the trace gives the sum over the different modes. If the bias is small,

$$|\mu_p - \mu_q| \ll k_\mathrm{B}T, \tag{A.70}$$

we can linearize Eq. (A.67) to obtain,

$$I_p = \sum_q G_{pq}\left(V_p - V_q\right), \tag{A.71}$$

where we have used $\mu_p = eV_p$ and we have introduced the conductance matrix element,

$$G_{pq} = \frac{2e^2}{h}\int \bar{T}_{pq}(E)\left(-\frac{\partial f_0}{\partial E}\right)\mathrm{d}E, \tag{A.72}$$

where $f_0(E)$ is the equilibrium Fermi function, that is, the Fermi function evaluated at $\mu = E_f$. At low temperatures, $k_\mathrm{B}T \ll \hbar\omega_c$, we obtain,

$$G_{pq} = \frac{2e^2}{h}\bar{T}_{pq}. \tag{A.73}$$

This is the generalization of the Laudauer conductance formula for a system with many channels and many leads.

Appendix B

Mean field theory of superconductivity: BCS and BdG

Contents

The superconducting state correspond to a state in which the electrons form pairs due to an attractive energy between them. We start by introducing the basic phenomena of superconductivity and then we follow the Asano's book [Asano 2021, Chap. 3] to derive the mean field Hamiltonian of superconductors. In all this manuscript we focus on conventional superconductors also called weak-coupling or BCS superconductors. The name weak-coupling comes from the weakness of the attractive energy compared to the Debye energy, that is, the characteristic phonon energy scale. The microscopic theory of such superconductors was proposed by Bardeen, Cooper and Schrieffer (BCS) in 1957 [Bardeen *et al.* 1957] from where the name of BCS superconductors. We will present the BCS Hamiltonian and then apply the mean field approximation leading to the so-called BdG Hamiltonian. Finally we will see that the solutions of the BdG Hamiltonian are particle-hole symmetric; a convenient property allowing us to simplify some calculations.

B.1 Basic phenomena of superconductivity

The superconducting state was discovered in 1911 at Leiden by Kamerlingh Onnes (for a review, see Ref. [van Delft & Kes 2010]). The discovery has been realized by measuring the electrical resistivity of mercury at very low temperatures thanks to liquid helium. Indeed, Onnes found that, below a critical temperature $T_c \simeq 4.25$K, the electrical resistance of mercury fall to zero; from where the name of superconductivity. Since then, superconductivity has been measured in hundreds of materials. Not only a high temperature destroys the superconductivity but also a high magnetic field makes a superconductor transit in its normal state (i.e. a state with non-zero resistivity). We denote by H_c the critical field above which superconductivity is destroyed whose temperature dependence is approximatively given by,

$$H_c(T) \simeq H_c^0 \left[1 - \left(\frac{T}{T_c}\right)^2\right], \tag{B.1}$$

where H_c^0 is the critical field at zero-temperature and is different for each superconducting material. A superconductor is not only a material with zero resistivity but it is also a perfect diamagnet. Indeed, Meissner and Ochsenfeld [Meissner & Ochsenfeld 1933] have shown that a superconductor expels any applied magnetic field lower than H_c as depicted in Fig. B.1. This is known as the Meissner effect. Actually, a more detailed study of this effect shows that the magnetic field penetrates into the superconductor over a distance λ known as the penetration depth. It turns out that the complete story of the Meissner effect is a bit more complicated. To see that we recall that superconductivity is explained by considering pairs of electrons and we introduce the typical size of such pairs ξ known as the superconducting coherence

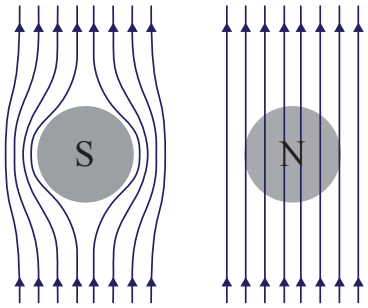

Figure B.1: Field lines around a superconductor. (a) For $H < H_c$ the material is superconducting and behaves as a perfect diamagnet and (b) for $H > H_c$ the material is normal.

length (more details on these pairs, called Cooper pairs, are provided in the next section). Then we define an important dimensionless parameter, known as the Ginzburg-Landau parameter, that is the ratio of the penetration depth to the coherence length,

$$\kappa = \frac{\lambda}{\xi}. \tag{B.2}$$

The value of this ratio distinguish between two types of superconductors whose phase diagram are represented in Fig. B.2. Type I superconductors are those with $\kappa < 1/\sqrt{2}$ and type II superconductors

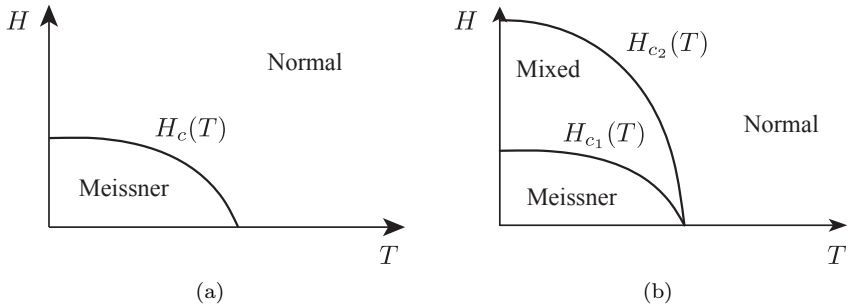

Figure B.2: Phase diagram for (a) type I and (b) type II superconductors.

those with $\kappa > 1/\sqrt{2}$. Type I superconductors are the ones discussed above, i.e. they are perfect diamagnet at fields below the thermodynamic critical field $H_c(T)$ while superconductivity is destroyed at fields exceeding $H_c(T)$ (see Fig. B.2a). On the other hand, type II superconductors exhibit perfect diamagnetism up to a critical field $H_{c_1}(T)$, known as the lower critical field. Above this field, magnetic flux begins to penetrate the sample, producing the mixed phase (or vortex phase), but does not destroy the superconductivity until the so-called higher critical field $H_{c_2}(T)$ has been reached (see Fig. B.2b). In the extreme type II limit, $\kappa \gg 1$, we have the following hierarchy [Girvin & Yang 2019, p. 573], $H_{c_1} \ll H_c \ll H_{c_2}$.

B.2 BCS Hamiltonian

The BCS theory works for a weak attractive interaction between two electrons on the Fermi surface with opposite momenta and spins. The repulsive Coulomb interaction still holds but it is dominated by the attractive one. While, in the Coulomb gauge, the Coulomb repulsion is instantaneous, the attractive interaction is not. Indeed the latter is mediated by the phonons of the crystal that have a velocity

$v_{ph} \sim 100\text{m/s}$ which is much slower than the Fermi velocity v_F. This delay allows for two electrons to form a so-called Cooper pair. The pairing mechanism can be explained semi-classically as follows. An electron comes at a given place at a time $t = 0$ and stands here during a time $t_e \sim \hbar/\varepsilon_F$ (ε_F being the Fermi energy). During time t_e this electron attracts the surrounding ions of the crystal. On the other hand, it takes $t_{ph} \sim 1/\omega_D \gg t_e$ for the ions to move toward the electron, where ω_D is the Debye frequency. At $t = t_{ph}$, the electron has already moved but remaining ions charge the place positively so that a second electron is attracted. This explains the pairing of two electrons due to this, non-local in time, attractive interaction. Quantum mechanically, the electron-electron interaction is described by the second-quantization Hamiltonian,

$$\mathcal{H}_I = \frac{1}{2}\sum_{\alpha,\beta}\int \mathrm{d}\vec{r}\int \mathrm{d}\vec{r}'\, \Psi^\dagger_\alpha(\vec{r})\Psi^\dagger_\beta(\vec{r}')V(\vec{r}-\vec{r}')\Psi_\beta(\vec{r}')\Psi_\alpha(\vec{r}), \tag{B.3}$$

where V is the interaction potential, α and β stand for the degrees of freedom of the two electrons (here the up and down spins) and $\Psi_{\alpha,\beta}$ are their field operators. The total Hamiltonian is then given by $\mathcal{H} = \mathcal{H}_0 + \mathcal{H}_I$, where $\mathcal{H}_0$ is the single-particle Hamiltonian for free electrons,

$$\mathcal{H}_0 = \sum_\alpha \int \mathrm{d}\vec{r}\,\Psi^\dagger_\alpha(\vec{r})\left[-\frac{\hbar^2\nabla^2}{2m} - \varepsilon_F\right]\Psi^\dagger_\alpha(\vec{r}). \tag{B.4}$$

The fermionic operators respect the following anticommutation relations,

$$\left\{\Psi_\alpha(\vec{r}),\ \Psi^\dagger_\beta(\vec{r}')\right\} = \delta\left(\vec{r}-\vec{r}'\right), \tag{B.5}$$

$$\left\{\Psi_\alpha(\vec{r}),\ \Psi_\beta(\vec{r}')\right\} = 0. \tag{B.6}$$

We can diagonalize the single-particle Hamiltonian by going in momentum-space through Fourier transformation,

$$\Psi_\alpha(\vec{r}) = \frac{1}{\sqrt{V_{vol}}}\sum_{\vec{k}} c_{\vec{k},\alpha}e^{i\ \vec{k}\cdot\vec{r}}, \tag{B.7}$$

where V_{vol} is the volume of the solid. The normalization condition and the completeness are satisfied by the basis functions,

$$\frac{1}{V_{vol}}\int \mathrm{d}\vec{r}\, e^{i(\vec{k}-\vec{k}')\cdot\vec{r}} = \delta_{\vec{k},\vec{k}'}, \tag{B.8}$$

$$\frac{1}{V_{vol}}\sum_{\vec{k}} e^{i\vec{k}\cdot(\vec{r}-\vec{r}')} = \frac{1}{(2\pi)^d}\int \mathrm{d}\vec{k}\, e^{i\vec{k}\cdot(\vec{r}-\vec{r}')} = \delta(\vec{r}-\vec{r}'), \tag{B.9}$$

where d is the spatial dimension of the solid. It is then easy to find the anticommutation relations for the fermionic operators in momentum-space,

$$\left\{c_{\vec{k},\alpha}, c^\dagger_{\vec{p},\beta}\right\} = \delta_{\alpha,\beta}\delta_{\vec{k},\vec{p}}, \tag{B.10}$$

$$\left\{c_{\vec{k},\alpha}, c_{\vec{p},\beta}\right\} = 0. \tag{B.11}$$

Applying the Fourier transformation to the single-particle Hamiltonian we obtain,

$$\mathcal{H}_0 = \sum_\alpha\sum_{\vec{k}} \xi_{\vec{k}} c^\dagger_{\vec{k},\alpha}c_{\vec{k},\alpha}, \tag{B.12}$$

where,

$$\xi_{\vec{k}} = \frac{\hbar^2\vec{k}^2}{2m} - \varepsilon_F, \tag{B.13}$$

is the kinetic energy of an electron relative to the Fermi level. To write the interaction Hamiltonian in momentum space we introduce the Fourier transform of the interaction potential,

$$V(\vec{r}) = \frac{1}{V_{vol}} \sum_{\vec{q}} V_{\vec{q}}\, e^{i\vec{q}\cdot\vec{r}}, \tag{B.14}$$

and we assume the following conditions are satisfied.

- The interaction is attractive and independent of $\vec{q}$, i.e., $V_{\vec{q}} = -g$ with g a positive constant.
- The attraction works between two electrons at $\vec{k}_2 = -\vec{k}_1$ and $\beta = -\alpha$.
- The two electrons have energies in an energy window near the Fermi level ε_F and delimited by the Debye energy $\hbar\omega_D$.

Under these conditions we obtain,

$$\mathcal{H}_I = \frac{1}{V_{vol}} \sum_{\vec{k},\vec{k}'} V\left(\vec{k},\vec{k}'\right) c^\dagger_{-\vec{k}',\downarrow} c^\dagger_{\vec{k}',\uparrow} c_{\vec{k},\uparrow} c_{-\vec{k},\downarrow}, \tag{B.15}$$

$$V\left(\vec{k},\vec{k}'\right) = -g\,\Theta(-|\xi_{\vec{k}}| + \hbar\omega_D)\Theta(-|\xi_{\vec{k}'}| + \hbar\omega_D). \tag{B.16}$$

We can finally write the total Hamiltonian as,

$$\mathcal{H} = \sum_{\vec{k},\alpha} \xi_{\vec{k}} c^\dagger_{\vec{k},\alpha} c_{\vec{k},\alpha} - \frac{g}{V_{vol}} \sum_{\vec{k}}{}' \sum_{\vec{k}'}{}' c^\dagger_{-\vec{k}',\downarrow} c^\dagger_{\vec{k}',\uparrow} c_{\vec{k},\uparrow} c_{-\vec{k},\downarrow}, \tag{B.17}$$

$$\sum_{\vec{k}}{}' = \sum_{\vec{k}} \Theta(-|\xi_{\vec{k}}| + \hbar\omega_D). \tag{B.18}$$

This Hamiltonian is the so-called BCS (or pairing) Hamiltonian. The interaction potential in real space at this last expression reads,

$$V(\vec{r} - \vec{r}') = -g\delta(\vec{r} - \vec{r}'), \tag{B.19}$$

which is local in space and time. This locality differs from what we said about the phonon-mediated attractive mechanism. However, this model describes very well the physics of conventional superconductors and so the space and time dependencies play in fact a minor role.

B.3 Mean field approximation and BdG Hamiltonian

The interaction term in the BCS Hamiltonian (B.17) cannot be diagonalized such that one needs to simplify it in order to find the energies and the eigenstates of the superconductor. For this reason we apply the mean field approximation to the interaction term. We thus introduce the average of operators,

$$\Delta e^{i\phi} \equiv \frac{g}{V_{vol}} \sum_{\vec{k}}{}' \left\langle c_{\vec{k},\uparrow} c_{-\vec{k},\downarrow} \right\rangle, \tag{B.20}$$

where $\Delta e^{i\phi}$ is called the pair potential (or superconducting order parameter) with amplitude $\Delta > 0$ and plays a central role in the theory of superconductivity. In particular, it describes the Cooper pairs and it is anti-symmetric under the permutation of the two spins. Thus, a Copper pair is in the spin-singlet s-wave symmetry class (see for example [Asano 2021, Eq. (3.59)]). The typical size of a Cooper pair is also related to the pair potential through the relation,

$$\xi_{BCS} = \frac{\hbar v_F}{\pi\Delta}, \tag{B.21}$$

where ξ_{BCS} is the BCS superconducting coherence length (see for example [Girvin & Yang 2019, Eq. (20.90)]). Next, we use the mean field averaging to write,

$$c_{\vec{k},\uparrow}c_{-\vec{k},\downarrow} = \left\langle c_{\vec{k},\uparrow}c_{-\vec{k},\downarrow}\right\rangle + \left[c_{\vec{k},\uparrow}c_{-\vec{k},\downarrow} - \left\langle c_{\vec{k},\uparrow}c_{-\vec{k},\downarrow}\right\rangle\right], \tag{B.22}$$

$$c^\dagger_{-\vec{k},\downarrow}c^\dagger_{\vec{k},\uparrow} = \left\langle c^\dagger_{-\vec{k},\downarrow}c^\dagger_{\vec{k},\uparrow}\right\rangle + \left[c^\dagger_{-\vec{k},\downarrow}c^\dagger_{\vec{k},\uparrow} - \left\langle c^\dagger_{-\vec{k},\downarrow}c^\dagger_{\vec{k},\uparrow}\right\rangle\right], \tag{B.23}$$

where the first terms are the mean field average and the second ones are the fluctuations from the average. We also introduce the complex conjugation of the pair potential,

$$\Delta e^{-i\phi} = \frac{g}{V_{vol}}{\sum_{\vec{k}}}' \left\langle c^\dagger_{-\vec{k},\downarrow}c^\dagger_{\vec{k},\uparrow}\right\rangle. \tag{B.24}$$

The mean field approximation then consists in considering small fluctuations such that we can expand the interaction Hamiltonian at first order in the fluctuations. This gives us,

$${\sum_{\vec{k}'}}' c^\dagger_{-\vec{k}',\downarrow}c^\dagger_{\vec{k}',\uparrow}{\sum_{\vec{k}}}' c_{\vec{k},\uparrow}c_{-\vec{k},\downarrow} \simeq -\frac{V_{vol}^2\Delta^2}{g^2} + \frac{V_{vol}}{g}{\sum_{\vec{k}}}'\left[\Delta e^{-i\phi}c_{\vec{k},\uparrow}c_{-\vec{k},\downarrow} + \Delta e^{i\phi}c^\dagger_{-\vec{k},\downarrow}c^\dagger_{\vec{k},\uparrow}\right], \tag{B.25}$$

and we can finally write the mean-field Hamiltonian for superconductivity as,

$$\mathcal{H}_{MF} = \sum_{\vec{k},\alpha}\xi_{\vec{k}}\,c^\dagger_{\vec{k},\alpha}c_{\vec{k},\alpha} - {\sum_{\vec{k}}}'\left[\Delta e^{-i\phi}c_{\vec{k},\uparrow}c_{-\vec{k},\downarrow} + \Delta e^{i\phi}c^\dagger_{-\vec{k},\downarrow}c^\dagger_{\vec{k},\uparrow}\right] + \frac{V_{vol}\Delta^2}{g} \tag{B.26}$$

$$= \sum_{\vec{k}}\begin{pmatrix}c^\dagger_{\vec{k},\uparrow} & c_{-\vec{k},\downarrow}\end{pmatrix}\begin{pmatrix}\xi_{\vec{k}} & \Delta e^{i\phi}\\ \Delta e^{-i\phi} & -\xi_{\vec{k}}\end{pmatrix}\begin{pmatrix}c_{\vec{k},\uparrow}\\ c^\dagger_{-\vec{k},\downarrow}\end{pmatrix} + \frac{V_{vol}\Delta^2}{g} \tag{B.27}$$

$$= \sum_{\vec{k}} C^\dagger_{\vec{k}}H_{BdG}(\vec{k})C_{\vec{k}} + \frac{V_{vol}\Delta^2}{g}, \tag{B.28}$$

where the high-energy cut off in the $\vec{k}$-sum should be considered if necessary. In Eq. (B.28) we have introduced the Nambu spinor,

$$C_{\vec{k}} = \begin{pmatrix}c_{\vec{k},\uparrow}\\ c^\dagger_{-\vec{k},\downarrow}\end{pmatrix}, \tag{B.29}$$

and the so-called BdG Hamiltonian [de Gennes 2018],

$$H_{BdG}(\vec{k}) = \begin{pmatrix}\xi_{\vec{k}} & \Delta e^{i\phi}\\ \Delta e^{-i\phi} & -\xi_{-\vec{k}}\end{pmatrix}, \tag{B.30}$$

$$\xi_{\vec{k}} = \frac{\hbar^2\vec{k}^2}{2m} - \mu, \tag{B.31}$$

where we now replace the Fermi energy by the chemical potential μ in the expression of $\xi_{\vec{k}}$[1]. Note that we used the notation $-\xi_{-\vec{k}}$ in the BdG Hamiltonian (B.30) in order to be more general but the the minus sign in $-\vec{k}$ has no importance when considering a parabolic dispersion as here. We can then diagonalize the mean-field Hamiltonian by solving the Schrödinger equation,

$$\begin{pmatrix}\xi_{\vec{k}} & \Delta e^{i\phi}\\ \Delta e^{-i\phi} & -\xi_{\vec{k}}\end{pmatrix}\begin{pmatrix}a\\ b\end{pmatrix} = E\begin{pmatrix}a\\ b\end{pmatrix}, \tag{B.32}$$

where the resulting system yields the so-called BdG equations. This eigenvalue problem has two solutions; one corresponding to an electron-like particle at energy $E_{\vec{k}}$ and the second corresponding to a hole-like particle at energy $-E_{\vec{k}}$ with,

$$E_{\vec{k}} = \sqrt{\xi_{\vec{k}}^2 + \Delta^2}. \tag{B.33}$$

[1] At small temperatures $k_BT \ll \varepsilon_F$ the chemical potential and the Fermi energy are the same quantities.

From this dispersion we see that the spectrum is gapped by 2Δ. For this reason, Δ is referred as the superconducting gap. The quasi-electron $(+)$ and quasi-hole $(-)$ eigenvectors are respectively given by,

$$\psi_{+,\vec{k}} = \begin{pmatrix} u_{\vec{k}} \\ v_{\vec{k}} e^{-i\phi} \end{pmatrix}, \quad \psi_{-,\vec{k}} = \begin{pmatrix} -v_{\vec{k}} e^{i\phi} \\ u_{\vec{k}} \end{pmatrix}. \tag{B.34}$$

where we have introduced,

$$u_{\vec{k}} = \sqrt{\frac{1}{2}\left(1 + \frac{\xi_{\vec{k}}}{E_{\vec{k}}}\right)}, \quad v_{\vec{k}} = \sqrt{\frac{1}{2}\left(1 - \frac{\xi_{\vec{k}}}{E_{\vec{k}}}\right)}, \tag{B.35}$$

and we have,

$$|\psi_{+,\vec{k}}|^2 = |\psi_{-,\vec{k}}|^2 = u_{\vec{k}}^2 + v_{\vec{k}}^2 = 1. \tag{B.36}$$

Sometimes it can be useful to use the following expressions,

$$u_{\vec{k}} = \frac{1}{\sqrt{2}}, \quad v_{\vec{k}} = \frac{1}{\sqrt{2}} \frac{E_{\vec{k}} - i\sqrt{\Delta^2 - E_{\vec{k}}^2}}{\Delta}, \tag{B.37}$$

which still preserve the relation (B.36). Another useful relation which is frequently used to write the eigenvectors when $|E| < \Delta$ is provided by,

$$\frac{E \pm i\sqrt{\Delta^2 - E^2}}{\Delta} = e^{\pm i \arccos(E/\Delta)}. \tag{B.38}$$

We can summarize the diagonalization of the BdG Hamiltonian as follows,

$$\begin{pmatrix} \xi_{\vec{k}} & \Delta e^{i\phi} \\ \Delta e^{-i\phi} & -\xi_{\vec{k}} \end{pmatrix} = \begin{pmatrix} u_{\vec{k}} & -v_{\vec{k}} e^{i\phi} \\ v_{\vec{k}} e^{-i\phi} & u_{\vec{k}} \end{pmatrix} \begin{pmatrix} E_{\vec{k}} & 0 \\ 0 & -E_{\vec{k}} \end{pmatrix} \begin{pmatrix} u_{\vec{k}} & v_{\vec{k}} e^{i\phi} \\ -v_{\vec{k}} e^{-i\phi} & u_{\vec{k}} \end{pmatrix}, \tag{B.39}$$

and we can write the mean-field Hamiltonian in a diagonal form as,

$$\mathcal{H}_{MF} = \sum_{\vec{k}} \begin{pmatrix} \gamma^\dagger_{\vec{k},\uparrow} & \gamma_{-\vec{k},\downarrow} \end{pmatrix} \begin{pmatrix} E_{\vec{k}} & 0 \\ 0 & -E_{-\vec{k}} \end{pmatrix} \begin{pmatrix} \gamma_{\vec{k},\uparrow} \\ \gamma^\dagger_{-\vec{k},\downarrow} \end{pmatrix} + \frac{V_{vol}\Delta^2}{g} \tag{B.40}$$

$$= \sum_{\vec{k}} E_{\vec{k}} \left(\gamma^\dagger_{\vec{k},\uparrow} \gamma_{\vec{k},\uparrow} + \gamma^\dagger_{-\vec{k},\downarrow} \gamma_{-\vec{k},\downarrow} - 1 \right) + \frac{V_{vol}\Delta^2}{g}, \tag{B.41}$$

with,

$$\begin{pmatrix} \gamma_{\vec{k},\uparrow} \\ \gamma^\dagger_{-\vec{k},\downarrow} \end{pmatrix} = \begin{pmatrix} u_{\vec{k}} & v_{\vec{k}} e^{i\phi} \\ -v_{\vec{k}} e^{-i\phi} & u_{\vec{k}} \end{pmatrix} \begin{pmatrix} c_{\vec{k},\uparrow} \\ c^\dagger_{-\vec{k},\downarrow} \end{pmatrix}, \tag{B.42}$$

$$\begin{pmatrix} c_{\vec{k},\uparrow} \\ c^\dagger_{-\vec{k},\downarrow} \end{pmatrix} = \begin{pmatrix} u_{\vec{k}} & -v_{\vec{k}} e^{i\phi} \\ v_{\vec{k}} e^{-i\phi} & u_{\vec{k}} \end{pmatrix} \begin{pmatrix} \gamma_{\vec{k},\uparrow} \\ \gamma^\dagger_{-\vec{k},\downarrow} \end{pmatrix}. \tag{B.43}$$

These last relations are called Bogoliubov transformation [Bogoliubov 1958a, Bogoliubov 1958b] and the quasiparticle created by the operator $\gamma^\dagger_{\vec{k},\alpha}$ is called a Bogoliubov quasiparticle or bogoliubon. It is easy to check that the ladder operators of the bogoliubons preserve the fermionic anticommutation relations,

$$\left\{ \gamma_{\vec{k},\alpha}, \gamma^\dagger_{\vec{p},\beta} \right\} = \delta_{\vec{k},\vec{p}} \delta_{\alpha,\beta}, \tag{B.44}$$

$$\left\{ \gamma_{\vec{k},\alpha}, \gamma_{\vec{p},\beta} \right\} = 0, \tag{B.45}$$

and we can define the "vacuum" of Bogoliubov quasiparticles as,

$$\gamma_{\vec{k},\ \alpha}|\tilde{0}\rangle = 0, \tag{B.46}$$

where $|\tilde{0}\rangle$ denotes the superconducting ground state. It follows that the creation of Bogoliubov quasiparticles describe the elementary excitations in a BCS superconductor.

The last missing information is the value of the pairing potential. From its definition in Eq. (B.20) and using the Bogoliubov transformation (B.43) we can write it in a self-consistent way as follows,

$$\Delta e^{i\phi} = \frac{g}{V_{vol}}{\sum_{\vec{k}}}' u_{\vec{k}} v_{\vec{k}} e^{i\phi}\left[1 - 2f(E_{\vec{k}})\right] = \frac{g}{V_{vol}}{\sum_{\vec{k}}}' \frac{\Delta e^{i\phi}}{2E_{\vec{k}}} \tanh\left(\frac{E_{\vec{k}}}{2k_B T}\right), \tag{B.47}$$

where we have used,

$$\left\langle \gamma^{\dagger}_{\vec{k},\alpha}\gamma_{\vec{p},\beta}\right\rangle = f(E_{\vec{k}})\delta_{\vec{k},\vec{p}}\delta_{\alpha,\beta}, \quad \left\langle \gamma_{\vec{k},\alpha}\gamma_{\vec{p},\beta}\right\rangle = 0, \tag{B.48}$$

with $f(E_{\vec{k}}) = \{1 + \exp[(E_{\vec{k}} - \mu)/(k_B T)]\}^{-1}$ the Fermi distribution function. The pair potential can thus be determined by solving Eq. (B.47) which is known as the gap equation. To proceed further we introduce the density of state per volume per spin,

$$n(\xi) = \frac{1}{V_{vol}}\sum_{\vec{k}} \delta(\xi - \xi_{\vec{k}}), \tag{B.49}$$

so that the gap equation becomes,

$$1 = g\int_0^{\hbar\omega_D} \mathrm{d}\xi \frac{n(\xi)}{\sqrt{\xi^2 + \Delta^2}} \tanh\left(\frac{\sqrt{\xi^2 + \Delta^2}}{2k_B T}\right). \tag{B.50}$$

Considering the zero-temperature density of states as approximatively constant and equals to n_0 (where n_0 is the density of states at the Fermi level) and denoting the zero-temperature pair potential by Δ_0, we can solve the gap equation by setting $T = 0$ and we get,

$$1 \simeq g n_0 \ln(2\hbar\omega_D/\Delta_0). \tag{B.51}$$

The amplitude of the pair potential at zero temperature is thus given by,

$$\Delta_0 = 2\hbar\omega_D e^{-\frac{1}{g n_0}}. \tag{B.52}$$

On the other hand, close to the critical temperature T_c we can take the limit $\Delta \to 0$ and, in the limit $\hbar\omega_D \ll k_B T_c$, the gap equation becomes,

$$1 \simeq g n_0 \ln\left(\frac{2\hbar\omega_D\gamma_0}{\pi k_B T_c}\right), \tag{B.53}$$

where γ_0 is the Euler constant. From this equation we finally get,

$$T_c = \frac{2\hbar\omega_D\gamma_0}{\pi k_B} e^{-\frac{1}{g n_0}} = \frac{\gamma_0}{\pi k_B}\Delta_0, \tag{B.54}$$

from which we can write,

$$2\Delta_0 = 3.5 k_B T_c. \tag{B.55}$$

B.4 Particle-hole symmetry

We have seen that the BdG Hamiltonian has two solutions $\psi_{+,\vec{k}}$ and $\psi_{-,\vec{k}}$ with energies respectively given by $E = \pm E_{\vec{k}}$, where the + (−) solution corresponds to a quasi-electron (quasi-hole). Moreover, the eigenstates $\psi_{+,\vec{k}}$ and $\psi_{-,\vec{k}}$ are not independent since they involve the same functions $u_{\vec{k}}$ and $v_{\vec{k}}$. These relations between the two solutions are captured by the so-called particle-hole symmetry. Indeed, defining the particle-hole symmetry operator as,

$$\mathcal{P} = i\tau_y\kappa, \tag{B.56}$$

where τ_y is the second Pauli matrix in electron-hole space and κ the complex conjugation, the second-quantized mean-field Hamiltonian preserves particle-hole symmetry,

$$\mathcal{H}_{MF} = \mathcal{P}\mathcal{H}_{MF}\mathcal{P}^{-1}. \tag{B.57}$$

For the single-particle BdG Hamiltonian the particle-hole symmetry reads,

$$H_{BdG}(\vec{k}) = -\mathcal{P}H_{BdG}(-\vec{k})\mathcal{P}^{-1}, \tag{B.58}$$

where we explicitly write the relation $\vec{k} \to -\vec{k}$ between left- and right-hand sides even if only $\vec{k}^2$ enters in the Hamiltonian.[2] From Eq. (B.58) it follows that, if there is a solution of the BdG Hamiltonian with eigenvalue and eigenvector respectively given by,

$$E_{\vec{k}}, \quad \psi_{\vec{k}}, \tag{B.61}$$

then its particle-hole partner is obtained by taking,

$$-E_{-\vec{k}}, \quad \mathcal{P}^{-1}\psi_{-\vec{k}}. \tag{B.62}$$

This is exactly what we have found in the previous section.

[2] This is important for linear dispersions. We also mention that the BdG Hamiltonian is sometimes written in a different basis in which it reads,

$$H'_{BdG} = \begin{pmatrix} \xi_{\vec{k}} & \Delta e^{i\phi} \\ -\Delta e^{-i\phi} & -\xi_{-\vec{k}} \end{pmatrix}. \tag{B.59}$$

In this case the particle-hole symmetry operator is given by,

$$\mathcal{P}' = \tau_x\kappa. \tag{B.60}$$

Appendix C

Tight-binding models

Contents

In condensed matter physics continuous Hamiltonians are usually used to describe low-energy processes (compared to the Fermi level). In practice, a lattice model (or tight-binding (TB) model) is often used instead of a continuous model to access the topological properties of the system. Indeed, the wave vector is restricted to the first Brillouin zone in such lattice models so that one can define topological invariants over it (as we did in Sec. 2.3 or for the TKNN invariant in Sec. 2.2.7). Also, TB models are very useful to describe the band structure of solids. Moreover, in this thesis, we often use the Kwant package [Groth *et al.* 2014] to perform TB simulations. In this appendix we derive TB Hamiltonians by starting from their continuous version. This procedure is known as the finite-difference method. We end the appendix by discussing about tight binding models in second quantization formalism.

C.1 Discretization of a Schrödinger Hamiltonian

In this section we widely follow the Datta book [Datta 1997, Sec. 3.5]. We start from the continuous Schrödinger Hamiltonian,

$$H(\vec{r}) = \frac{(i\hbar\vec{\nabla} - e\vec{A})^2}{2m} + U(\vec{r}). \tag{C.1}$$

C.1.1 Matrix representation for H in 1D

In one dimension, with $\vec{A} = 0$, H simplifies to,

$$H = -\frac{\hbar^2}{2m}\frac{\mathrm{d}^2}{\mathrm{d}x^2} + U(x). \tag{C.2}$$

To obtain a matrix representation for this operator, we consider the quantity $HF(x)$ where $F(x)$ is any function of x. Now we choose a discrete lattice where points are located at $x = ja$, j being an integer (see Fig. C.1), and write

$$[HF]_{x=ja} = \left[-\frac{\hbar^2}{2m}\frac{\mathrm{d}^2F}{\mathrm{d}x^2}\right]_{x=ja} + U_jF_j, \tag{C.3}$$

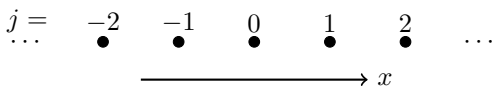

Figure C.1: An infinite linear chain discretized into a lattice.

where,

$$F_j = F(x = ja), \qquad U_j = U(x = ja). \tag{C.4}$$

We now use the method of finite differences to approximate the derivative operators. Assuming a is small we can approximate the first derivative by,

$$\left[\frac{\mathrm{d}F}{\mathrm{d}x}\right]_{x=ja} \longrightarrow \frac{1}{2a}[F_{j+1} - F_{j-1}], \tag{C.5}$$

and the second derivative by,

$$\left[\frac{\mathrm{d}^2F}{\mathrm{d}x^2}\right]_{x=ja} \longrightarrow \frac{1}{a^2}[F_{j+1} + F_{j-1} - 2F_j]. \tag{C.6}$$

With this approximation we can write from Eq. (C.3),

$$[HF]_{x=ja} = (U_j + 2t)F_j - tF_{j+1} - tF_{j-1}, \tag{C.7}$$

where,

$$t \equiv \frac{\hbar^2}{2ma^2}. \tag{C.8}$$

We can rewrite Eq. (C.7) in the form,

$$[HF]_{x=ja} = \sum_i H(j,i)F_i, \tag{C.9}$$

where

$$H(j,i) = \begin{cases} U_i + 2t & \text{if } i = j \\ -t & \text{if } i \text{ and } j \text{ are nearest neighbors} \\ 0 & \text{otherwise} \end{cases}. \tag{C.10}$$

This gives us the desired matrix representation of the Hamiltonian operator for a 1D linear chain,

$$H = \begin{bmatrix} \cdots & -t & 0 & 0 & 0 \\ -t & U_{-1} + 2t & -t & 0 & 0 \\ 0 & -t & U_0 + 2t & -t & 0 \\ 0 & 0 & -t & U_1 + 2t & -t \\ 0 & 0 & 0 & -t & \cdots \end{bmatrix}. \tag{C.11}$$

Each site is linked to its nearest neighbor by the element t, while the diagonal elements are give by the potential energy plus $2t$. It is interesting to note the similarity of this discretized Hamiltonian to the TB Hamiltonian which is widely used in condensed matter physics. In the TB model the wave function is expressed in terms of localized atomic orbitals, one at each site (s-orbital). Orbitals on neighboring sites are connected by what is referred to as a *hopping matrix element* or an *overlap integral*. The local potential U_j ($+2t$) in our model plays the role of the energy of the orbital localized at site j (also called onsite potential) while t ($\equiv \hbar^2/2ma^2$) plays the role of the overlap integral between orbitals on neighboring sites (also called hopping energy). This is represented in Fig .C.2. The price to pay for this discretization is that the dispersion cancels for $k = 0$ and $k = \pi$.

C.1.2 Matrix representation for H in 2D

It is straightforward to extend Eq. (C.10) to two or more dimensions. In general the matrix elements of $[H]$ are given by,

$$[H]_{ij} = H_{ij} = \begin{cases} U(\vec{r}_i) + zt & \text{if } i = j \\ -\tilde{t}_{ij} & \text{if } i \text{ and } j \text{ are nearest neighbors} \\ 0 & \text{otherwise} \end{cases}, \tag{C.12}$$

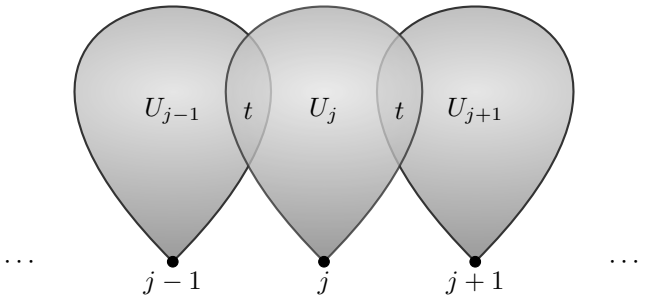

Figure C.2: Representation of the tight binding model with onsite atomic potential U_j and hopping overlap integral t.

where (i) z is the number of nearest neighbors ($z = 2$ for a linear chain and $z = 4$ for a square lattice), (ii) $\vec{r}_i$ is the position vector for lattice site i. If the vector potential is zero, then the nearest neighbor hopping is equal to $-t$ as in the 1D example. With a non-zero vector potential it is modified to,

$$\tilde{t}_{ij} = te^{\mathrm{i}\phi_{ij}} \tag{C.13}$$

where ϕ_{ij} is the Peierls phase defined as [Peierls 1933, Hofstadter 1976],

$$\phi_{ij} = \frac{e}{\hbar}\int_{\vec{r}_i}^{\vec{r}_j} \vec{A}(\vec{r}) \cdot \mathrm{d}\vec{r}, \tag{C.14}$$

where the vector potential is evaluated at a point halfway between sites i and j, that is, at $(\vec{r}_i + \vec{r}_j)/2$. We can write the TB Hamiltonian (C.12) in a compact form as follows,

$$H_{ij} = [U(\vec{r}_i) + zt]\,\delta_{\vec{r}_i,\vec{r}_j} - \sum_{\vec{R}_a} \tilde{t}_{ij}\delta_{\vec{r}_i-\vec{r}_j,\vec{R}_a}, \tag{C.15}$$

where $\delta_{a,b}$ is the Kronecker-δ which equals one if $a = b$ and zero otherwise and $\{\vec{R}_a\}$ is the set of the nearest neighbour vectors. For example, in two dimensions we have $\{\vec{R}_a\} = \{\hat{u}_x, -\hat{u}_x, \hat{u}_y, -\hat{u}_y\}$. Note that all terms that don't depend on k will enter in the TB Hamiltonian as onsites. Thus, if we want to deal with a Hamiltonian relative to the Fermi level we just have to add $-\mu$ in the onsite potential.

C.2 Discretization of a Dirac Hamiltonian

Here we focus on the one-dimensional massive Dirac Hamiltonian,

$$H = vp_x\sigma_x + m(x)v^2\sigma_z = -i\hbar v\partial_x\sigma_x + m(x)v^2\sigma_z, \tag{C.16}$$

where we consider a position-dependent mass term $m(x)$. In order to describe a topological insulator we need to introduce a quadratic correction in $\vec{p}$ to the mass term [Shen *et al.* 2011] and we obtain the modified Dirac Hamiltonian,

$$H = vp_x\sigma_x + \left[m(x)v^2 - Bp_x^2\right]\sigma_z = -i\hbar v\partial_x\sigma_x + \left[m(x)v^2 + \hbar^2 B\partial_x^2\right]\sigma_z \tag{C.17}$$

Such a modified Dirac Hamiltonian is extensively used in the book by Shen [Shen 2012]. To discretize this Hamiltonian on a linear chain we substitute $x \to ja$ and, applying the above Hamiltonian on a wave

function ψ, we obtain,

$$-i\hbar v\frac{\partial\psi}{\partial x}\sigma_x = -\frac{i\hbar v}{2a}\left(\psi_{j+1}-\psi_{j-1}\right)\sigma_x, \tag{C.18}$$

$$m(x)v^2\psi(x)\sigma_z = m_j v^2\psi_j\sigma_z, \tag{C.19}$$

$$\hbar^2 B\frac{\partial^2\psi}{\partial x^2}\sigma_z = \frac{\hbar^2 B}{a^2}(\psi_{j+1}+\psi_{j-1}-2\psi_j)\sigma_z \tag{C.20}$$

where we have used Eqs. (C.5) and (C.6) for the derivatives and we use the notation $f_j = f(x = ja)$. Using the following definitions,

$$\varepsilon \equiv \frac{\hbar v}{2a}, \tag{C.21}$$

$$t \equiv -\frac{B\hbar^2}{a^2}, \tag{C.22}$$

$$\tilde{m} \equiv mv^2, \tag{C.23}$$

the discrete Dirac Hamiltonian reads,

$$H_{ij} = \begin{cases} (\tilde{m}_j + 2t)\sigma_z & \text{if } i = j \\ -\mathrm{i}\varepsilon\sigma_x - t\sigma_z & \text{if } i = j+1 \\ +\mathrm{i}\varepsilon\sigma_x - t\sigma_z & \text{if } i = j-1 \\ 0 & \text{otherwise} \end{cases}. \tag{C.24}$$

We can write the above Hamiltonian in a compact form as,

$$H_{ij} = (\tilde{m}_j + 2t)\sigma_z\delta_{\vec{r}_i,\vec{r}_j} - \sum_{\vec{R}_a}\left[t\sigma_z + i\varepsilon\left(\vec{r}_i - \vec{r}_j\right)\cdot\vec{\sigma}\right]\delta_{\vec{r}_i-\vec{r}_j,\vec{R}_a}, \tag{C.25}$$

where $\vec{r}_{i,j}$ are position vectors, $\{\vec{R}_a\} = \{\hat{u}_x, -\hat{u}_x\}$ are nearest neighbour vectors, and $\vec{\sigma}$ is the vector of Pauli matrices.

C.3 Tight-binding models in second quantization: momentum-space representation and dispersion

A natural way to deal with lattice Hamiltonians is provided by the second quantization formalism. The second quantization Hamiltonian $\mathcal{H}$ is expressed in terms of the first quantization one through the relation,

$$\mathcal{H} = \sum_{ij}\Psi_i^\dagger H_{ij}\Psi_j, \tag{C.26}$$

where $\Psi_i^\dagger$ and Ψ_j are (eventually one-dimensional) spinors containing annihilation and/or creation operators. Here we consider the simplest (Schrödinger) TB Hamiltonian, that is, in one dimension without onsite potential and without spin,

$$\mathcal{H} = -t\sum_{\langle ij\rangle}(c_i^\dagger c_j + c_j^\dagger c_i), \tag{C.27}$$

where $\langle ij\rangle$ stands for nearest neighbors. Here $c_i^\dagger c_j$ annihilates a fermion at $\vec{r}_j$ and creates one at $\vec{r}_i$, which we can physically interpret as a fermion going from $\vec{r}_j$ to $\vec{r}_i$. In order to go from position-space to momentum-space we give the relations,

$$\begin{aligned} c_j^\dagger &= \frac{1}{\sqrt{N}}\sum_{\vec{k}} e^{-i\vec{k}\cdot\vec{r}_j}c_{\vec{k}}^\dagger, \\ c_j &= \frac{1}{\sqrt{N}}\sum_{\vec{k}} e^{i\vec{k}\cdot\vec{r}_j}c_{\vec{k}}, \end{aligned} \tag{C.28}$$

and inversely,

$$\begin{aligned} c_{\vec{k}}^{\dagger} &= \frac{1}{\sqrt{N}} \sum_j e^{i\vec{k}\cdot\vec{r}_j} c_j^{\dagger}, \\ c_{\vec{k}} &= \frac{1}{\sqrt{N}} \sum_j e^{-i\vec{k}\cdot\vec{r}_j} c_j, \end{aligned} \tag{C.29}$$

where N is the number of sites. The total number of particle is conserved,

$$\sum_j n_j = \sum_j c_j^{\dagger} c_j = \sum_{\vec{k}} c_{\vec{k}}^{\dagger} c_{\vec{k}}, \tag{C.30}$$

and we have the following orthogonality relations,

$$\frac{1}{N} \sum_j e^{i(\vec{k}-\vec{k}')\cdot\vec{r}_j} = \delta_{\vec{k},\vec{k}'}, \tag{C.31}$$

$$\frac{1}{N} \sum_j e^{i\vec{k}\cdot(\vec{r}_j-\vec{r}_{j'})} = \delta_{j,j'}. \tag{C.32}$$

To go in the momentum-space representation we first rewrite the sum over nearest neighbors as,

$$\sum_{\langle ij \rangle} (c_i^{\dagger} c_j + c_j^{\dagger} c_i) = \frac{1}{2} \sum_j \sum_{\vec{\delta}} (c_j^{\dagger} c_{j+\vec{\delta}} + c_{j+\vec{\delta}}^{\dagger} c_j), \tag{C.33}$$

where the sum over $\vec{\delta}$ is carried out over the nearest-neighbor vectors $\vec{\delta}_1$, $\vec{\delta}_2$, ..., $\vec{\delta}_z$, $c_{j+\vec{\delta}}^{\dagger}$ creates a fermion at position $\vec{r}_j + \delta$, and the factor $1/2$ is to avoid double counting. Then, rewriting the fermionic operators in momentum space using Eq. (C.28) we have,

$$\mathcal{H} = -t \sum_{\vec{k}} \sum_{\vec{\delta}} \cos(\vec{k}\cdot\vec{\delta}) c_{\vec{k}}^{\dagger} c_{\vec{k}} = \sum_{\vec{k}} \varepsilon_{\vec{k}}\, c_{\vec{k}}^{\dagger} c_{\vec{k}}, \tag{C.34}$$

from which we obtain the TB dispersion relation,

$$\varepsilon_{\vec{k}} = -t \sum_{\vec{\delta}} \cos(\vec{k}\cdot\vec{\delta}). \tag{C.35}$$

For a 1D wire along the x-axis with nearest-neighbor vectors,

$$\vec{\delta}_1 = a\hat{x}, \qquad \vec{\delta}_2 = -a\hat{x}, \tag{C.36}$$

where a is the lattice constant, the energy dispersion writes,

$$\varepsilon_{k,1D} = -2t\cos(ka). \tag{C.37}$$

For the 2D square lattice with nearest-neighbor vectors,

$$\vec{\delta}_1 = a\hat{x}, \qquad \vec{\delta}_2 = -a\hat{x}, \qquad \vec{\delta}_3 = a\hat{y}, \qquad \vec{\delta}_4 = -a\hat{y}, \tag{C.38}$$

where a is the lattice constant, the energy dispersion relation then reads,

$$\varepsilon_{\vec{k},2D} = -2t[\cos(k_x a) + \cos(k_y a)]. \tag{C.39}$$

If we restore the t-dependent terms of the onsite potential as defined in Eq. (C.12), $U_{onsite} = zt$ with $z = 2$ for the 1D wire and $z = 4$ for the 2D square lattice, the above energy dispersions become,

$$\varepsilon_{k,1D} = 2t[1 - \cos(ka)] \xrightarrow[ka\to 0]{} \frac{\hbar^2 k^2}{2m}, \tag{C.40}$$

$$\varepsilon_{\vec{k},2D} = 2t[1 - \cos(k_x a)] + 2t[1 - \cos(k_y a)] \xrightarrow[\substack{k_x a\to 0 \\ k_y a\to 0}]{} \frac{\hbar^2 \vec{k}^2}{2m}, \tag{C.41}$$

where we have used $t = \hbar^2/(2ma^2)$ and the same kind of relation holds in 3D. Thus, the tight-binding and continuum models are equivalent for $\vec{k} \cdot \hat{a} \to 0$, where $\hat{a} = a(\hat{x}, \hat{y}, \hat{z})$.

For free electrons in a 1D wire, the continuum energy dispersion (relative to the Fermi level μ) can be written as $E = \hbar^2 k^2/(2m) - \mu$. In that case we have $k = \pm(1/\hbar)\sqrt{2m(E+\mu)}$ and, for low-energy states with $|E| \ll \mu$, the condition $ka \to 0$ is satisfied if $t/\mu \gg 1$.

Appendix D

CAES velocity, simulation parameters, and dependencies of τ

Contents

This appendix is a supplement to Chap. 3 in which we detail the analytical calculation of the CAES velocity v, we discuss the choice of parameters for the numerical simulations, and we study the dependency of the Andreev conversion τ on the system parameters.

D.1 Analytical result for the CAES velocity

Here we detail the analytical calculation of the CAES velocity v defined in Eq. (3.39) as,

$$\tilde{v} = \frac{v}{\sqrt{2} l_B \omega_c} = - \left. \frac{\partial_\kappa \tilde{s}(\varepsilon, \kappa)}{\partial_\varepsilon \tilde{s}(\varepsilon, \kappa)} \right|_{\substack{\varepsilon = 0 \\ \kappa = \kappa_0}}, \tag{D.1}$$

where the dimensionless secular equation $\tilde{s}(\varepsilon, \kappa)$ is defined in Eq. (3.35),

$$\tilde{s}(\varepsilon, \kappa) = A \tilde{G} \tilde{H} - B \partial_\kappa \tilde{G}\, \partial_\kappa \tilde{H} - \frac{\varepsilon}{\sqrt{\delta^2 - \varepsilon^2}} C (\tilde{G} \partial_\kappa \tilde{H} + \tilde{H} \partial_\kappa \tilde{G}) + D (\tilde{G} \partial_\kappa \tilde{H} - \tilde{H} \partial_\kappa \tilde{G}) = 0, \tag{D.2}$$

and the dimensionless quantities have been introduced in Eqs. (3.36) and (3.37),

$$A = \tilde{c}^2 + \tilde{d}^2,\ B = \frac{m_{SC} \hbar \omega_c}{m_{QH} \mu_{SC}},\ C = \sqrt{B} \tilde{c},\ D = \sqrt{B} \tilde{d}, \quad \tilde{c} = \frac{\mathrm{Re}\{q\}}{k_F^{SC}},\ \tilde{d} = \frac{\mathrm{Im}\{q\}}{k_F^{SC}} + Z\, \frac{v_F^{QH}}{v_F^{SC}}, \tag{D.3}$$

$$\varepsilon = \frac{E}{\hbar \omega_c},\ \kappa = \sqrt{2} l_B k_y,\ \delta = \frac{\Delta}{\hbar \omega_c},\ \tilde{G}(\varepsilon, \kappa) = U\left(-\frac{\nu}{2} - \varepsilon, \kappa\right),\ \tilde{H}(\varepsilon, \kappa) = U\left(-\frac{\nu}{2} + \varepsilon, -\kappa\right), \tag{D.4}$$

with $U(a, z)$ the parabolic cylinder function introduced in Eq. (2.78). In order to calculate the derivatives appearing in the definition (D.1) we introduce the shorthand notations,

$$\partial_1 = \partial_\varepsilon,\ \partial_2 = \partial_\kappa,\ \partial_{12} = \partial_\varepsilon \partial_\kappa,\ \partial_{22} = \partial_\kappa^2, \tag{D.5}$$

and we rewrite the dimensionless secular equation (D.2) as,

$$\tilde{s}(\varepsilon, \kappa) = A \tilde{G} \tilde{H} - B \partial_2 \tilde{G}\, \partial_2 \tilde{H} - \frac{\varepsilon}{\sqrt{\delta^2 - \varepsilon^2}} C (\tilde{G} \partial_2 \tilde{H} + \tilde{H} \partial_2 \tilde{G}) + D (\tilde{G} \partial_2 \tilde{H} - \tilde{H} \partial_2 \tilde{G}) = 0. \tag{D.6}$$

In order to simplify the ε and κ derivatives involved in the secular equation we neglect the energy and momentum dependencies of the momentum q, $q \simeq k_{F,sc} \sqrt{1 + i\Delta/\mu_{sc}}$, such that we only need to

differentiate the parabolic cylinder functions and the derivatives appearing in the definition (D.1) read,

$$\left.\frac{\partial\tilde{s}(\varepsilon,\kappa)}{\partial\varepsilon}\right|_{\substack{\varepsilon=0\\ \kappa=\kappa_0}} = A_0(\tilde{G}_0\partial_1\tilde{H}_0 + \tilde{H}_0\partial_1\tilde{G}_0) - B_0(\partial_2\tilde{G}_0\ \partial_{12}\tilde{H}_0 + \partial_2\tilde{H}_0\partial_{12}\tilde{H}_0) \tag{D.7}$$
$$- \frac{1}{\delta}C_0(\tilde{G}_0\partial_2\tilde{H}_0 + \tilde{H}_0\partial_2\tilde{G}_0) + D_0(\tilde{G}_0\partial_{12}\tilde{H}_0 - \tilde{H}_0\partial_{12}\tilde{G}_0 + \partial_1\tilde{G}_0\partial_2\tilde{H}_0 - \partial_1\tilde{H}_0\partial_2\tilde{G}_0),$$

$$\left.\frac{\partial\tilde{s}(\varepsilon,\kappa)}{\partial\kappa}\right|_{\substack{\varepsilon=0\\ \kappa=\kappa_0}} = A_0(\tilde{G}_0\partial_2\tilde{H}_0 + \tilde{H}_0\partial_2\tilde{G}_0) - B_0(\partial_2\tilde{G}_0\partial_{22}\tilde{H}_0 + \partial_2\tilde{H}_0\partial_{22}\tilde{G}_0) + D_0(\tilde{G}_0\partial_{22}\tilde{H}_0 + \tilde{H}_0\partial_{22}\tilde{G}_0), \tag{D.8}$$

where the indices 0 stand for $\varepsilon = 0$ and $\kappa = \kappa_0$. To go further, we simplify the parabolic cylinder functions by using the asymptotic expansion (3.44) leading to the simplified expressions of $\tilde{G}$ and $\tilde{H}$ given in Eqs. (3.46) and (3.47),

$$\tilde{G}(\varepsilon,\kappa), \tilde{H}(\varepsilon,\kappa) = U\left(-\frac{\nu}{2} \mp \varepsilon, \pm\kappa\right) = F_\pm\cos(\alpha_\pm + \beta_\pm), \tag{D.9}$$

with,

$$F_\pm = \frac{\Gamma\left(\frac{1+\nu}{4} \pm \frac{\varepsilon}{2}\right)}{2^{\frac{1-\nu}{4}\mp\frac{\varepsilon}{2}}\sqrt{\pi}}, \quad \alpha_\pm = \left(\frac{1-\nu}{4} \mp \frac{\varepsilon}{2}\right)\pi, \quad \beta_\pm = \Gamma_\pm\kappa, \quad \Gamma_\pm = \sqrt{2}\frac{\Gamma\left(\frac{3+\nu}{4} \pm \frac{\varepsilon}{2}\right)}{\Gamma\left(\frac{1+\nu}{4} \pm \frac{\varepsilon}{2}\right)}. \tag{D.10}$$

Furthermore, at $\varepsilon = 0$ and $\kappa = \kappa_0$ we have $F_+ = F_- = F_0$, $\alpha_+ = \alpha_- = \alpha_0$, and $\beta_+ = \beta_- = \beta_0$, with,

$$F_0 = \frac{\Gamma\left(\frac{1+\nu}{4}\right)}{2^{\frac{1-\nu}{4}}\sqrt{\pi}}, \quad \alpha_0 = \frac{1-\nu}{4}\pi, \quad \beta_0 = \Gamma_0\kappa_0, \quad \Gamma_0 = \sqrt{2}\frac{\Gamma\left(\frac{3+\nu}{4}\right)}{\Gamma\left(\frac{1+\nu}{4}\right)}, \tag{D.11}$$

where $\Gamma_0 \in]0.8, 1.5[$ for $\nu \in]1, 3[$. We can thus write the previous terms involving parabolic cylinder functions at zero bias as,

$$\tilde{G}_0 = F_0\cos(\alpha_0 + \beta_0), \quad \tilde{H}_0 = F_0\cos(\alpha_0 - \beta_0), \tag{D.12}$$
$$\partial_\kappa\tilde{G}_0 = -F_0\Gamma_0\sin(\alpha_0 + \beta_0), \quad \partial_\kappa\tilde{H}_0 = +F_0\Gamma_0\sin(\alpha_0 - \beta_0), \tag{D.13}$$

and, to perform the ε-derivatives appearing in Eqs. (D.7) and (D.8), we consider $F_\pm \simeq F_0$ and $\Gamma_\pm \simeq \Gamma_0$. This allows us to write

$$\tilde{G}_0, \tilde{H}_0 = F_0\cos(\alpha_0 \pm \beta_0), \tag{D.14}$$
$$\partial_1\tilde{G}_0, \partial_1\tilde{H}_0 = \pm F_0\frac{\pi}{2}\sin(\alpha_0 \pm \beta_0), \tag{D.15}$$
$$\partial_2\tilde{G}_0, \partial_2\tilde{H}_0 = \mp F_0\Gamma_0\sin(\alpha_0 \pm \beta_0), \tag{D.16}$$
$$\partial_{12}\tilde{G}_0, \partial_{12}\tilde{H}_0 = F_0\frac{\pi}{2}\Gamma_0\cos(\alpha_0 \pm \beta_0), \tag{D.17}$$
$$\partial_{22}\tilde{G}_0, \partial_{22}\tilde{H}_0 = -F_0\Gamma_0^2\cos(\alpha_0 \pm \beta_0), \tag{D.18}$$

so that the terms appearing in (D.7) and (D.8) are given by,

$$\tilde{G}_0\partial_2\tilde{H}_0 + \tilde{H}_0\partial_2\tilde{G}_0 = -F_0^2\ \Gamma_0\sin 2\beta_0, \tag{D.19}$$
$$\partial_2\tilde{G}_0\partial_{22}\tilde{H}_0 + \partial_2\tilde{H}_0\partial_{22}\tilde{G}_0 = F_0^2\Gamma_0^3\sin 2\beta_0, \tag{D.20}$$
$$\tilde{G}_0\partial_{22}\tilde{H}_0 - \tilde{H}_0\partial_{22}\tilde{G}_0 = 0, \tag{D.21}$$
$$\tilde{G}_0\partial_1\tilde{H}_0 + \tilde{H}_0\partial_1\tilde{G}_0 = F_0^2\frac{\pi}{2}\ \Gamma_0\sin 2\beta_0, \tag{D.22}$$
$$\partial_2\tilde{G}_0\partial_{12}\tilde{H}_0 + \partial_2\tilde{H}_0\partial_{12}\tilde{H}_0 = -F_0^2\frac{\pi}{2}\Gamma_0^2\sin 2\beta_0, \tag{D.23}$$
$$\tilde{G}_0\partial_{12}\tilde{H}_0 - \tilde{H}_0\partial_{12}\tilde{G}_0 = 0, \tag{D.24}$$
$$\partial_1\tilde{G}_0\partial_2\tilde{H}_0 - \partial_1\tilde{H}_0\partial_2\tilde{G}_0 = 0, \tag{D.25}$$

leading to the following analytical result for the dimensionless velocity,

$$\tilde{v} = \frac{B_0\Gamma_0^2 + A_0}{\frac{\pi}{2\Gamma_0}(B_0\Gamma_0^2 + A_0) + \frac{1}{\delta}C_0}. \tag{D.26}$$

D.2 Choice of parameters for the numerical simulations

In this appendix we discuss the choice of parameters for the numerical simulations. We first determine the parameter regimes where the tight-binding model agrees with the continuum model. In fact, we want to find regimes where lattice and finite-size effects do not change the energy spectrum of the CAES obtained from the tight-binding model to that obtained from the continuum model. To do so, we compare the energy spectrums obtained from these two models for different values of t/μ_{SC}, μ_{QH}/Δ, μ_{SC}/μ_{QH} and Z, as well as for different values of the QH and SC lengths L_{QH} and L_{SC} shown in Fig. D.1. As finite-size effects can be sources of variations of the scattering probabilities, we then study the dependency of the Andreev conversion τ on the system's dimensions. This will allow us to determine the size of the simulation box such that the value of τ has converged. As we will see, the corresponding dimensions depend on which values have been chosen for the angles θ_{QH} and θ_{SC}. In all this appendix we set $t = 1$.

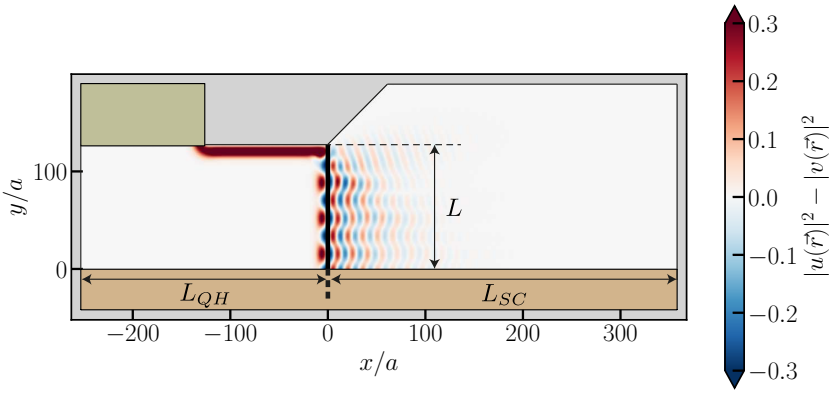

Figure D.1: Probability density $|u(\vec{r})|^2 - |v(\vec{r})|^2$ of an incoming electron state for $\theta_{SC} = 45°$ and $\theta_{QH} = 90°$. The interference of CAES along the QH-SC interface (black line) can be clearly seen. Note that the wave function does not have any weight in the vicinity of the SC-vacuum boundary. The parameters are $\mu_{QH} = \mu_{SC} = 10\Delta$, $\nu = 2$ and $Z = 0$. This figure is the same as Fig. 3.18 in the main text.

D.2.1 Comparison between tight-binding and continuum spectra

In this subsection we compare the energy spectra obtained from the tight-binding and continuum models for different values of the system dimensions and parameters to determine the regime for which they give the same results. We start by varying the system parameters with sufficiently large values of the system dimensions so that no finite size effects come into play. We then vary the system dimensions to determine the minimum values of L_{QH} and L_{SC} that allow the tight-binding model to recover the continuum model. In all plots presented here, the energy spectra obtained with the continuum model are represented by red dots, while those obtained with the lattice model are represented by black lines.

In Fig. D.2 we compare the energy spectra for different values of t/μ_{SC} with $\mu_{QH} = \mu_{SC} = 10\Delta$, $\nu = 2$, $Z = 0$, $L_{QH} = 10l_B$, and $L_{SC} = 4\xi$. According to this figure, we find a satisfactory agreement between the two models for $t/\mu_{SC} \gtrsim 10$. In the following we take $t/\mu_{SC} = 20$.

In Fig. D.3 we compare the energy spectra for different values of μ_{QH}/Δ with $t/\mu_{SC} = 20$, $\mu_{QH} = \mu_{SC}$, $\nu = 2$, $Z = 0$, $L_{QH} = 10l_B$, and $L_{SC} = 4\xi$. According to this figure, we find a satisfactory agreement between the two models for $\mu_{QH}/\Delta \gtrsim 5$. In the following we take $\mu_{QH}/\Delta = 10$.

In the two preceding figures we considered ideal interfaces with $\mu_{QH} = \mu_{SC}$ and $Z = 0$. We now look at non-ideal interfaces by considering a Fermi mismatch and a potential barrier. In Fig. D.4 we

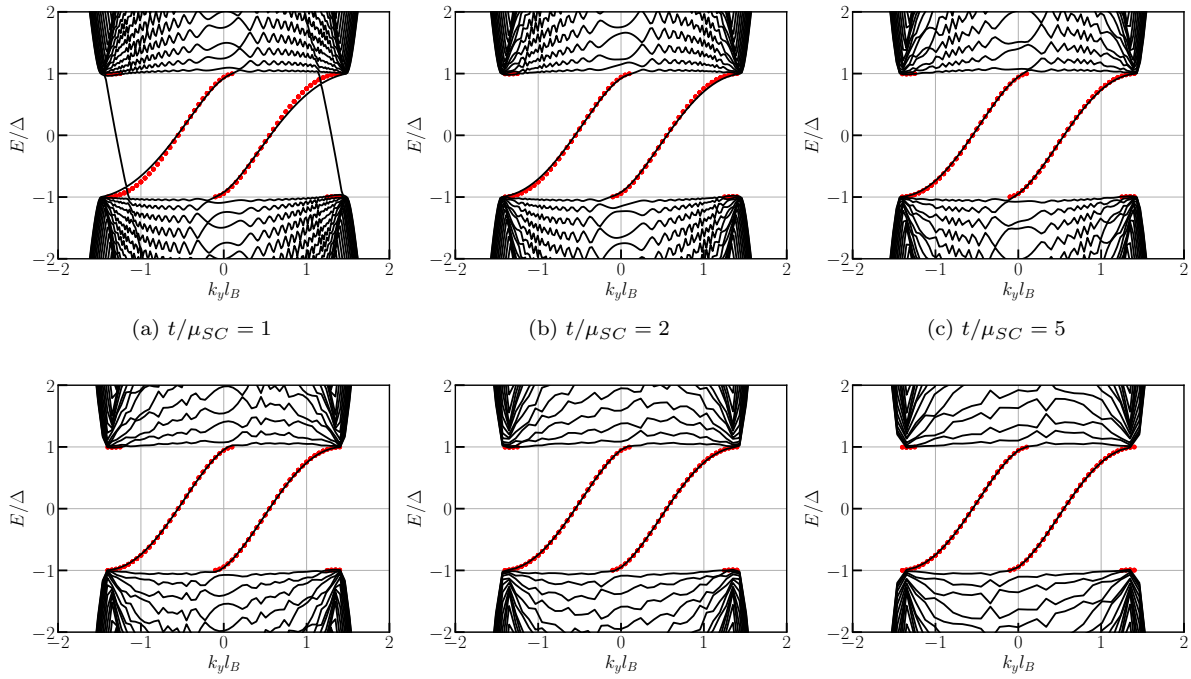

(a) $t/\mu_{SC} = 1$ (b) $t/\mu_{SC} = 2$ (c) $t/\mu_{SC} = 5$

(d) $t/\mu_{SC} = 10$ (e) $t/\mu_{SC} = 20$ (f) $t/\mu_{SC} = 40$

Figure D.2: Comparison between continuum and tight-binding spectra for various values of t/μ_{SC}. We set (a) $t/\mu_{SC} = 1$, (b) $t/\mu_{SC} = 2$, (c) $t/\mu_{SC} = 5$, (d) $t/\mu_{SC} = 10$, (e) $t/\mu_{SC} = 20$, and (f) $t/\mu_{SC} = 40$.

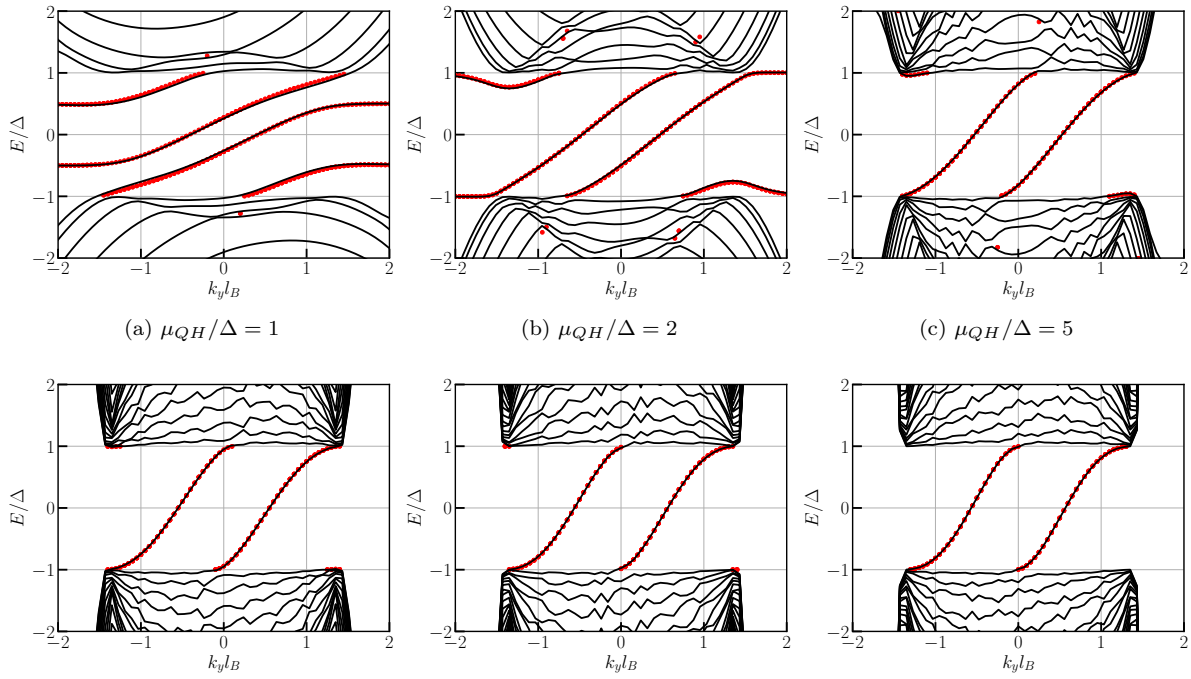

(a) $\mu_{QH}/\Delta = 1$ (b) $\mu_{QH}/\Delta = 2$ (c) $\mu_{QH}/\Delta = 5$

(d) $\mu_{QH}/\Delta = 10$ (e) $\mu_{QH}/\Delta = 20$ (f) $\mu_{QH}/\Delta = 40$

Figure D.3: Comparison between continuum and tight-binding spectra for various values of μ_{QH}/Δ: (a) $\mu_{QH}/\Delta = 1$, (b) $\mu_{QH}/\Delta = 2$, (c) $\mu_{QH}/\Delta = 5$, (d) $\mu_{QH}/\Delta = 10$, (e) $\mu_{QH}/\Delta = 20$, and (f) $\mu_{QH}/\Delta = 40$.

compare the energy spectra for different values of μ_{SC}/μ_{QH} with $t/\mu_{SC} = 20$, $\mu_{QH} = 10\Delta$, $\nu = 2$, $Z = 0$, $L_{QH} = 10l_B$, and $L_{SC} = 4\xi$. According to this figure, we see that the Fermi mismatch leads to small deviations between the two models, which can be attributed to lattice effects.

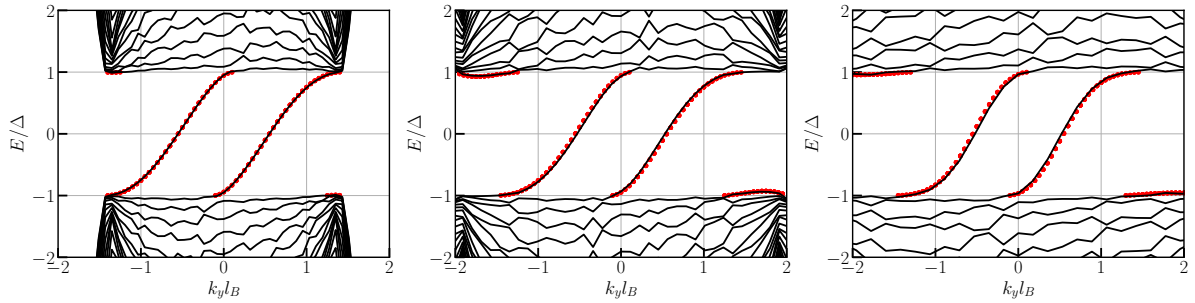

(a) $\mu_{SC}/\mu_{QH} = 1$ (b) $\mu_{SC}/\mu_{QH} = 2$ (c) $\mu_{SC}/\mu_{QH} = 5$

Figure D.4: Comparison between continuum and tight-binding spectra for various values of μ_{SC}/μ_{QH}.

Finally, in Fig. D.5 we compare the energy spectra for different values of Z with $t/\mu_{SC} = 20$, $\mu_{QH} = \mu_{SC} = 10\Delta$, $\nu = 2$, $L_{QH} = 10l_B$, and $L_{SC} = 4\xi$. According to this figure, the two models agree regardless of the value of the potential barrier.

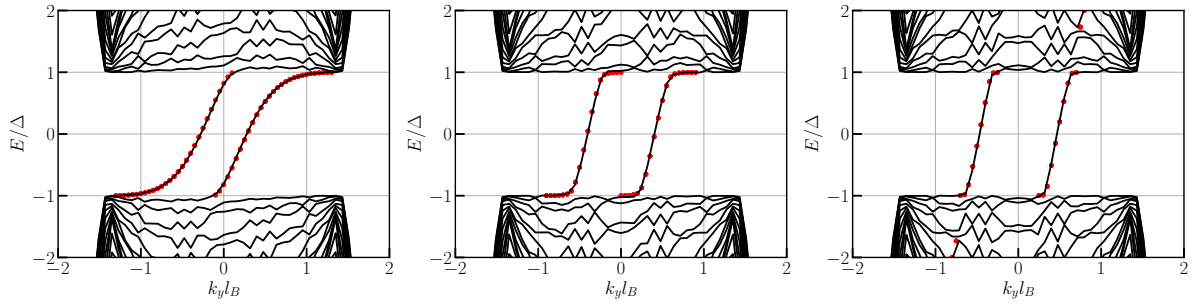

(a) $Z = 1$ (b) $Z = 5$ (c) $Z = 10$

Figure D.5: Comparison between continuum and tight-binding spectra for various values of Z.

Now that we have determined the parameter regimes that allow satisfactory agreement between the continuous and lattice models, we want to determine for what minimum values of L_{QH} and L_{SC} these two models agree. To study these dependencies we choose $t/\mu_{SC} = 20$, $\mu_{QH} = \mu_{SC} = 10\Delta$, $\nu = 2$, and $Z = 0$. In Fig. D.6 we set $L_{QH} = 10l_B$ and consider different values of L_{SC} while in Fig. D.7 we set $L_{SC} = 4\xi$ and consider different values of L_{SC}. These figures show a satisfactory agreement between the two models when $L_{SC}/\xi \gtrsim 4$ and $L_{QH}/l_B \gtrsim 4$.

D.2.2 Dependency of τ on the system dimensions

In the previous subsection we determined the parameters as well as the values of L_{QH} and L_{SC} that allow a satisfactory agreement between the continuous and the tight-binding models. Here we want to determine the minimum dimensions of the system such that the value of τ has converged. As we will see, these minimum dimensions depend on the angles θ_{QH} and θ_{SC} that we choose.

In Fig. D.8 we represent the dimensions that come into play in defining the system. We show two cases: $\theta_{QH}, \theta_{SC} < 90°$ (Fig. D.8a) and : $\theta_{QH}, \theta_{SC} > 90°$ (Fig. D.8b). The QH and SC regions are each separated into two parts: a part close to the QH-SC interface, characterized by the angle θ_{QH} for the QH

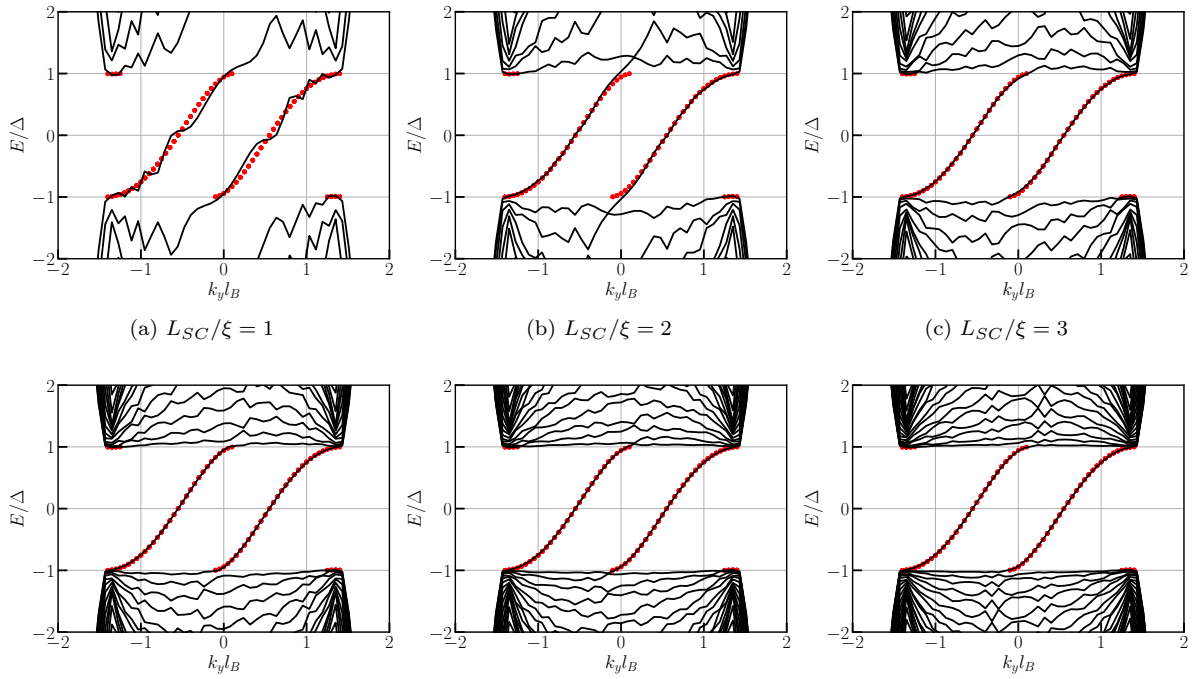

(a) $L_{SC}/\xi = 1$ (b) $L_{SC}/\xi = 2$ (c) $L_{SC}/\xi = 3$

(d) $L_{SC}/\xi = 4$ (e) $L_{SC}/\xi = 5$ (f) $L_{SC}/\xi = 6$

Figure D.6: Comparison between continuum and tight-binding spectra for various values of L_{SC}/ξ.

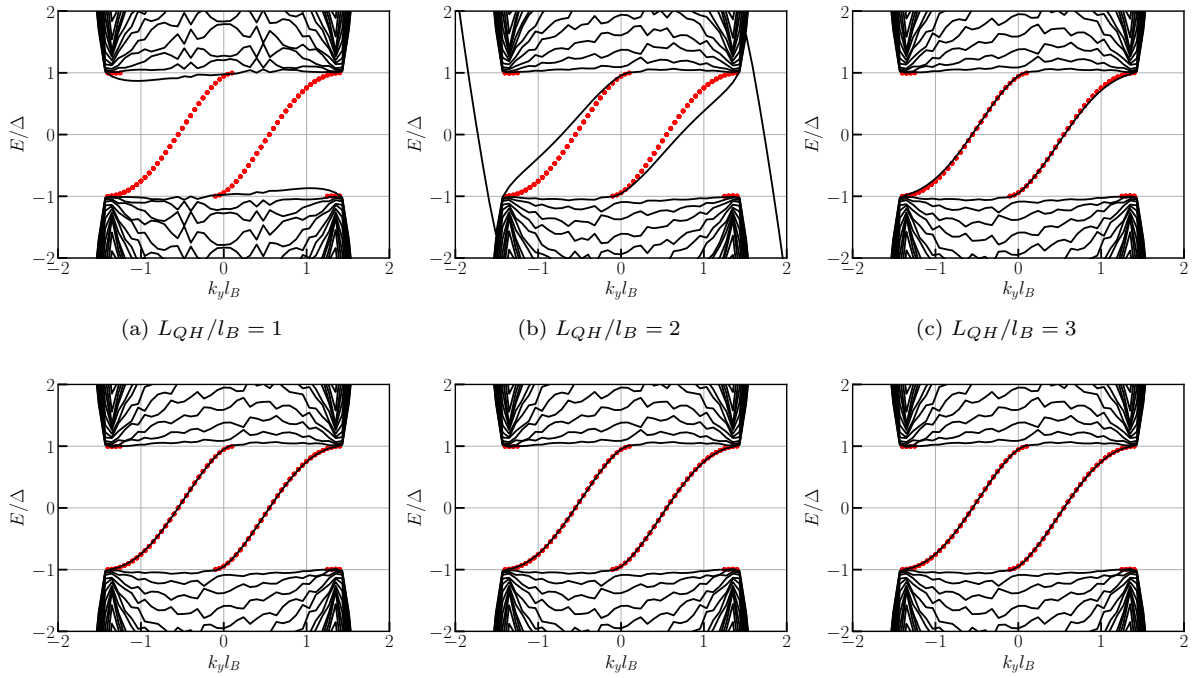

(a) $L_{QH}/l_B = 1$ (b) $L_{QH}/l_B = 2$ (c) $L_{QH}/l_B = 3$

(d) $L_{QH}/l_B = 4$ (e) $L_{QH}/l_B = 5$ (f) $L_{QH}/l_B = 6$

Figure D.7: Comparison between continuum and tight-binding spectra for various values of L_{QH}/l_B.

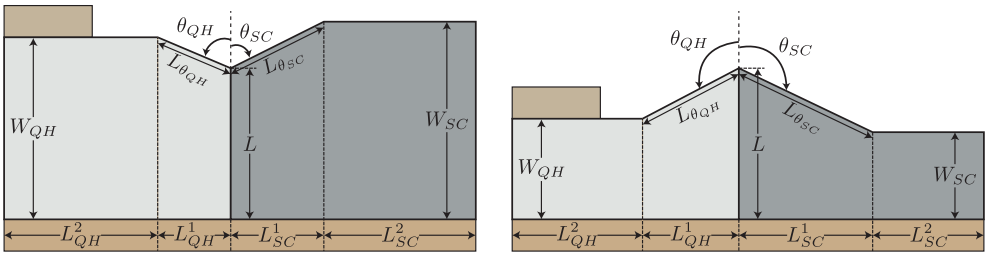

Figure D.8: System dimensions with (a) $\theta_{QH}, \theta_{SC} < 90°$ and (b) $\theta_{QH}, \theta_{SC} > 90°$.

region and by θ_{SC} for the SC region, and a rectangular part that extends the QH and SC regions to the left and right, respectively. The parts near the QH-SC interface are delimited by L, $L^1_{QH,SC}$, $W_{QH,SC}$ and $L_{\theta_{QH},\theta_{SC}}$, while the rectangular parts are bounded by $W_{QH,SC}$ and $L^2_{QH,SC}$. We define the system with such rectangular regions because it is easier to implement. Note that the lengths L_{QH} and L_{SC} represented in Fig. D.1 are given by $L_{QH} = L^1_{QH} + L^2_{QH}$ and $L_{SC} = L^1_{SC} + L^2_{SC}$. These dimensions must be sufficiently large to obtain a value of τ that has converged. Note that we must also satisfy the condition $L_{\theta_{QH}}, L_{\theta_{SC}} < L$ so that the Kwant system can be constructed for any angles, when larger than 90°. Moreover, the value of $L_{\theta_{SC}}$ must be large enough for the edge state wave function to vanish in the vicinity of the corner when $\theta_{SC} > 90°$, while this length is not important when $\theta_{SC} < 90°$, since the decay of the wave function is not affected by the shape of the corner in this case (see Fig. D.1). We thus set[1] $L_{\theta_{SC}} = 2\xi$ when $\theta_{SC} < 90°$ and $L_{\theta_{SC}} = 60 l_B$ when $\theta_{SC} > 90°$. On the other hand, if $\theta_{QH} > 90°$, the length $L_{\theta_{QH}}$ must be large enough so that the incident state does not hit the QH-SC interface before reaching the corner. For this reason we choose $L_{\theta_{QH}} = 18 l_B$. These conditions on $L_{\theta_{QH}}$ and $L_{\theta_{SC}}$ imply a minimum value for the length L of the QH-SC interface when an angle is greater than 90°. So we choose $L = 20 l_B$ when $\theta_{SC} < 90°$ and $L = 80 l_B$ when $\theta_{SC} > 90°$. Furthermore, the lengths L_{QH} and L_{SC} must be large enough to overcome the lengths $L_{\theta_{QH,SC}}$ if one of the angles is larger than 90°. For this reason we choose $L_{QH} = 40 l_B$ and $L_{SC} = 6\xi$. Two examples of Kwant systems constructed under these conditions are shown in Fig. D.9.

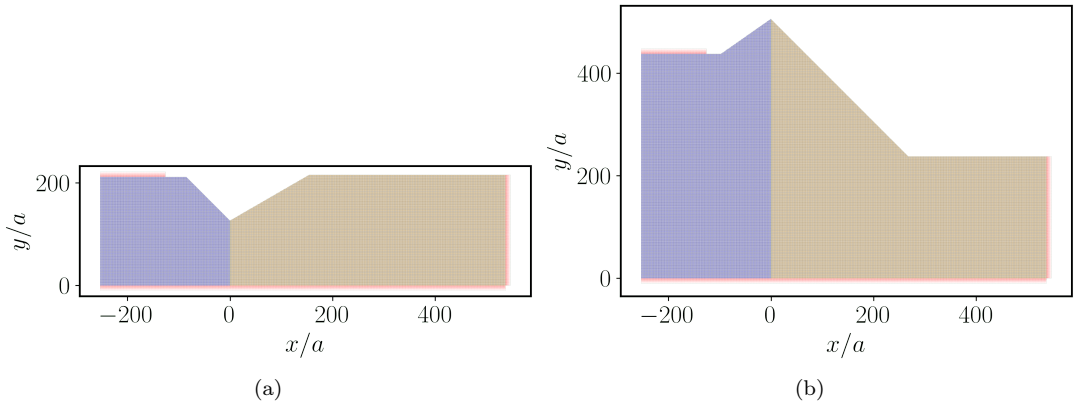

Figure D.9: Kwant system with (a) $\theta_{QH} = 45°, \theta_{SC} = 60°$ and (b) $\theta_{QH} = 125°, \theta_{SC} = 135°$.

We now check that the Andreev conversion τ has converged when using the dimensions defined above. In Fig. D.10 we thus plot the evolution of τ as a function of L, L_{QH} and L_{SC} for the same parameters as in Fig. D.1, namely $\mu_{QH} = \mu_{SC} = 10\Delta$, $\nu = 2$, $Z = 0$, $\theta_{QH} = 90°$, and $\theta_{SC} = 45°$.

[1] For $\theta_{SC} > 90°$ we could have chosen $L_{\theta_{SC}} = 4\xi$, but we use $L_{\theta_{SC}} = 60 l_B$ to satisfy the condition $L_{\theta_{SC}} < L$. In our parameter regimes, this value is sufficient for the wave function to decay completely near the corner region.

In Fig. D.10a we set $L_{QH} = 40l_B$, $L_{SC} = 6\xi$ and vary the length L of the QH-SC interface located in the scattering region. As we can see, τ doesn't depend on L. This was expected as the hybrid reservoir extends the QH-SC interface indefinitely and because τ should depend only on the corner properties.
In Fig. D.10b we vary L_{QH} with $L = 20l_B$ and $L_{SC} = 6\xi$. Here we observe that τ has converged for $L_{QH} \gtrsim 10l_B$. So the value we chose above, $L_{QH} = 40l_B$, is large enough.
Fig. D.10c shows the evolution of τ with L_{SC} while $L = 20l_B$ and $L_{QH} = 40l_B$. Here we see that τ has converged for $L_{SC} \gtrsim 6\xi$. So the value $L_{SC} = 6\xi$ we chose above is sufficient.

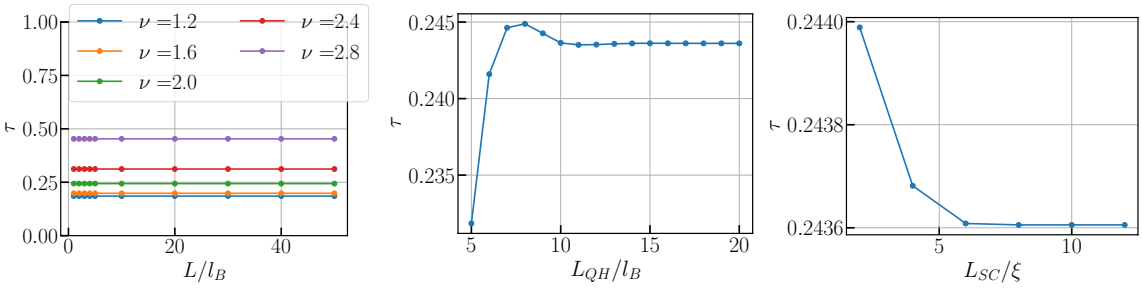

Figure D.10: Dependency of the Andreev conversion τ on the system's dimensions. In (a) we set $L_{QH} = 40l_B$ and $L_{SC} = 6\xi$, and plot τ as function of L/l_B for different values of the filling factor ν. We then choose $L = 20l_B$ and $\nu = 2$, and plot the evolution of τ (b) as function of L_{QH}/l_B with $L_{SC} = 6\xi$ and (c) as function of L_{SC}/ξ with $L_{QH} = 40l_B$. The other parameters are the same as in Fig. D.1.

We have thus determined the dimensions of the system such that τ has converged. We end this appendix by investigating some parameter dependencies that we don't want to discuss in the main text.

D.3 Dependency of τ on the system parameters

We now study dependencies in the system parameters that we don't discuss in the main text. Namely, we study the dependencies of τ on t/μ_{SC}, μ_{QH}/Δ, μ_{SC}/μ_{QH}, and Z, while the dependencies in the filling factor and the corner geometry, which are the most interesting ones, are discussed in the main text.

In Fig. D.11 we plot the evolution of τ with the ratio t/μ_{SC} for two different geometries, namely $\theta_{QH} = 90°, \theta_{SC} = 45°$ (Fig. D.11a) and $\theta_{QH} = 90°, \theta_{SC} = 135°$ (Fig. D.11b). From this figure we observe that we reach an asymptotic regime when $t/\mu_{SC} \gtrsim 20$. We thus set $\mu_{SC} = t/20$ in the main text and in the remainder of this appendix.

In Fig. D.12 we plot the evolution of τ with the ratio μ_{QH}/Δ for the same geometries as in Fig. D.11. As shown in Sec. 3.3.2.2, additional non-chiral edge states may appear upon decreasing Δ. Here we restrict ourselves to values of ν so that such additional states are absent in the range of values of Δ plotted. (In particular, we show results for $\nu = 2.75$ rather than $\nu = 2.8$ as in the previous figures.) For $\theta_{SC} = 45°$ (Fig. D.12a), the electron-hole conversion probability depends on Δ only very weakly. This is consistent with the analytic results of Sec. 3.3.3, which show that the properties of the edge states are almost independent of Δ in the considered parameter regime. We thus choose $\mu_{QH}/\Delta = 10$ in the main text and in the remainder of this appendix. However, for $\theta_{SC} = 135°$ (Fig. D.12b), a stronger dependence is seen, in particular for ν close to 1 and 3. For angles $\theta_{SC} > 90°$, the decay length of the edge state in the superconductor plays a more important role. Namely as the decay may reach the superconductor-vacuum interface, a stronger dependence of τ on Δ, which controls the decay length in the superconductor, is expected. The modified decay is illustrated in Fig. D.13.

In Fig. D.14 we look at the effects of a Fermi mismatch $\mu_{SC} \neq \mu_{QH}$ and a non-zero potential barrier $Z \neq 0$. We see that τ is lowered as μ_{SC}/μ_{QH} increases. Moreover, we observe that τ vanishes as $Z \gg 1$ while it is enhanced in an intermediate region for $\nu > 2$, as we found for the hole content f_h^+ in Fig. 3.10b.

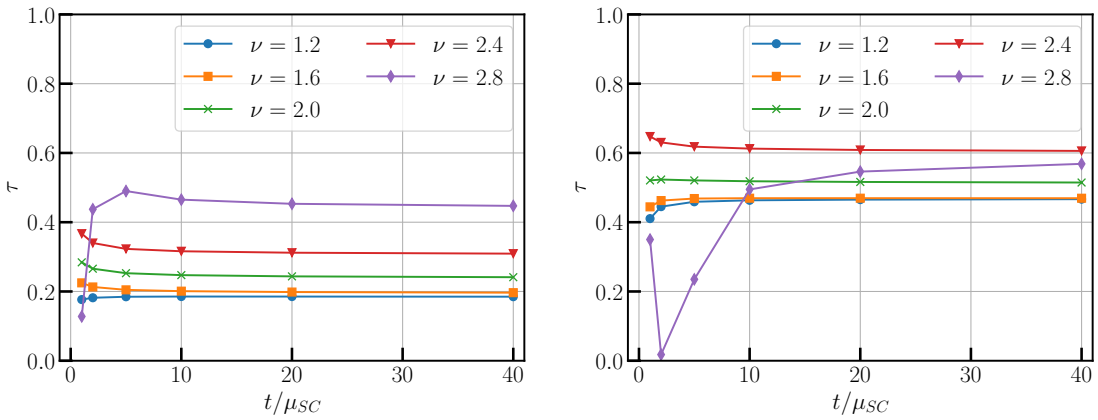

Figure D.11: Dependency of the Andreev conversion τ on t/μ_{SC}. (a) $\theta_{QH} = 90°$, $\theta_{SC} = 45°$ and (b) $\theta_{QH} = 90°$, $\theta_{SC} = 135°$. The other parameters are $\mu_{QH} = \mu_{SC} = 10\Delta$ and $Z = 0$.

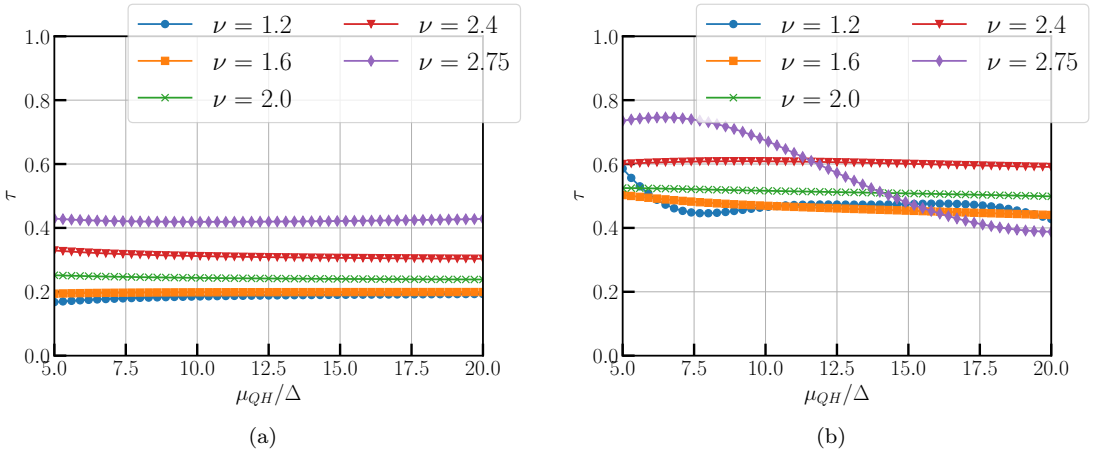

Figure D.12: Dependence of τ on the superconducting gap Δ. The parameters are $t/\mu_{SC} = 20$, $\mu_{QH} = \mu_{SC}$, $Z = 0$, and $\theta_{QH} = 90°$. (a) At $\theta_{SC} = 45°$, the electron-hole conversion probability very weakly depends on Δ in the regime $\Delta \ll \mu_{QH}$. (b) At $\theta_{SC} = 135°$, a stronger dependence is seen. This can be attributed to the observation that for angles $\theta_{SC} > 90°$ the superconductor-vacuum interface comes into play and may modify the decay as illustrated in Fig. D.13.

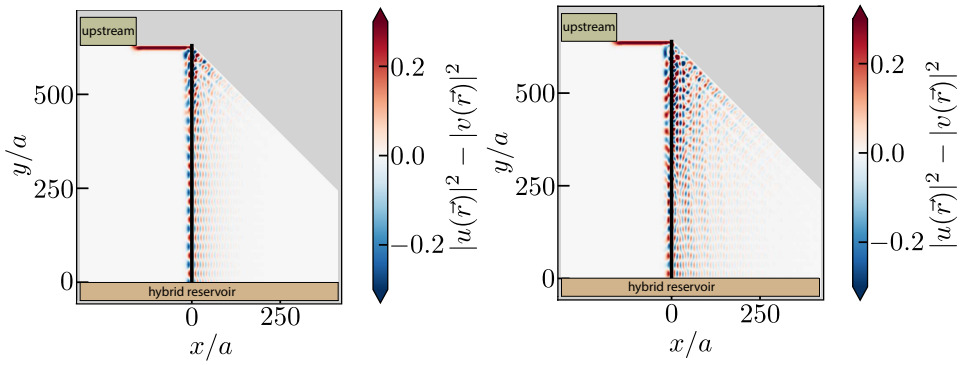

(a) (b)

Figure D.13: Probability density $|\psi_e(\mathbf{r})|^2 - |\psi_h(\mathbf{r})|^2$ of an incoming electron state for $\theta_{SC} = 135°$ and $\theta_{QH} = 90°$. Other parameters are $\nu = 2.75$, $\mu_{SC} = \mu_{QH}$, and $Z = 0$.(a) $\mu_{QH}/\Delta = 10$. (b) $\mu_{QH}/\Delta = 20$. The modified decay in the superconductor and the effect of the superconductor-vaccum interface can be clearly seen.

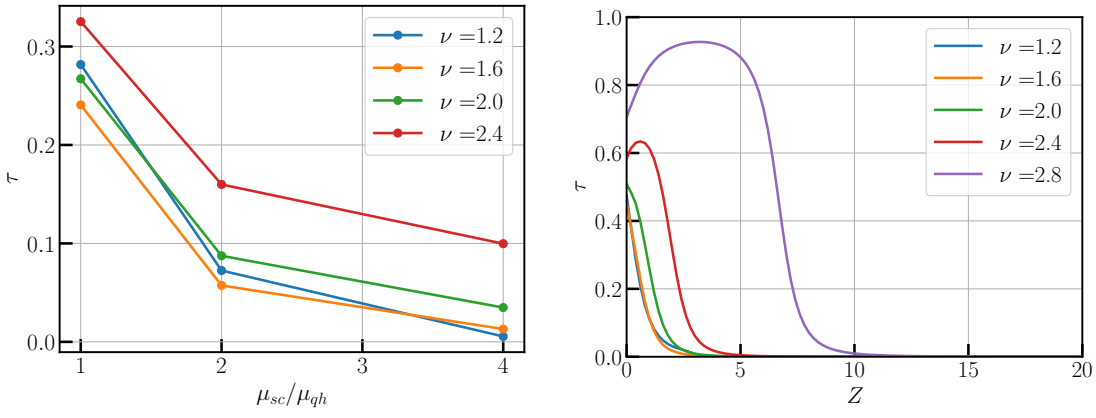

(a) (b)

Figure D.14: Dependency of τ on the (a) Fermi mismatch μ_{SC}/μ_{QH} with $Z = 0$, $\theta_{QH} = 0°$, $\theta_{SC} = 90°$, and on (b) the barrier strength Z with $\mu_{SC} = \mu_{QH}$ and $\theta_{QH} = \theta_{SC} = 90°$. The other parameters are $t = 20\mu_{SC}$, $\mu_{QH} = 10\Delta$, and $\nu = 2$.

Appendix E

Calculation details for the hinge modes wave functions

Contents

This appendix is a supplement to Chap. 5 in which we provide calculation details for the hinge modes wave functions derived in Sec. 5.5.

E.1 Calculation of the vectors χ_{sn}

Here we provide a detailed calculation for the vector χ_{++} associated to the orbital function Ω_{++} while the others are found using the same procedure. Let us recall the notations introduced in Eq. (5.53),

$$\Omega_{sn} = \omega_{s+} + n\sqrt{\frac{\Delta + svk_y^0}{\Delta - svk_y^0}}\omega_{s-}, \quad \omega_{sn} = u_{s+} + nv_{s-}, \quad v_{sn} = -iu_{sn}. \tag{E.1}$$

Since the chiralities (valleys) are decoupled we focus on $s = +$ (valley $-$) and the vector associated to the solution Ω_{++} can be found by setting $\Omega_{+-} = 0$ in Eq. (E.1), leading to $w_{++} = \sqrt{\frac{\Delta + vk_y^0}{\Delta - vk_y^0}}w_{+-}$. Then, using the relations of Eq. (E.1) we get

$$u_{++} = -i\frac{\Delta + \sqrt{\Delta^2 - (vk_y^0)^2}}{vk_y^0}u_{+-}. \tag{E.2}$$

According to the definitions introduced in Eq. (5.41) we can then write

$$u_5 = \frac{\sqrt{\Delta^2 - (vk_y^0)^2} - ivk_y^0}{\Delta}u_2, \tag{E.3}$$

and using the conditions (5.39) and (5.40) we can finally write the vector χ_{++} as

$$\chi_{++} = \begin{pmatrix} 0 & 1 & 0 & 1 & \frac{\sqrt{\Delta^2 - (vk_y^0)^2} - ivk_y^0}{\Delta} & 0 & -\frac{\sqrt{\Delta^2 - (vk_y^0)^2} - ivk_y^0}{\Delta} & 0 \end{pmatrix}^T, \tag{E.4}$$

where we have set $u_1 = u_3 = u_6 = u_8 = 0$ because we focus on the valley $-$.

E.2 Normalization and orthogonality

In this section we determine the normalization constants C_{sn} and we look if the wave functions are orthogonal. Using the normalization condition $\int_{-\infty}^{+\infty} |\phi_{sn}(y)|^2 \, \mathrm{d}y = 1$, the normalization constants are given by (up to a phase factor),

$$C_{sn} = \frac{1}{|\chi_{sn}|}\left\{\int_{-\infty}^{+\infty} |f_{sn}(y)|^2 \, \mathrm{d}y\right\}^{-1/2}, \tag{E.5}$$

with $f_{sn}(y)$ the function introduced in Eq. (5.51) and,

$$|\chi_{sn}| = \sqrt{2(1+g^*_{sn}g_{sn})} = 2, \tag{E.6}$$

where the last equality holds if $vk_y^0 < \Delta$, which is ensured by the condition (5.20). In order to obtain an explicit form of the integral (which is necessary to plot the wave functions), we need an explicit form of the mass surface gap $m(y)$ and so we take the same as in Eq. (5.3), $m(y) = m_0 \tanh(y/y_0)$, such that the integral of the mass function appearing in the definition of $f_{sn}(y)$ is given by,

$$\exp\left[-\frac{1}{v}\int_0^y m(s)\mathrm{d}s\right] = (\mathrm{sech}y/y_0)^{m_0y_0/v}. \tag{E.7}$$

We can then write the orbital part of the wave functions as,

$$\Omega_{sn}(y) = C_{sn}(\mathrm{sech}y/y_0)^{m_0y_0/v}\exp\left\{\frac{1}{v}\left[sB^z + n\sqrt{\Delta^2-(vk_y^0)^2}\,\right]y\right\}. \tag{E.8}$$

Imposing the condition (5.20) the argument of the exponential is real and we obtain the following normalization constants,

$$C_{sn} = \frac{1}{2}\left\{\int(\mathrm{sech}y/y_0)^{2m_0y_0/v}\exp\left[\frac{2}{v}\left(sB^z + n\sqrt{\Delta^2-(vk_y^0)^2}\,\right)y\right]\mathrm{d}y\right\}^{-1/2} = \frac{1}{2\sqrt{I_{sn}}}, \tag{E.9}$$

where we have introduced the integrals,

$$I_{sn} = \int(\mathrm{sech}y/y_0)^{2m_0y_0/v}\exp\left[\frac{2}{v}\left(sB^z + n\sqrt{\Delta^2-(vk_y^0)^2}\,\right)y\right]\mathrm{d}y, \tag{E.10}$$

for which we find two distinct solutions for the two cases $s = n$ and $s \neq n$. For $s = n$ we find,

$$\begin{aligned} I_{sn} =& y_0 2^{\frac{2m_0y_0}{v}-1}(-1)^{-\frac{y_0m_0}{v}}\times \\ &\times\left[(-1)^{\frac{y_0}{v}\left(B^z+\sqrt{\Delta^2-(vk_y^0)^2}\right)}\beta\left(-1,-\frac{y_0}{v}\left(B^z-m_0+\sqrt{\Delta^2-(vk_y^0)^2}\right),1-\frac{2m_0y_0}{v}\right)\right. \\ &\left.+(-1)^{-\frac{y_0}{v}\left(B^z+\sqrt{\Delta^2-(vk_y^0)^2}\right)}\beta\left(-1,\frac{y_0}{v}\left(B^z+m_0+\sqrt{\Delta^2-(vk_y^0)^2}\right),1-\frac{2m_0y_0}{v}\right)\right], \end{aligned} \tag{E.11}$$

provided that $B^z + \sqrt{\Delta^2-(vk_y^0)^2} < m_0$, while for $s \neq n$ we find,

$$\begin{aligned} I_{sn} =& y_0 2^{\frac{2m_0y_0}{v}-1}(-1)^{-\frac{y_0m_0}{v}}\times \\ &\times\left[(-1)^{\frac{y_0}{v}\left(-B^z+\sqrt{\Delta^2-(vk_y^0)^2}\right)}\beta\left(-1,\frac{y_0}{v}\left(B^z+m_0-\sqrt{\Delta^2-(vk_y^0)^2}\right),1-\frac{2m_0y_0}{v}\right)\right. \\ &\left.+(-1)^{-\frac{y_0}{v}\left(-B^z+\sqrt{\Delta^2-(vk_y^0)^2}\right)}\beta\left(-1,\frac{y_0}{v}\left(-B^z+m_0+\sqrt{\Delta^2-(vk_y^0)^2}\right),1-\frac{2m_0y_0}{v}\right)\right], \end{aligned} \tag{E.12}$$

provided that $B^z < m_0 + \sqrt{\Delta^2-(vk_y^0)^2}$ and $\sqrt{\Delta^2-(vk_y^0)^2} < m_0 + B^z$. Here we have introduced the incomplete beta function defined as $\beta(z,a,b) = \int_0^z t^{a-1}(1-t)^{b-1}\mathrm{d}t$. We now have determined entirely the wave functions and we plot the corresponding probability densities $|\phi_{sn}(y)|^2$ in Fig. E.1. From this figure we observe four probability density maxima for the four states where each are located at different positions. We will come back to this spatial splitting later in Sec. 5.5.3.

We now want to check if the states $|\phi_{sn}\rangle$ form an orthogonal basis, namely we want to check if the following relation holds,

$$\langle\phi_{s'n'}|\phi_{sn}\rangle = \chi^\dagger_{s'n'}\cdot\chi_{sn}\int\Omega^*_{s'n'}(y)\;\Omega_{sn}(y)\mathrm{d}y \overset{?}{=} \delta_{ss'}\;\delta_{nn'}. \tag{E.13}$$

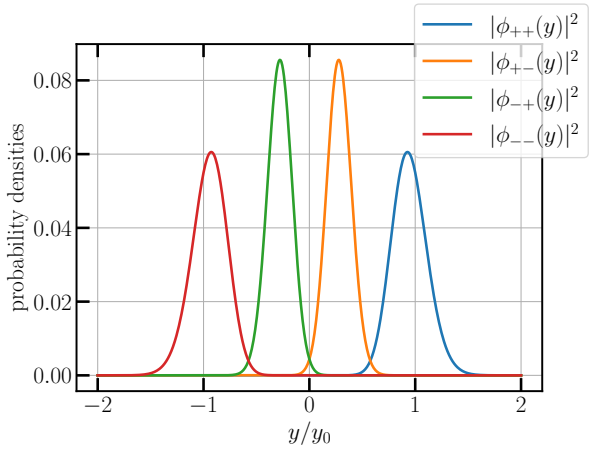

Figure E.1: Probability densities $|\phi_{sn}(y)|^2$. The parameters are (arbitrary units) $y_0 = 40$, $v = 1$, $k_y^0 = 0.1$, $m_0 = 1$, $B^z = 0.5$, $\Delta = 0.25$.

First, the dot product in Eq. (E.13) is equal to the following,

$$\chi^\dagger_{s'n'} \cdot \chi_{sn} = 2(1 + g^*_{s'n'} g_{sn})\delta_{ss'}. \tag{E.14}$$

from where we have the contribution $\delta_{ss'}$ and we thus have to compute the scalar product with $s = s'$. Since the case $n = n'$ is nothing but the normalization condition, it remains to compute the scalar product with $n = -n'$,

$$\begin{aligned}\langle \phi_{s,-n} | \phi_{sn} \rangle &= 2(1 + g^*_{s,-n} g_{sn}) \int \Omega^*_{s,-n}(y)\ \Omega_{sn}(y) \mathrm{d}y \qquad (E.15)\\ &= 2(1 + g^*_{s,-n} g_{sn}) C^*_{s,-n} C_{sn} y_0 2^{\frac{2m_0 y_0}{v} - 1} (-1)^{-\frac{y_0 m_0}{v}} \times \\ &\quad \times \left[(-1)^{\frac{y_0 B^z}{v}} \beta\left(-1, \frac{y_0}{v}\left(m_0 - B^z\right), 1 - \frac{2m_0 y_0}{v}\right) \right. \\ &\quad \left. + (-1)^{-\frac{y_0 B^z}{v}} \beta\left(-1, \frac{y_0}{v}\left(m_0 + B^z\right), 1 - \frac{2m_0 y_0}{v}\right) \right] = \delta. \qquad (E.16)\end{aligned}$$

We thus have a non-zero overlap δ between the states with same s and opposite n which can be seen in Fig. E.1. Due to their overlap these states can hybridize and gap each other. However, as seen from Fig. E.2, this overlap decreases exponentially with $y_0 m_0 / v$. Hence, for a sufficiently large value of $y_0 m_0 / v$, the orthogonality condition (E.13) is approximatively true.

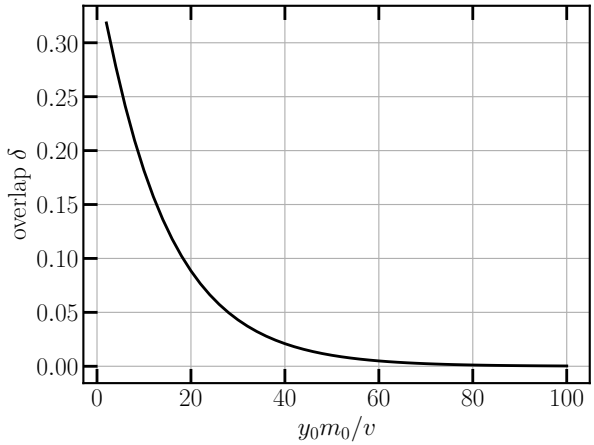

Figure E.2: Overlap δ. The parameters are the same as in Fig. E.1.

Bibliography

[Abramowitz & Stegun 1964] M. Abramowitz and I. A. Stegun. Handbook of mathematical functions with formulas, graphs, and mathematical tables, volume 55. US Government printing office, 1964. (Cited on pages 27 and 28.)

[Akhmerov *et al.* 2009] A. R. Akhmerov, J. Nilsson and C. W. J. Beenakker. Electrically detected interferometry of Majorana fermions in a topological insulator. Physical review letters, vol. 102, no. 21, page 216404, 2009. (Cited on page 125.)

[Alicea 2012] J. Alicea. New directions in the pursuit of Majorana fermions in solid state systems. Reports on progress in physics, vol. 75, no. 7, page 076501, 2012. (Cited on pages 8 and 82.)

[Altland & Zirnbauer 1997] A. Altland and M. R. Zirnbauer. Nonstandard symmetry classes in mesoscopic normal-superconducting hybrid structures. Physical Review B, vol. 55, no. 2, page 1142, 1997. (Cited on pages 4 and 52.)

[Anderson 1958] P. W. Anderson. Absence of diffusion in certain random lattices. Physical review, vol. 109, no. 5, page 1492, 1958. (Cited on page 35.)

[Ando & Fu 2015] Y. Ando and L. Fu. Topological crystalline insulators and topological superconductors: From concepts to materials. Annu. Rev. Condens. Matter Phys., vol. 6, no. 1, pages 361–381, 2015. (Cited on page 52.)

[Andreev 1965] A. F. Andreev. Thermal conductivity of the intermediate state of superconductors II. Sov. Phys. JETP, vol. 20, page 1490, 1965. (Cited on pages 5 and 19.)

[Asano & Kato 2000] Y. Asano and T. Kato. Andreev reflection and cyclotron motion of a quasiparticle in high magnetic fields. Journal of the Physical Society of Japan, vol. 69, no. 4, pages 1125–1135, 2000. (Cited on page 55.)

[Asano 2021] Y. Asano. Andreev reflection in superconducting junctions. Springer, 2021. (Cited on pages 19, 141 and 144.)

[Asbóth *et al.* 2016] J. K. Asbóth, L. Oroszlány and A. Pályi. A short course on topological insulators, volume 919. Springer, 2016. (Cited on pages 41 and 51.)

[Avron *et al.* 2003] J. E. Avron, D. Osadchy and R. Seiler. A topological look at the quantum Hall effect. Physics today, vol. 56, no. 8, pages 38–42, 2003. (Cited on page 39.)

[Bardeen *et al.* 1957] J. Bardeen, L. N. Cooper and J. R. Schrieffer. Theory of superconductivity. Physical review, vol. 108, no. 5, page 1175, 1957. (Cited on pages 4 and 141.)

[Beconcini *et al.* 2018] M. Beconcini, M. Polini and F. Taddei. Nonlocal superconducting correlations in graphene in the quantum Hall regime. Physical Review B, vol. 97, no. 20, page 201403, 2018. (Cited on page 102.)

[Beenakker 1994] C. W. J. Beenakker. Quantum transport in semiconductor-superconductor microjunctions. "Mesoscopic Quantum Physics", edited by E. Akkermans, G. Montambaux, J.-L. Pichard, and J. Zinn-Justin (North-Holland, Amsterdam, 1995), 1994. (Cited on pages 16, 20 and 21.)

[Bernevig & Hughes 2013] B. Bernevig and T. L. Hughes. Topological insulators and topological superconductors. Princeton university press, 2013. (Cited on pages 37, 39, 41, 43 and 46.)

[Bernevig *et al.* 2006] B. Andrei Bernevig, T. L. Hughes and S.-C. Zhang. Quantum spin Hall effect and topological phase transition in HgTe quantum wells. science, vol. 314, no. 5806, pages 1757–1761, 2006. (Cited on pages 3 and 46.)

[Blonder *et al.* 1982] G. E. Blonder, M. Tinkham and T. M. Klapwijk. Transition from metallic to tunneling regimes in superconducting microconstrictions: Excess current, charge imbalance, and supercurrent conversion. Physical Review B, vol. 25, no. 7, page 4515, 1982. (Cited on pages 14, 19, 20, 61 and 62.)

[Bogoliubov 1958a] N. N. Bogoliubov. A new method in the theory of superconductivity 1. Soviet Physics JETP-USSR, vol. 7, no. 1, pages 41–46, 1958. (Cited on page 146.)

[Bogoliubov 1958b] N. N. Bogoliubov. A new method in the theory of superconductivity 3. Soviet Physics JETP-USSR, vol. 7, no. 1, pages 51–55, 1958. (Cited on page 146.)

[Büttiker 1986] M. Büttiker. Four-terminal phase-coherent conductance. Physical review letters, vol. 57, no. 14, page 1761, 1986. (Cited on pages 138 and 140.)

[Büttiker 1988] M. Büttiker. Absence of backscattering in the quantum Hall effect in multiprobe conductors. Physical Review B, vol. 38, no. 14, page 9375, 1988. (Cited on pages 138 and 140.)

[Cage *et al.* 1985] M. E. Cage, R. F. Dziuba and B. F. Field. A test of the quantum Hall effect as a resistance standard. IEEE transactions on instrumentation and measurement, no. 2, pages 301–303, 1985. (Cited on pages 36 and 37.)

[Chang *et al.* 2013] C.-Z. Chang, J. Zhang, X. Feng, J. Shen, Z. Zhang, M. Guo, K. Li, Y. Ou, P. Wei, L.-L. Wanget al. Experimental observation of the quantum anomalous Hall effect in a magnetic topological insulator. Science, vol. 340, no. 6129, pages 167–170, 2013. (Cited on pages 40 and 41.)

[Choi *et al.* 2020] Y.-B. Choi, Y. Xie, C.-Z. Chen, J. Park, S.-B. Song, J. Yoon, B. J. Kim, T. Taniguchi, K. Watanabe, J. Kimet al. Evidence of higher-order topology in multilayer WTe2 from Josephson coupling through anisotropic hinge states. Nature Materials, vol. 19, no. 9, pages 974–979, 2020. (Cited on pages 53 and 104.)

[Chtchelkatchev & Burmistrov 2007] N. M. Chtchelkatchev and I. S. Burmistrov. Conductance oscillations with magnetic field of a two-dimensional electron gas–superconductor junction. Physical Review B, vol. 75, no. 21, page 214510, 2007. (Cited on page 55.)

[Chtchelkatchev *et al.* 2002] N. M. Chtchelkatchev, G. Blatter, G. B. Lesovik and T. Martin. Bell inequalities and entanglement in solid-state devices. Physical Review B, vol. 66, no. 16, page 161320, 2002. (Cited on page 21.)

[Chtchelkatchev 2001] N. M. Chtchelkatchev. Conductance of a semiconductor(2DEG)-Superconductor junction in high magnetic field. Journal of Experimental and Theoretical Physics Letters, vol. 73, no. 2, pages 94–97, 2001. (Cited on page 55.)

[Clarke *et al.* 2013] D. J. Clarke, J. Alicea and K. Shtengel. Exotic non-Abelian anyons from conventional fractional quantum Hall states. Nature communications, vol. 4, no. 1, pages 1–9, 2013. (Cited on page 102.)

[Clarke *et al.* 2014] D. J. Clarke, J. Alicea and K. Shtengel. Exotic circuit elements from zero-modes in hybrid superconductor–quantum-Hall systems. Nature Physics, vol. 10, no. 11, pages 877–882, 2014. (Cited on pages 55, 80 and 102.)

[Datta 1997] S. Datta. Electronic transport in mesoscopic systems. Cambridge university press, 1997. (Cited on pages 79, 138 and 149.)

[David *et al.* 2023] A. David, J. S. Meyer and M. Houzet. Geometrical effects on the downstream conductance in quantum-Hall–superconductor hybrid systems. Physical Review B, vol. 107, no. 12, page 125416, 2023. (Cited on pages 7 and 55.)

[de Gennes 2018] P.-G. de Gennes. Superconductivity of metals and alloys. CRC Press, 2018. (Cited on pages 15, 16 and 145.)

[Deutscher & Feinberg 2000] G. Deutscher and D. Feinberg. Coupling superconducting-ferromagnetic point contacts by Andreev reflections. Applied Physics Letters, vol. 76, no. 4, pages 487–489, 2000. (Cited on page 21.)

[Dimmock *et al.* 1966] J.O. Dimmock, I. Melngailis and A. J. Strauss. Band structure and laser action in $Pb_xSn_{1-x}Te$. Physical Review Letters, vol. 16, no. 26, page 1193, 1966. (Cited on page 52.)

[Eroms *et al.* 2005] J. Eroms, D. Weiss, J. De Boeck, G. Borghs and U. Zülicke. Andreev Reflection at High Magnetic Fields: Evidence for Electron and Hole Transport in Edge States. Physical Review Letters, vol. 95, no. 10, aug 2005. (Cited on page 5.)

[Falci *et al.* 2001] G. Falci, D. Feinberg and F. W. J. Hekking. Correlated tunneling into a superconductor in a multiprobe hybrid structure. EPL (Europhysics Letters), vol. 54, no. 2, page 255, 2001. (Cited on page 21.)

[Fu & Kane 2007] L. Fu and C. L. Kane. Topological insulators with inversion symmetry. Physical Review B, vol. 76, no. 4, page 045302, 2007. (Cited on page 50.)

[Fu & Kane 2008] L. Fu and C. L. Kane. Superconducting proximity effect and Majorana fermions at the surface of a topological insulator. Physical review letters, vol. 100, no. 9, page 096407, 2008. (Cited on page 5.)

[Fu & Kane 2009] L. Fu and C. L. Kane. Probing neutral Majorana fermion edge modes with charge transport. Physical review letters, vol. 102, no. 21, page 216403, 2009. (Cited on page 125.)

[Fu 2011] L. Fu. Topological crystalline insulators. Physical Review Letters, vol. 106, no. 10, page 106802, 2011. (Cited on pages 4, 52 and 104.)

[Galambos *et al.* 2022] T. H. Galambos, F. Ronetti, B. Hetényi, D. Loss and J. Klinovaja. Crossed Andreev reflection in spin-polarized chiral edge states due to the Meissner effect. Physical Review B, vol. 106, no. 7, 2022. (Cited on page 102.)

[Giazotto *et al.* 2005] F. Giazotto, M. Governale, U. Zülicke and F. Beltram. Andreev reflection and cyclotron motion at superconductor—normal-metal interfaces. Physical Review B, vol. 72, no. 5, 2005. (Cited on page 55.)

[Girvin & Yang 2019] S. M. Girvin and K. Yang. Modern condensed matter physics. Cambridge University Press, 2019. (Cited on pages 15, 35, 46, 62, 142 and 145.)

[Groth *et al.* 2014] C. W. Groth, M. Wimmer, R. Akhmerov A. and X. Waintal. Kwant: a software package for quantum transport. New Journal of Physics, vol. 16, no. 6, page 063065, jun 2014. (Cited on pages 38, 69, 122 and 149.)

[Gül *et al.* 2022] Ö. Gül, Y. Ronen, S. Y. Lee, H. Shapourian, J. Zauberman, Y. H. Lee, K. Watanabe, T. Taniguchi, A. Vishwanath, A. Yacoby and P. Kim. Andreev reflection in the fractional quantum Hall state. Physical Review X, vol. 12, no. 2, page 021057, 2022. (Cited on pages 6, 7, 8, 55, 56, 75, 83 and 102.)

[Haldane 1988] F. D. M. Haldane. Model for a quantum Hall effect without Landau levels: Condensed-matter realization of the" parity anomaly". Physical review letters, vol. 61, no. 18, page 2015, 1988. (Cited on pages 3 and 40.)

[Hall 1879] E. H. Hall. On a new action of the magnet on electric currents. American Journal of Mathematics, vol. 2, no. 3, pages 287–292, 1879. (Cited on page 25.)

[Halperin 1982] B. I. Halperin. Quantized Hall conductance, current-carrying edge states, and the existence of extended states in a two-dimensional disordered potential. Physical Review B, vol. 25, no. 4, page 2185, 1982. (Cited on pages 1 and 29.)

[Hasan & Kane 2010] M. Z. Hasan and C. L. Kane. Colloquium: topological insulators. Reviews of modern physics, vol. 82, no. 4, page 3045, 2010. (Cited on pages 39, 45 and 46.)

[Hatefipour *et al.* 2022] M. Hatefipour, J. J. Cuozzo, J. Kanter, W. M. Strickland, C. R. Allemang, T.-M. Lu, E. Rossi and J. Shabani. Induced superconducting pairing in integer quantum Hall edge states. Nano Letters, vol. 22, no. 15, pages 6173–6178, 2022. (Cited on pages 6, 7, 56, 62 and 75.)

[Hofstadter 1976] D. R. Hofstadter. Energy levels and wave functions of Bloch electrons in rational and irrational magnetic fields. Physical Review B, vol. 14, no. 6, pages 2239–2249, 1976. (Cited on pages 37 and 151.)

[Hoppe *et al.* 2000] H. Hoppe, U. Zülicke and G. Schön. Andreev Reflection in Strong Magnetic Fields. Physical Review Letters, vol. 84, no. 8, pages 1804–1807, 2000. (Cited on pages 55 and 62.)

[Hsieh *et al.* 2012] T. H. Hsieh, H. Lin, J. Liu, W. Duan, A. Bansil and L. Fu. Topological crystalline insulators in the SnTe material class. Nature communications, vol. 3, no. 1, pages 1–7, 2012. (Cited on pages 52 and 107.)

[Jackiw & Rebbi 1976] R. Jackiw and C. Rebbi. Solitons with fermion number 1/2. Physical Review D, vol. 13, no. 12, page 3398, 1976. (Cited on page 4.)

[Jackson 1998] J. D. Jackson. Classical electrodynamics. Wiley, 1998. (Cited on page 34.)

[Jeckelmann & Jeanneret 2007] B. Jeckelmann and B. Jeanneret. The application of the Josephson and quantum Hall effects in electrical metrology. In Metrology and Fundamental Constants, pages 135–179. IOS Press, 2007. (Cited on page 35.)

[Kane & Mele 2005] C. L. Kane and E. J. Mele. Quantum spin Hall effect in graphene. Physical review letters, vol. 95, no. 22, page 226801, 2005. (Cited on page 3.)

[Ketterson & Song 1999] J. B. Ketterson and S. N. Song. Superconductivity. Cambridge University Press, jan 1999. (Cited on page 21.)

[Khalaf 2018] E. Khalaf. Higher-order topological insulators and superconductors protected by inversion symmetry. Physical Review B, vol. 97, no. 20, page 205136, 2018. (Cited on page 108.)

[Khaymovich *et al.* 2010] I. M. Khaymovich, N. M. Chtchelkatchev, I. A. Shereshevskii and A. S. Mel'nikov. Andreev transport in two-dimensional normal-superconducting systems in strong magnetic fields. EPL (Europhysics Letters), vol. 91, no. 1, page 17005, 2010. (Cited on pages 55, 58, 59 and 71.)

[Kitaev 2001] A. Y. Kitaev. Unpaired Majorana fermions in quantum wires. Physics-uspekhi, vol. 44, no. 10S, page 131, 2001. (Cited on pages 8 and 9.)

[Kjærgaard *et al.* 2016] M. Kjærgaard, F. Nichele, H. J. Suominen, M. P. Nowak, M. Wimmer, A. R. Akhmerov, J. A. Folk, K. Flensberg, J. Shabani, C. J. Palmstrømet al. Quantized conductance doubling and hard gap in a two-dimensional semiconductor–superconductor heterostructure. Nature communications, vol. 7, no. 1, pages 1–6, 2016. (Cited on page 21.)

[Kohmoto 1985] M. Kohmoto. Topological invariant and the quantization of the Hall conductance. Annals of Physics, vol. 160, no. 2, pages 343–354, 1985. (Cited on page 38.)

[Konig *et al.* 2007] M. Konig, S. Wiedmann, C. Brune, A. Roth, H. Buhmann, L. W Molenkamp, X.-L. Qi and S.-C. Zhang. Quantum spin Hall insulator state in HgTe quantum wells. Science, vol. 318, no. 5851, pages 766–770, 2007. (Cited on pages 3 and 46.)

[König *et al.* 2008] M. König, H. Buhmann, L. W. Molenkamp, Taylor Hughes, C.-X. Liu, X.-L. Qi and S.-C. Zhang. The quantum spin Hall effect: theory and experiment. Journal of the Physical Society of Japan, vol. 77, no. 3, page 031007, 2008. (Cited on page 46.)

[Kulik 1969] I. O. Kulik. Macroscopic quantization and the proximity effect in SNS junctions. Soviet Journal of Experimental and Theoretical Physics, vol. 30, page 944, 1969. (Cited on page 19.)

[Kurilovich & Glazman 2022] V. D. Kurilovich and L. I. Glazman. Criticality in the crossed Andreev reflection of a quantum Hall edge. arXiv preprint, vol. arXiv:2209.12932, 2022. (Cited on pages 75 and 102.)

[Kurilovich *et al.* 2022] V. D. Kurilovich, Z. M. Raines and L. I. Glazman. Disorder in Andreev reflection of a quantum Hall edge. arXiv preprint, vol. arXiv:2201.00273, 2022. (Cited on pages 7, 56 and 75.)

[Lambert *et al.* 1993] CJ Lambert, VC Hui and SJ Robinson. Multi-probe conductance formulae for mesoscopic superconductors. Journal of Physics: Condensed Matter, vol. 5, no. 25, page 4187, 1993. (Cited on page 58.)

[Landau & Lifshitz 2013] L. D. Landau and E. M. Lifshitz. Quantum mechanics: non-relativistic theory, volume 3. Elsevier, 2013. (Cited on page 139.)

[Landau 1930] L. D. Landau. Diamagnetismus der metalle. Zeitschrift für Physik, vol. 64, no. 9, pages 629–637, 1930. (Cited on pages 1 and 26.)

[Landauer 1957] R. Landauer. Spatial variation of currents and fields due to localized scatterers in metallic conduction. IBM Journal of research and development, vol. 1, no. 3, pages 223–231, 1957. (Cited on page 138.)

[Landauer 1992] R. Landauer. Conductance from transmission: common sense points. Physica Scripta, vol. 1992, no. T42, page 110, 1992. (Cited on page 138.)

[Lee *et al.* 2017] G.H. Lee, K.F. Huang, D. K. Efetov, Di S. Wei, S. Hart, T. Taniguchi, K. Watanabe, A. Yacoby and P. Kim. Inducing superconducting correlation in quantum Hall edge states. Nature Physics, vol. 13, no. 7, pages 693–698, 2017. (Cited on pages 6, 7, 8, 55, 56, 83 and 102.)

[Lindner *et al.* 2012] N. H. Lindner, E. Berg, G. Refael and A. Stern. Fractionalizing majorana fermions: Non-abelian statistics on the edges of abelian quantum hall states. Physical Review X, vol. 2, no. 4, page 041002, 2012. (Cited on page 102.)

[Liu *et al.* 2016] C.-X. Liu, S.-C. Zhang and X.-L. Qi. The quantum anomalous Hall effect: theory and experiment. Annual Review of Condensed Matter Physics, vol. 7, pages 301–321, 2016. (Cited on page 40.)

[Ludwig 2015] A. W. W. Ludwig. Topological phases: classification of topological insulators and superconductors of non-interacting fermions, and beyond. Physica Scripta, vol. 2016, no. T168, page 014001, 2015. (Cited on page 52.)

[Lutchyn *et al.* 2010] R. M. Lutchyn, J. D. Sau and S. D. Sarma. Majorana fermions and a topological phase transition in semiconductor-superconductor heterostructures. Physical review letters, vol. 105, no. 7, page 077001, 2010. (Cited on page 9.)

[Majorana 1937] E. Majorana. Teoria simmetrica dell'elettrone e del positrone. Il Nuovo Cimento (1924-1942), vol. 14, pages 171–184, 1937. (Cited on page 8.)

[Manesco *et al.* 2022] A. Manesco, I. M. Flór, C.-X. Liu and A. R. Akhmerov. Mechanisms of Andreev reflection in quantum Hall graphene. SciPost Physics Core, vol. 5, no. 3, page 045, 2022. (Cited on pages 7, 56 and 65.)

[Markoš & Soukoulis 2008] P. Markoš and C. M. Soukoulis. Wave propagation. from electrons to photonic crystals and left-handed materials, princeton university press. Princeton University Press, 2008. (Cited on page 132.)

[Martin 2005] T. Martin. Noise in mesoscopic physics. In Les Houches Session LXXXI. H. Bouchiat et. al. eds. (Elsevier), 2005. (Cited on page 138.)

[Meissner & Ochsenfeld 1933] W. Meissner and R. Ochsenfeld. Ein neuer effekt bei eintritt der supraleitfähigkeit. Naturwissenschaften, vol. 21, no. 44, pages 787–788, 1933. (Cited on pages 4 and 141.)

[Michelsen *et al.* 2023] A. B. Michelsen, P. Recher, B. Braunecker and T. L. Schmidt. Supercurrent-enabled Andreev reflection in a chiral quantum Hall edge state. Physical Review Research, vol. 5, no. 1, page 013066, 2023. (Cited on pages 75 and 82.)

[Mineev & Samokhin 1999] V. P. Mineev and K. Samokhin. Introduction to unconventional superconductivity. CRC Press, 1999. (Cited on page 93.)

[Moessner & Moore 2021] R. Moessner and J. E. Moore. Topological phases of matter. Cambridge University Press, 2021. (Cited on pages 39 and 40.)

[Mong *et al.* 2014] R. S. K. Mong, D. J. Clarke, J. Alicea, N. H. Lindner, P. Fendley, C. Nayak, Y. Oreg, A. Stern, E. Berg, K. Shtengelet al. Universal topological quantum computation from a superconductor-abelian quantum hall heterostructure. Physical Review X, vol. 4, no. 1, page 011036, 2014. (Cited on pages 55, 80 and 102.)

[Nayak *et al.* 2008] C. Nayak, S. H. Simon, A. Stern, M. Freedman and S. D. Sarma. Non-Abelian anyons and topological quantum computation. Reviews of Modern Physics, vol. 80, no. 3, page 1083, 2008. (Cited on pages 9, 55 and 80.)

[Neupert & Schindler 2018] T. Neupert and F. Schindler. Lecture Notes on Topological Crystalline Insulators. arXiv:1810.03484, 10 2018. (Cited on page 53.)

[Niu *et al.* 1985] Q. Niu, D. J. Thouless and Y.-S. Wu. Quantized Hall conductance as a topological invariant. Physical Review B, vol. 31, no. 6, page 3372, 1985. (Cited on page 39.)

[Novoselov *et al.* 2004] K. S. Novoselov, A. K. Geim, S. V. Morozov, D.-E. Jiang, Y. Zhang, S. V. Dubonos, I. V. Grigorieva and A. A. Firsov. Electric field effect in atomically thin carbon films. science, vol. 306, no. 5696, pages 666–669, 2004. (Cited on page 6.)

[Oreg *et al.* 2010] Y. Oreg, G. Refael and F. Von Oppen. Helical liquids and Majorana bound states in quantum wires. Physical review letters, vol. 105, no. 17, page 177002, 2010. (Cited on page 9.)

[Paalanen *et al.* 1982] M. A. Paalanen, D. C. Tsui and A. C. Gossard. Quantized Hall effect at low temperatures. Physical Review B, vol. 25, no. 8, page 5566, 1982. (Cited on page 2.)

[Peierls 1933] R. Peierls. Zur Theorie des Diamagnetismus von Leitungselektronen. Zeitschrift für Physik, vol. 80, no. 11-12, pages 763–791, nov 1933. (Cited on pages 37 and 151.)

[Prada *et al.* 2020] E. Prada, P. San-Jose, M W. A. de Moor, A. Geresdi, E. J. H. Lee, J. Klinovaja, D. Loss, J. Nygård, R. Aguado and L. P. Kouwenhoven. From Andreev to Majorana bound states in hybrid superconductor–semiconductor nanowires. Nature Reviews Physics, vol. 2, no. 10, pages 575–594, 2020. (Cited on page 102.)

[Prange & Girvin 1990] R. E. Prange and S. M. Girvin, editors. The quantum hall effect. Springer New York, 1990. (Cited on page 35.)

[Prange 1981] R. E. Prange. Quantized Hall resistance and the measurement of the fine-structure constant. Physical Review B, vol. 23, no. 9, page 4802, 1981. (Cited on pages 35 and 36.)

[Qi *et al.* 2006] X.-L. Qi, Y.-S. Wu and S.-C. Zhang. Topological quantization of the spin Hall effect in two-dimensional paramagnetic semiconductors. Physical Review B, vol. 74, no. 8, page 085308, 2006. (Cited on page 41.)

[Queiroz & Stern 2019] R. Queiroz and A. Stern. Splitting the Hinge Mode of Higher-Order Topological Insulators. Physical Review Letters, vol. 123, no. 3, 2019. (Cited on pages 5, 10, 104, 105, 107, 108, 114, 118, 121, 122, 124, 125 and 128.)

[Recher *et al.* 2001] P. Recher, E. V. Sukhorukov and D. Loss. Andreev tunneling, Coulomb blockade, and resonant transport of nonlocal spin-entangled electrons. Physical Review B, vol. 63, no. 16, page 165314, 2001. (Cited on page 21.)

[Russo *et al.* 2005] S. Russo, M. Kroug, T. M. Klapwijk and A. F. Morpurgo. Experimental observation of bias-dependent nonlocal Andreev reflection. Physical review letters, vol. 95, no. 2, page 027002, 2005. (Cited on page 21.)

[Schiller *et al.* 2022] N. Schiller, B. A. Katzir, A. Stern, E. Berg, N. H. Lindner and Y. Oreg. Interplay of superconductivity and dissipation in quantum Hall edges. arXiv preprint, vol. arXiv:2202.10475, 2022. (Cited on pages 7, 56 and 75.)

[Schindler *et al.* 2018a] F. Schindler, A. M. Cook, M. G. Vergniory, Z. Wang, Stuart SP Parkin, B. A. Bernevig and T. Neupert. Higher-order topological insulators. Science advances, vol. 4, no. 6, page eaat0346, 2018. (Cited on pages 4, 53, 104, 105 and 107.)

[Schindler *et al.* 2018b] F. Schindler, Z. Wang, M. G. Vergniory, A. M. Cook, A. Murani, S. Sengupta, A. Y. Kasumov, R. Deblock, S. Jeon, I. Drozdovet al. Higher-order topology in bismuth. Nature physics, vol. 14, no. 9, pages 918–924, 2018. (Cited on pages 4, 53, 104 and 107.)

[Schindler 2020] F. Schindler. Dirac equation perspective on higher-order topological insulators. Journal of Applied Physics, vol. 128, no. 22, page 221102, 2020. (Cited on page 53.)

[Shen *et al.* 2011] S.-Q. Shen, W.-Y. Shan and H.-Z. Lu. Topological insulator and the Dirac equation. Spin, vol. 1, no. 01, pages 33–44, 2011. (Cited on pages 4, 122 and 151.)

[Shen 2012] Shun-Qing Shen. Topological insulators, volume 174. Springer, 2012. (Cited on page 151.)

[Takagaki 1998] Y. Takagaki. Transport properties of semiconductor-superconductor junctions in quantizing magnetic fields. Physical Review B, vol. 57, no. 7, page 4009, 1998. (Cited on page 55.)

[Takane & Ebisawa 1992] Y. Takane and H. Ebisawa. Conductance formula for mesoscopic systems with a superconducting segment. Journal of the Physical Society of Japan, vol. 61, no. 5, pages 1685–1690, 1992. (Cited on pages 20 and 23.)

[Tanaka *et al.* 2012] Y. Tanaka, Z. Ren, T. Sato, K. Nakayama, S. Souma, T. Takahashi, K. Segawa and Y. Ando. Experimental realization of a topological crystalline insulator in SnTe. Nature Physics, vol. 8, no. 11, pages 800–803, 2012. (Cited on page 52.)

[Thouless *et al.* 1982] D. J. Thouless, M. Kohmoto, M. P. Nightingale and M. den Nijs. Quantized Hall conductance in a two-dimensional periodic potential. Physical review letters, vol. 49, no. 6, page 405, 1982. (Cited on pages 3, 38 and 40.)

[Tong 2016] D. Tong. Lectures on the Quantum Hall Effect. arXiv:1606.06687, 2016. (Cited on pages 31 and 39.)

[Usher & Elliott 2009] A. Usher and M. Elliott. Magnetometry of low-dimensional electron and hole systems. Journal of Physics: Condensed Matter, vol. 21, no. 10, page 103202, 2009. (Cited on page 35.)

[van Delft & Kes 2010] D. van Delft and P. Kes. The discovery of superconductivity. Physics Today, vol. 63, no. 9, pages 38–43, sep 2010. (Cited on pages 4 and 141.)

[Van Houten *et al.* 1989] H. Van Houten, C. W. J. Beenakker, J. G. Williamson, M. E. I. Broekaart, P. H. M. Van Loosdrecht, B. J. Van Wees, J. E. Mooij, C. T. Foxon and J. J. Harris. Coherent electron focusing with quantum point contacts in a two-dimensional electron gas. Physical Review B, vol. 39, no. 12, page 8556, 1989. (Cited on page 28.)

[van Ostaay *et al.* 2011] J. A. M. van Ostaay, A. R. Akhmerov and C. W. J. Beenakker. Spin-triplet supercurrent carried by quantum Hall edge states through a Josephson junction. Physical Review B, vol. 83, no. 19, 2011. (Cited on pages 55, 68 and 82.)

[von Klitzing *et al.* 1980] K. von Klitzing, G. Dorda and M. Pepper. New method for high-accuracy determination of the fine-structure constant based on quantized Hall resistance. Physical review letters, vol. 45, no. 6, page 494, 1980. (Cited on pages 1 and 25.)

[Wang *et al.* 2019] Z. Wang, B. J Wieder, J. Li, B. Yan and B. A. Bernevig. Higher-Order Topology, Monopole Nodal Lines, and the Origin of Large Fermi Arcs in Transition Metal Dichalcogenides X Te 2 (X= Mo, W). Physical review letters, vol. 123, no. 18, page 186401, 2019. (Cited on pages 53 and 104.)

[Zhao *et al.* 2020] L. Zhao, E. G. Arnault, A. Bondarev, A. Seredinski, T. FQ Larson, A. W. Draelos, H. Li, K. Watanabe, T. Taniguchi, F. Ametet al. Interference of chiral Andreev edge states. Nature Physics, vol. 16, no. 8, pages 862–867, 2020. (Cited on pages 6, 7, 55, 56 and 75.)

[Zhao *et al.* 2022] L. Zhao, Z. Iftikhar, T. F. Q. Larson, E. G. Arnault, K. Watanabe, T. Taniguchi, F. Amet and G. Finkelstein. Loss and decoherence at the quantum Hall-superconductor interface. arXiv preprint, vol. arXiv:2210.04842, 2022. (Cited on pages 55 and 56.)

[Zülicke *et al.* 2001] U. Zülicke, H. Hoppe and Gerd Schön. Andreev reflection at superconductor–semiconductor interfaces in high magnetic fields. Physica B: Condensed Matter, vol. 298, no. 1, pages 453–456, 2001. International Conference on High Magnetic Fields in Semiconductors. (Cited on page 55.)